THE UNIVERSITY of ADELAIDE

Soft glass optical fibres for telecommunications applications

by

H. Tilanka Munasinghe

A thesis submitted in partial fulfillment for the degree of Doctor of Philosophy

in the

Faculty of Sciences
School of Physical Sciences

May 2015

Declaration of Authorship

I, Hashan Tilanka Munsinghe, declare that this thesis titled, 'Soft glass optical fibres for telecommunications applications' and the work presented in it are my own.

I certify that this work contains no material which has been accepted for the award of any other degree or diploma in any university or other tertiary institution and, to the best of my knowledge and belief, contains no material previously published or written by another person, except where due reference has been made in the text.

I certify that no part of this work will, in the future, be used in a submission for any other degree or diploma in any university or other tertiary institution without the prior approval of the University of Adelaide and where applicable, any partner institution responsible for the joint-award of this degree.

I give consent to this copy of my thesis when deposited in the University Library, being made available for loan and photocopying, subject to the provisions of the Copyright Act 1968. The author acknowledges that copyright of published works contained within this thesis resides with the copyright holder(s) of those works.

I also give permission for the digital version of my thesis to be made available on the web, via the University's digital research repository, the Library catalogue and also through web search engines, unless permission has been granted by the University to restrict access for a period of time.

Signed: _____

Date: _____

UNIVERSITY OF ADELAIDE

Abstract

Faculty of Sciences
School of Physical Sciences

Doctor of Philosophy

by H. Tilanka Munasinghe

As the appetite for data use across telecommunications networks is predicted to continue to grow rapidly in the coming years, there is an increasing need to address the bandwidth gap that exists between the optical links that underpin high speed networks and the electronic layer typically used for processing signals at the endpoints. Nonlinear fibre optics is a potential avenue to addressing this bandwidth bottleneck, where nonlinear optical phenomena can be exploited to perform signal processing tasks, thereby allowing the broad bandwidth of optical media to be used for signal processing as well as transmission. Indeed the development of such optical signal processing devices is crucial to moving towards the next generation of communications technology – where ultra fast telecommunication networks with speeds approaching 1 Tb/s are required.

This work explored the use of the enhanced optical nonlinearity and dispersion engineering possible in soft glass microstructured fibres as a basis for developing devices for broadband telecommunications applications at 1.55 µm. Two applications were considered in this research, namely multicasting and phase sensitive amplification – both of which are signal processing applications that are important to the realisation of all optical networks.

A number of soft glass materials were studied in this research, primarily those with high nonlinear refractive indices such as chalcogenides, tellurites, bismuth oxide based glasses and germanates. During the course of this work a novel lead germanate glass was also developed. This glass was shown to have a high nonlinear index and relatively high mechanical strength when compared to tellurite glasses of similar refractive indices.

Dispersion tailored, soft glass fibre designs were developed for both multicasting and phase sensitive amplification. The design geometry, referred to as a 'hexagonal wagon wheel design', was a hybrid model combining a hexagonal array geometry for dispersion engineering with a suspended core or 'wagon wheel' geometry for high nonlinearity. The fibre designs were optimised for each application by using a genetic algorithm

based optimisation technique to achieve high and broad gain suitable for efficient signal processing at extremely high bit rates.

Each fibre design was modelled for its intended application to demonstrate, numerically, that the designs were indeed capable of performing their intended application over a broad band. The modelling work used a numerical beam propagation model and demonstrated that the designs were capable of operating at the extremely high bit rate of 640 Gb/s.

Advances were made to fabrication techniques during the fabrication trials of these novel designs due to the complex nature of the designs and, in some cases, the use of novel materials. A first generation, simplified hexagonal wagon wheel fibre was fabricated in the novel germanate glass developed earlier. A number of characterisation experiments were also performed on fabricated microstructured fibres, including a measurement of the dispersion profile for a tellurite fibre (that was shown to be in good agreement with modelling results) and the measurement of the nonlinear index for a fibre fabricated with the novel germanate glass – one of the few such measurements in the literature for this family of glasses.

In addition to these fabrication advances and characterisation experiments, a study of dispersive waves was performed on previously fabricated hexagonal wagon wheel fibres in collaboration with colleagues at the University of California, Merced. These experiments were used to study soliton propagation in these fibres at near infrared wavelengths. Comparison of experimental data to theoretical models is shown to have good agreement – an important validation of the modelling technique.

Acknowledgements

This thesis would not be possible without the contributions of many others throughout my research journey. First and foremost, I would like to thank my supervisors, Prof. Tanya Monro and A/Prof. Shahraam Afshar Vahid, for their continuous guidance and commitment throughout my candidature. I would also like to thank A/Prof. Heike Ebendorff-Heidepriem for taking the time to provide valuable input and guidance on the glass and fibre fabrication aspects of this work.

I would also like to acknowledge my colleague Dr. Wen Qi Zhang for his help and for providing some of the modelling code that is used in this work.

Finally, I must express my gratitude to my family and those close to me for their encouragement and support throughout.

Contents

Abbreviations

CW	**C**ontinuous **W**ave
DPSK	**D**ifferential **P**hase **S**hift **K**eying
DSC	**D**ifferential **S**canning **C**alorimetry
EDFA	**E**rbium **D**oped **F**ibre **A**mplifier
ETDM	**E**lectrical **T**ime **D**omain **M**ultiplexing
FFT	**F**ast **F**ourier **T**ransform
FEM	**F**inite **E**lement **M**ethod
FWM	**F**our **W**ave **M**ixing
FWHM	**F**ull **W**idth at **H**alf **M**aximum
HWW	**H**exagonal **W**agon **W**heel
HNLF	**H**ighly **N**on**L**inear **F**ibre
MOF	**M**icrostructured **O**ptical **F**ibre
MPASS	**M**ulticast **P**arametric **S**ynchronous **S**ampling
NSE	**N**onlinear **S**chrödinger **E**quation
OOK	**O**n **O**ff **K**eyed
OPO	**O**ptical **P**arametric **O**scillator
OSA	**O**ptical **S**pectrum **A**nalyser
OTD	**O**ptical **T**ime **D**ivision
PCF	**P**hotonic **C**rystal **F**ibre
PSA	**P**hase **S**ensitive **A**mplification
PPM	**P**ulse **P**ropagation **M**odel
SEM	**S**canning **E**lectron **M**icrograph
SPM	**S**elf **P**hase **M**odulation
SBS	**S**timulated **B**rillouin **S**cattering
SRS	**S**timulated **R**aman **S**cattering

VASE **V**ariable **A**ngle **S**pectroscopic **E**llipsometry

WDM **W**avelength **D**ivision **M**ultiplexing

XPM **C**ross **P**hase **M**odulation

ZDW **Z**ero **D**ispersion **W**avelength

List of Figures

List of Tables

Chapter 1

Introduction

Fibre optic technology forms the backbone of modern telecommunication systems the world over. Since they were first conceived, in the late 1960s, optical fibres have revolutionised the telecommunications industry, replacing long haul copper links due to the better data transmission capacity, low attenuation and resistance to electromagnetic interference that they provide.

Current commercial telecommunications networks are able to deliver throughput rates in the Mb/s to Gb/s regime by leveraging a combination of optical fibre and electronic technology – typically, optical fibres are used for the transmission of data, especially over long distances, while electronic systems are used in the processing of data at the network endpoints.

As the amount of bandwidth used across these networks increases, future systems will be required to operate at much higher bit rates – from 100s of Gb/s to 1 Tb/s and beyond. At these bit rates fibre optics will have an increasingly important role to play, beyond simply the transmission of data. The high speed processing required for these future networks is best achieved in optical media, due to the inherently high bandwidth they provide.

Consequently, there is a need for all optical devices in the processing layer to work alongside the optical links used for data transmission. Such devices would be able to utilise the inherent bandwidth of optical fibres to perform high speed signal processing and thus avoid costly and inefficient optical-to-electrical conversion.

The research project documented in this thesis, investigated the use of novel materials and fibre structures to fabricate fibres with high nonlinearity and engineered dispersion that may be used as the basis for such signal processing devices.

The background and motivation behind this work is discussed in Section 1.1. The aims and methodology used in this work are presented in Section 1.2, followed by an overall outline of the subsequent chapters of this thesis in Section 1.3. A statement of original work detailing the author's contributions to this work and original content may be found in Section 1.4. This chapter concludes with a list of publications related to this thesis in Section 1.5.

1.1 Background and motivation

The concept of using optical fibres for communication networks was first introduced to the world by the ground breaking work of Charles Kao in the 1960s. In a seminal paper entitled *'Dielectric-fibre surface waveguides for optical frequencies'*, Kao and his team were the first to realistically propose using light guided in optical fibres to boost the bandwidth of telecommunication networks [10]. Published in 1966, this date is widely regarded as being the point at which the field of optical communications was born.

Kao *et. al.* showed that optical fibre links could be incorporated into communication networks, if waveguides at optical frequencies could be fabricated with losses lower than 20 dB/km – a threshold that was also forecast as achievable due to it being much lower that the loss limit imposed by fundamental material properties. This was a revolutionary idea since, at the time, the most transparent glasses had losses of roughly 200 dB/km – thought to be predominantly due to intrinsic scattering loss[1] of the material. The results from Kao's team however showed that the contribution from scattering loss could be as low as 1 dB/km and that the bulk of the loss was instead caused by impurities in the glass, specifically Fe^{++} and Fe^{+++} ions. Kao's team proposed that the 20 dB/km threshold could be reached by focussing on reducing the level of iron impurities in the glass to approximately 1 part per million.

[1]The scattering loss, in this case, refers to the loss caused by the scattering of the light wave by density fluctuations that occur during fabrication of the glass. Scattering loss can also be caused if the glass contains particle impurities that are comparable in size to the wavelength of the light.

It would take another four years before sub 20 dB/km loss fibres were actually fabricated – researchers at the Corning Glass Company were the first to demonstrate a 'low loss' fibre, with a loss of 17 dB/km at 0.63 µm [11]. Two years later, they produced a fibre with approximately 4 dB/km loss by modifying the glass material.

The first commercial fibre network was deployed shortly after, in 1976, using Ga-As semiconductor lasers as the source and operating at a wavelength 0.8 µm. Subsequent developments in optical sources and materials moved the operating wavelength for optical fibre networks to 1.3 µm and, then to the currently used wavelength of 1.55 µm when Miya *et. al.* fabricated an 'ultimate low-loss' fibre with attenuation of only 0.2 dB/km at 1.55 µm [12].

Since the deployments of the first commercial fibre networks in the 1970s and 1980s, the fibre industry has expanded quite significantly. Optical fibres are now commonplace in modern telecommunications systems, criss-crossing the globe and enabling networks with capacities of up to hundreds of megabytes a second. Their capacity for data transmission, especially over long distances have seen them largely replace copper as the backbone high speed information networks. The significance of Kao's work in realising these modern communication networks was recognized in 2009, when he was awarded half of the Nobel prize in physics [13].

The development of low loss fibres eventually led to a new field – nonlinear fibre optics. Nonlinear optics is the study of how light behaves in media where the dielectric polarisation responds in a nonlinear fashion to the electric field of the interacting light. It had been studied both experimentally and theoretically throughout the 1960s, shortly after the invention of the laser. However, using fibres for nonlinear optics had not been seriously considered due to the relatively low intrinsic nonlinearity and high losses in glass fibres at the time. This changed once low loss fibres became available as the long interaction length coupled with the small spot size (and thus high field intensity) of the guided wave in optical fibres made them much more conducive to generating observable nonlinear effects. Interest in the field of nonlinear fibre optics was increased further when optical fibres were shown to be able to support the transmission of optical solitons [14] – pulses that are remarkably resistant to distortion, maintaining their shape over large distances due to a combination of dispersive and nonlinear effects.

In the decades since, the field of nonlinear fibre optics has grown quite rapidly, leading to a number of significant developments for optical communications such as Raman fibre optic amplifiers operating in the region of 1.55 µm, which have had significant ramifications for long haul communication systems [15]. This growth in the field of nonlinear fibre optics has been significantly aided by the advent of microstructured optical fibres (MOFs) in the late 1990s, which created numerous possible applications by allowing the dispersion to be controlled and the nonlinearity to be enhanced and thus generate a wide range of dynamic effects [16].

As the appetite for data use across telecommunications networks is predicted to grow rapidly in the coming years (extrapolation of empirical data predicts a growth rate of approximately 10 times Moore's law for integrated circuits [17]), there is an increasing need to address the bandwidth gap that exists between the optical links and the electronic processing layer. Nonlinear fibre optics is a potential avenue to addressing this bandwidth bottleneck. Nonlinear optical phenomena can be exploited to perform signal processing tasks such as wavelength conversion [18, 19], 3R (reamplification, reshaping, and retiming) signal regeneration [20, 21], switching [22, 23], amplification [24] and multiplexing/demultiplexing [25], thereby allowing the broad bandwidth of optical media to be used for signal processing as well as transmission. Indeed the development of such optical signal processing devices is crucial to moving towards the next generation of communications technology – where ultra fast telecommunication networks with speeds approaching 1 Tb/s are required, well beyond the 40-160 Gb/s signal processing range of the best electronic systems currently available [26, 27].

These nonlinear signal processing devices may be created by harnessing the dispersion and nonlinearity control provided by microstructured optical fibres (MOFs). MOFs (also sometimes known as holey fibres or photonic crystal fibres [PCFs]) generally consist of a core region surrounded by a cladding that contains a number of small air holes or other small features that affect the guidance of light within the fibre. It is the arrangement of these 'microstructures' that determine key optical properties such as nonlinearity and dispersion. The fibre characteristics can therefore be engineered via the geometry to enhance specific nonlinear phenomena.

The realisation of efficient nonlinear devices that are able to operate at bit rates approaching 1 Tb/s and beyond may also require looking beyond silica as the substrate

material. While silica has long been the material of choice for fibre optic applications due to its excellent transmission and robustness, the potential for using silica in broadband nonlinear optics applications is limited by its relatively low nonlinear refractive index of 0.2×10^{-19} m^2W^{-1} [28]. This, in turn, limits the effective nonlinear coefficient – a key parameter that determines nonlinear signal processing performance (Section 2.2.3 describes this parameter in detail) and requires relatively high powers and/or long fibre lengths, typically in the order of 100 m, to be used when using silica based fibres for nonlinear applications.

This has seen soft glass fibres emerge as an attractive platform for the fabrication of nonlinear optical devices. Soft glasses typically possess both a higher linear and nonlinear index, relative to fused silica. The nonlinear index can sometimes be higher by orders of magnitude – IG5 chalcogenide glass, for instance, has a nonlinear refractive index of 400×10^{-19} m^2W^{-1} [29] (see Table 3.2 for a comparison of refractive indices between silica and soft glasses). They are also, as the name suggests relatively much 'softer' – the temperature at which the glass softens is generally around a few hundred degrees, which enables the fabrication of complex structures via extrusion through steel (see Figure 6.1 for some examples). The extrusion based fabrication technique for MOFs allows the fabrication of fibre geometries that are not readily attainable by alternative methods such as the 'stack and draw' technique typically used when fabricating silica MOFs [30, 31] (Section 6.2 describes these fabrication techniques in detail). This ability to fabricate complex geometries into the glass enables dispersion control that may be finer and applied over a broader range – another key parameter in nonlinear signal processing applications (again, refer to Section 2.2.3 for details).

Consequently soft glass microstructured optical fibres, with broad band dispersion control via engineering the fibre geometry, are promising candidates for the fabrication of next generation nonlinear fibre optic devices. This research investigated coupling a number of promising compositions of soft glasses (namely tellurites, germanates and chalcogenides) with an optimised fibre design to produce fibres with the required optical properties for broadband nonlinear applications. The work involved numerical modelling, design of novel fibre geometries, fabrication trials in soft glass materials and experimental work characterising fibres. The main aims and methodologies used in this research are described in the following section.

1.2 Thesis aims and methodology

The aim of this work was to develop soft glass microstructured fibres for two specific nonlinear telecommunications applications at 1.55 µm, while improving the understanding of how dispersion engineering in soft glasses, using a genetic algorithm optimisation method, can be used to develop a tailored fibre design for these applications. The two applications investigated were: multicasting and phase sensitive amplification (PSA) – both of which are based on the four wave mixing (FWM) phenomenon. Multicasting is used to copy a signal into a number of copies for processing while PSA is a regeneration application for reducing noise in phase encoded signals. These applications are described in detail in Section 2.4, which also contains a review of the relevant literature pertaining to each application.

The desired dispersion characteristics for the fibres developed in this research were that the dispersion be low and flat over a broad band centred around 1.55 µm. In addition to this, the fibres needed to have a high nonlinear coefficient so that the gain would be high across the low dispersion band. To meet these goals, this research explored the premise of using soft glass microstructured optical fibres, where the intrinsically high nonlinearity of the soft glass could be combined with a tailored microstructured fibre geometry to produce fibres with the desired optical characteristics for the application at hand.

The pursuit of the primary goal of this research may be broken down into the following set of objectives

- The identification, via theoretical analysis, of the set of optical parameters required of the fibre for it to be used in the desired application, with practical input power.
- The identification of suitable soft glass materials for fibre fabrication. This work eventually led to the development and optical characterisation of a novel lead glass composition which was found to have a high nonlinearity and mechanical strength
- The development of computational models for both the design of the fibre and the evaluation of these designs via a numerical pulse propagation model.
- The development and advancement of fibre fabrication techniques to produce the designed fibres.

- The experimental characterisation of the fabricated fibres.
- The confirmation of the numerical modelling procedure via fibre experiments.

The methodology used in this thesis may be summarised as follows.

The initial stages of this work comprised of a theoretical analysis of the intended application. This was aimed at broadly determining the characteristics, such as nonlinearity and dispersion profile, required of the fibre.

Once this was determined, the next step was deciding what material and design geometry to use in the fabrication of the fibre, such that it would have the required nonlinearity and dispersion. Soft glasses were chosen to be the substrate materials in these fibres for two main reasons: they typically have a high nonlinear refractive refractive index which leads to a high nonlinear coefficient; and soft glasses may be extruded into complex geometries which allow for dispersion control over extremely broad bandwidths [31].

The approach used in the design process was to combine two commonly used microstructured fibre geometries: the suspended core design (shown in Figure 1.1(a)) and the hexagonal array design (also referred to as the triangular array design, shown in Figure 1.1(b)), into a hybrid geometry termed the 'hexagonal wagon wheel' design. The suspended core design enables a high nonlinearity as the mode is guided in a small area which, as described in Section 4.2, is inversely proportional to the nonlinear coefficient. The hexagonal design facilitates engineering of the dispersion profile as the size and placement of the holes can be used to control the effective index of the mode over a range of wavelengths, and thus the dispersion of the waveguide (again, details on how this is achieved are given in Section 4.2).

The hexagonal wagon wheel design combines the nonlinearity enhancement of the suspended core design with the dispersion engineering ability of the hexagonal array. The hybrid geometry was also optimised for the intended application by using a genetic algorithm based optimisation procedure.

Computational modelling was used in the design phase and to model the final design to predict and validate the behaviour of the fibre before fabrication. Modelling was also used to validate optical properties such as dispersion for some fabricated fibres.

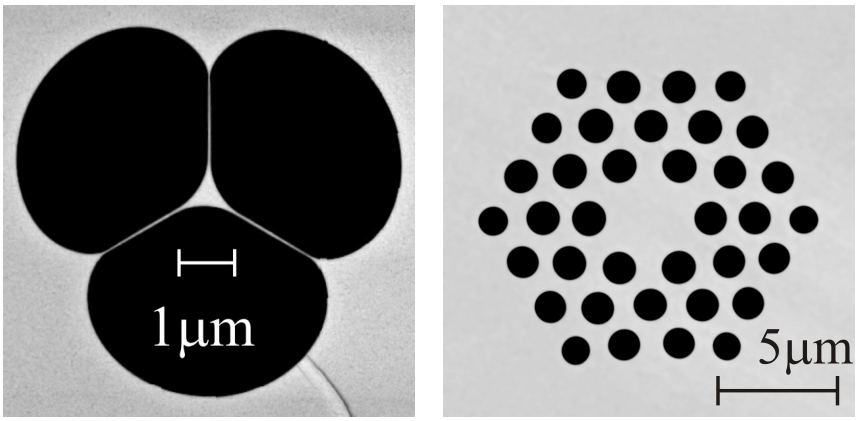

(a)) (b)

FIGURE 1.1: An example of the suspended core or 'wagon wheel' type fibre design is shown on the left in (a) [1], while the hexagonal array design is shown on the right in (b) [2]. The approach used in this work was to combine the two design types to create a hybrid geometry termed the 'hexagonal wagon wheel' design (Section 4.5 describes the design process in detail).

The fibre fabrication was done using the extrusion technique, where custom made steel dies were used to fabricate the designed structure into the fibre.

The following section outlines the rest of this thesis, describing the aspects of the work contained in each chapter.

1.3 Thesis outline

The structure of the rest of this thesis may be outlined as follows

Chapter 2 – Nonlinear telecommunications applications

This chapter covers the theoretical underpinnings of nonlinear fibre optics and how it relates to the nonlinear telecommunications applications studied in this research. The aim is to show how fibre nonlinearities and nonlinear phenomena may be harnessed to perform telecommunications applications, specifically the signal processing applications studied in this research. The focus in this chapter is on the four wave mixing phenomenon as it is the basis for the signal processing applications studied herein. This chapter also contains a review of the literature, discussing the state of the art in the two signal processing applications that this work relates to.

Chapter 3 – Soft glass

Due to the important role played by the fibre properties, such as dispersion and nonlinearity, in optical signal processing applications, the choice of fibre material is consequently also an important one. In this chapter soft glasses are presented as promising candidates for the fabrication of fibres for nonlinear signal processing applications. This chapter covers the fundamentals of glasses before delving into the particular characteristics of soft glasses, such as the high nonlinear refractive index, which facilitate the development of fibres for nonlinearity based applications.

This chapter also describes the fabrication of a novel, germanate soft glass. This glass is shown to have good potential for use in nonlinear fibres use due to its high material nonlinearity and relatively high mechanical and thermal stability. The measurement of the nonlinear index for this glass is one of the few characterisations of nonlinearity for germanate glasses. This work was published and can be found in Reference [32].

Chapter 4 – Fibre design

This chapter builds on the theoretical work outlined in Chapter 2 and the properties of soft glasses described in Chapter 3 to describe the fibre design process and how the specific choice of material and fibre geometry affect the key fibre properties such as nonlinearity, dispersion and loss. It describes how soft glasses may be harnessed for the development of nonlinear telecommunications applications fibres by using the fibre geometry to engineer the key fibre properties, especially dispersion, into a optimal profile for the application of interest.

This chapter outlines the various fibre designs that have been used in the literature for dispersion engineering and then introduces the design approach used in this research – a genetic algorithm based optimisation of a a fibre design that is a hybrid of a hexagonal array MOF and a suspended core, or wagon wheel, fibre. This design is referred to as the hexagonal wagon wheel (HWW) fibre design.

Chapter 5 – Modelling of fibre designs

This chapter documents the pulse propagation modelling work done on the optimised hexagonal wagon wheel fibre designs presented in the previous chapter. The modelling work was done to to demonstrate, numerically, that the designed fibres were indeed capable of performing their intended application.

The modelling work on the fibre designed for phase sensitive amplification was published and can be found in Reference [33].

Chapter 6 – Fibre fabrication

This chapter describes the work done on fabricating the fibres designed and modelled in Chapters 4 and 5, respectively. This fibre fabrication work was based on using the extrusion technique to create glass preforms which are then drawn down into fibre. Results are presented on fabrication trials, with both the tellurite and germanate soft glasses glasses, aimed at realising a fibre with the hexagonal wagon wheel structure. These results document the advances made to fabrication techniques as a result of the complex structures and, in some cases, novel materials that were used in the fabrication process.

Chapter 7 – Fibre characterisation

Characterisation experiments performed on various fibres, including those fabricated in Chapter 6 are documented in this chapter. This includes measurements of fundamental fibre properties such as nonlinearity, dispersion and loss. The nonlinearity characterisation experiments were carried out on the novel germanate glass, first introduced in Chapter 3 and published in Reference [32].

Chapter 8 –Dispersive wave generation

In addition to the characterisation experiments described in Chapter 7, the experimental study of nonlinear processes is also key to fully characterising fabricated fibres and verifying the modelling process by providing experimental results to compare with

simulations. As such, this chapter describes a body of work done in collaboration with colleagues at the University of California, Merced where the opportunity was taken to study soliton propagation and the generation of dispersive waves in hexagonal wagon wheel fibres. This experimental work demonstrates how such fibres can be used to generate new wavelengths via nonlinear effects. The experimental data is compared with theoretical models and shown to have good agreement – an important validation of the modelling technique.

Chapter 9 – Conclusion

This is the final chapter of this thesis. It provides a general conclusion and outlines some potential areas for future work.

1.4 Statement of Original Work and Author Contribution

The content presented herein was written by myself under the guidance of my supervisors whose feedback was used in the editing of this thesis. In general this work is, to the best of our knowledge, original and the declaration below describes the author's contribution to the aspects of each chapter.

- **Chapter 2**

  The fundamentals of nonlinear optical theory presented in Section 2.2.1 are well known theories adapted from various sources, mainly References [34] and [35]. The theory for the multicasting application is adapted from References [36] and [37]. The theoretical description of phase sensitive amplification is adapted from [38]. In all cases these well known theories were collated by the author and adapted to the formalism used in this work. The content presented in Section 2.4 is based on a review of the literature conducted by the author.

- **Chapter 3**

  The background information on glasses in general, soft glasses and their properties was written based on a review of the various literature on these subjects, with

references in the content. The work on the development of the novel germanate glass presented in Section 3.5 was done in conjunction with researchers from within the author's own research institute and colleagues from other institutes. The glass fabrication work and measurement of density and thermal properties were carried out by Anja Winterstein-Beckmann from the Otto-Schott-Institute at the University of Jena and and Christian Schiele from the Department of Materials Science at the University of Erlangen. The measurements of the Raman spectra were conducted by Danilo Manzani while the loss measurements were conducted by Heike Ebendorff-Heidepriem, both from the same institution as the author. The measurements of refractive index and nonlinearity were carried out by the author.

- **Chapter 4**

  The wave propagation fundamentals presented in Section 2.2.2 were adapted from [34, 35, 39] and again collated and presented in the formalism used throughout the rest of this work. All the design and modelling work was done by the author. The program used to run the genetic algorithm was developed internally by a colleague, Wen Qi Zhang, however its application and analysis of results were all undertaken by the author.

- **Chapter 5**

  All the modelling work and analysis were done by the author.

- **Chapter 6**

  All the extrusion work was done by the author. The fibre draws were performed in conjunction with draw tower operators Roger Moore and Alastair Dowler.

- **Chapter 7**

  The experimental setup used in the dispersion measurement was based on a setup used by a colleague Matthew Henderson to measure dispersion in Silica fibres. All the experimental work in this chapter was done by the author.

- **Chapter 8**

  The dispersive wave experiments were performed in collaboration with Leily Kiani and Jay Sharping from the University of California (UC), Merced. The experiments were performed by the author in collaboration with Leily Kiani in the labs supervised by Jay Sharping at UC, Merced with fibres fabricated at the author's institution. The subsequent analysis, modelling and comparisons to theory were done by the author.

1.5 List of publications

The publications resulting from this work are listed below

Journal publications

1. H. Tilanka Munasinghe, Shahraam V Afshar, and Tanya M Monro. Highly Nonlinear and Dispersion-Flattened Fiber Design for Ultrafast Phase-Sensitive Amplification. *Journal of Lightwave Technology*, 30(21):3440–3447, 2012. doi: 10.1109/JLT.2012.2215307. URL http://ieeexplore.ieee.org/xpl/articleDetails.jsp?arnumber=6286974

2. H. Tilanka Munasinghe, Anja Winterstein-Beckmann, Christian Schiele, Danilo Manzani, Lothar Wondraczek, Shahraam Afshar V., Tanya M. Monro, and Heike Ebendorff-Heidepriem. Lead-germanate glasses and fibers: a practical alternative to tellurite for nonlinear fiber applications. *Optical Materials Express*, 3(9):1488, August 2013. ISSN 2159-3930. doi: 10.1364/OME.3.001488. URL http://www.opticsinfobase.org/ome/abstract.cfm?URI=ome-3-9-1488

Conference publications

1. H Tilanka Munasinghe, Wen Qi Zhang, Nikola Alic, Camille-sophie Bres, Stojan Radic, Tanya M Monro, and Shahraam Afshar V. Design of a Tellurite Microstructured Optical Fibre for Self-Seeded Multicasting for Ultra-Fast Signal Processing. In *Proceedings of the Australasian Conference on Optics, Lasers and Spectroscopy and Australian Conference on Optical Fibre Technology in association with the International Workshop on Dissipative Solitons*, pages 280–281, 2009. URL http://digital.library.adelaide.edu.au/dspace/handle/2440/57712

2. H Tilanka Munasinghe, Tanya M Monro, and Shahraam V Afshar. The effect of sub-wavelength guidance on mode propagation and dispersion in high index optical waveguides. In *2010 Conference on Optoelectronic and Microelectronic Materials and Devices*, pages 75—-76, Canberra, Australia, 2010. doi: 10.1109/COMMAD.2010.5699787

3. H. Tilanka Munasinghe, Shahraam V Afshar, and Tanya M Monro. Highly nonlinear, low dispersion fibres for telecommunications applications. *... on Optical Fibre ...*, 57:4–5, 2010. URL http://digital.library.adelaide.edu.au/dspace/handle/2440/63657

4. H. Tilanka Munasinghe, Shahraam Afshar V., David J. Richardson, and Tanya M. Monro. Nonlinear fibre design for broadband phase sensitive amplification. In *Proceedings of the*

International Quantum Electronics Conference and Conference on Lasers and Electro-Optics Pacific Rim 2011, page C702. Optical Society of America, August 2011. URL http://www.opticsinfobase.org/abstract.cfm?URI=CLEOPR-2011-C702

5. Leily Kiani, Tilanka Munasinghe, Wen Qi Zhang, Shahraam Afshar, and Jay Sharping. Linear and nonlinear properties in soft glass optical fibers for device applications. *Bulletin of the American Physical Society*, Volume 57,, February 2012. URL http://meetings.aps.org/link/BAPS.2012.MAR.S1.9

Chapter 2

Nonlinear telecommunications applications

2.1 Introduction

With careful design, the nonlinearity in optical fibres can be utilised to create devices that may be used in several telecommunications applications [45]. All optical switching [46–48] and optical signal regeneration [49–52], for instance, are examples of nonlinear telecommunications applications that can be performed in optical fibre based devices. A key advantage to using optical nonlinearity for these applications is that the signal is processed optically instead of electronically, where it has access to the significantly larger bandwidth that fibres provide (in comparison to copper). This facilitates the development of all optical telecommunications networks which are becoming increasingly important as signal rates approaching 1 Tb/s become more common [53].

To comprehend how these applications work and design for them, one must first develop an understanding of nonlinear effects in optical fibres. Indeed such an understanding is crucial to the overall design of optical telecommunications networks. For long haul transmission links over thousands of kilometres, where losses are very low, even small nonlinearities build up and can lead to a host of undesirable effects. These include pulse broadening [54, 55], cross talk [56, 57] or even physical damage. Additionally, Kerr nonlinear effects (discussed in detail in Section 2.2.1), can cause signal distortions

and introduce nonlinear noise which, according to the Shannon theorem [58], limits the information transmission capacity [59] of the fibre.

Thus, when optical fibres are used in the *transmission* of data, it is important to manage these nonlinear effects by ensuring that the light wave travelling down the fibre is kept within appropriate power thresholds [60, 61].

However, the same processes that give rise to undesirable nonlinear effects in signal transmission can also be used in the processing of optical signals. These nonlinear processes are generally one of the following types: stimulated Brillouin scattering (SBS), stimulated Raman scattering (SRS), self phase modulation (SPM), cross phase modulation (XPM), and four wave mixing (FWM) [34]. While they have all been used for a variety of applications, the applications considered in this work revolve around signal regeneration and amplification and thus we chose to focus on FWM. The FWM process is useful for such applications due to its ability to generate new, phase conjugated wavelengths from an initial signal, across a broad bandwidth.

The aim of this chapter is to review the relevant background literature and provide a theoretical basis for the two FWM based signal processing applications that this research is based on – multicasting and phase sensitive amplification (PSA). It is organised as follows: theoretical fundamentals describing the basis for the optical phenomena relevant to this work are presented in Section 2.2, including how nonlinearity originates and how it leads to effects such as the nonlinear refractive index and a description of the key fibre parameters such as nonlinearity and dispersion. The theoretical foundations of the four wave mixing process, that both multicasting and phase sensitive amplification are based on, is discussed in Section 2.3. Section 2.4 then describes how FWM is applied in optical signal processing, with a focus on the multicasting (Section 2.4.1.2) and phase sensitive amplification (Section 2.4.1.2) applications studied in this research.

Each application subsection within Section 2.4 consists of a theoretical overview and a discussion on the design considerations that must be taken into account when designing optical fibres for the application. The theoretical overview is based on existing literature and summarises the underlying physics behind each application. The design considerations build on the previously presented theoretical knowledge, outlining how the requirements for the key fibre properties, such as dispersion and nonlinearity, can be met during the fibre design process.

2.2 Theoretical fundamentals

This section provides a theoretical overview of optical nonlinearity and wave propagation in dielectric media and also introduces some key fibre parameters that are used in the design and modelling of optical fibres. It is organised into subsections as follows: Section 2.2.1 introduces optical nonlinearity and describes how it originates within dielectric materials in the presence of an optical field. Section 2.2.2 describes the equations that govern the propagation of an optical wave and discusses how they are derived from Maxwell's fundamental equations for all electromagnetic waves. The form of the solutions to these equations is also presented and used to show how some key parameters, such as the propagation constant, originate. Section 2.2.3 follows from this and describes the major fibre parameters, such as dispersion and nonlinearity, that are used in the fibre design process.

The derivations and formalism presented in this section have been adapted mainly from References [34, 35, 39]. They have been collated here to provide a theoretical framework that will be used in the discussion of the design and modelling work presented in the rest of this thesis.

2.2.1 Optical nonlinearity

For most conditions under which light interacts with a dielectric medium, the response of the medium to the incident light is linear. However, if the intensity of the incident electromagnetic wave is of a sufficiently high intensity, this response becomes nonlinear and results in a host of interesting nonlinear effects. The light intensity required to trigger these nonlinear effects is generally one that is comparable to the electric fields between the electrons and nuclei that make up the dielectric medium [62].

Physically, this is a consequence of how the bound electrons in the medium interact with the electric field of the light wave. The opposing influence, on the electrons of the medium, of the electric field of the light wave and their host nuclei results in an induced polarisation. This strength of this induced polarisation is dependent on the strength of the electric field (which is why it takes light of a sufficiently high intensity for nonlinear effects to become apparent) In general, we may write the induced polarisation as

$$\mathbf{P}(\mathbf{r},t) = \varepsilon_0 \left(\chi^{(1)}\mathbf{E}(\mathbf{r},t) + \chi^{(2)}[\mathbf{E}(\mathbf{r},t)]^2 + \chi^{(3)}[\mathbf{E}(\mathbf{r},t)]^3 + ... + \chi^{(n)}[\mathbf{E}(\mathbf{r},t)]^n \right), \quad (2.1)$$

where ε_0 is the free space permittivity, $\chi^{(1)}$ is the linear susceptibility, $\chi^{(2)}$ is the second order susceptibility and so on up to $\chi^{(n)}$ – the n^{th} order susceptibility which is a tensor of rank $n+1$. The predominant contribution to $\mathbf{P}$ comes from the linear susceptibility as the higher order terms are typically many orders of magnitude lower.

For amorphous materials, such as glasses, the molecules possess an inversion symmetry (also known as centrosymmetry) where any point at (x, y, z) in the lattice is indistinguishable from the point $(-x, -y, -x)$. As a consequence $\chi^{(2)}$, and indeed all even order susceptibilities, are zero for such materials. To see how this originates we first consider the polarisation induced by an electric field propagating in a certain direction. According to Equation 2.1, this is given by

$$\mathbf{P} = \varepsilon_0 \left(\chi^{(1)}\mathbf{E} + \chi^{(2)}(\mathbf{E})^2 + \chi^{(3)}(\mathbf{E})^3 + ... \right). \quad (2.2)$$

If we then consider a field propagating in the opposite direction, $-\mathbf{E}$, it will, due to centrosymmetry, result in an induced polarisation of $-\mathbf{P}$. This may be written as

$$-\mathbf{P} = \varepsilon_0 \left(\chi^{(1)}-\mathbf{E} + \chi^{(2)}(\mathbf{E})^2 + \chi^{(3)}(-\mathbf{E})^3 + ... \right). \quad (2.3)$$

Summing Equations 2.2 and 2.3 together then leaves us with

$$0 = 2\left(\chi^{(2)}(\mathbf{E})^2 + \chi^{(4)}(\mathbf{E})^4 + \chi^{(6)}(\mathbf{E})^6 + ... \right), \quad (2.4)$$

$$= \sum_{i=1}^{n} \chi^{(2i)}(\mathbf{E})^{2i}, \quad (2.5)$$

showing that the contribution of all even order terms to the nonlinear polarisation is zero, as each term on the right hand side of the equation responds to a different

frequency. However, the odd order susceptibilities remain and these give rise to the nonlinear component of the induced polarisation.

It is useful then to split the induced polarisation term in Equation 2.1 into its linear and nonlinear components and write it as

$$\mathbf{P} = \mathbf{P}_{\mathrm{L}} + \mathbf{P}_{\mathrm{NL}}, \tag{2.6}$$

where $\mathbf{P_L}$ is the linear component and $\mathbf{P_{NL}}$ is the nonlinear component. Both components are related to the electric field via Equation 2.1 – $\mathbf{P_L}$ contains the $\chi^{(1)}$ term while $\mathbf{P_{NL}}$ accounts for all the higher order terms.

In optical fibres the biggest contribution to the nonlinear polarisation arises from third order $\chi^{(3)}$ effects. Indeed the nonlinear polarisation may be considered to be predominantly due to $\chi^{(3)}$ effects since, as mentioned before, even order terms for centrosymmetric materials such as glasses disappear and the higher order odd terms are negligible. The nonlinear polarisation may thus be written as

$$\mathbf{P}_{\mathrm{NL}} \cong \mathbf{P}^{(3)} = \varepsilon_0 \chi^{(3)} (\mathbf{E})^3. \tag{2.7}$$

If we consider a monochromatic wave of the form

$$\mathbf{E} = \mathbf{E_0} \cos(\omega t), \tag{2.8}$$

and the light to be linearly polarised so that the tensor form of χ may be avoided, Equation 2.7 becomes

$$\mathbf{P}_{\mathrm{NL}} = \varepsilon_0 \chi^{(3)} (\mathbf{E_0})^3 \cos^3(\omega t). \tag{2.9}$$

The trigonometric identity $\cos^3(\omega t) = 1\cos(3\omega t) + 3\cos(\omega t)$ may then be used to express the nonlinear polarisation as

$$\mathbf{P}_{\mathrm{NL}} = \varepsilon_0 \left[\frac{1}{4} \chi^{(3)} (\mathbf{E_0})^3 \cos(3\omega t) + \frac{3}{4} \chi^{(3)} (\mathbf{E_0})^3 \cos(\omega t) \right]. \tag{2.10}$$

The first term in Equation 2.10 oscillating at frequency 3ω gives rise to the third harmonic effect – where three waves at frequency ω combine to form a single, frequency up shifted wave at 3ω. The second term gives rise to a host of other nonlinear effects such as four wave mixing and nonlinear refraction. Four wave mixing in particular is an important nonlinear optical phenomenon for telecommunications applications and, as such, it forms the basis for much of this research. It is discussed in detail in Section 2.3.

2.2.1.1 Nonlinear refractive index

One of the most important ramifications of the third order susceptibility is the addition of an intensity dependent, nonlinear component to the refractive index. In $\chi^{(3)}$ media, the refractive index is written as

$$n = n_0 + n_2 I, \tag{2.11}$$

where n_0 is the linear refractive index, n_2 is the nonlinear refractive index and I intensity of the propagating wave. This nonlinear component of the refractive index is often referred to as the optical Kerr effect.

To see how n_2 is related to $\chi^{(3)}$ we must refer back to Equation 2.10. The first term in this equation oscillates at the third harmonic of the carrier frequency and is not significant unless the phase of the waves at frequency ω can be phase matched to those at 3ω so that energy transfer may occur (phase matching between waves propagating at different frequencies is discussed on more detail in Section 2.3 where four wave mixing is introduced). In general, this is not possible in optical fibres[1] so we may write the nonlinear polarisation as

$$\mathbf{P}_{\mathrm{NL}} = \varepsilon_0 \frac{3}{4} \chi^{(3)} (\mathbf{E})^3. \tag{2.12}$$

If a monochromatic plane wave as in Equation 2.8 is again assumed, with intensity given by

[1] While phase matching from ω to 3ω in an optical fibre is generally not possible within the same mode, third harmonic generation has been demonstrated by using intermodal phase patching [63].

$$I = \frac{1}{2} c\varepsilon_0 n_0 (\mathbf{E})^2, \tag{2.13}$$

where c is the speed of light. The total polarisation may then be written as

$$\mathbf{P} = \varepsilon_0 \chi^{(1)} + \frac{3\chi^{(3)}}{2c\varepsilon_0 n_0} I \cdot \mathbf{E}, \tag{2.14}$$

$$= \varepsilon_0 \chi_{eff} \mathbf{E}, \tag{2.15}$$

where we have introduced a new term, the effective susceptibility χ_{eff}, given by

$$\chi_{eff} = \chi^{(1)} + \frac{3\chi^{(3)}}{2c\varepsilon_0 n_0} I. \tag{2.16}$$

Using the relationship between effective refractive index and effective susceptibility below [35]

$$n^2 = 1 + \chi_{eff}. \tag{2.17}$$

The refractive index becomes

$$n^2 = 1 + \chi^{(1)} + \frac{3\chi^{(3)}}{2c\varepsilon_0 n_0} I. \tag{2.18}$$

If Equation 2.11 is inserted into the left hand side of the relation above and expanded assuming the nonlinear component is much smaller than the linear one, we may consider only terms up to order I and write the relation as [62]

$$n_0^2 + 2n_0 n_2 I = 1 + \chi^{(1)} + \frac{3\chi^{(3)}}{2c\varepsilon_0 n_0} I \tag{2.19}$$

which gives the following expressions for the linear and nonlinear component of the refractive index

$$n_0 = (1 + \chi^{(1)})^{\frac{1}{2}}, \tag{2.20}$$

$$n_2 = \frac{3\chi^{(3)}}{4c\varepsilon_0 n_0^2}. \tag{2.21}$$

The nonlinear refractive index is therefore determined by the third order susceptibility as per Equation 2.21. This nonlinear index is also used to define the nonlinear coefficient γ for optical fibres, as described in the section.

2.2.2 Wave propagation

To discuss the important fibre parameters that characterise nonlinear phenomena within optical fibres an understanding of the basic concepts and equations of electromagnetic wave theory is required. All electromagnetic phenomena are governed by Maxwell's equations which, in standard form, may be written as

$$\nabla \times \mathbf{E} = -\frac{\partial \mathbf{B}}{\partial t}, \tag{2.22}$$

$$\nabla \times \mathbf{H} = \mathbf{J} + \frac{\partial \mathbf{D}}{\partial t}, \tag{2.23}$$

$$\nabla \cdot \mathbf{D} = \rho_f, \tag{2.24}$$

$$\nabla \times \mathbf{B} = 0, \tag{2.25}$$

where $\mathbf{E}$ and $\mathbf{H}$ are the electric and magnetic field vectors, respectively and $\mathbf{D}$ and $\mathbf{B}$ represent the electric and magnetic flux densities, respectively. $\mathbf{J}$ is the free current within the material and ρ_f is the material's free charge density. In a glass medium such as an optical fibre where there are no free charges $\mathbf{J} = 0$ and $\rho_f = 0$.

The flux densities are related to the fields via the constitutive relations below

$$\mathbf{D} = \varepsilon_0 \mathbf{E} + \mathbf{P}, \tag{2.26}$$

$$\mathbf{B} = \mu_0 \mathbf{H} + \mathbf{M}, \tag{2.27}$$

where ε_0 and μ_0 represent the permittivity and and permeability (in free space), respectively. $\mathbf{P}$ is the induced electric polarisation given in Equation 2.1 and $\mathbf{M}$ is the induced magnetic polarisation, which is zero for nonmagnetic media such as optical fibres.

The electric field may be decoupled from the equations above into an individual wave equation by taking the curl of Equation 2.22 and then using Equations 2.23, 2.26 and 2.27 to eliminate the other fields. This results in the equation

$$\nabla \times \nabla \times \mathbf{E} = -\frac{1}{c^2}\frac{\partial^2 \mathbf{E}}{\partial t^2} - \mu_0 \frac{\partial^2 \mathbf{P}}{\partial t^2}, \tag{2.28}$$

where c is the speed of light in vacuum and P is again the induced electric polarisation, related to the electric field by Equation 2.1. By using the vector calculus identity [35]

$$\nabla \times (\nabla \times \mathbf{A}) = \nabla(\nabla \cdot \mathbf{A}) - \nabla^2 \mathbf{A}, \tag{2.29}$$

and splitting the induced polarisation into a linear and nonlinear component as in Equation 2.6, a general equation for wave propagation can be derived and written as

$$\nabla^2 \mathbf{E} - \frac{1}{c^2}\frac{\partial^2 \mathbf{E}}{\partial t^2} = \mu_0 \frac{\partial^2 \mathbf{P}_{\mathrm{L}}}{\partial t^2} + \mu_0 \frac{\partial^2 \mathbf{P}_{\mathrm{NL}}}{\partial t^2}. \tag{2.30}$$

Equation 2.30 provides a general basis from which to study light waves in optical fibres. A derivation of the solutions to this equation is outside the scope of this work, however a detailed treatment may be found in References [35] and [34]. For the purpose of this derivation, only the generalised solution for an electromagnetic pulse propagating down the longitudinal axis of an optical fibre is shown. Assuming that this longitudinal axis is z and that the fibre is longitudinally invariant and weakly guiding, the pulse may be represented as

$$\mathbf{E} = \frac{1}{2}\hat{\mathbf{k}}[E(x,y)A(z,t)e^{i(\beta z - \omega t)} + c.c.], \tag{2.31}$$

where $E(x, y)$ represents the transverse field, $A(z, t)$ is the pulse envelope, ω is the central angular frequency (related to the linear frequency f by the relation $\omega = 2\pi f$), β is the propagation constant of the mode, $\hat{\mathbf{k}}$ is a unit vector along the polarisation axis and *c.c.* denotes the complex conjugate. Note that when the fields in Equation 2.31 are evaluated they are taken to be the real parts of this equation. A similar equation also exists for the magnetic field.

This propagation constant in the equations above is the eigenvalue of the mode and its value is obtained by solving the corresponding eigenvalue equation. The form of this equation depends on the assumptions used to simplify Equation 2.30 and the geometry of the fibre – its derivation is again out of the scope of this work, but details on the procedure may be found in both [35] and [39].

The frequency dependence of this propagation constant is also closely related to the fibre dispersion parameter, discussed in the next section.

It it also useful to characterise each mode by defining an effective index n_{eff} that is related to the propagation constant by the equation

$$n_{eff} = \frac{\lambda\beta}{2\pi}. \tag{2.32}$$

This effective mode index is analogous to the refractive index for a material and in waveguides such as optical fibres it is determined by the refractive index regions that the transverse field is confined in.

With these definitions in hand we may now proceed to discussing the key fibre parameters that drive the selection of a fibre design – nonlinearity, dispersion and loss. This is done so in Section 2.2.3 that follows.

2.2.3 Fibre nonlinearity and dispersion

When designing optical fibres for nonlinear telecommunications applications, two parameters are paramount in the design considerations: the fibre nonlinearity and the dispersion profile.

The nonlinearity of a waveguide is measured by the effective nonlinear coefficient. This parameter, which is obtained through the derivation of the pulse propagation equation for nonlinear waveguides (described in Section 2.2.3.1), is defined as

$$\gamma = \frac{2\pi}{\lambda}\frac{n_2}{A_{eff}}, \tag{2.33}$$

where n_2 is the nonlinear refractive index, λ is the central wavelength and A_{eff} is the effective area of the fibre mode. The effective mode area is based on the modal field distribution and is usually defined as [34]

$$A_{eff} = \frac{\left(\int |E(x,y)|^2 \, \mathrm{d}A\right)^2}{\int |E(x,y)|^4 \, \mathrm{d}A}, \tag{2.34}$$

where $E(x,y)$ is the electric field distribution across the transverse axes x, y and the integrals are evaluated over the transverse area.

However this definition of the effective area in Equation 2.34 originates from a scalar set of solutions to Equation 2.30, which assume a weak guidance of the propagating mode in addition to ignoring the vectorial nature of the field. The weak guidance approximation greatly simplifies the analysis of the propagating modes and may be assumed if the refractive index between the core and the cladding region of the fibre is negligible, i.e. $n_{core}/n_{cladding} \approx 1$, where n_{core} is the refractive index of the core and $n_{cladding}$ is that of the cladding [35]. Such an approximation is valid for refractive index differences of up to 1% – such as conventional silica SMF-28 fibres, where the refractive index difference between the core and the cladding is around 0.4%. However for a strongly guiding waveguide, such as a soft glass nanowire (where the refractive index difference can be on the order of 100%) this weak guidance approximation is obviously inappropriate.

For these strongly guiding waveguides, the weak guidance approximation may instead be dispensed with by considering full vectorial solutions to Maxwell's equations. Afshar *et. al.* [64] have developed such a formalism and obtained a revised definition for the nonlinear coefficient, written as

$$\gamma^v = \frac{2\pi}{\lambda}\frac{\overline{n_2}}{A^v_{eff}}, \tag{2.35}$$

where the material nonlinearity is weighted by field distribution and represented by the average nonlinear index $\overline{n_2}$, written as

$$\overline{n_2} = \frac{\varepsilon_0 k_0}{\mu_0}\frac{\int n^2(x,y)n_2(x,y)(2|\mathbf{E}|^4 + |\mathbf{E}^2|^2)\,\mathrm{d}A}{3\int |(\mathbf{E}\times\mathbf{H}\cdot\hat{\mathbf{z}})|^2\,\mathrm{d}A}, \tag{2.36}$$

and the effective area has also replaced by a vectorial version A^v_{eff}, written as

$$A^v_{eff} = \frac{\left|\int (\mathbf{E}\times\mathbf{H})\cdot\hat{\mathbf{z}}\,\mathrm{d}A\right|^2}{\int |(\mathbf{E}\times\mathbf{H})\cdot\hat{\mathbf{z}}|^2\,\mathrm{d}A}. \tag{2.37}$$

In Equations 2.36 and 2.37 above $\mathbf{E}$ and $\mathbf{H}$ represent the vector electric and magnetic fields, respectively; while $n(x,y)$ and $n_2(x,y)$ represent the transverse distributions of the linear and nonlinear refractive index. The axis of propagation in these equations is set to be the z axis, with the unit vector $\hat{\mathbf{z}}$.

By taking into account the vectorial nature of the fields, the nonlinear coefficient in Equation 2.35 is shown to be significantly higher that the scalar version in Equation 2.33 for strongly guiding fibres, in small core regimes [65]. The reason for this difference is the z component of the electric field (i.e. the component in the propagating direction), which is significant in small core regimes where the mode is tightly confined. For large core diameters and weak guiding regimes this $\hat{\mathbf{z}}$ component goes to zero and consequently γ^v approaches the standard γ definition.

The other main parameter that affects fibre performance is the dispersion, which arises from the frequency dependence of the propagation constant β. When describing the effect of dispersion on an optical wave is is useful to expand the propagation constant β via a Taylor series expansion around the carrier frequency ω_0 as

$$\beta(\omega) = \beta^{(0)} + (\omega-\omega_0)\beta^{(1)} + \frac{1}{2}(\omega-\omega_0)^2\beta^{(2)} + ... \tag{2.38}$$

where $\beta^{(0)}$ is the propagation constant at the carrier frequency (i.e. $\beta^{(0)} = \beta(\omega_0)$) and the higher order terms may be defined as

$$\beta^{(m)} = \left(\frac{d^m\beta}{d\omega^m}\right)_{\omega=\omega_0} \qquad (m = 1, 2, 3, ...). \tag{2.39}$$

The first order term in Equation 2.38 is related to the group velocity v_g (which determines the overall delay on a pulse) by the equation

$$\beta^{(1)} = \frac{d\beta}{d\omega} = \frac{1}{v_g}. \tag{2.40}$$

The second order term in Equation 2.38 is known as the group velocity dispersion and is used in the definition of the dispersion parameter D that is generally used when quantifying dispersion in optical fibres. This dispersion parameter is usually expressed in units of $\mathrm{ps}^{-1}\mathrm{nm}^{-1}\mathrm{km}^{-1}$ and is defined as

$$D = -\frac{2\pi c}{\lambda^2}\beta^{(2)} = -\frac{2\pi c}{\lambda^2}\frac{d^2\beta}{d\omega^2} = \frac{2\pi c}{v_g^2\lambda^2}\frac{dv_g}{d\omega}, \tag{2.41}$$

where β is the propagation constant of the mode, λ is the wavelength, ω is the angular frequency, c is the speed of light in vacuum and v_g is the group velocity. Wavelengths where D is negative are known as the normal dispersion regime – in this region shorter wavelength components of an optical pulse would travel slower than longer wavelength components, resulting in temporal pulse broadening. Conversely, wavelengths where $D > 0$ correspond to anomalous dispersion – in this region shorter wavelength components of an optical pulse would travel faster than longer wavelength components, causing the pulse to contract (in time).

2.2.3.1 Nonlinear pulse propagation

When analysing nonlinear effects in fibres, it is useful to convert the wave equation shown in Equation 2.28 into a form that is in terms of the nonlinear parameters introduced earlier. This results in the a form of the Nonlinear Schrödinger Equation (NSE), for

wave propagation in nonlinear dielectric media. The NSE forms the basis for much of the pule propagation modelling work in this thesis and thus, its derivation is summarised here. A detailed treatment may be found in [34], from where the following formalism has been adapted.

First a slowly varying approximation is assumed for the electric field envelope and a Fourier transformed is applied on the field, defined as

$$\tilde{E}(\mathbf{r}, \omega - \omega_0) = \int_{-\infty}^{+\infty} E(\mathbf{r}, t) \exp[i(\omega - \omega_0)t] dt. \tag{2.42}$$

This transformed electric field satisfies the Helmholtz equation [34]

$$\nabla^2 \tilde{E} - \epsilon_0 n^2 k_0^2 \tilde{E} = 0, \tag{2.43}$$

where $k_0 = \omega/c$. This equation may be solved by separating variables and assuming a solution of the form

$$\tilde{E}(\mathbf{r}, \omega - \omega_0) = F(x, y)\tilde{A}(z, \omega - \omega_0) \exp(i\beta^{(0)} z), \tag{2.44}$$

where $\tilde{A}(z, \omega)$ is the slowly varying pulse envelope and $F(x, y)$ is the transverse field distribution. Using the Helmholtz relation in Equation 2.43, the separated variables are found to obey the relations

$$\frac{\partial^2 F}{\partial x^2} + \frac{\partial 2F}{\partial y^2} + [\epsilon(\omega)k_0^2 - \tilde{\beta}^2]F = 0, \tag{2.45}$$

$$2i\beta^{(0)} \frac{\partial \tilde{A}}{\partial z} + \left(\tilde{\beta}^2 - {\beta^{(0)}}^2\right) \tilde{A} = 0. \tag{2.46}$$

Note that in deriving Equation 2.46, the second derivative term was neglected since the pulse envelope A is assumed to be slowly varying.

The pulse propagation equation is then obtained by making making some simplifications such as treating the nonlinear component of the refractive index (which is included in the

ϵ term in the above equations) as a small perturbation, using a Taylor series expansion for β such as in Equation 2.38 and then moving back to the time domain by taking the inverse Fourier transform of Equation 2.46, defined as

$$A(z,t) = \frac{1}{2\pi}\int_{-\infty}^{+\infty} \tilde{A}(z,\omega-\omega_0)\exp[-i(\omega-\omega_0)t]d\omega. \tag{2.47}$$

This results in the pulse propagation equation

$$\frac{\partial A}{\partial z} + \beta^{(1)}\frac{\partial A}{\partial t} + i\frac{\beta^{(2)}}{2}\frac{\partial^2 A}{\partial t^2} + \frac{\alpha}{2}A = i\gamma(\omega_0)|A|^2 A, \tag{2.48}$$

Where, in this formalism, γ is the nonlinear coefficient defined in Equation 2.33 and α is the fibre attenuation, which is defined later in Equation 4.2. It should be noted that the nonlinear coefficient γ is defined via the derivation of this pulse propagation equation (Equation 2.48). Additionally, note that in the inverse Fourier transform operation the $(\omega-\omega_0)$ term is replaced by the differential operator $i\frac{\partial}{\partial t}$ [34].

Equation 2.48 represents a form of the Nonlinear Schrödinger Equation that governs the propagation of pulses under the effects of nonlinearity, group velocity dispersion and loss. This equation may be solved numerically if the pulse and fibre properties are known and is thus an extremely useful tool for modelling nonlinear effects in fibres. In the modelling process used in this research, a further generalised version of this equation was used to include higher order dispersion and the effect of other nonlinear phenomena such as stimulated Raman scattering. This process is described in detail in Section 5.2.

2.3 Four wave mixing

Four wave mixing is a nonlinear process that involves the interaction of four light waves. It is classed as a third order parametric process as it results in a modulation of the refractive index through the third order susceptibility $\chi^{(3)}$. The two signal processing applications considered in this research, multicasting and phase sensitive amplification, are both based on FWM and thus a theoretical overview of the process is provided in this section.

If we consider four waves oscillating at angular frequencies ω_i (where $i = 1$ to 4) we can broadly categorise FWM into two types: the case in which three photons transfer their energy to a single photon such that $\omega_4 = \omega_1 + \omega_2 + \omega_3$; and the case in which two photons are annihilated and two new ones created such that $\omega_3 + \omega_4 = \omega_1 + \omega_2$. In both cases energy and momentum must be conserved and, as the interaction depends on the relative phases of the waves, it requires that the phases of the all four waves be matched. In general, the phase matching condition for the former case (where three photons combine to form one) is much harder to achieve. However it may be used for third harmonic generation by setting $\omega_1 = \omega_2 = \omega_3$ [63]. The latter case (where two photons combine to generate two other photons) is widely used for many applications, such as wavelength conversion [66, 67], supercontinuum generation [68], and fibre lasing [69, 70].

In general, the two input waves are at distinct frequencies and they generate two distinct output waves. This is known as non-degenerate FWM. However, it is also possible to have cases where both inputs waves, or both output waves, can be at the same frequency i.e. $\omega_1 = \omega_2$ or $\omega_3 = \omega_4$. This is known as degenerate FWM. This is illustrated in Figure 2.1.

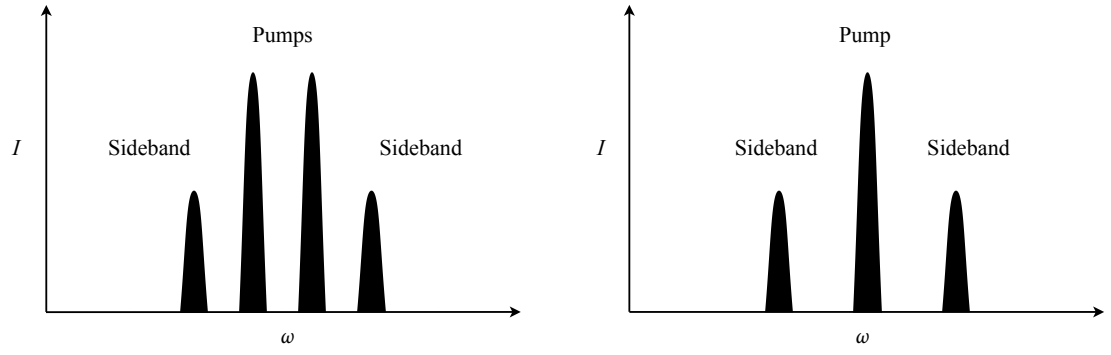

FIGURE 2.1: This schematic shows the difference between non-degenerate FWM (on the left) and degenerate FWM (on the right). In the degenerate case two photons from a pump at a single wavelength interact to give the side bands, whereas in the non-degenerate case the two pump photons are at different frequencies.

While the term degenerate FWM generally refers to the pump wavelength, the degeneracy can also be at the signal/idler wavelength, i.e. two pump photons at different frequencies interact with the signal photon to create an idler at the same wavelength (as the signal). Indeed such a setup is used in the phase sensitive amplification mechanism described in Section 2.4.2.

The main interest in FWM, from a telecommunications perspective, is the ability to use light at a certain wavelength to generate light at new wavelengths. This is especially useful for applications such as switching [46–48] where, for instance, a data signal can be switched to a FWM idler by using a control signal as a FWM pump and setting it to be ether above or below the threshold required for there to be sufficient gain at the idler wavelength. FWM is also useful for signal regeneration [49–51] as it can be used to frequency convert, reamplify, reshape and retime a signal based on the FWM configuration used [49].

2.3.1 Theory of FWM

Four wave mixing originates from the third order term of the induced polarisation. In this instance, the nonlinear polarisation is given by

$$\mathbf{P_{NL}} = \varepsilon_0 \chi^{(3)} \mathbf{E}^3, \tag{2.49}$$

where $\mathbf{E}$ is again the total electric field of the propagating waves.

To understand how some of the key aspects FWM process, such as efficiency and bandwidth, are affected by the fibre parameters we start with a set of coupled equations. These describe the evolution of the amplitude of each mode, at frequencies ω_1, ω_2, ω_3 and ω_4.

These coupled amplitude equations may be derived from the wave equation given in Equation 2.30. A quasi-CW form is assumed for the electric field where each mode has a propagation constant $\beta_j = \widetilde{n}_j \omega_j / c$, where $\widetilde{n}_j$ is the (complex) mode index ($j = 1$ to 4 and corresponds to the mode at frequency ω_j). This leads to corresponding CW form for the nonlinear polarisation (via the relation in Equation 2.49) which may be substituted into the wave equation along with a similar expression for the linear term. The time dependence of the electric field is neglected (due to the quasi-CW assumption) and it is split into spatial and amplitude components, written as

$$E_j(\mathbf{r}) = F_j(x, y) A_j(z). \tag{2.50}$$

By integrating over the spatial distribution of each fibre mode $F_j(x, y)$, the coupled amplitude equations may be obtained, in scalar form, as [34]

$$\frac{dA_1}{dz} = i\left[\left(\gamma(\omega_1)|A_1|^2 + 2\sum_{k\neq 1}\gamma(\omega_1)|A_k|^2\right)A_1 + 2\gamma(\omega_1)A_2^* A_3 A_4 e^{i\Delta kz}\right], \tag{2.51}$$

$$\frac{dA_2}{dz} = i\left[\left(\gamma(\omega_2)|A_2|^2 + 2\sum_{k\neq 2}\gamma(\omega_2)|A_k|^2\right)A_2 + 2\gamma(\omega_2)A_1^* A_3 A_4 e^{i\Delta kz}\right], \tag{2.52}$$

$$\frac{dA_3}{dz} = i\left[\left(\gamma(\omega_3)|A_3|^2 + 2\sum_{k\neq 3}\gamma(\omega_3)|A_k|^2\right)A_3 + 2\gamma(\omega_3)A_4^* A_1 A_2 e^{-i\Delta kz}\right], \tag{2.53}$$

$$\frac{dA_4}{dz} = i\left[\left(\gamma(\omega_4)|A_4|^2 + 2\sum_{k\neq 4}\gamma(\omega_4)|A_k|^2\right)A_4 + 2\gamma(\omega_4)A_3^* A_1 A_2 e^{-i\Delta kz}\right]. \tag{2.54}$$

where A_j is the amplitude of the wave at frequency ω_j, γ is the nonlinear coefficient and Δk is the phase mismatch, given by Equation 2.55 in terms of the propagation constants β_j (again, the subscript corresponds to the frequency of the mode).

$$\Delta k = \beta_3 + \beta_4 - \beta_1 = -\beta_2, \tag{2.55}$$

In Equations 2.51 to 2.54 we have already made the approximation that the spatial overlap of the electric fields at each frequency are the same, such that they have the same effective area. We have also assumed that the variation in the nonlinear coefficient across the four frequencies is negligible, i.e. $\gamma(\omega) = \gamma$. As γ depends on the nonlinear refractive index and the effective mode area according to Equation 2.35, this assumption is only valid for small frequency separations – where it can be assumed that the nonlinear refractive index and effective mode area are essentially the same for all four waves.

To obtain an exact analytical solution for Equations 2.51 to 2.54 the waveguide must also be assumed to be weakly guiding [71]. For strongly guiding waveguides, where there is a high index contrast between the core and cladding regions, obtaining a solution requires a numerical approach instead. To derive an analytical solution we must also assume that the pump waves are considerably more intense than the generated waves and that their power does not get depleted during the process.

For the purpose of this discussion, it is sufficient to show how an approximate solution may be obtained using these approximations, as it still allows us to glean physical insight into the FWM process.

By solving Equations 2.51 and 2.52 for the two pump waves we obtain the following solutions:

$$A_1(z) = \sqrt{P_1}e^{[i\gamma(P_1+2P_2)z]}, \tag{2.56}$$

$$A_2(z) = \sqrt{P_2}e^{[i\gamma(P_2+2P_1)z]}, \tag{2.57}$$

where z is the propagation axis of the fibre and P_j are the incident pump powers, given by $P_j = |A_j(z=0)|^2$.

By then substituting these equations into 2.53 and 2.54 and introducing a transformed amplitude B we are able to obtain an equation of the form

$$\frac{d^2B_j}{dz^2} + i\kappa\frac{dB_j}{dz} - (4\gamma^2 P_1 P_2)B_j = 0 \qquad (j = 3, 4), \tag{2.58}$$

where the transformed amplitude is given by

$$B_j = A_j e^{-2i\gamma(P_1+P_2)z} \qquad (j = 3, 4). \tag{2.59}$$

From Equation 2.58 we are able to obtain a general solution which may be written in the form

$$B_3(z) = (a_3 e^{gz} + b_3^{-gz})e^{-i\kappa z/2}, \tag{2.60}$$

$$B_4^*(z) = (a_4 e^{gz} + b_4^{-gz})e^{\kappa z/2}, \tag{2.61}$$

where a_3, b_3, a_4 and b_4 are parameters determined by the boundary conditions.

The general solutions obtained in Equations 2.60 and 2.61 show us that the amplitude of the generated signal and idler waves depend on two parameters: the gain g and the effective phase mismatch κ, given by

$$g = \left(4\gamma^2 P_1 P_2 - \frac{\kappa^2}{2}\right)^{1/2}, \tag{2.62}$$

$$\kappa = \Delta k + \gamma(P_1 + P_2). \tag{2.63}$$

When designing fibres for broad band FWM based applications, one generally seeks to maximise this gain parameter over the bandwidth required. This is done by both increasing the nonlinearity, and minimising the phase mismatch over the wavelength range. In Section 2.4 that follows, we discuss applying FWM for signal processing and show how this results in specific requirements on the gain and phase mismatch, and the consequent fibre design considerations that this entails.

2.4 Signal processing applications based on FWM

To realise next generation networks, at speeds of 1 Tb/s and beyond, optical signal processing techniques are desirable. Currently, this processing is done electronically and involves costly, inefficient electrical–optical conversion, back and forth, between the transmitting link (optical) and the signal processor (electronic). In addition to this, conventional electronic signal processing schemes such as electrical time domain multiplexing (EDTM) are generally limited to operating at the ethernet standards of 40 Gb/s to 100 Gb/s [72], although laboratory experiments have shown that this may be pushed to 160 Gb/s [27]. In any case, this is well below the bandwidth of the transmitting optical fibres and thus represents a significant bottleneck in the network infrastructure.

To get higher bit rates and utilise the full capacity of the optical fibre transmission links, these applications must be performed in the optical domain. The use of a nonlinear phenomenon such as FWM is a way by which an all optical network architecture may be developed, as FWM may be utilised to perform processing functions such as signal regeneration and amplification.

In this research we have looked at two major four wave mixing based telecommunications applications: multicasting and phase sensitive amplification. Multicasting is a technique whereby a signal is duplicated for transmission to multiple receivers, while phase sensitive amplification is a signal regeneration application used to transmit signals over long haul links with high fidelity. Each application is described in below – multicasting in Section 2.4.1 and phase sensitive amplification in Section 2.4.2. Each of these sections provides an overview of the theory behind each application and, following on from this, the design considerations that must be taken into account when designing optical fibres for the application.

2.4.1 Multicasting

Multicasting is the simultaneous replication of a single signal into multiple copies and is an important tool in many signal processing techniques. Optical time division (OTD) demultiplexing is one such technique, which can be used to decompose a fast optical signal into copies at lower speeds. This allows for the electronic processing of a signal with a bit rate that is higher than that of the available electronic components by decomposing the original signal into components that have lower bit rates – in line with the processing capacity of electronic components. Thus, OTD demultiplexing may be used in the creation of an all-optical preprocessing layer to bridge the existing gap between the rate at which data can be transported down an optical line and the rate at which it can be processed by electronic components at the end.

However conventional OTD devices operate in a single channel demultiplexing scheme that is difficult to scale up with increasing network speeds [37]. The difficulty arises from the fact that these single channel devices would need to be duplicated into a parallel architecture to encompass a high input bandwidth. This motivated Bres *et. al.* to develop a preprocessing architecture called multicast parametric synchronous sampling (MPASS), where multiple output tributaries are produced in a single gate in a manner that is both efficient and scalable with input bit rate [36]. This architecture was used to experimentally demonstrate demultiplexing of a 320 Gb/s signal using a 1-to-8 multicasting scheme [37].

The work documented in this research was based on this MPASS architecture and aimed to use a soft glass based microstructured fibre design to extend the scheme to generate

more signal copies, in an effort to multicast signals at 640 Gb/s. Highly nonlinear soft glasses have been previously shown to be able demultiplex 160 Gb/s signals in both fibre [73, 74] and optical chip devices [75].

Optical multicasting can also be used in the creation of optical wavelength division multiplexing (WDM) systems [76], which are key to creating single point to multipoint connections in telecommunications networks. Optical multicasting has also been used in the creation of optical 'superchannels' capable of transporting data with high spectral efficiency at speeds beyond 1 Tb/s [77, 78].

2.4.1.1 Theory

Multicast parametric synchronous sampling can be broken down into three distinct operations: multicasting, synchronisation and sampling. First the data, at input transmission rate B (measured in bits per unit time) is multicast into M multicoloured copies, each centred at a wavelengths λ_j (where $i = 1$ to M) and at a (lower) rate of transmission, R. These copies are then shifted in time such that they are delayed with respect to each other before being simultaneously sampled by a gate operating at $1/R$. The time delay is set up such that when all the copies are sampled they result in time shifted slices of the original signal at different wavelengths. These can then be demultiplexed and then sent off for electronic processing.

To process the high rate input signal at B, the number of signal copies (M) and subrate transmission rate (R) must be adjusted such that its product is that of the original high rate signal B, i.e., we must satisfy the condition $B = M \times R$. Therefore, to accommodate an increase in input signal bandwidth one must either generate more signal copies M or increase the rate R at which these copies can be sampled. Generally, R is fixed by the limits of electronics processing – typically 40 Gb/s. Therefore, to process an input signal at, for instance, 320 Gb/s at a subrate of 40 Gb/s one must generate 8 copies; to process 640 Gb/s one needs 16; and so on.

This generation of the signal copies within the multicasting block requires a combination of cascaded four wave mixing processes. The simplest form of FWM multicasting can be thought of as a 1-to-2 operation where the interaction of the signal with a single pump produces one idler via degenerate FWM. Extending this out to two pumps allows for the

generation of three idlers via a combination of degenerate and non degenerate FWM, i.e. 1-to-4 multicasting. By increasing the number of pumps more idlers can be generated and consequently the multicasting ratio increases. This is represented schematically in Figure 2.2.

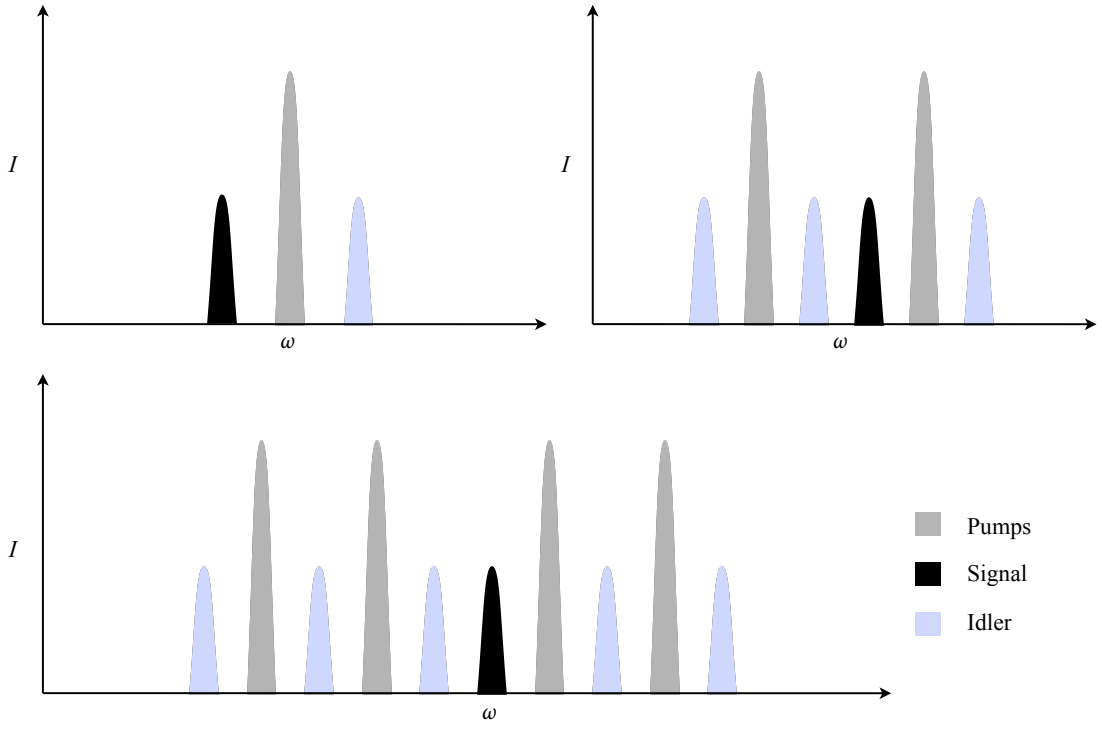

FIGURE 2.2: The top left diagram shows a 1-to-2 scheme that uses degenerate FWM to generate an idler wave from a signal, and thus a total of two versions of the signal. The scheme can be cascaded by adding a secondary pump which may then be used for 1-to-4 multicasting (top right). Further FWM can create more pump waves naturally, leading to further cascading of the process to 1-to-8 multicasting (bottom) and so on provided the gain bandwidth and transmission window of the device are wide enough.

Previous work has demonstrated successful multicasting of a 320 Gb/s signal into 8 copies at the lower transmission subrate of 40 Gb/s [37]. In this setup a pair of CW pumps, asymmetrically positioned around the signal wavelength, along with the signal, were inserted into a silica highly nonlinear fibre (HNLF). The side bands generated by FWM between the two primary pumps generated a secondary set of pumps, which then interact with the signal to generate multiple idlers.

While the architecture used in Reference [37] is indeed scalable to deal with input signals at higher speeds, it is limited by the bandwidth of the silica HNLF. Thus, to extend capability out to higher speeds the operating bandwidth of the nonlinear

optical component must be increased. The requirements of such a fibre are discussed in Section 2.4.1.2.

2.4.1.2 Design considerations

In this research we looked at designing a fibre to multicast of a 640 Gb/s signal into 16 copies at 40 Gb/s. The fibre would have to operate within the architecture described in Reference [37] and would therefore need to work under approximately the same input conditions, such as pump power.

The FWM gain requirements on such a fibre are twofold: the gain needs to be high enough to ensure that 16 signal copies can be generated via FWM over a practical length; and the gain needs to be sufficiently flat across the operating bandwidth to ensure that the signal to noise ratio is the same across all copies.

This places quite tight requirements on the dispersion as it requires phase matching over a very broad band – approximately 200 nm worth, in this case, to be able to fit all 16 copies of the signal, and secondary pump waves. Therefore we chose a high index tellurite glass and a highly tailorable fibre design, optimised via a genetic algorithm to produce the required properties. This design is discussed in more detail in Chapter 4 where it is shown to have a wide band of near zero dispersion centred around 1.55 µm. Further pulse propagation modelling of the design is presented in detail in Chapter 5 where it is shown to be able to produce the required 16 copies, albeit with some noise ripple at the edges of the spectrum.

2.4.2 Phase sensitive application

Phase sensitive amplification is a parametric amplification process where the gain of the signal is dependent on its phase distribution – the parts of the signal that satisfy a phase matching condition are amplified while those that do not are attenuated. Four wave mixing, for example, is a phase sensitive amplification process as the gain (defined later in Equation 2.73) depends on the phase mismatch between the signal, idler and pumps (Equation 2.55). In contrast, an Erbium doped fibre amplifier (EDFA) is a phase insensitive amplifier as any signal within its operating band will be amplified, irrespective of its phase. Figure 2.3 shows the difference between these two types of amplifiers.

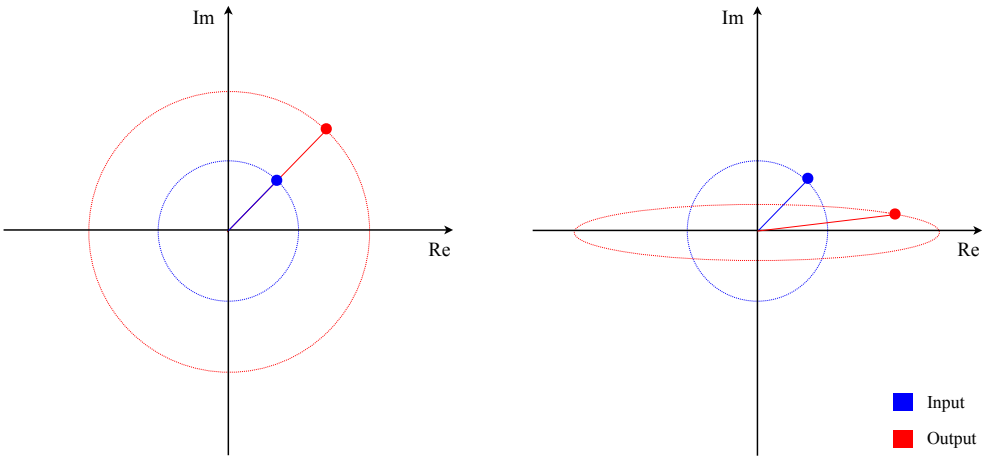

FIGURE 2.3: Phasor schematic of phase insensitive amplification (PIA, left) versus phase sensitive amplification (PSA, right). In PIA the input signal is amplified by the same amount regardless of its phase, which is also unchanged. In PSA the signal amplification depends on its phase which is squeezed to the gain axis – in this case this is the real axis. Meanwhile, quadrature components along the imaginary axis are attenuated.

From a telecommunications perspective, phase sensitive amplification is an interesting phenomenon as it has the potential to be used for all optical noise correction and signal regeneration. These applications are essential parts of signal processing systems, and having an all optical mechanism is a step towards the realisation of the all optical network architectures required for next generation networks. PSA has therefore attracted considerable interest recently as it has numerous optical signal processing applications [79–82].

One application of particular interest is the reduction in phase noise introduced during transmission of phase modulated signal formats such as differential phase shift keying (DPSK). Such phase-keyed formats are generally considered more robust and offer many advantages compared to traditional on-off keyed (OOK) formats including extended transmission distance and enhanced line capacity [83, 84]. In addition to facilitating the use of DPSK type formats phase sensitive amplifiers can also, in principle, operate with a theoretical noise figure of 0 dB – as opposed to phase insensitive counterparts which have the standard quantum noise limit of 3 dB [85, 86] that originates from the uncertainty principle. As phase sensitive amplifiers only amplify the components of the signal that are in phase, while simultaneously deamplifying the components that are out of phase, they are able to achieve a theoretical low of 0 dB noise without violating the uncertainty principle [87]. Recent work has, in fact, experimentally demonstrated a

phase sensitive amplifier with a record low 1.1 dB noise figure [88].

In fibre optic systems phase sensitive amplification can be realised either through the use of a nonlinear optical loop mirror (NOLM) [89, 90] or via four wave mixing [91–93]. While both have successfully been demonstrated, the four wave mixing approach is advantageous as it offers the possibility of using multiple channels and therefore supports wavelength division multiplexing (WDM) type applications. However, experimental realisation of phase sensitive amplifiers using four wave mixing has been difficult due to the need to maintain a fixed phase relationship between the signal and the pumps at the input [94].

However, experimental work [93] has shown that this can be overcome by generating the pump waves from part of the signal before amplifying it in a two-stage process. [93, 94].This 'black box' configuration automatically locks the phase of the pump and signal waves and offers a pragmatic approach to processing real world signals.

While the experimental configuration is an important practical consideration, the nonlinear medium in which the parametric process occurs is crucial to the efficient functionality of the device. When this research begun and and even during its progress, the nonlinear medium generally used in PSA architectures was dispersion shifted silica based highly nonlinear fibres (HNLFs) with nonlinearities in the order of 10 $W^{-1}km^{-1}$. These fibres are quite robust and have relatively low loss but the operating length required to perform PSA on even a 40 Gb/s signal is nearly 200 m long and requires approximately 2.5 W (CW) of total power (across the pumps and signal) [94].

Extending the operating bandwidth of phase sensitive amplifiers to higher bit rate signals, especially those approaching 1 Tb/s has been the PSA focus of this research. This requires an optical medium with a gain profile that is both broad enough to encapsulate extremely high signal bandwidths and high enough to work with reasonable levels of signal and pump power, and fibre length. Using soft glass microstructured fibres is one possible way to access such a regime – where the gain, per length, is both higher and, by design, can be prevalent over a broader band. This allows us to potentially fabricate devices with fibre lengths in the order of meters, compared to the hundreds of metres that are generally required when using silica based HNLFs. For some applications there may also be a significant reduction in the required optical power, to sub Watt levels. Consequently this research investigated the use of a soft glass microstructured

fibre based design to perform phase sensitive amplification on a 640 Gb/s signal using a similar degenerate FWM configuration to that presented in Reference [94].

More recently, since the time when this research was completed (in early 2013) and was being written up, PSA has been demonstrated in glasses other than silica – highly nonlinear materials similar to those that have been considered in this research. PSA has been demonstrated on a chalcogenide based chip waveguides using a degenerate FWM scheme [95, 96], and also in silicon based waveguides [97, 98]. Very recent work has also demonstrated phase sensitive amplification of 16-quadrature amplitude modulated signals at a data rate of 40 Gb/s for the first time using a non degenerate FWM scheme in periodically poled lithium niobate (PPLN) waveguides [99, 100]. Recent theoretical work has also investigated the use of a seven wave, dual pump, degenerate scheme to simultaneously perform phase sensitive amplification and 1-to-9 multicasting of a 40 Gb/s signal in silica HNLF [101].

2.4.2.1 Theory of phase sensitive amplification

Consider the case of two pump degenerate four wave mixing, where the frequency condition $2\omega_{s,i} = \omega_{P1} + \omega_{P2}$ is satisfied, i.e. where the signal and idler are degenerate and lie between the pumps. The signal, idler and pump waves are also assumed to be coplanar. A theoretical description of this scenario, along with some others, is well covered in Reference [38]. The same formalism is adopted here.

We begin by writing the coupled amplitude equations, under the nondepleted pump approximation. These equations are essentially the same as 2.51 to 2.54, but simplified for this particular pump, signal and idler frequency combination.

$$\frac{dA_{P1}}{dz} = i\gamma(|A_{P1}|^2 + 2|A_{s,i}|^2 + 2|A_{P2}|^2)A_{P1} + i\gamma A_{s,i}^2 A_{P2}^* \exp(i\Delta\beta z), \tag{2.64}$$

$$\frac{dA_{s,i}}{dz} = i\gamma(2|A_{P1}|^2 + |A_{s,i}|^2 + 2|A_{P2}|^2)A_{s,i} + i2\gamma A_{P2} A_{P1} A_{s,i}^* \exp(-i\Delta\beta z), \tag{2.65}$$

$$\frac{dA_{P2}}{dz} = i\gamma(2|A_{P1}|^2 + 2|A_{s,i}|^2 + |A_{P2}|^2)A_{P2} + i\gamma A_{P1}^* A_{s,i}^2 \exp(i\Delta\beta z). \tag{2.66}$$

A_{P1} and A_{P2} represent the field amplitudes at the pump wavelengths and $A_{s,i}$ is the field at the degenerate signal/idler wavelengths. The fibre nonlinearity is represented

by the nonlinear coefficient γ and $\Delta\beta$ is the phase mismatch, defined below in Equation 2.71. After propagation the final output $A_{s,i}$ can be written as below, in terms of the transformed signal amplitude $B_{s,i}$ and transfer functions μ and ν.

$$A_{s,i}(z) = B_{s,i}(z)\exp[-i\Delta\beta z/2 + i3\gamma(P_{P2} + P_{P1})z/2], \tag{2.67}$$

$$B_{s,i}(z) = \mu(z)B_{s,i}(0) + \nu(z)B^*_{s,i}(0), \tag{2.68}$$

$$\mu = \cosh(gz) - i\frac{\kappa}{2g}\sinh(gz), \tag{2.69}$$

$$\nu = i\frac{2\gamma A_{P1}(0)A_{P2}(0)}{g}\sinh(gz). \tag{2.70}$$

The input pump fields are given by $A_{P1}(0)$ and $A_{P2}(0)$ and we have used the quantities $\Delta\beta$, κ, and g for the phase mismatch, phase matching factor and parametric gain, respectively. They are defined below, where $\beta_{s,i}$ is the propagation constant at the signal/idler wavelength, while β_{P1}, β_{P2} are those for the two pumps. The pump powers are denoted by P_{P1} and P_{P2}, where $P_{Pi} = |A_{Pi}|^2 (i = 1, 2)$.

$$\Delta\beta = 2\beta_{s,i} - \beta_{P1} - \beta_{P2}, \tag{2.71}$$

$$\kappa = \Delta\beta + \gamma(P_{P1} + P_{P2}), \tag{2.72}$$

$$g = \left(4\gamma^2 P_{P1}P_{P2} - \frac{\kappa^2}{2}\right)^{1/2}. \tag{2.73}$$

Note that given Equation 2.73, the transfer functions satisfy the condition $|\mu|^2 - |\nu|^2 = 1$. The phase dependent nature of the gain can be easily seen by considering the simple case where the phase is perfectly matched such that $\kappa = 0$. In this case we can write

$$\begin{aligned} B_{s,i}(z) &= \cosh(gz)B_{s,i}(0) + i\sinh(gz)B^*_{s,i}(0), \\ &= \frac{e^{gz}+e^{-gz}}{2}B_{s,i}(0) + i\frac{e^{gz}-e^{-gz}}{2}B^*_{s,i}(0), \\ &= e^{gz}\frac{B_{s,i}(0)+iB^*_{s,i}(0)}{2} + e^{-gz}\frac{B_{s,i}(0)-iB^*_{s,i}(0)}{2}. \end{aligned} \tag{2.74}$$

Showing that the signal quadrature $\frac{1}{2}[B_{s,i}(0) + iB^*_{s,i}(0)]$ is amplified by the factor e^{gz} while the $\frac{1}{2}[B_{s,i}(0) - iB^*_{s,i}(0)]$ quadrature is attenuated by the same factor. Thus the phase sensitive gain, given by the ratio of the amplified factor to the attenuated one, is given by $G_{PSA} = e^{2gz}$.

This analytical description illustrates the nature of phase sensitive amplification for the two-pump scheme. The gain factor, g, presented in this analysis (see Equation 2.73) is crucial in determining how well a fibre may work as a PSA device and is therefore used in the optimisation procedure of the fibre design (details of which are presented in Section 4.5.4).

However it should be noted that the above analysis is only valid in the small signal regime where the pumps are not depleted. Hence, pulse propagation is modelled numerically to evaluate the PSA performance without the need for the small signal approximation. This allows us to, for instance, evaluate PSA performance in the saturated regime where the pumps are depleted. This modelling procedure is covered in detail in Section 5.2

Phase sensitive amplification has also long been known in quantum mechanics as a mechanism for producing so-called 'squeezed states' of light – nonclassical photon states where the noise in one complex phasor can be squeezed past the minimum quantum uncertainty limit, at the expense of the other quadrature component[2]. These squeezed states have many interesting applications and thus motivated much of the early work into PSA [102–104]. To date, some of the most successful experimental generations of squeezed optical states has been through the use of a nonlinear parametric process such as phase sensitive amplification [105, 106].

[2] quadrature components are those that are separated in phase by $\frac{\pi}{4}$

2.4.2.2 Design considerations

Equations 2.71 to 2.73 show that the gain for the nonlinear four wave mixing process, g, is highest when κ is lowest. Given that $\gamma(P_{P1} + P_{P2})$ is a slow function of λ, this means the gain is largely dependent on the phase mismatch, $\Delta\beta$ between the signal/idler and pump waves. This phase mismatch parameter, in turn, depends on the wavelength dependence of the propagation constant within the fibre, i.e. its dispersion. Thus, for high gain and ideal performance, one must engineer a fibre that has both low dispersion and low dispersion slope.

The other important fibre parameter in determining the gain, as we see from Equations 2.72 and 2.73, is the nonlinearity – a high nonlinearity coefficient, γ, leads to proportionally higher gain. A soft glass based optical fibre, with high intrinsic nonlinearity and ability to be fabricated into complex geometries for dispersion tailoring, is therefore a promising candidate for this application.

Additionally, the loss of the fibre is also an important parameter. While the loss was not explicitly included in the theoretical description of PSA above for simplicity, the fibre loss will reduce the gain of the amplified signal components and thus reduce the overall signal to noise ratio. Soft glasses have a higher loss than silica fibres (typically by several orders of magnitude), however this can potentially be compensated for by the relatively higher intrinsic nonlinearity. Thus, when evaluating soft glass materials for fibre based devices, it is useful to define a figure of merit (FOM) that takes both the loss and nonlinearity into account. This is discussed further in Section 3.3, with a definition of the FOM in Equation 3.5.

2.5 Conclusion

This chapter outlines the theoretical underpinnings for nonlinear fibre optics with a particular focus on the four wave mixing phenomenon, due to its signal regeneration and amplification applications. It also describes the theory behind the two FWM based applications, multicasting and phase sensitive amplification, that this research is focussed on and outlines the relevant background literature on each application. This provides a

basis for understanding the design considerations that must be taken into account when fabricating fibres for each application.

For both multicasting and PSA, the major design considerations that would allow us to achieve a fibre with the required gain profile to enable high speed signal processing are: a high nonlinearity and the ability to engineer the dispersion profile into a low, flat profile across the required band. Consequently, the choice of material in which to fabricate these fibres is an important one, as both the dispersion and nonlinearity depend heavily on material properties. In the case of the dispersion, the material dispersion has to be compensated for with waveguide dispersion to achieve the required profile (this process is described in more detail in Section 2.2.3); for the nonlinearity, the nonlinear coefficient is directly proportional to the material's nonlinear refractive index and also depends on the effective area which, in turn, is related to the linear refractive index as it affects the confinement of the mode.

Soft glasses present themselves as promising candidates for these fibre materials due to the fact that they have high intrinsic nonlinearity and a relatively low softening point – which enables them to the fabricated into complex geometries for broad band dispersion engineering using glass extrusion techniques. Although soft glasses have a relatively higher loss than silica glasses, this may be compensated for by the high intrinsic nonlinear index – this is discussed in more detail in Section 3.3, where a figure of merit that includes both the loss and nonlinearity is introduced (see Equation 3.5). Due to overall attractiveness of soft glass fibres as a platform for nonlinearity base applications, these glasses were chosen as the materials in which to design fibres for multicasting and PSA. They are described in detail in Chapter 3.

Chapter 3

Soft glass

3.1 Introduction

This chapter focuses on the materials that underpin the fibres that were designed and fabricated as part of this research. When developing fibres for nonlinearity based applications, the choice of material plays a very important role as it sets a base value for critical properties such as dispersion, nonlinearity and loss. The choice of material also affects the fibre fabrication approach as properties such as mechanical strength, thermal stability and surface tension must be considered in the fabrication procedure.

The materials considered in this research were some form of soft glass – glasses that are characterised by the fact that they soften at temperatures much lower than conventional, silica based glasses.

To understand soft glasses, their benefits and why they were chosen for this research a basic understanding of the chemistry of the glassy state is required. This is covered in Section 3.2. Section 3.3 then describes the characteristics of soft glasses and outlines why they are attractive materials for nonlinearity based telecommunication applications.

Section 3.4 presents an overview of some of the more common types of soft glasses that have been studied in the literature. The chemical composition of each of these soft glass types is described along with a discussion of their respective strengths and weaknesses for use in a nonlinear fibre device. The focus of the chapter then moves to a novel lead germanate glass that was developed and characterised with the aim of providing a glass

with a high nonlinearity and mechanical stability. These novel germanate glasses are shown to share many of the favourable properties of tellurite glasses but with a higher mechanical and thermal stability, thus presenting a practical alternative to tellurite based glasses for nonlinear applications. This work involved a detailed characterisation of the glass including an analysis of the effect of composition on glass stability, the thermal properties, Raman gain, loss, refractive index, dispersion and nonlinearity; it forms the bulk of this chapter and can be found in Section 3.5.

3.2 Glass fundamentals

The definition of what counts as a glass is somewhat difficult to express in a way that appropriately describes its properties without being too restrictive. On the outside, a glass appears to to be a solid with similar physical properties to those of crystals. However, unlike crystals, glasses do not have a fixed melting point (rather softening and then melting over a temperature range); they do not generally cleave along a preferred axis (unless there are physical stresses in the material); and, most importantly, glasses are isotropic, i.e. the internal structure appears uniform in all directions.

The isotropy of glassy materials makes them quite similar to liquids. This similarity is seen in the arrangement of atoms in glasses which, as is typical in liquids, display a long range disorder (even though the material is in a solid state).

The generally accepted definition of a glass then is that they are amorphous materials that, when heated, undergo an unique 'glass transition' into a non-solid state [3]. This transition goes both ways[1] so it is possible to start with a liquid material and cool it into a solid glass – indeed, this is the way most glasses are made. Figure 3.1 shows a volume–temperature (V–T) diagram highlighting this glass transition.

The V–T diagram is a useful tool to describe how a glass is formed and when a material is considered to be in a glassy state. If we start by considering a liquid at the point a on the diagram, as it cools the volume of the material travels down the line ab until it reaches the melting temperature T_m. This melting temperature can be described as the temperature at which the liquid and solid states of the material are in thermal

[1] Although a glassy material may transition from a solid to a liquid and vice versa, the path that the transition takes, in terms of the volume to temperature relationship, is not the same each way.

equilibrium. More technically, T_m is the temperature at which the solid and liquid states have the same vapour pressure or Gibbs energy (the capacity of the system to do non-expansive work, analogous to potential energy).

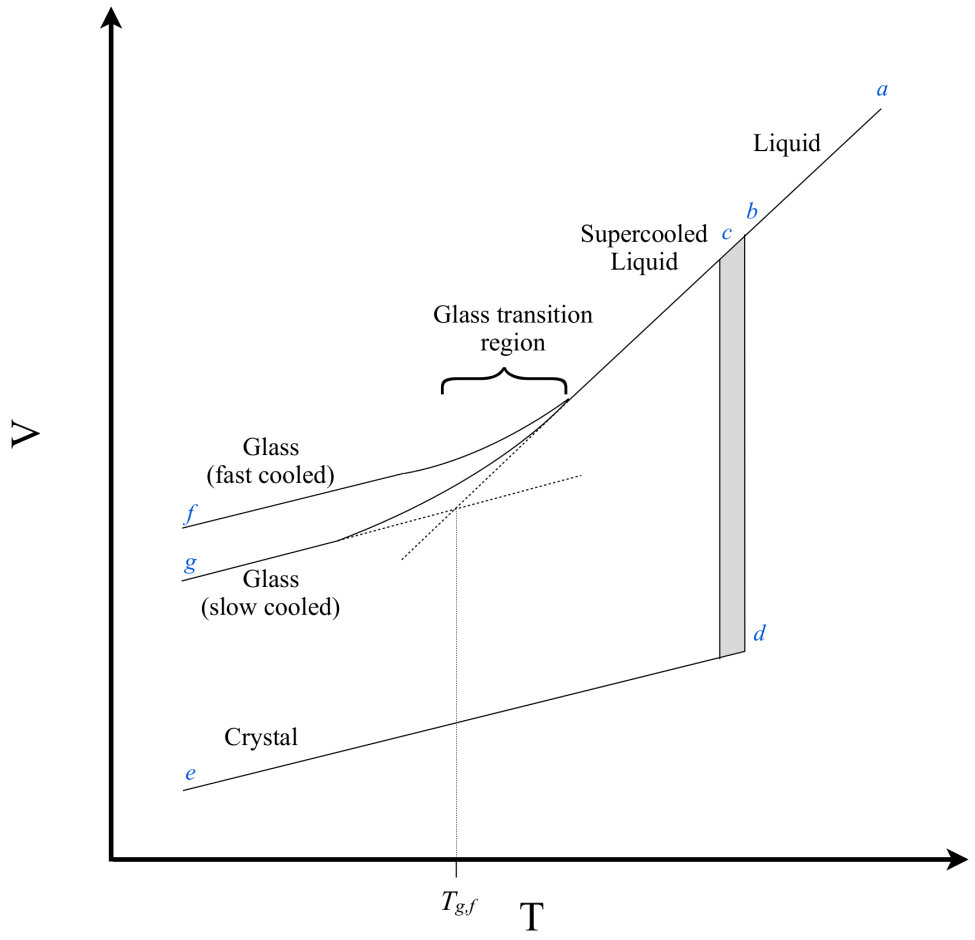

FIGURE 3.1: A typical volume–temperature diagram for a glass material [3]. This diagram shows how the volume changes with temperature as the material is cooled from the liquid to the glassy state. $T_{g,f}$ is the characteristic temperature of the glass transition region for the slow cooled glass – this temperature is interchangeably referred to as the fictive temperature T_f or the glass transition temperature T_g. The transition temperature for the fast cooled glass can also be derived in a similar fashion.

Once at this temperature what happens next, as the temperature drops to just below T_m along the line bc, depends on the rate of cooling. If there are enough nuclei in the material and the cooling rate is slow enough to allow for the growth of crystals, then crystallisation will occur throughout the material. This results in a sudden drop in volume to the point d, and any further cooling will cause the crystals to shrink along the line de. The point c can vary depending on various kinetic factors, such as the velocity at which the atoms can move to the interface at which the liquid crystallisation occurs. It is therefore represented by a shaded region in the diagram.

If the liquid is cooled fast enough such that the processes required for crystallisation do not have time to occur, it will continue to decrease volume linearly with temperature along the extrapolation of the line *abc* into the 'supercooled liquid' state. Further cooling of the material will result in a deviation of the volume compression rate dV/dT from the line *abc* to a lower rate as the material transitions into a solid. The start of this deviation marks the end of the supercooled liquid state and the start of the glass transition. This transition ends once the material has reached a solid state and resumes cooling at a constant dV/dT. The final volume also depends on the cooling rate – if the material has been cooled quickly it will end up at the point f with a higher volume, otherwise it will end up at g with a lower volume.

One of the defining characteristics of glasses is that this transition region, from the liquid to the solid state, happens over a temperature range instead of a fixed temperature. However, this transition may still be characterised via the intersection point of the extrapolation of the solid and supercooled liquid states. This temperature is generally defined to be the fictive temperature T_f – a concept first introduced by Arthur Tool [107] to quantify the temperature at which the structure of the supercooled liquid is essentially frozen into the glass. However this point is also sometimes interchangeably referred to as the glass transition temperature T_g.

There is generally no agreed upon description in the literature for the relationship between T_g and T_f. The choice of which characteristic temperature label to use is usually determined by how it has been measured – T_g is determined by cooling from the liquid state, whereas T_f is done so by heating from the glassy state and is generally found to be slightly lower than T_g [108]. T_g is also sometimes defined in terms of the viscosity, where the transition temperature is that at which the viscosity is equal to 10^{12} Pa·s [109]. However, as the viscosity can change quite rapidly in this transition region measuring T_g this way can lead to large errors.

While there is no straightforward link between T_g and T_f both are, nevertheless, useful characteristic glass parameters. The glass transition temperature is particularly important when considering glasses for fibre fabrication – while no deformation actually occurs at T_g, the temperature at which the glass does soften, T_s, is related[2]. Knowing the

[2]The softening point for glasses is usually measured as the point at which the glass softens under its own weight. This is known as the Littleton softening temperature [110] – defined as the temperature at which the glass viscosity is $10^{6.6}$ Pa·s

value of the transition temperature is therefore crucial to determining the appropriate conditions for extrusion – a key part of the fibre fabrication process that is described in detail in Section 6.2.

3.2.1 Optical properties

When considering glasses for nonlinear applications the most important optical properties are the loss and the refractive index, both linear and nonlinear. Ultimately we seek glasses with a high nonlinearity index and good transparency at the wavelengths of interest.

The transmission is predominantly determined by the absorption coefficient of the material, which is derived in terms of the Beer–Lambert law

$$I_{out}(\lambda) = I_{in}(\lambda)e^{-\alpha(\lambda)z}, \tag{3.1}$$

where α is the absorption coefficient, z is the propagation length within the material, I_{in} is the intensity at the input end of the waveguide at the wavelength λ and I_{out} is the intensity at the output end of the waveguide, also at the wavelength λ. The absorption coefficient may be extracted from Equation 3.1 and written as

$$\alpha(\lambda) = \frac{1}{z}\ln\left(\frac{I_{in}(\lambda)}{I_{out}(\lambda)}\right). \tag{3.2}$$

The absorption coefficient in Equation 3.2 has units of m^{-1} and is commonly used in fields such as spectroscopy. However, when discussing optical fibre loss, it is more common to define the absorption coefficient in dB/m units as

$$\alpha_{\mathrm{dB}} = \frac{10}{z}\frac{\ln(I_{in}/I_{out})}{\ln(10)} = 4.34\alpha. \tag{3.3}$$

This absorption coefficient for bulk samples is generally obtained by using a spectrometer to measure the transmission spectrum through a sample of known thickness. This measurement provides the intensity ratio I_{out}/I_{in} which, when combined with the known value for thickness, can be used to calculate the absorption coefficient via Equation 3.2.

Care must be taken when making this measurement to ensure that the surface is free of imperfections that may introduce scattering losses as these would otherwise make the absorption appear higher than it actually is. Additionally, the refractive index of the glass must also be known to account for the loss in transmitted intensity due to Fresnel reflections at the surfaces.

When measuring the loss in optical fibres Fresnel reflections do not need be taken into account, as the cutback technique is used. In this procedure the output power is measured as a function of length, starting from a long initial fibre length and then for successively shorter lengths that are cutback from the output end of the fibre. This procedure is described in detail in Section 7.4.1, which precedes experimental results for a cutback loss measurement on a microstructured optical fibre fabricated as part of this work.

The refractive index, n, is the other crucial optical property that determines how well a given glass would function in a nonlinear optical device. Fundamentally, the refractive index determines the velocity v at which an optical wave travels through the medium via the relation $v = c/n$ – where c is the speed of light in free space and n is the refractive index.

As described in Chapter 2, the refractive index consists of both a linear and a nonlinear component. In amorphous materials such as glasses this nonlinear component is intensity dependent due to the optical Kerr effect [111] – a discussion on the origin of this nonlinear component can be found in Section 2.2.1. The total refractive index is then written as

$$n = n_0 + n_2 I, \tag{3.4}$$

where n_0 is the linear refractive index, n_2 is the nonlinear refractive index and I intensity of the light beam in the material. Both of these components are especially important for nonlinear applications as they largely determine the nonlinear coefficient γ. This is due to the fact that γ is directly proportional to n_2 and the confinement of the optical mode within the fibre (determined by n_0). This is explained in detail in Chapter 4.

The refractive index may be measured by a number of methods, the most common methods involve either measuring the angles of incidence and reflection off a sample surface or the angle of total internal reflection and then deriving the refractive index

from Snell's law of refraction. The Prism coupling technique is an example of this [112], where the angle of total internal internal reflection (off the glass sample into a prism of known index) is measured and used to calculate the refractive index. While these techniques can be used to measure the refractive index of a glass with good accuracy and relative ease, they are limited to a few laser wavelengths, typically just one. In this research, the refractive indices for a novel set of glasses was measured using the ellipsometry technique. Ellipsometry is generally less accurate than prism coupling, however its main advantage is that the refractive index can be measured over a large wavelength range with high resolution. This is extremely useful for calculating the dispersion for a glass sample. The refractive index measurement experiment and results are discussed in detail in Section 3.5.3.

3.2.2 Fabrication procedure

The fabrication of a glass billet starts by combining all the raw ingredients, in dry powder form, into a crucible. The crucible is made of an inert metal such as gold or platinum, as these precious metals are not very reactive and thus the least likely to be corroded by and contaminate the glass melt. However, for some glasses, such as chalcogenides, even inert metals cannot be used and other materials, such as vitreous carbon, must be used for the crucible – the choice of crucible material is ultimately determined by the type of glass being fabricated. Once the raw materials have been batched together at the appropriate weights, the crucible with its content is placed in an oven which is then set to rise to a temperature high enough to melt the raw materials.

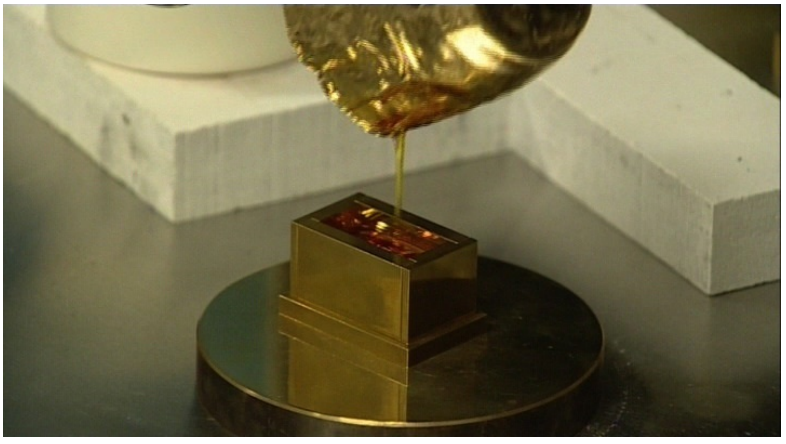

FIGURE 3.2: Glass being poured from a gold crucible into a rectangular brass mould. The relatively small rectangular blocks produced from this type of mould is used for characterisation of the bulk material.

Once the glass is in molten form, the crucible may be temporarily removed from the furnace and its contents swirled to ensure a homogeneous distribution of the glass molecules. This is usually done right before the glass is ready to be cast out, but it may also be done intermittently during the melt.

FIGURE 3.3: A cylindrical mould of the type in this picture is used to produce glass billets (seen at the bottom of the picture) for extrusion.

When the raw materials are completely molten and glass melt is homogenised within the crucible, the melt is poured out into a preheated brass mould. The glass is then allowed to cool inside this mould until it reaches room temperature. This happens in two stages: first the glass melt in the mould is cooled down rapidly in open air until it is almost solid but at a temperature warmer than T_g; the mould containing the glass is then placed in an annealing oven an allowed to cool slowly to room temperature. The first stage in this process ensures that the cooling is quick enough to avoid crystallisation within the glass as these crystals can act as scattering spots within the glass, leading to high optical loss.

The cooled glass is then removed from the mould and placed back in the oven for post-annealing. This is a process where the glass is slowly heated up to its annealing point and then allowed to very slowly cool down again (usually at a rate of 0.1 to 0.5 °C per minute). During this annealing process the glass molecules absorb enough energy to rearrange themselves into the lowest energy state; but not so much that the glass deforms. The actual annealing point is defined to be the temperature at which the

viscosity is approximately 10^{12} Pa·s [113][3]. The post-annealing procedure ensures that any internal stresses that may have been introduced into the glass due to the fast cooling (done to prevent crystallisation) are relieved, thus making the billet more robust for later fabrication into fibres.

3.3 Characteristics of soft glasses

The defining characteristic of soft glasses, and indeed the characteristic for which they are named, is the softening temperature, T_s – a glass is deemed 'soft' if its softening temperature is significantly lower than that of silica glass, typically on the order of a few hundred degrees. There is no strict definition for the upper limit of T_s for a material to be categorised as a soft glass, however the highest it typically tends to be is around 500-550 °C. At the lower end of the scale, for glasses such as some chalcogenides, the softening point can even be below 100 °C [114].

The relatively low softening temperature of soft glasses is extremely useful for optical fibre device fabrication as it enables these glasses be fabricated into complex, almost arbitrary, structures via the extrusion technique. This fibre fabrication technique (described in detail in Chapter 6) essentially relies on forcing the softened glass through a steel structure, called a 'die', to generate a structured glass 'preform' from which a microstructured fibre can be drawn. It relies on the fact that steel die retains its mechanical strength and does not deform at the temperature at which the glass softens. Consequently the softened glass can be forced through the die and have the structure of the steel longitudinally imprinted on itself.

Soft glasses usually also have a high refractive index (both in the linear and nonlinear components), relative to the fused silica glasses that are used in commercial optical fibres[4]. The linear refractive index for fused silica at 1.55 µm is approximately 1.4 [115], whereas for most soft glasses n ranges from 1.8 to 2.9 (see Table 3.2). The difference in the nonlinear refractive index is significantly more pronounced – for silica the nonlinear refractive index is approximately 2.8×10^{-19} m^2/W, however for soft glasses n_2 is at least an order of magnitude higher, and for some chalcogenides it may be orders of magnitude

[3]Recall that the transition temperature is also sometimes defined in terms of viscosity this way, thereby making the annealing temperature and transition temperature very close for most glasses

[4]This is true for most soft glass families, however some soft glass types, such as fluoride based glasses, have similar refractive indices to silica

more (again see Table 3.2). This difference in the nonlinear index is, however, expected since soft glasses already have a higher linear index and, in accordance with the empirical Miller rule [116], the nonlinear refractive index should increase proportionally and thus also be higher. The Miller rule can also observed within the various families of soft glasses – those glasses with the highest linear refractive indices (such as chalcogenide) also have the highest nonlinear refractive index.

The combination of high nonlinear index and the ability to fabricate complex structures into the fibres is what makes soft glasses an attractive proposition for the fabrication of fibres for telecommunication applications. Using soft glass for fibre fabrication results in fibres that have an inherently higher nonlinear coefficient and may be engineered into a geometry with extremely low dispersion across a broad band.

There are also many soft glasses with high nonlinearity that have good transmission in the infrared region around 1.55 µm, albeit with a relatively higher loss than that of fused silica[5]. However as the nonlinearity and, consequently, the gain is much higher in soft glass fibres they require much less power and can thus be used with a much shorter operating length. This nonlinear performance may be quantified using a figure of merit (FOM) that is based on the required input power to achieve a certain nonlinear phase shift. Using the definition for this FOM given in Reference [117], it may be written as

$$\text{FOM} = \gamma L_{eff}, \tag{3.5}$$

where γ is the nonlinear coefficient and L_{eff} is the effective length – the latter term takes into account optical loss, α, and the fibre length, L, and may be written as

$$L_{eff} = \frac{1 - e^{-\alpha L}}{\alpha}. \tag{3.6}$$

The FOM given in Equation 3.5 is a good indicator of nonlinear performance as the higher it is, the lower the optical power required to get a certain nonlinear phase shift. Although the performance of a FWM based device is more complex than this, Equation 3.5 serves as a good base point for comparing fibres for use in nonlinear telecommunications devices.

[5] Absorption for soft glasses fibres is usually around 0.1 to 5 dB/m, while the loss for fused silica fibre is approximately 0.2 dB/km

Fibre	Loss (dB/m)	γ ($W^{-1}km^{-1}$)	$L_{eff}(L=1)$ (m)	FOM ($10^{-3}W^{-1}$)	Reference
Silica HNLF	0.16	10.3	0.98	10	–
SF57 MOF	3.0	270	0.72	194	[118]
Tellurite MOF	0.4	675	0.96	648	[117]
Bismuth MOF	3.4	1100	0.69	759	[117]

TABLE 3.1: Figures of merit (FOMs) for various nonlinear optical fibres. The silica HNLF is a commercially available fibre used in our lab, while the rest are taken from the literature. The FOMs show that although the soft glass fibres have a higher loss, they score highly when considering nonlinear fibres for compact devices.

Table 3.1 provides a comparison of FOMs for various nonlinear optical fibres where the FOM has been evaluated as per Equation 3.5, with the fibre length set to 1 m for comparison. The results in this table show that the relatively high loss of the soft glass fibres is compensated for by the higher nonlinearity, giving them high figures of merit when considering fibre devices with the typically short fibre lengths required when using such fibres.

Soft glass fibres are therefore promising candidates for the broad band applications discussed in Chapter 2. In the following section, some of the families of soft glasses commonly used in nonlinear optics applications are described, along with a short discussion of the pros and cons of each.

3.4 Families of soft glasses

Soft glasses may be categorised into 'families', based on their composition – specifically, the molecule that acts as the glass network former [119]. Glasses within a family will have similar compositions, with the specific elemental quantities varying over a range. For example, in the germanate family of soft glasses, the primary molecule is germanium oxide (GeO_2). In the germanate glasses developed in this research GeO_2 accounted for 60% of the glass composition, with 30–40% PbO and 0–10% of La_2O_3 and/or Na_2O.

Various such families of soft glasses exist, such as fluorides, silicates, germanates, tellurites, chalcogenides and so on – each with different physical and chemical properties. When considering telecommunications applications, glasses such as tellurites and chalcogenides have proven to be popular choices, generally due to the high nonlinearity

that these glasses provide and, especially in the case of tellurites, good transparency at 1.55 µm.

The sections below describe some of the soft glass families that have been considered in this research. This list is by no means exhaustive, however it contains most of the glasses that have been investigated in the literature for nonlinear telecommunications applications. Among these glasses, special attention is given to a relatively new family of soft glasses: lead germanates. Section 3.5 follows on from this and describes, in detail, the development and characterisation of a new lead germanate glass for telecommunications applications.

3.4.1 Chalcogenide

Glasses that are composed of one or more chalcogen elements (such as S, Se, Te) combined with other elements such as As, Ge, Sb or Ga are known as chalcogenide glasses [120]. Even amongst soft glasses they are noted for their extremely high nonlinearity and broad transmission window, which extends well into the infrared.

The linear index of chalcogenide glasses, at telecommunications wavelengths, is generally well above 2 and ranges from 2.45 to 2.93 at 1.55 µm for As—S—Se compositions [121]. The nonlinearity scales along with the linear refractive index and has been measured as up to 930 times that of fused silica at 1.55 µm [121].

The softening temperature for chalcogenide classes is, as with the refractive index, dependent on composition. For most Ge—As—Se—Te based chalcogenide glasses T_g is approximately between 220 °C and 360 °C [122]. Other compositions have been shown to have even lower softening temperatures, some in the sub-100 °C [114] range.

This limits the temperatures that can be used during the processing and general fabrication of these glasses. Consequently extrusion and drawing of chalcogenide based structures into complex microstructured optical fibres has proven difficult. However, significant progress has been made by using novel methods such composite chalcogenide and polymer preforms [123] and preform casting into structured moulds [124].

For telecommunications applications it is the high nonlinearity that is of particular interest [125]. Recent work has demonstrated tapered chalcogenide fibres with a nonlinear

coefficient γ of approximately 54,100 $W^{-1}km^{-1}$ [126], which is 50,000 times that of silica fibre. The use of chalcogenide glass for telecommunications systems as either a fibre [127, 128] or an optical 'chip' [129, 130] has also been successfully investigated.

As part of this work preliminary investigations were conducted into the use of a composite chalcogenide—tellurite glasses for the fabrication of highly nonlinear fibres. The glasses used were a commercially available IG5 chalcogenide glass, and an in-house tellurite composition. This work is presented in Section 6.3.

3.4.2 Lead silicate

Lead silicate glasses are composed of mainly PbO and SiO_2. These glasses are robust nonlinear materials that are readily commercial available. The Schott SF57 glass, for instance, has a refractive index at 1.55 µm for 1.8 and has been used in the fabrication of fibres for nonlinearity based telecommunications applications [131]. The commercial availability of multiple types of lead silicate glasses (such as the Schott SF6 and LLF1), with varying refractive index but very similar chemical and visco-mechanical properties means they can be readily fabricated into composite fibres for dispersion engineering [132].

3.4.3 Bismuth silicate

Bismuth glasses consist mainly of bismuth oxide (Bi_2O_3) combined with SiO_2 and B_2O_3. It has a high nonlinear index of approximately 2 at 1.55 µm [117] and is known for having good mechanical, chemical and thermal stability [133]. Additionally, it has been shown that bismuth silicate fibres can be fusion spliced to silica fibres [134], thus making them compatible with most current silica-based optical networks.

The mechanical stability and high nonlinearity of these glasses led us to design a fibre based on the Asahi AB061 bismuth glass for phase sensitive amplification. This design work is covered in detail in Section 4.5.4; the published version can be found via Reference [33].

3.4.4 Tellurite

Tellurite glasses are composed predominantly of tellurium oxide (TeO_2), combined with varying amounts of other metal oxides such ZnO, Na_2O or La_2O_3. Tellurite has been used for optical fibre applications in the IR region due to its many favourable properties, such as a wide transmission window (0.35 µm to 5 µm), good glass stability, a relatively low phonon energy and a high linear and nonlinear refractive index [135]. In recent years, tellurite glasses have been used for mid-infrared fibre applications such as lasing [136], fibre amplifiers [137, 138] and supercontinuum generation [139, 140].

To date, the major application for tellurite glass based devices within the telecommunications window has been the development of C-band fibre amplifiers, usually by using an Erbium doped composition to generate gain [137, 141]. However, the high nonlinearity of tellurite glasses means that they can also be used to fabricate broadband parametric amplifiers that utilise nonlinear phenomena (such as FWM), instead of a material transition, to generate gain. The bandwidth of such a parametric amplifier is mainly limited by the dispersion of the fibre. Thus, by engineering this to be low and flat, these devices can be made to operate with a high gain over broad bandwidths.

In this research, a tellurite based fibre design was used for considered for use in multicasting – an extremely broad bandwidth signal conversion application (Section 2.4.1 described this application in detail). This work is presented in Section 4.5.3.

3.4.5 Germanate

Germanate glasses (which are another type of heavy metal oxide based glass) are very similar to tellurites. Where tellurites are composed mainly of tellurium oxide, the main component of germanate glasses is germanium oxide (GeO_2). The remainder of the glass is, again similarly to tellurite, usually composed of other metal oxides such PbO, ZnO, Na_2O or La_2O_3

The similarity of the two glass families also extends to their optical properties – they have similar phonon energies and similar mid-IR transmission properties. However germanates have a higher glass transition temperature leading to better mechanical and thermal stability [142]. Thus they offer many of the same advantages while doing away

Glass	Code	n	$n_2(\times 10^{-19})$ m^2W^{-1}	λ_n(µm)	Reference(s)
Silica		1.41	0.2	1.55	[28]
Lead silicate	SF6	1.76	2.2	1.55	[144]
Lead silicate	SF57	1.80	4.1	1.55	[145]
Bismuth	AB061	1.98	3.2	1.55	[146]
Tellurite	La10	1.98	5.9	1.55	[147]
Germanate	VIR-3	1.84	2.6	1.06	[148]
Germanate	QS	1.94	4.2	1.06	[148]
Chalcogenide	As_2S_3	2.48	250	1.06	[149]
Chalcogenide	IG5	2.67	400	1.55	[29]
Chalcogenide	$As_{39}Se_{55}Cu_5$	2.93	170	1.55	[121]

TABLE 3.2: Refractive indices, both linear and nonlinear, for various soft glasses and, for reference, conventional fused silica glass. In this table λ_n refers to the wavelength at which the refractive index n is obtained; n_2 is the nonlinear component of the refractive index.

with some of the main drawbacks found in the practical use of tellurite glass, making them attractive alternative materials for fibre applications in the mid-infrared. Tm-doped step index germanate fibres, for example, have already been used to demonstrate high power lasing at 2 µm [143].

The prospect of using germanate glasses to fabricate fibres that have similar optical properties to tellurite, but with better mechanical stability led us to investigate the development of some novel lead germanate glasses. As this family of glasses is relatively unexplored in the literature, this work contributes to the basic material and fabrication science of these glasses as well as their potential for use in the development of all optical devices for telecommunications applications. This work is presented in the following section.

3.5 Development and characterisation of new germanate glasses

Heavy metal oxide based glasses such as tellurite, germanate and gallate are attractive choices for applications in the telecoms and mid-IR bands (up to around 5 µm) where a high nonlinear refractive index is required. Of these, tellurite in particular has been an especially popular choice in the literature leading to a host of tellurite based fibre applications – as mentioned earlier in Section 3.4.4. Germanate glasses share many of the properties that make tellurite an attractive proposition for nonlinear fibre devices,

however they are mechanically more stable due to the fact they have a higher glass transition temperature [150].

This motivated the development of a novel germanate glass – one that would have the same favourable optical properties as tellurite (such as a high refractive index and transmission) but better mechanical stability, leading to more robust fibres.

The glass type that was chosen for development was a lead germanate. This glass type was chosen mainly because, within the germanate family, they show the highest refractive index. Moreover their suitability for step-index fibre fabrication has already been demonstrated [150, 151]. They have also been shown to be highly transparent in the visible [151] and near-IR spectral range [152], unlike bismuth germanates which also have a high refractive index but exhibit complex absorption phenomena (associated with the bismuth species) that span the visible to near-IR range [152].

Part of this development included an investigation of the effect of melting the glass in a controlled dry atmosphere – oxide glasses such as tellurite and germanate typically exhibit a high content of hydroxyl (OH) groups when melted in an open atmosphere. These OH groups are undesirable as they lead to intense and broad absorption at 3-4 µm, with an overtone at 1.4-1.5 µm that can affect loss in the main telecommunications window. Several methods have been investigated to fabricate both tellurite and germanate glasses with low OH content, such as the use of fluorides in the glass batch. However, this significantly changes the glass properties, making them more similar to those of fluoride glasses. This is undesirable for high gain lasers and nonlinear devices as it reduces the glass transition temperature and refractive index [153, 154]. To mitigate the effect of these OH groups a different approach was used, outlined in Reference [155, 156] – where, for tellurite glasses, significant reduction of the OH content (by 1-2 order(s) of magnitude) was achieved by using a controlled dry atmosphere for glass melting.

The impact of La_2O_3 in the glass composition on stability has also been studied. This builds on previous work within the group that showed that, for a Na-Zn-tellurite glass, addition of La_2O_3 increased the glass stability and allowed incorporation of active rare earth ions without significantly changing the glass properties [9]. In addition to this, the Raman spectra, linear refractive index and nonlinear refractive index were measured for some glass compositions.

Where appropriate, the analysed properties of the new lead-germanate glasses have been compared with a Zn-tellurite glass. Zn-tellurite glasses were chose for comparison as these glasses have been widely investigated for mid-IR applications [136, 137, 139, 140, 157] and such a comparison would enable the study of the germanate glasses developed here as a practical alternative to tellurite. Within the Zn-tellurite glass system, the glass that was selected for comparison was a Na-Zn-La tellurite glass (TZNL) whose properties have been investigated in detail in previous work [9]. The TZNL glass has also been optimised for fabrication of microstructured fibres using the extrusion technique [9], which is same technique was used to fabricate the lead-germanate microstructured fibre in this work.

The development and characterisation of this germanate glass is presented in the following sections as follows: Section 3.5.1 describes the fabrication of the germanate glasses, including details of the particular compositions used; Section 3.5.2 covers measurements of the physical characteristics of the glass, such as its density and thermal properties; Section 3.5.6 details measurements of the Raman properties of the glass; finally the optical properties are presented in Sections 3.5.5, 3.5.3 and 3.5.4 which cover the loss, refractive index measurements and nonlinearity measurements, respectively.

It should be noted that the work in Sections 3.5.1 to 3.5.6 were done by other members of the group (see the statement of original work in Section 1.4 for details). They are however presented here for completeness. The experiments on the measurements of the linear and nonlinear refractive indices, however, were carried out by the author. These experiments allow the dispersion and nonlinearity of the material to be calculated, which is essential to designing fibres for nonlinear telecommunications applications using this glass.

This germanate research has also been published and can be found via Reference [32].

3.5.1 Glass fabrication

The composition of the germanate glasses developed were within the system $60{\cdot}GeO_2$ — $(40 - x - y){\cdot}PbO$ — $x{\cdot}La_2O_3$ — $y{\cdot}Na_2O$ with x ranging from 0 to 10 and $y = 0$ or 5. These glass compositions are shown in Table 3.3 along with the TZNL glass that was used in the comparison of glass properties described in the following sections.

To fabricate the glasses they were first prepared into 30-300g weights, batched using raw materials consisting of commercially sourced GeO_2, PbO, La_2O_3 and Na_2CO_3 with 99.99% or higher purity. The glass batches were then placed in a glove box and purged with dry nitrogen (≤10 ppmv water). All glass batches were then melted in platinum crucibles at 1250 °C for 0.5-5 h, depending on the batch weight. The resulting glass melts were finally cast into preheated brass moulds and annealed at 400-450 °C, depending on the glass composition and batch weight.

Glass code	GeO_2	PbO	La_2O_3	Na_2O	Density (g/cm^3)	T_g (°C)	T_x (°C)	T_x-T_g (°C)	n_0 at 1.55 µm	n_2 (10^{-20} m^2/W)
GP	60	40			6.27	422	570	148		
GPL2	60	38	2		6.24	444	576	132		
GPL5	60	35	5		6.16	478	598	120	1.916	
GPL10	60	30	10		6.13	cast glass partially crystallized				
GPN	60	35		5	5.90	395	608	213		
GPNL2	60	33	(2)[a]	5	5.93	415	663	248	1.869	
GPNL5	60	30	5	5	5.83	455	692	244	1.868	57
TZNL	(73)[b]	(20)[c]	2	5	5.37[d]	315[d]	480[d]	165[d]	1.983[d]	55[e]

TABLE 3.3: Nominal glass composition (in mol%), density, glass transition temperature (T_g), onset of glass crystallization (T_x), glass stability ($T_x - T_g$), linear (n_0) and nonlinear (n_2) indices of germanate glasses made and tellurite glass TZNL published in Reference [9][f].

[a]For this sample, 2 mol% Tm_2O_3 instead of La_2O_3 was used.

[b]This value refers to the TeO_2 content.

[c]This value refers to the ZnO content.

[d]Values taken from [9].

[e]Value taken from [147].

[f]The measurement errors for the germanate glass properties are ±0.01 g/cm^3 for the density, ±2 °C for T_g and T_x, ± 0.02 for n_0 and ± 6.3 × 10^{-20} m^2W^{-1} for n_2.

The majority of the glasses were melted, swirled, cast and annealed in open atmosphere; these glasses were used for thermal and spectroscopic measurements and unstructured fibre fabrication. However a few glasses were melted, swirled, cast and annealed in dry atmosphere. The dry atmosphere environment was created by using a melting facility consisting of a melting furnace purged with a gas mixture with similar composition to air (80% nitrogen and 20% oxygen), an annealing furnace and glove box purged with

dry nitrogen with water content ≤ 10 ppmv. This dry atmosphere glass fabrication was used to minimise the amount of hydroxyl (OH) groups in the final glass. As mentioned before, these OH groups are undesirable as they lead to intense and broad absorption at 3 to 4 µm.

The resulting glass samples were made into three distinct types: rectangular glass blocks of dimensions $15\times10\times30$ mm^3 for thermal and spectroscopic measurements; cylindrical glass billets of 30 mm diameter and approximately 30 mm height for unstructured fibre fabrication; and cylindrical glass billets of 50 mm diameter and approximately 20 mm height for suspended core fibre fabrication. The unstructured germanate fibres were used along with some unstructured tellurite (TZNL) fibres to perform a preliminary evaluation of fibre strength via a measurement of the bend radius (the radius at which the fibre breaks [158]). This yielded values of 21.5 ± 8.7 mm and 16.3 ± 5.9 mm for the TZNL and GPL5 unstructured fibres (solid fibres made of a single material with no microstructure), respectively. The smaller bend radius for the germanate fibre indicates higher fibre strength, however further investigations need to be conducted to thoroughly quantify the fibre strengths of tellurite and germanate fibres.

Polished plates made from the glass blocks or polished billets were used to measure the IR absorption and the linear refractive index. The glass blocks as a whole were used for density measurements, and glass pieces from blocks were used for thermal analysis measurements. These measurements are described in the following sections.

3.5.2 Density and thermal properties

The density of the glasses was measured using the Archimedes buoyancy method. The weight of the sample is first measured whilst suspended in air, and then measured again after being immersed in a bath of water at a known temperature and density. The difference is used to calculate the buoyancy force which, by the Archimedes principle, is equal to the weight of water displaced. The Archimedes principle also states that the volume of liquid displaced will be equal to that of the sample. The density can then be calculated by first taking the ratio of the weight of the sample in air to the buoyancy force. This gives

$$\frac{W_{s,air}}{F_b} = \frac{W_{s,air}}{W_{s,air} - W_{s,liq}} = \frac{\rho_s V_s}{\rho_{liq} V_{liq}}, \tag{3.7}$$

where $W_{s,air}$ is the weight of the sample in air, F_b is the buoyancy force, $W_{s,liq}$ is the weight of the sample when immersed in liquid; and ρ, V represent the density and volume, respectively, with the subscript s denoting that of the sample and liq that of the liquid. Using the fact that $V_{liq} = V_s$ (via Archimedes), the equation above simplifies to

$$\frac{\rho_s}{\rho_{liq}} = \frac{W_{s,air}}{W_{s,air} - W_{s,liq}}, \tag{3.8}$$

which may be used to calculate the density of the sample.

Not surprisingly, the results of the density measurements showed that the density of the Na-free germanate glasses (6.1 to 6.3 g/cm^3) is significantly higher than that of the Na-containing glasses (5.8 to 5.9 g/cm^3). Both types of germanate glasses have a higher density compared with Na-Zn-tellurite glass (see Table 3.3), which is attributed to the high amount of the heavy metal oxide PbO.

The glass transition temperature (T_g) and onset of glass crystallization temperature (T_x) were measured using differential scanning calorimetry (DSC). DSC is a thermal analysis technique that essentially measures the change in heat capacity of a material with temperature. The sample is heated such that its temperature increases at a constant rate and the heat flow is tracked as a function of temperature. The resulting plot can then be used to determine the phase transitions in the material and the temperatures at which they occur. The glass transition temperature, for instance, can be determined from the glass relaxation peak – an endothermic dip in the heat flow graph represents the heat flowing into the sample as it transitions from the glass phase to the super liquid phase. Similarly, the crystallisation temperature is determined via the crystallisation peak. Figure 3.4 shows a DSC graph for the GPNL2 germanate glass with the glass relaxation peak, centred at approximately 667 °C, and the crystallisation peak, centred at approximately 741 °C.

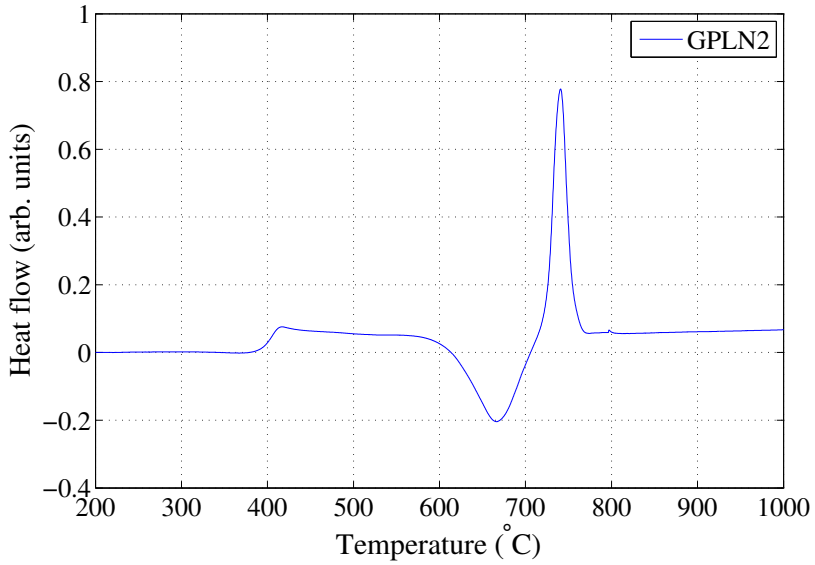

FIGURE 3.4: DSC data for the GPNL2 germanate glass shows the glass relaxation peak, centred at approximately 667 °C, and the crystallisation peak, centred at approximately 741 °C.

In these analyses glass disks of 30 to 60 mg weight and a heating rate of 20 K/min were used. The measurements also allowed the glass stability to be quantified using the temperature difference $T_x - T_g$.

Figure 3.5 shows the glass transition temperature as a function of increasing La_2O_3 content of the germanate glasses. For both the Na-free and the Na-containing glasses, T_g increases with increasing replacement of PbO by La_2O_3, which is of benefit for developing glasses with higher thermal stability, which in turn aids the fibre fabrication process.

Within the Na-free glasses, the glass stability ($T_x - T_g$) slightly decreases as PbO is increasingly replaced with La_2O_3 (Figure 3.5). For the glass GPL10 with 10 mol% La_2O_3, crystals were observed in the glass melt before casting. This result indicates that larger amounts of La_2O_3 (> 5 mol%) in GPLx result in low glass stability and thus make the glass unsuitable for fibre fabrication.

Compared with the Na-free germanate glasses, the Na-containing glasses have a considerably higher glass stability. This result is consistent with the glass stabilizing effect of small amounts of Na_2O in lead-silicate and tellurite glasses [135, 159]. Within the Na-containing glasses, the glasses with La_2O_3 have a slightly higher glass stability than the glass without La_2O_3, which demonstrates that the presence of Na_2O enhances the solubility of La_2O_3 in the glass matrix.

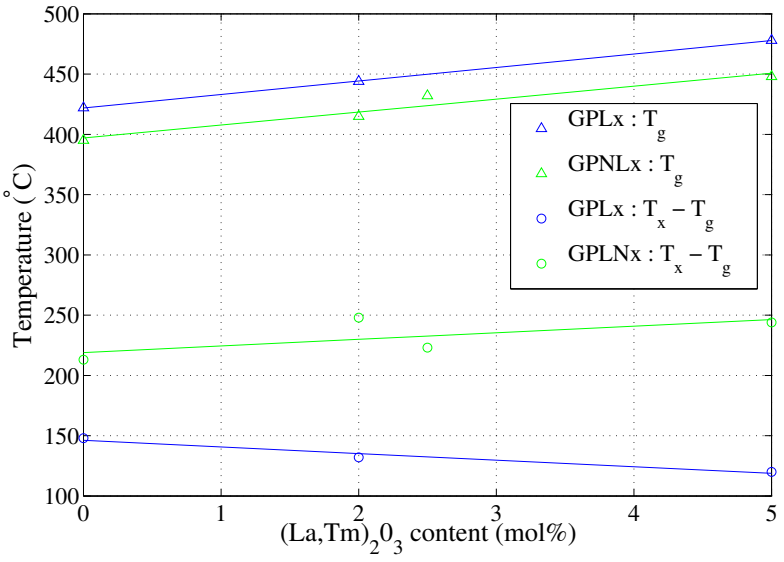

FIGURE 3.5: Glass transition temperature (T_g) as a function of the $(La,Tm)_2O_3$ content of Na-free germanate glasses (GPL) and Na-containing germanate glasses (GPNL).

3.5.3 Refractive index measurements via ellipsometry

For the GPL5, GPNL2 and GPNL5 germanate glasses and for a TZN tellurite glass with similar composition to TZNL (TZN in mol%: 80·TeO_2 — 10·ZnO — 10·Na_2O), the linear refractive index was measured over the broad range of 500 to 2000 nm using variable angle spectroscopic ellipsometry – a broad band technique that measures the change in polarization of light as it reflects from (or transmits through) a material, for a range of wavelengths and incidence angles. The ellipsometric technique does not directly measure the optical constants of the material, however the measured response depends on the dielectric properties and thickness of the material and can therefore be used to infer the values of optical constants, such as the refractive index [160].

For this investigation, the ellipsometer used was one manufactured by the J. A. Woollam company (V-VASE), set up in a in fairly typical ellipsometry configuration: linearly polarized light (of known polarisation but arbitrary azimuth) was reflected from the sample surface and the reflected beam analysed via a rotating polariser to determine its polarization. The phase change imparted onto the beam on reflection changes its polarisation from linear to, generally speaking, elliptical in nature.

By the comparing the polarization ellipse of this reflected bean with the known linear polarization of the incident light, the system is able to determine the change in both

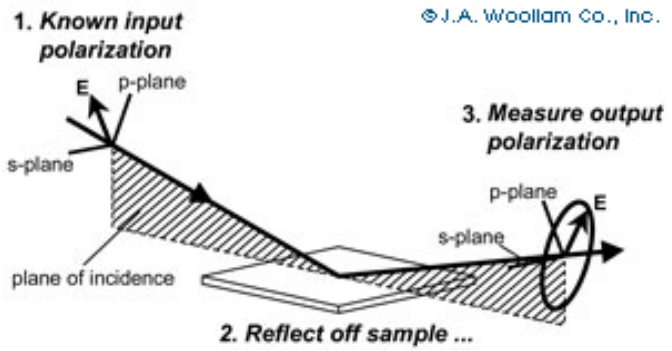

FIGURE 3.6: Schematic for a typical ellipsometry measurement. Linearly polarised light of a known polarisation is reflected off a sample and then the output polarisation is measured via a rotating analyser. This figure was taken from the J.A. Woollam Co. Inc. website [4].

amplitude and phase of the s-polarized and p-polarized constituents. This change in polarization is represented by the complex reflectance ratio ρ, given below in terms of parameters Ψ and Δ

$$\rho = \tan(\Psi)e^{i\Delta} = \frac{\widetilde{R}_s}{\widetilde{R}_p}, \tag{3.9}$$

where $\widetilde{R}_s$ and $\widetilde{R}_p$ are the Fresnel reflection coefficients of the s-polarized and p-polarized light, respectively. There are given by

$$\widetilde{R}_s = \left(\frac{n_a \cos\theta - \widetilde{n}_s \sqrt{1 - \left(\frac{n_a}{\widetilde{n}_s}\sin\theta\right)^2}}{n_a \cos\theta + \widetilde{n}_s \sqrt{1 - \left(\frac{n_a}{\widetilde{n}_s}\sin\theta\right)^2}} \right)^2, \tag{3.10}$$

$$\widetilde{R}_p = \left(\frac{n_a \sqrt{1 - \left(\frac{n_a}{\widetilde{n}_s}\sin\theta\right)^2} - \widetilde{n}_s \cos\theta}{n_a \sqrt{1 - \left(\frac{n_a}{\widetilde{n}_s}\sin\theta\right)^2} + \widetilde{n}_s \cos\theta} \right)^2, \tag{3.11}$$

where n_a is the refractive index of air (assumed not to be complex), $\widetilde{n}_s$ is the complex refractive index of the substrate and θ is the angle of incidence/reflection. The relationship between $\widetilde{n}_s$ and the parameters Ψ and Δ in the equations above is what allows the refractive index to be derived via ellipsometry.

The software on the ellipsometer uses a model of the substrate (i.e. bulk dielectric, thin film etc.) to predict the expected values for the parameters Ψ and Δ, for a given

wavelength and angle of incidence. These are then compared to the experimentally measured values and the model parameters are adjusted to minimise the difference between the generated data and the experimental values. This minimisation is done using a fitting procedure which, in this instrument, is based on the Levenberg–Marquardt algorithm. The error in the fit is quantified by a parameter known as a root mean squared error (MSE), defined as

$$\mathrm{MSE} = \sqrt{\frac{1}{2N-M}\sum_{i=1}^{N}\left[\left(\frac{\Psi_i^{Mod}-\Psi_i^{Exp}}{\sigma_{\Psi,i}^{Exp}}\right)+\left(\frac{\Delta_i^{Mod}-\Delta_i^{Exp}}{\sigma_{\Delta,i}^{Exp}}\right)\right]}, \tag{3.12}$$

where N is the number of spectrum points, M is the number of variable parameters in the model, Ψ^{Mod} and Δ^{Mod} are the parameter values generated by the model, Ψ^{Exp} and Δ^{Exp} are those measured by the experiment, σ_{Ψ}^{Exp} is the error in Ψ^{Exp} and σ_{Δ}^{Exp} is the error in Δ^{Exp}. For a perfect fit (with no systematic errors) the MSE will be 1. In experiments, the aim is therefore to get as close to a MSE of 1 as possible.

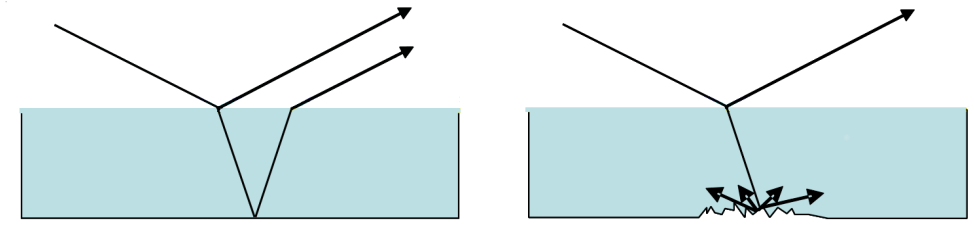

FIGURE 3.7: This figure highlights the difference between having a smooth back surface, versus a rough one. For the smooth surface on the left, back reflections may be in parallel with those beams reflected from the front surface. However if the back surface is rough the light is scattered and does not interfere with reflections from the front surface.

Since ellipsometry measures a change in polarization, anything that contributes to depolarization, such as surface roughness, will add error to the results. To minimize such errors glass samples of 8-10 mm thickness were prepared with polished surfaces. On the top surface, where the light from the ellipsometer reflects, the glass was finely polished to ensure that the average surface roughness, R_a, was as low as possible. However on the bottom surface, the sample was roughed up with a coarse grade paper. This was done to prevent any reflections from the back surface coming back in parallel to those from the top surface. Such reflections are not ideal when measuring the optical properties for bulk samples as accounting for them adds complexity to the measurement – the simplest scenario is to remove them altogether. The easiest way to do this is by roughing up the

back surface to scatter any light that strikes it. Figure 3.7 demonstrates how this is achieved. Back surface reflections can also be eliminated by using an index matching, absorbent material at the back of the sample.

For both surfaces, once the polishing was complete the surface was analysed with a surface profiler. This enabled us to quantify the roughness of the surface, via the average roughness parameter R_a. The results of this analysis, for one of the samples is shown in Figure 3.8. We see a significant decrease in the roughness of the top surface from $R_a = 63.95$ nm to $R_a = 15.98$ nm. The results for the other samples used were similar, with R_a averaging from 15 nm to 20 nm across the samples. Analysis of the effect of surface roughness on the apparent value of the refractive index in Reference [161] shows that, for glass samples, a negligible effect is observed for roughness values up to 30 nm. As these samples were comfortably under this threshold we may be confident that surface roughness does not contribute any significant error to the results.

We also see in Figure 3.8 that, for the bottom surface, the roughness increased to just over 1 µm – a value that is comparable to the wavelength of the light used in the measurement and thus likely to scatter all light off the back surface.

In addition to carefully polishing the surface each spectral was also averaged (100 scans per point) along with incidence angle (12 scans per angle for 5 angles). Given the bulk nature of these samples (i.e. not thin films), the surface polishing and the high averaging, the error in the measurements is estimated to be no more than 1-2% [162–164].

The results of the refractive index measurement, in the visible and near-IR range, are shown in Figure 3.9. From these measurements we are able to fit a Sellmeier equation of the form shown in Equation (3.13) to the data.

$$n^2(\lambda) = 1 + \sum_{i=1}^{3} \frac{B_i \lambda^2}{\lambda^2 - C_i}. \tag{3.13}$$

The values of the fitted Sellmeier coefficients are given in Table 3.4. The values at 1.55 µm are listed in Table 3.3.

Not surprisingly, the Na-free germanate glass GPL5 has a significantly higher index that the Na-containing glasses GPNL2 and GPNL5. This result is consistent with the higher density for Na-free germanate glasses as described in Section 3.5.2. Despite different

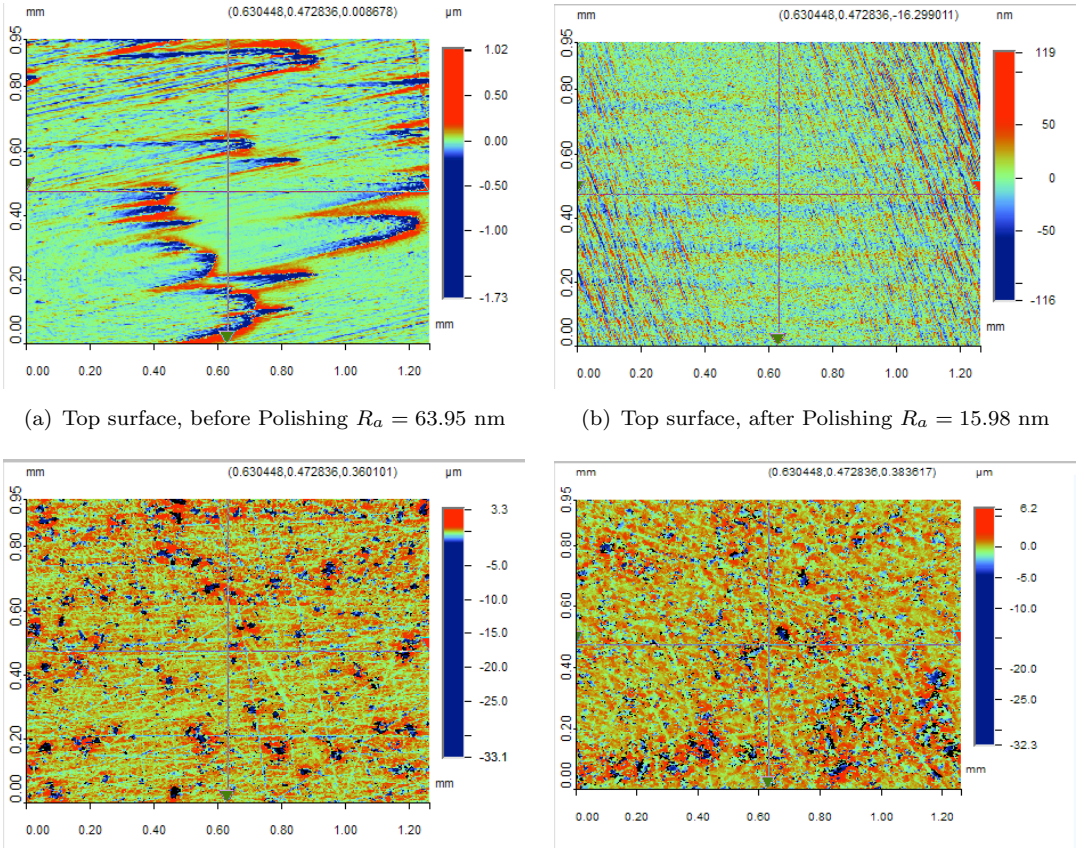

(a) Top surface, before Polishing $R_a = 63.95$ nm

(b) Top surface, after Polishing $R_a = 15.98$ nm

(c) Bottom surface, before Polishing $R_a = 413$ nm

(d) Bottom surface, after Polishing $R_a = 1089$ nm

FIGURE 3.8: Analysis of the surface roughness of one of the germanate samples. (a) and (b) show the top surface before and after polishing, respectively. Similarly (c) and (d) show the bottom surface, before and after polishing. The roughness of the any particular point in the plots is given by its colour bar on the right of each plot.

TABLE 3.4: Sellmeier coefficients for germanate and tellurite glasses

Glass	B_1	B_2	B_3	C_1	C_2	C_3
GPL	1.458	1.203	23.06	0.03138	0.03064	2287.0
GPNL5	1.065	1.399	1.849	0.02663	0.02663	2555.6
GPNL2	1.538	0.934	1.120	0.01417	0.04078	782.1
TZN	1.378	1.511	3.435	0.04756	0.00744	411.3

content of the heavy metal oxide PbO and different density, GPNL2 and GPNL5 exhibit almost identical refractive indices. In GPNL2 and GPNL5, 2 mol% and 5 mol% PbO are replaced with Tm_2O_3 and La_2O_3, respectively. Both Tm_2O_3 and La_2O_3 are lanthanide oxides (Ln_2O_3). Hence, the almost identical refractive indices of GPNL2 and GPNL5 indicate that PbO and Ln_2O_3 have comparable impact on the refractive index.

The lead-germanate glasses have somewhat lower indices than the TZN and TZNL tellurite glasses, which is attributed to the lower polarisability of Ge^{4+} compared with

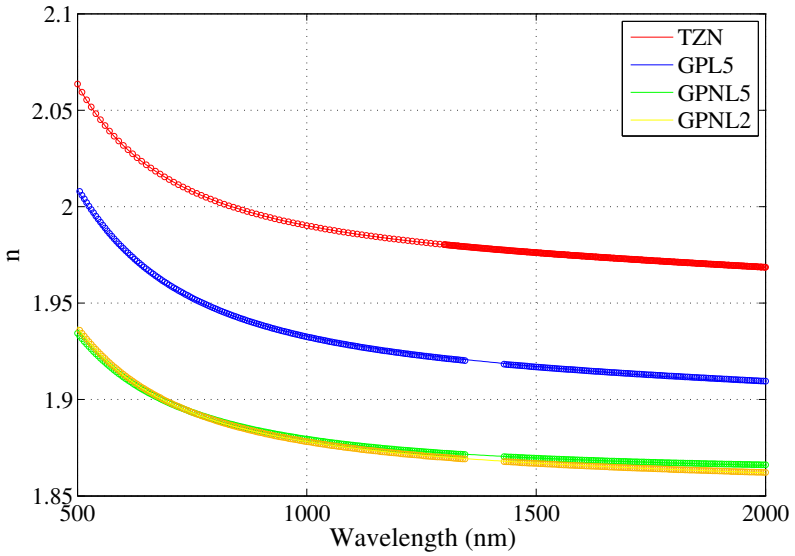

FIGURE 3.9: Refractive indices of of GPL5, GPNL2 and GPNL5 germanate glasses and TZNL tellurite glass. Circles are measured points; the line shows the Sellmeier fit.

Te^{4+} [165].

3.5.4 Nonlinearity

The nonlinear refractive index for the GPNL5 glass was measured using a suspended core fibre that had previously been fabricated by colleagues within the author's institution. This fibre was fabricated from a relatively large billet (180 g) melted for the first time in a controlled atmosphere glass melting facility. Due to unoptimized conditions for this first large glass melt, particles from the furnace liner were unintentionally introduced into the melt. As a result, the fibre had sections of varying loss. To account for this in the measurements, fibre segments with relatively short lengths (< 1 m) were used and both the nonlinearity and loss was measured for each length of fibre. The loss of these fibre segments varied from 4.5 to 8.8 dB/m. Given that this is a first generation fibre of this material and structure we are confident that, in future trials, the loss can be made consistent and lowered to a value much closer to the measured bare fibre loss for this material, i.e. < 1.5 dB/m at 1550 nm.

The nonlinear refractive index for the GPNL5 suspended core fibre was determined by first calculating the value of the nonlinear coefficient (using the method described in Reference [166]), which is based on measuring the phase shift, ϕ, induced by the Self Phase Modulation (SPM) phenomenon [34]. It involves pumping a fibre with a

dual frequency signal and observing the generation of side bands via four wave mixing (FWM) [34]. The details of this experiment are covered in Section 7.3 of the fibre characterisation chapter. The results are summarised here, to complete the analysis of the germanate glass.

From the experimental data, the nonlinear coefficient was measured to be $\gamma = 1177 \pm 128$ $W^{-1}km^{-1}$ for this fibre. To calculate the effective area A_{eff} a SEM image of the cross section of the fibre end used in the experiment was first scanned and inserted into a finite element model. This allowed calculation of the electric and magnetic fields of the fundamental mode propagating through the fibre and thus the effective area A_{eff} – calculated, in this case, to be 1.951 μm^2 (see Section 4.3 for details on this modelling procedure). By then using the equation $\gamma = 2\pi n_2/\lambda A_{eff}$ the value for the nonlinear refractive index was found to be $n_2 = 56 \pm 6 \times 10^{-20}$ m^2W^{-1}.

The nonlinear index of the TZNL glass was measured to be $n_2 = 55 \pm 2 \times 10^{-20}$ m^2W^{-1} [147] for a polished glass plate using the Z-scan technique as described in Reference [167]. Within the measurement error, we see that the nonlinear indices of TZNL and GPNL5 glass are identical.

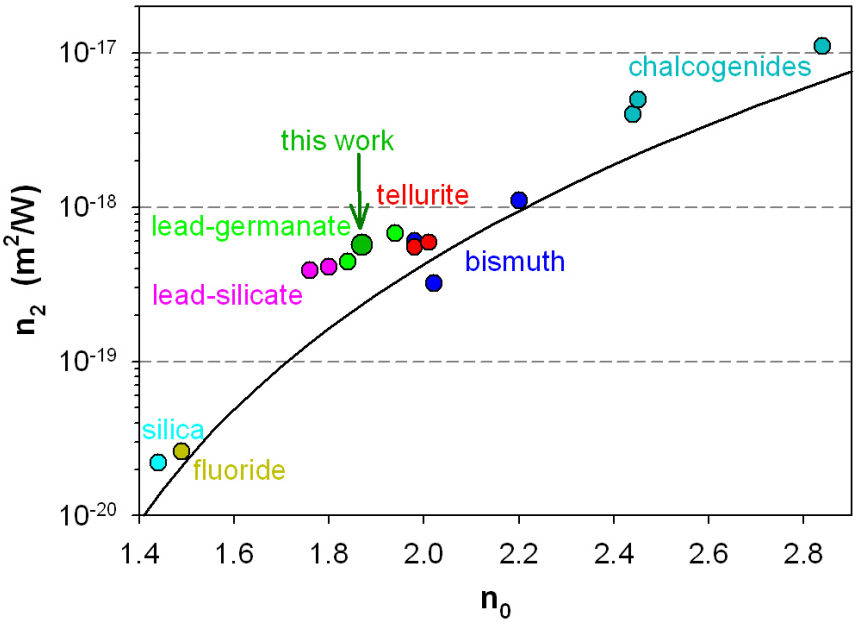

FIGURE 3.10: Nonlinear index of GPNL5 compared with other soft glasses. The solid line represents the Miller's rule, as per Reference [5].

Figure 3.10 compares the measured value for the optical nonlinearity of the germanate glasses presented here with values found in the literature for other soft glasses, including other lead-germanates. The curve represented by the solid line in this figure corresponds to the expected nonlinear refractive index, for a given linear refractive index in accordance with the empirical Miller rule [116]. For the lead germanates extracted from the literature, the n_2 values have been obtained by converting the third order optical susceptibility $\chi^{(3)}$ values measured by Hall *et. al.* [148] using the equation

$$n_2 \ [\mathrm{m}^2/\mathrm{W}] = K\frac{160\pi}{cn_0^2}\chi^{(3)} \ [\mathrm{esu}], \tag{3.14}$$

where n_0 is the linear index, c is the speed of light and K is a constant. Whilst there is some uncertainty in the literature as to the appropriate value of this constant, $K = 6$ was chosen as this value converts, for lead-silicate glass, the $\chi^{(3)}$ [esu] value measured by Hall to an n_2 [m^2/W] value that is similar to the n_2 value which was measured by Friberg *et. al.* [145] and independently confirmed by Petropoulos *et. al.* [168].

It is worth noting that the relationship between the linear and nonlinear index for the lead-germanate glasses presented here agrees well with those measured by Hall *et. al.* [148] for 60·GeO_2 — 40·PbO and 75·GeO_2 — 25·PbO glasses. To the best of our knowledge, these are the only other measurements of the optical nonlinearity of lead-germanate glasses to date.

3.5.5 Loss

The experiments to determine the loss of the glasses were done in two parts: in one the absorption of the bulk samples in the mid-IR was measured; in the other the loss was evaluated for unstructured fibres in the visible and near-IR regimes. The measurements on the bulk samples were made to determine the effect of the dry absorption glass fabrication technique on the OH induced loss peak generally found in these types of glasses – the aim was to evaluate if the fabrication in a dry atmosphere had indeed reduced this peak. However as the loss in the mid-IR range is not particularly relevant to telecommunications applications these results are not included in this thesis (they may be found in Reference [32]).

The experiments on the unstructured fibres serve as a baseline test for the loss that can be expected in microstructured fibres made from this glass. They also let us determine if the fibre fabrication procedure introduces any extra losses into the material. These results are presented below in Section 3.5.5.1.

3.5.5.1 Visible and near-IR loss of unstructured fibres

To determine the material loss that can be achieved in extruded germanate glass fibres, broadband fibre loss spectra were measured for the GPL5 and GPNL5 unstructured fibres using the standard cutback technique. The light source was a tungsten filament bulb, and the fibre output was coupled via a bare fibre adaptor to a commercial optical spectrum analyser ranging from 400 to 1700 nm. Several cleaves were performed at each cutback length to ensure that cleave variability could be averaged out of the results. The measurement error is 10%.

Figure 3.11(a) shows the loss spectra of GPL5, GPNL5 and TZNL unstructured fibres. All three fibres have a similar minimum loss of 0.5-1 dB/m at approximately 1.3 µm. Preliminary absolute absorption measurements of the bulk GPNL5 glass indicated that reduction of the minimum loss of germanate glass fibres to approximately 0.2 dB/m is possible by improving the extrusion and fibre drawing conditions.

The band at 1.45 µm is the overtone of the fundamental absorption of free OH groups at approximately 3.0 µm [156]. The higher intensity of the overtone of free OH groups in germanate glasses compared with tellurite glass is consistent with the larger intensity of the fundamental absorption of free OH groups in germanate glasses.

The shift of the free OH overtone from 1.44 µm in the germanate glasses to 1.47 µm in the tellurite glass is consistent with the wavelength shift of the fundamental vibration of strongly bonded OH groups (4.3 µm for germanate and 4.4 µm for tellurite). Due to the overlap of the fundamental vibrations of free and weakly bonded OH groups, any wavelength shift cannot be resolved for these two vibration bands. We attribute the red shift of the OH bands, i.e. the shift to lower frequency, from germanate to tellurite glasses to decreasing bond strength from Ge-O to Te-O similarly to the lower frequency shift from the Ge-O to the Te-O stretching vibration observed in the Raman spectra (Section 3.5.6 and Figure 3.12).

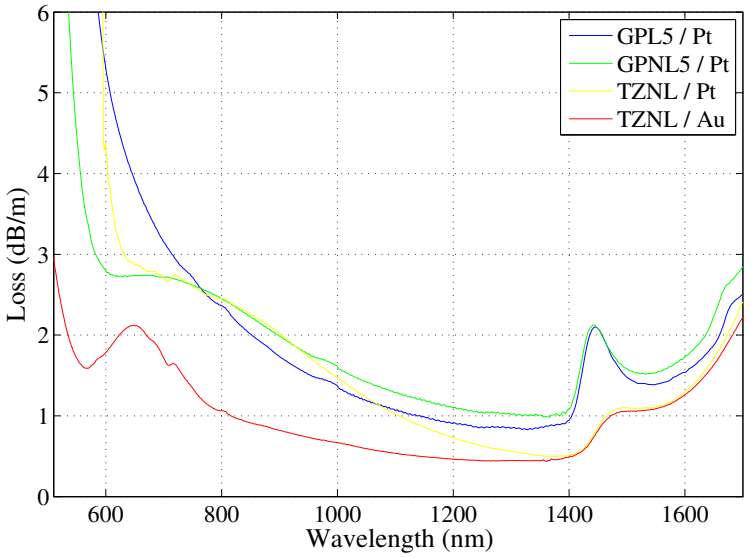

FIGURE 3.11: Loss spectra of unstructured fibres.

For tellurite glass, melting in a platinum crucible (compared with melting in a gold crucible) was found to cause additional absorption at $\leq$ 600 nm due to the presence of platinum impurities in the glass as a result of crucible corrosion by the glass melt [156] (Figure 3.11(a)). The short wavelength edge of the germanate fibres is at a similar position to that of the tellurite glass fibre made from glass melted in a platinum crucible. This result indicates that in germanate glass fibres the short wavelength loss is limited by the absorption of platinum species and not by the intrinsic absorption edge of the glass.

3.5.6 Raman characteristics

Stimulated Raman scattering (SRS) is a nonlinear optical process with applications in a range of fields such as spectroscopy [169–171] fibre lasers [172, 173] and fibre amplifiers [174, 175]. Measuring the Raman gain thus forms an important part of the characterisation procedure for any nonlinear glass. Additionally, knowledge of Raman parameters, such as the Raman fraction and Raman gain bandwidth, is important when modelling nonlinear processes within fibres (see Section 5.2 for details).

SRS is when the interaction of a strong pump wave with the vibrational modes of medium scatters photons into a frequency down shifted Stokes wave. The amount of energy transferred to the Stokes wave (sometimes simply referred to as the Raman

wave) depends on a parameter known as the Raman gain coefficient [176]. The Raman characteristics for a medium are quantified by measuring the spectral variation of this Raman gain.

The Raman spectra were measured for the two unstructured fibres made from GPL5 and GPNL5 glasses and for a TZNL unstructured fibre also made using the extrusion technique as described in Reference [9]. An argon ion continuous wave laser beam at 514.5 nm was launched into a fibre piece of approximately 30 cm in length. A low power of 56 mW was used to avoid photo-induced structural changes. From the same fibre end, the output light was imaged onto a spectrometer (Horiba Jobin Yvon – iHR 320). The laser line was blocked using a bandpass filter. This filter caused the Raman spectra to be cut-off at 250 cm^{-1}. The wavelength of the spectrometer was calibrated using the argon ion laser line at 514.5 nm. Note that the same Raman spectrum was obtained using a higher energy laser beam at 488 nm, indicating that photo-induced structural changes did not occur under the experimental conditions.

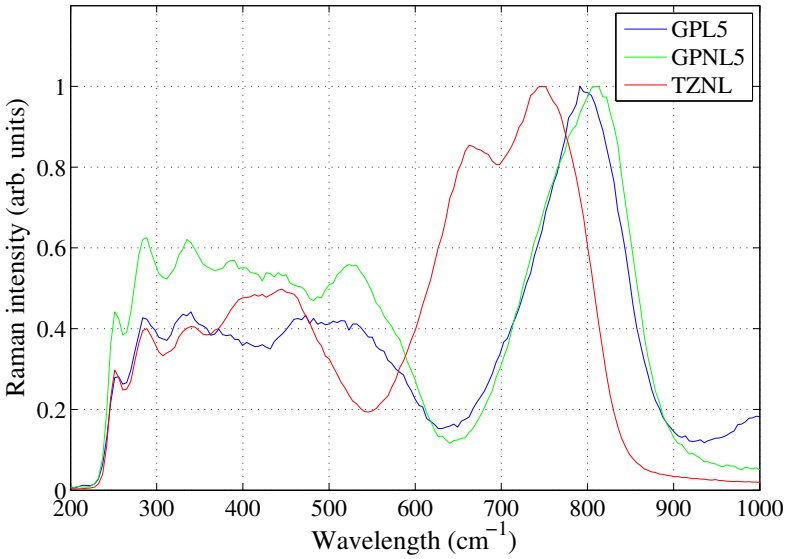

FIGURE 3.12: Raman spectra of germanate glasses (GPL5, GPNL5) and tellurite glass (TZNL).

Figure 3.12 shows the Raman spectra for the two germanate fibres and the tellurite fibre. For both germanate glasses, the highest-frequency Raman band is situated at approximately 800 cm^{-1}. This Raman band is composed of two peaks attributed to Ge-O stretching vibrations [150]. The highest-frequency Raman band of the tellurite fibre is at 750 cm^{-1} and is composed of two peaks attributed to Te-O stretching vibrations

[167] . The position of the highest-frequency Raman bands agrees with other tellurite and lead-germanate glasses [150, 167, 177–179].

The frequency of diatomic molecule stretching vibrations increases with increasing bond strength and decreasing weight of the atoms [159]. Therefore, the shift of the network former stretching vibration to higher frequency from Te-O to Ge-O is attributed to both the higher bond strength of Ge-O (due to higher field strength of Ge^{4+} compared with Te^{4+} [165]) and lower mass of Ge compared with Te.

3.5.7 Summary

We have developed and characterized a range of lead-germanate glasses that, when compared with other infrared transmitting high index glasses (such as tellurites) stand out for having the desirable properties of low phonon energy and high refractive index (both linear and nonlinear) without compromising on fibre stability, due to the fact that they retain higher glass transition temperatures.

In the lead germanate glasses studied here, partial replacement of PbO by La_2O_3 up to 5 mol% was found to increase glass transition temperature without decreasing glass stability or refractive index.

We have also fabricated a suspended core microstructured fibre from one of these glasses and used it to measure a nonlinear refractive index that is comparable to that of tellurite and bismuth glasses. This is a significant result as it demonstrates both the fabrication of a small core microstructured fibre and showcases the high nonlinearity of the material ($n_2 = 56 \pm 6 \times 10^{-20}$ m^2W^{-1}). The extrusion based fabrication technique is also readily expandable and thus this fibre represents a first step in the potential fabrication of more complex geometries, such as those required for dispersion engineered fibres. This is explored in Section 4.7, where the refractive index data measured for this glass is used to design a germanate based fibre for nonlinear telecommunications applications.

3.6 Conclusion

This chapter covers many of the fundamentals of glassy materials. This understanding is essential to being able to describe and understand the kinds of materials that qualify as soft glasses – which are the primary materials used in this research, due to their low softening points and high nonlinear refractive indices. As such, some of the commonly used families of soft glasses are described, along with a discussion of what each offers when considering glasses for nonlinear telecommunications devices.

This chapter also details the development and characterisation of a novel range of lead germanate glasses. The properties of these glasses have been investigated in detail, particularly the refractive index and the nonlinearity as knowledge of these parameters is essential to fibre design. These glasses have also been shown to be robust and highly nonlinear, making them promising candidates for use in optical fibre devices.

Now that the materials used in the fibre design process have been discussed, the following chapter moves on to fibre design. This next chapter (Chapter 4) covers how the optical properties of the glasses, such as refractive index and nonlinearity, are used to construct fibre designs for a particular application, and the mathematical tools involved in this process.

Chapter 4

Fibre design

4.1 Introduction

This chapter describes the process of designing dispersion engineered optical fibres for telecommunications applications. It describes how fibre parameters such as dispersion and nonlinearity are affected by the geometry of the waveguide and how the geometry can therefore be used to engineer these parameters. The chapter also outlines some of the types of geometries typically used for this engineering before then detailing the specifics of the approach taken in this research to engineer fibres optimised for the applications described in Chapter 2 – namely multicasting and phase sensitive amplification.

Parts of the work presented in this chapter were performed in parallel with the work shown in the modelling chapter (Chapter 5) and some of these modelling results were used to inform and improve upon the design process. For example, the insight gained from the modelling of a fibre designed for multicasting was used to refine the methodology used in designing the fibre for phase sensitive application.

This chapter is organised as follows: Section 4.2 discusses the design considerations that must be taken when designing fibres for four wave mixing based applications, including how the key fibre properties, such as nonlinearity and dispersion, can be engineered and optimised via the fibre geometry. Section 4.3 provides an overview of the finite element model (FEM) technique which was used to calculate the dispersion and nonlinearity for a fibre geometry and thus evaluate the potential of a specific fibre design for use in a given application. Section 4.4 outlines some types of geometries that are used to engineer

these properties for soft glass fibres. Section 4.5 describes in detail the approach used in this research – combining a microstructured fibre design, termed a 'hexagonal wagon wheel' (HWW) fibre, with a genetic algorithm to optimise the dispersion profile and nonlinearity for the required application. The final fibre designs for multicasting and phase sensitive amplification were evaluated via FEM modelling and these results are discussed in Sections 4.5.3 and 4.5.4, respectively.

A simplified version of the hexagonal wagon wheel design, using a novel lead germanate glass is also presented in Section 4.7. This fibre design does not have a dispersion profile or nonlinearity that is as favourable as the hexagonal wagon wheel fibre designs, but it is a much simpler design and was explored due to its relative ease of fabrication.

4.2 Design considerations

When designing optical fibres for broad band nonlinear telecommunications applications based on four wave mixing, two parameters are paramount in the design considerations: the fibre nonlinearity and the dispersion profile. The primary aim is to maximise the gain and spread it out over a broad spectral range. This is achieved by having a high nonlinearity and a dispersion profile tailored to suit the application.

The nonlinearity is measured by the effective nonlinear coefficient γ defined as in Equation 2.35, in terms of the nonlinear refractive index n_2 ad the effective area of the fibre mode A_{eff}. From this definition of γ, we see that there are two avenues to obtaining a high fibre nonlinearity: choosing a material with a high n_2 and minimising A_{eff} by designing for a tightly confined mode area. This has the effect of simultaneously increasing the numerator and decreasing the denominator in Equation 2.35. A soft glass nanowire, for instance, is a perfect example of this – the high linear index of the core contrasts highly with the air 'cladding' and tightly confines the mode, while the high intrinsic n_2 further enhances the nonlinearity. However this geometry has limited scope for dispersion engineering. Thus, when designing MOFs for nonlinearity based applications, we aim to minimise the mode area with a high effective nonlinear index whilst still maintaining enough flexibility in the geometry to be able to engineer the dispersion.

The dispersion of the fibre, defined in Equation 2.41, is the other main parameter that affects fibre performance. This fibre dispersion can be considered to be approximately the sum of the dispersion of the material and that of the waveguide, written as

$$D \approx D_{mat} + D_{wav}, \tag{4.1}$$

where D_{mat} and D_{wav} represent the dispersion due to material and waveguide, respectively [118]. In fibres where there is significant material refractive index variation (with respect to wavelength) across regions, such as graded index fibres, there is also another contribution to the dispersion known as the profile dispersion [180]. However, the profile dispersion in most fibre structures at visible and near-IR wavelengths is generally so small that it is negligible [39].

For FWM based nonlinear telecommunications applications, such as those introduced in Section 2.4, the gain depends on the phase mismatch between the interacting waves. For this gain profile to be both high and broad enough to cover the band of interest, the phase mismatch needs to be minimised across the band. As the phase mismatch is determined by the propagation constants of the interacting waves (as in Equation 2.55) this requires tailoring these propagation constants as required across the frequency band, i.e. tailoring the dispersion profile of the fibre. The material component of the dispersion is obviously fixed by the choice of glass, however the waveguide dispersion can be tailored via the fibre geometry. This follows from Equations 2.30 to 2.31, as the eigenvalue equation that determines the value of the mode's propagation constant depends on the fibre geometry and refractive index profile. Therefore, through the design of the fibre geometry and refractive index distribution the waveguide dispersion may be tailored to offset the material dispersion such that the net dispersion profile results in the phase mismatch being minimised, ideally to zero.

Soft glasses present an ideal medium for this sort of dispersion engineering as their low softening temperature enables them to be fabricated into a complex geometries via extrusion. This process involves heating the glass and then forcing it though a steel structure known as a die. This will imprint the inverse of the die structure through the glass as it passes through so, by carefully machining the steel die, a complex structure can be introduced into the glass. The major caveat is that the die must remain rigid at the

softening temperature of the glass, thus extrusion through a steel die cannot be used with glasses like silica that have much higher softening points. Although glasses like silica may be extruded using dies made of harder materials, such as ceramics, introducing complex microstructure is significantly more difficult as these materials are generally not able to be machined to the same precision as steel dies. This extrusion process is described in detail in Chapter 6.

In addition to these primary considerations (nonlinearity and dispersion), another major factor that must be taken into account is the optical loss. This is an important fibre parameter as it ultimately determines the efficiency of any fibre device. Optical losses in optical fibres are usually represented by the fibre attenuation coefficient α, defined as in Equation 4.2 in units of decibels (dB) per unit length.

$$\alpha \ \text{[dB/m]} = \frac{10}{l} \log\left(\frac{P_{in}}{P_{out}}\right), \tag{4.2}$$

where l is the fibre length and P_{in} and P_{out} are the input and output powers, respectively. This attenuation coefficient includes the effect of the bulk material loss, the confinement loss and any scattering losses that may occur due to surface roughness or from other scattering centres within the material. The bulk loss represents the losses incurred due to absorption by the substrate material and is independent of the fibre design while scattering losses typically occur as a result of imperfect fabrication conditions (and can thus be eliminated by refinement of the fabrication process). The confinement loss, on the other hand, is a consequence of the fibre design – it accounts for the power lost from the fibre via the exponential decay term that occurs in the electric field from Equation 2.31 (due to the imaginary component of β). This confinement loss is defined, in units of dB, as [181]

$$\text{CL} \ \text{[dB]} = \frac{20}{\ln(10)} \text{Im}\{\beta\}. \tag{4.3}$$

In any fibre design loss is obviously undesirable and thus attenuation must be minimised. This can be done by careful selection of materials, refinement of the material fabrication process, refinement of the fibre fabrication process and minimising the confinement loss through the fibre design.

There are several other factors that also need to be considered when designing fibres. They may be summarised as follows:

- Bend loss and bend radius: the bend loss is due to the extra attenuation caused by an increase in the confinement loss as the fibre bends and will thus affect the performance of a fibre device. The band radius is the maximum radius the fibre can bend before it breaks – a low bend radius means a fibre may not be coiled tightly.
- Tensile strength and structural rigidity: this ultimately determines the difficulty of handling the fibre and the mechanical stability of the substrate glass plays an important part.
- Modality: the number of modes present in the fibre will affect its performance. For most applications it is desirable to only have the fundamental mode present and thus single mode fibres are preferred. The high index contrast of soft glass fibres generally means they are multimode but due to the higher loss of these modes the fibre can be made effectively single mode by choosing a longer fibre length.

Ultimately however, it is the nonlinearity and dispersion that determine whether the fibre is able to perform the desired function. Consequently the design procedure focuses on these two key aspects, whilst still paying attention to all the other design considerations. A certain level of intuition is required at the start of this process to determine the materials and general design structure that broadly encompasses all of the necessary considerations required to achieve the end goals. This is then refined through a calculated process (described in Section 4.5) to produce the end result.

It is useful then to first have an understanding of how certain geometric structures match with fibre properties. Section 4.4 that follows, outlines some of the general types of fibre geometries that have been used for engineering optical fibre properties, and also contains a discussion on how the choice of structure contributes to the guidance properties of the fibre (especially the dispersion and nonlinearity).

4.3 Finite element method

The finite element method is a versatile numerical technique for solving differential equations that can be applied to the wave equations for an optical waveguide. The flexibility of this method is particularly useful for the case of complex MOFs considered here, as it can be applied to waveguide geometries of arbitrary shape and refractive index profile. As such the finite element method has established itself as one of the most common and powerful means of determining the propagation characteristics of optical waveguides [182–185].

The finite element method works by first taking a geometry and splitting it into a number of distinct, homogeneous subdomains to produce a mesh of finite elements. In the two dimensional work considered here the finite elements that form this mesh are either triangles or quadrilaterals, as shown in Figure 4.1(b) for an optical fibre cross section. The governing wave equations (in this case the Hemholtz wave equation [35]) are then solved for each for the discrete elements and combined via the appropriate boundary conditions to calculate the global solution(s) [185].

The accuracy of the FEM solution is heavily dependent on the density of the mesh – the greater the density the more accurate the final solution will be. However an increase in elements is accompanied by a corresponding increase in the number of individual calculations that must be performed. This obviously increases the required computational load, and hence time. In practice, the aim is to have a mesh density that allows the model to converge to an accurate solution in a reasonable time frame. This requires having sufficient density to provide an accurate solution but not so high that it requires an unreasonable amount of computing time to solve over. In the simulations of HWW fibres performed in this work, the sweet spot for mesh density was found to be around 45,000 elements across the geometry.

This meshing process is refined by having a mesh of that is relatively finer around the regions where the accuracy of the solution is particularly important, and coarser outside these areas. Areas where accuracy is especially important include: areas that contain fine structural features (such as around small holes); areas where the field intensity is relatively higher; and regions where sharp changes in the field distribution are expected

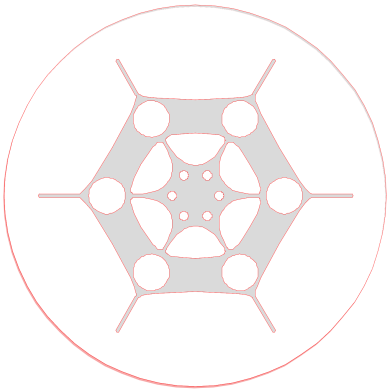

(a) The model geometry. Glass regions are are shown in grey while the regions corresponding to air (i.e. $n = 1$) are in white. Note that all of the cladding glass is not included in the model as it increases computation time but has negligible effect on the final solution since the light is predominantly concentrated in the central glass/air region.

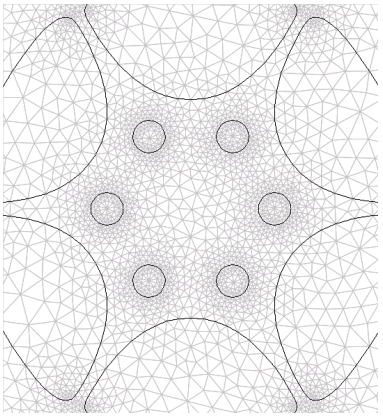

(b) Finite element mesh around the core region. Note how a finer mesh (i.e. with smaller and more finite elements) is used around areas with smaller features to get better accuracy because the light intensity is high in these regions.

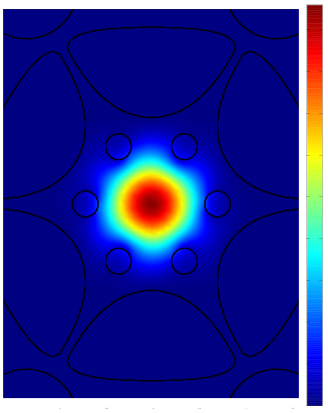

(c) The computed field intensity for the fundamental mode. Areas where the field intensity is strong are represented in redder hues, while regions where the field is weak are in blue – as indicated by the bar to the right.

FIGURE 4.1: The stages involved in modelling a given fibre geometry. The fibre geometry is first defined as in (a); a mesh of finite elements is then defined within this geometry as in (b); the wave equation is then solved over these elements to calculate the fibre modes, including the fundamental mode solution shown in (c).

(such as the fibre core). A non uniform mesh of this type balances solution accuracy with computational load better than one of uniform density.

In addition to using a non uniform mesh, the computational load can also be decreased by not modelling regions of the fibre such as the outer cladding where the field intensity would have decayed to essentially zero. For the HWW fibres modelled in this work this was done by using a geometry such as that shown in Figure 4.1(a), where sections were removed from the outer cladding so that they would not be included in the model.

Once the geometry and mesh have been set up, the next step is defining the boundary conditions. This includes the boundary conditions that tie the individual elements together and those that constitute the outer edge of the model (and thus limit the number of elements to a finite amount). For the internal regions of the structure, the boundary conditions are relatively less complex as the model considers just a dielectric waveguide and therefore only needs to ensure the continuity of the fields across individual elements [35]). The outer edge of the model is handled with one of two ways: it is defined to be a perfectly reflecting boundary or as a perfectly absorbing layer.

Having the outer boundary that perfectly reflects is the default case for the software package used in this research (details are given at the end of this section). However these reflections are unphysical (as they are introduced entirely by the numerical model) and would reduce the solution accuracy if they were significant in magnitude. One must therefore be careful to ensure that the reflecting boundary is far enough away such that the mode field intensity at this point is sufficiently low that any reflections are negligible. Another consequence of such a boundary is that the propagation constant will always be real, since this boundary does not account for any power loss due to confinement loss (confinement loss is defined in Equation 4.3).

The alternative to this is to instead use a perfectly absorbing layer as the outer boundary. This region, usually referred to as a perfectly matched layer (PML), is included into the model as a thin domain that is wrapped around the geometry and is set up to absorb all of the electromagnetic field that enters it. This effectively simulates the effect of surrounding the geometry with an infinite medium (which it would normally take for the field to otherwise decay to zero). The use of a PML is in fact the standard means of evaluating the confinement loss of optical fibres [186, 187].

In this work the RF module of the COMSOL Multiphysics® software package was used to generate and solve the FEM. When solving the model the program was configured to look for a fixed number of solutions, per wavelength, around a given guess value for the effective index. As only the fundamental mode is of interest for this work, the model was configured to only look for the two degenerate fundamental solutions with the initial guess value for the effective index set to be the refractive index of the core glass. The COMSOL Multiphysics® package was integrated with MATLAB® to calculate the dispersion, nonlinearity and other propagation characteristics, such as confinement loss.

4.4 Dispersion engineered fibre types

The various fibre geometries that have been used in the fabrication of dispersion engineered fibres may be categorised into two main types: Microstructured Optical fibres (MOFs) and all solid fibres. MOFs are generally made out of a single material and their structure is determined by an array of microstructured holes in the transverse fibre profile. All solid fibres on the other hand do not have any holes or voids within but are structured out of a composite set of materials. In the sections below each category is described, along with an outline of the respective advantages and disadvantages of each.

4.4.1 Microstructured optical fibres

Microstructured optical fibres are a class of fibres where the guidance of light is manipulated via structural modifications to the fibre cross section. Microstructured optical fibres (sometimes referred to as a holey fibres or Photonic Crystal fibres (PCFs)) were first envisioned by Phillip Russell in 1991 [16] and a few years later they were successfully fabricated for the first time by his team [188]. Since then, the unique properties of MOFs have, in addition to dispersion engineering, been used for other applications such as endlessly single mode fibres [189], large mode area fibres [190] and hollow core/photonic bandgap fibres [191].

The flexibility of modern fabrication processes has resulted in a plethora of varied geometries for MOFs – some of which are simple (consisting of just a few, symmetrically arranged holes) and others that are complex (with many holes arranged in complex formations). While the complex MOFs offer the most flexibility in design and thus

ability to engineer the dispersion and nonlinearity, the simple suspended core MOF designs offer advantages such as relative ease of fabrication with new glasses and are thus also considered here. The properties of both categories are described in the following sections.

4.4.1.1 Simple MOFs – the suspended core fibre

The suspended core fibre consists of a solid core surrounded by large air holes, which effectively form an air cladding. These holes are then surrounded by an outer glass cladding. Light is guided in the suspended core which behaves in a manner that approximates that of a glass nanowire suspended in air.

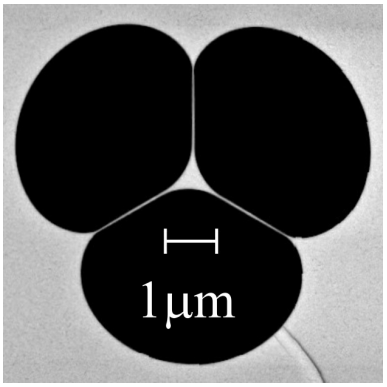

FIGURE 4.2: A suspended core fibre fabricated in a fluoride glass. This fibre was fabricated as part of research into fibre based optical sensing [1].

Figure 4.2 shows a suspended core fibre that consists of a triangular core of glass supported by three struts. This type of geometry is sometimes referred to as a 'wagon wheel' structure and represents the simplest form of microstructured fibre.

The high index contrast between the core glass and the air results in a high numerical aperture. When combined with a small core diameter this results in a tightly confined mode area and extremely high nonlinearity. Indeed suspended core bismuth optical fibres have been used to demonstrate γ values of 5400 $W^{-1}km^{-1}$ [192], and tapered chalcogenide fibres have pushed this even further with a nonlinear coefficient of $\gamma = 54{,}100$ $W^{-1}km^{-1}$ [126].

The ability to guide light in subwavelength scale core diameters also enables the fibre to have a very high anomalous waveguide dispersion. This can be used to compensate for the typically high normal material dispersion at short wavelengths and move the zero

dispersion wavelength to regions much shorter than the intrinsic material ZDW. This is demonstrated in Figure 4.3, where the dispersion and nonlinearity has been calculated by modelling a suspended core geometry over a range of core diameters and wavelengths, using the finite element method. In the 3D graphs shown in the left hand side of this figure, the ZDW is represented by intersection of the zero dispersion plane (the dark region) and the dispersion curves. We see that as the diameter d gets smaller the ZDW moves to shorter wavelengths. For small core diameters (less than around 1 µm) the fibre actually has two ZDWs in the 500 nm to 2000 nm range that was modelled. The graphs on the right hand side of Figure 4.3 also show that the nonlinearity increases significantly for small core fibres due to the increased confinement of the mode.

While the core diameter of the suspended core geometry can be used to alter the dispersion and nonlinearity of a fibre, this parameter is the only one which may be used to engineer the fibre properties (for a given glass). This limits the extent of dispersion tailoring that can be done. For example, it is extremely difficult to lower both the dispersion and the dispersion slope with the suspended core geometry.

Consequently the applicability of suspended core fibres is limited for broadband applications. However the high nonlinearity and the ability to move the zero dispersion make them useful for narrow bandwidth applications.

4.4.1.2 Complex MOFs

Broader control of the fibre guidance properties can be achieved by extending the microstructured approach to structures more complex than the suspended core geometry described earlier. A specifically designed array of holes around the core region creates an effective cladding of air and glass where the refractive index of this region is determined by the size and arrangement of the holes.

One such arrangement used to engineer the effective index is to have a hexagonal array of holes around a central glass core (which can be thought of as an omitted centre hole). An example of this type of structure is shown in Figure 4.4. The dispersion curve of these fibres is determined by two parameters: the diameter of the holes d and the pitch Λ (the distance between holes). By varying and modelling the effect of these two parameters one may design a structure with dispersion characteristics that suit the problem at hand.

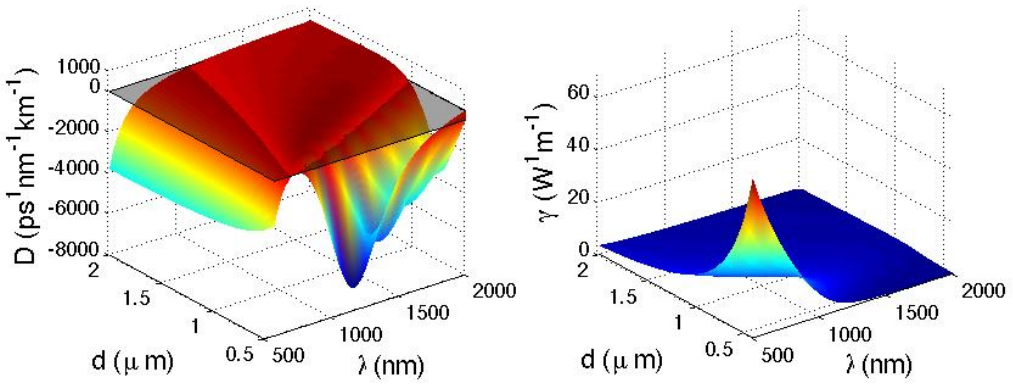

(a) Lead silicate (SF57)

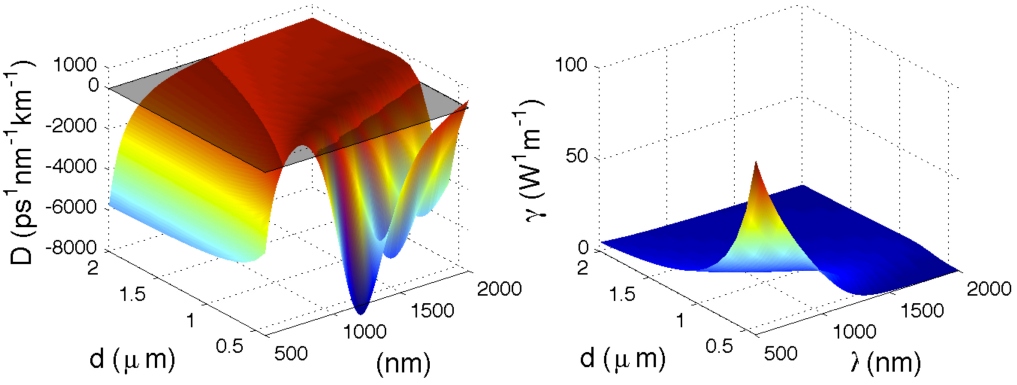

(b) Bismuth (AB061)

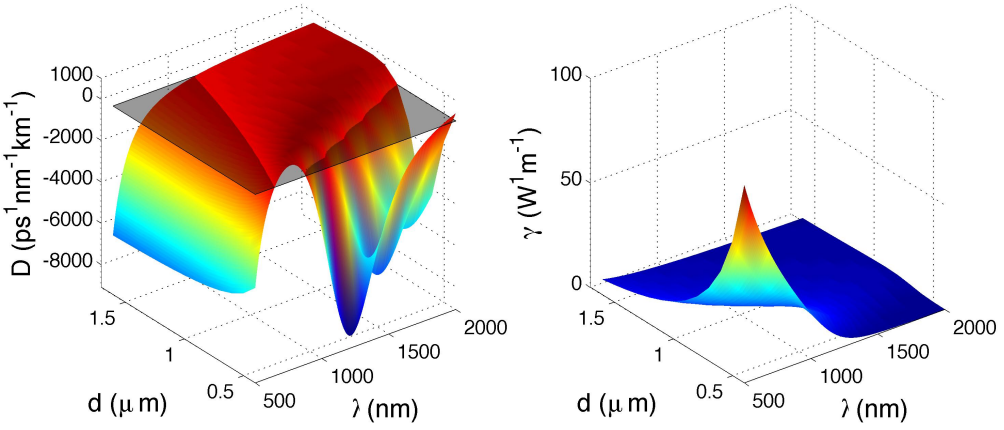

(c) Tellurite

FIGURE 4.3: Dispersion and nonlinearity of a various soft glass suspended core fibres, as a function of core diameter d and wavelength λ. The dark region on the graph on the left hand side is the zero dispersion plane – the intersection of this plane and the dispersion curves gives the ZDW. The graphs show that, for all the glasses, the ZDW moves to shorter wavelengths as the core diameter increases. Meanwhile, the nonlinear coefficient increases of smaller core diameters due to the increased confinement.

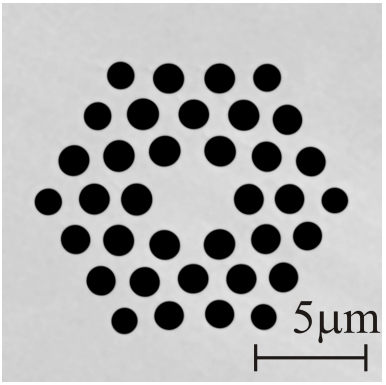

FIGURE 4.4: A hexagonal array MOF fabricated in a bismuth glass [2]

The geometry of this fibre design allows fabrication of hexagonal MOFs by either the 'stack and draw' [16, 188] or extrusion technique [2]. The former method may be used to fabricate such fibres in either silica [188] or soft glasses [193]. The extrusion technique, which is more flexible and can be used to fabricate a variety of geometries, is discussed in further detail in Chapter 6.

While the hexagonal hole array is the most popular method of engineering dispersion in MOFs, other structures such as 'grapefruit fibres' [194] and a composite (where a different glass is used in the cladding holes) MOF [195] have also been used to engineer the fibre dispersion and nonlinearity. These composite fibres are actually very similar to the all solid fibres discussed next.

4.4.2 All solid fibres

Instead of introducing holes into the fibre geometry, one may also engineer the dispersion by combining multiple glasses with different refractive indices. As with holey fibres, the combination of refractive indices is used to create a region with a variable, effective index. The key difference is that a glass/glass combination is used instead of an air/glass combination.

Recent work with lead silicate glasses have demonstrated that the all solid approach can be used to fabricate fibres with low dispersion at 1.55 µm for telecommunications applications [132, 196]

The main advantage of an all solid approach is that it overcomes some of the fabrication challenges associated with creating the complex subwavelength features required for

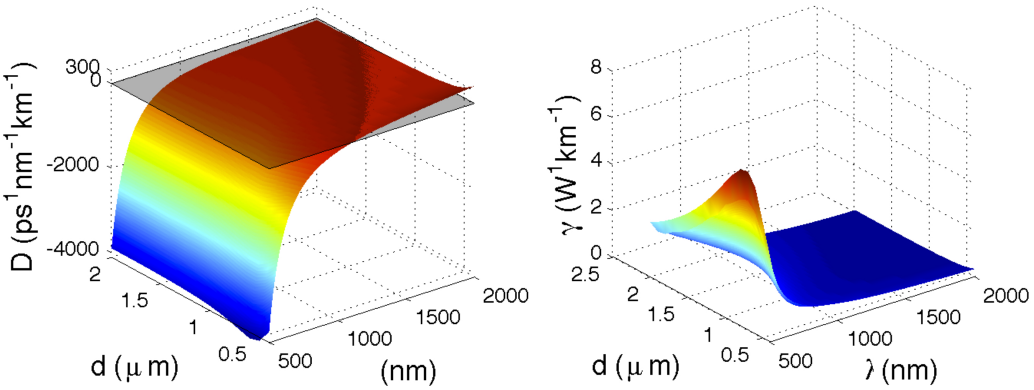

FIGURE 4.5: Dispersion and nonlinearity, as a function of core diameter d and wavelengths λ, for a solid fibre consisting of two commercial lead silicate glasses – SF57 for the core and SF6 for the cladding. The dark region on the graph on the left shows the zero dispersion plane. We can see that by combining two glasses it is possible to obtain a zero dispersion wavelength with a much lower dispersion slope compared to Figure 4.3.

some MOF designs. However, all solid fibres are limited by the fact that the constituent glasses must be chosen such that their chemical and physical properties are similar enough for them to be fabricated together. If, for example the 'billet stacking' method [196] is used for fabrication, it is critical that the softening points of the glasses are within a range narrow enough for them to all be extruded together.

4.5 Design approach

The approach to dispersion engineering taken in this research was to use a 'hexagonal wagon wheel' (HWW) fibre design and optimise the geometry using a genetic algorithm based optimisation procedure. The HWW geometry may be thought of as a hybrid of the hexagonal and suspended core type fibre designs and is based on previous work [65] on designing dispersion engineered fibres for supercontinuum generation in the mid infrared [197]. In this work, the same design methodology has been adapted, however the dispersion engineering is focussed on the telecoms band.

4.5.1 The hexagonal wagon wheel fibre

The hexagonal wagon wheel fibre design consists of a suspended core containing a ring of holes, as shown in Figure 4.6. This initial structure was chosen as it represents a

hybrid of the suspended core and hexagonal MOF type geometries – the larger, outer ring of holes create the suspended core region in which the mode is confined, while the ring of inner holes allow tailoring of the dispersion profile via their size and placement. Thus it allows the high confinement and nonlinearity of the suspended core geometry to be combined with the dispersion tailoring capabilities of the hexagonal microstructure.

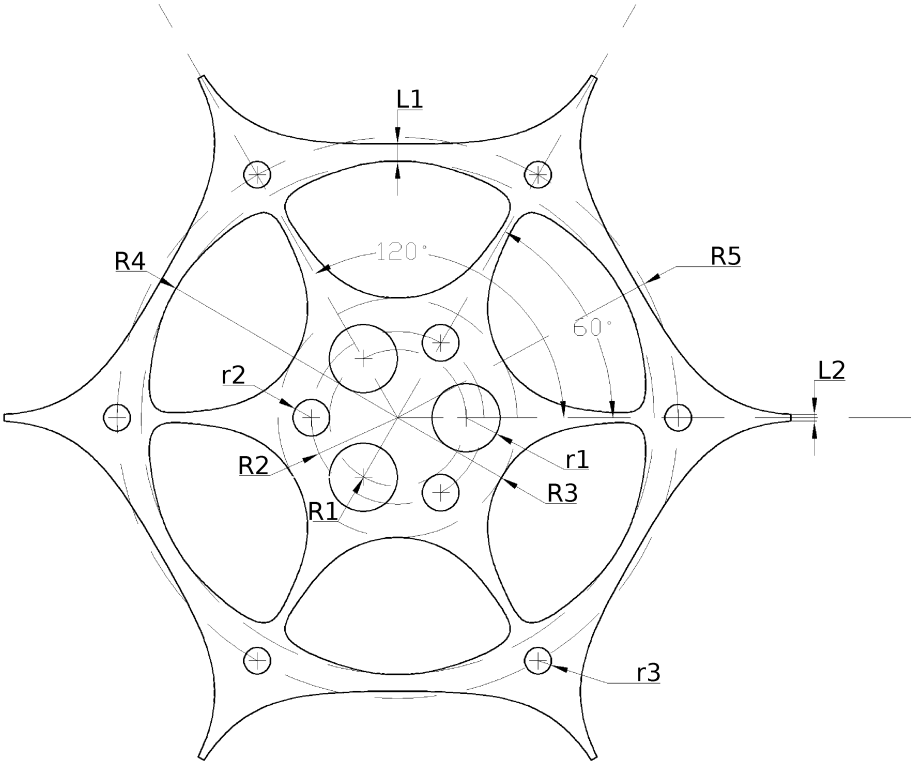

FIGURE 4.6: Initial fibre geometry. The fibre parameters shown above were used to optimise the design for low dispersion and high nonlinearity

Once the general fibre geometry has been chosen, the next step is to find the optimal version of this structure that gives the desired dispersion and nonlinearity. This is a classic example of an inverse problem – we have an input system, an output set of data and a physical model that produces the data for a given system but we seek to work backwards from a given set of data to find the input system that produces it. In this case the input system is the fibre geometry, the output data consists of the desired fibre characteristics (namely low, flat dispersion and high nonlinearity) and the model linking the two is derived from the wave propagation equations [35].

Inverse problems of this nature are typically nontrivial to solve. The main difficulty arises from the fact that multiple versions of the input system can produce the same output, i.e. there is no one–to–one mapping between input and output. In the context

of fibre design, this simply means that various fibre geometries can lead to the same dispersion and nonlinearity profile. Therefore, while it may be possible to make an educated guess and obtain *an* input set that gives the desired output, we cannot know if it is the best solution without exhaustively evaluating all the other input sets in the parameter space.

This is clearly not feasible so it is generally best to formalise most inverse problems into an optimisation problem instead. Such an approach is used routinely in many branches of physics and mathematics [198–200]. In this work a similar solution has been adopted, where a genetic algorithm was chosen as the optimisation method. This is discussed in further detail in Section 4.5.2 that follows.

To optimise this structure for dispersion tailoring we must first parametrise it. We do this as shown in Figure 4.6 via the parameters R1, R2, R3, R4, R5, r1, r2, r3, L1 and L2. Of those parameters, the ones that determine the dispersive and nonlinear properties of the fibre are R1, R2, R3, R4 r1 and r2 as they determine the arrangement of the holes in the inner cladding. R1 and r1 are describe one circular ring of three holes around the centre of the fibre and R2 and r2 similarly describe a second ring of holes, interleaved with the first. In both cases r1/r2 is the radius of the holes, while R1/R2 is the distance between the centres of these holes and the centre of the fibre. The presence of these two independently varying sets of inner holes, along with the outer holes, provides many degrees of freedom and consequently the ability to achieve extremely fine dispersion control.

4.5.2 Genetic algorithm optimisation

As mentioned earlier, the challenge of determining which variant of the HWW structure leads to a fibre with the characteristics best suited to meeting the aims of this research is a complex problem, best solved by the use of an optimisation procedure. This complexity mainly arises from the fact that the effect of each parameter is not independent; it is the interplay between them that determines the final fibre properties. Without an optimisation procedure the best we can do is infer trends for individual parameters. Consequently surmising the effect of varying multiple parameters simultaneously is difficult to ascertain and predict with any confidence. Unless a large number of exhaustive, extensive simulations are performed.

There are various optimisation techniques that have been explored in the literature to solve problems of this nature. They may generally be classified as either a minimisation procedure (such as simplex algorithms [201]) or an iterative procedure combined with a heuristic (such as genetic algorithms). The latter was chosen as it was thought to be more robust and better able to tackle this particular problem. The more traditional minimisation techniques generally converge to a solution quicker but are more prone to generating solutions corresponding to local minima, instead of the global minimum. Overcoming this requires resetting the program to cover multiple initial conditions in the hope that all local minima are uncovered. This is obviously inefficient and consequently gradient based optimisation techniques work best (and indeed outperform evolutionary algorithms) in cases where, for example. when the solution space is convex.

A genetic algorithm is better able to deal with the multidimensional parameter space presented by the HWW design as it implicitly handles multiple input conditions via the use of randomised populations [202]. It therefore does not need to be restarted and repeated. There are also other advantages, such as being able to search for solutions in noisy or nonstationary input conditions [203] and being able to operate without having to characterise the quality of a solution in terms of a least squared error.

The latter point is important as the error must be a specific quantity and thus requires an equally specific definition of the ideal case (the error is generally calculated to be representative of the difference between the solution and the ideal case). In this instance that would mean starting out by defining a fixed dispersion and nonlinearity profile. This is not ideal as we must be extremely careful to ensure that the ideal case is indeed the best possible outcome. Otherwise, since the solution can only converge towards this, the design may be limited to something that does not actually represent the best possible outcome. In a genetic algorithm solutions are evaluated in terms of a fitness function, which is much less restrictive as any definable function can be used.

A genetic algorithm was therefore chosen as the optimisation procedure. This enabled us to start with the generic geometry such in Figure 4.6 and iteratively improve on it to get an extremely tailored dispersion profile. This type or procedure has also been used in the past for dispersion tailoring of microstructured optical fibres [204].

The genetic algorithm procedure essentially mimics the natural selection process observed in nature. However the selection criteria in this case are imposed by a predefined

fitness function, as opposed to a natural environment. The procedure starts with a initial population of individuals – where each individual is defined by a set of genes and is a candidate solution to the optimisation problem. This initial population is generally best produced by randomly sampling across the space of all solutions (for practical purposes the sampling may be limited to a fixed space instead). In the case of the HWW fibre design each individual is a parameter set (i.e. R1, R2, R3, R4, R5, r1, r2, r3, L1 and L2), with its genes corresponding to a particular value (e.g. R1 = 100 nm).

The population is then evaluated by using the fitness function to rank each individual within it [205]. Once ranked, the search heuristic then determines how individuals will be paired in order to generate the next generation of offspring. Individuals of higher fitness correspond to solutions of higher quality and thus they are preferred to those of lower fitness. To reflect this, the probability that an individual will used in a pair to 'breed' a new solution is set to be determined by its fitness. This way those individuals with higher fitness have a correspondingly higher probability to pass their genes on. However, to prevent the population being dominated by elite individuals (i.e. those with the best fitness), individuals are prevented from pairing with themselves and any individual may be paired with multiple times.

Once paired, new individuals are then created from these existing individuals through a mating process. This involves crossing over the genes between parents to form those of the offspring. Mutations may also be introduced into the gene code by adding random changes to the genes. Doing this greatly increases the chances that the algorithm will converge to the global solution instead of being mired in a search for a local minimum.

After the creation of each generation the process is repeated and the entire population is evaluated again. If the average fitness of the population is deemed to be high enough the algorithm may be stopped at this point. However, it is better practice to instead track the fitness of each generation and observe if it converges to a certain value. If this is the case we may infer that the optimisation problem has been solved as further iterations are unlikely to produce better results.

In this genetic algorithm, the fitness function that was used was defined as

$$F = \frac{\gamma_0}{\sum_j |D_j|}, \tag{4.4}$$

where D_j is a set of dispersion values at wavelengths, λ_j, in the band of interest and γ_0 is the nonlinear coefficient at the central wavelength. The physical significance of this function is that it highlights those members of the population that have high nonlinearity and low dispersion in the band of interest. This is then the selection criteria used by the search heuristic to evolve the population towards better solutions.

To evaluate this fitness function for a particular geometry the finite element method was used to first calculate the dispersion and nonlinearity of the fundamental fibre mode. Essentially, this involves breaking up the fibre cross section into a finite number of small elements and solving Maxwell's equations in each one of them with appropriate boundary conditions [184, 206]. A combination of COMSOL Multiphysics® and MATLAB® were used to perform these calculations and the results were fed back into the genetic algorithm. This is covered in more detail in Section 4.3.

This process is summarised in Figure 4.7. The program to carry out this evolutionary optimisation was developed by a colleague as part of his Ph.D. research. The details may be found in his thesis [207]. A newer version of this program has also been released for public use [208].

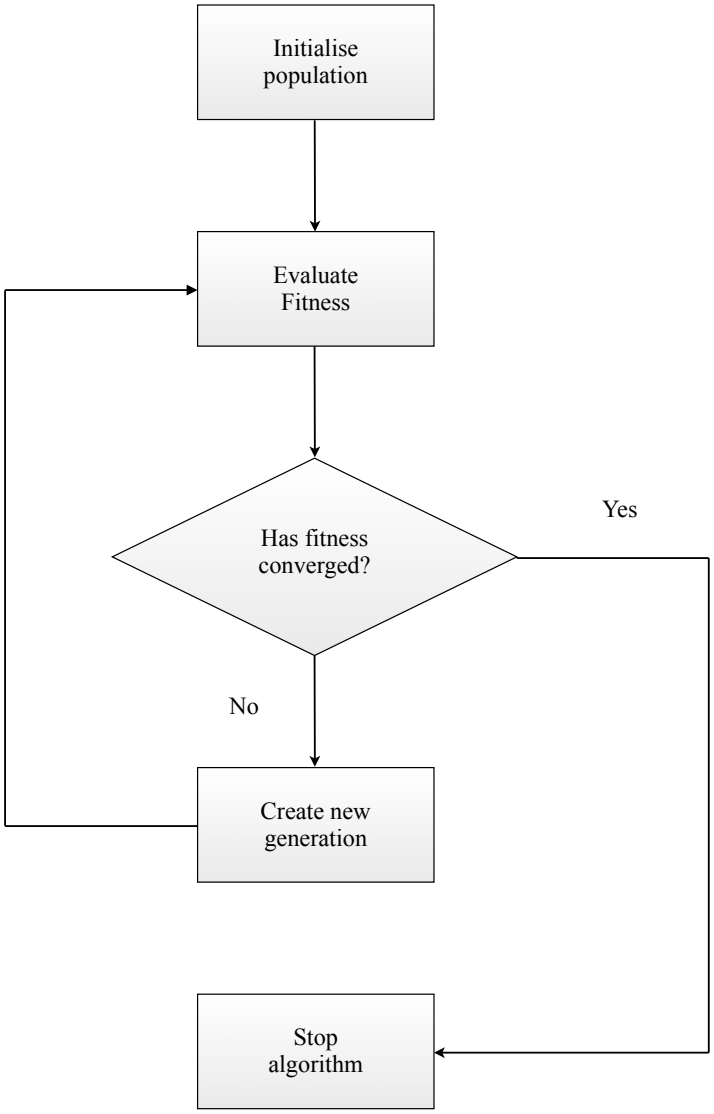

FIGURE 4.7: A simple flowchart summarising a typical genetic algorithm optimisation procedure.

4.5.3 Tellurite HWW for multicasting

As mentioned in Chapter 2, the major fibre requirements for this application were to have a broad, high gain profile to allow the FWM process to generate 16 copies of the input signal. The breadth of the gain would need to accommodate an operating bandwidth broad enough to fit 16 copies of the signal as well as four pairs of pump waves – all in all, this equates to 24 distinct waves. Therefore, based on the signal and pump bandwidths in Reference [36], an operating bandwidth of 1440 nm to 1650 nm was chosen, with 15 equally spaced points in this region used to evaluate the fitness function.

The other main requirement was of course a high nonlinearity. After a few preliminary

simulations it became apparent that the fitness function in Equation 4.4 was too weighted towards low dispersion. This meant that, as $\sum_j |D_j|$ moves toward zero, small changes in the denominator of Equation 4.4 have a proportionally larger effect than changes in the numerator. Consequently improvements to nonlinearity are trumped by a lowering of the dispersion, even if this lowering is by a marginal amount and may thus have a lower effect on gain than a relatively larger increase in nonlinearity. To counter this, the fitness function was slightly modified by introducing a constant to effectively amplify the effect of changes in γ. The new fitness function that was used may be written as

$$F = \frac{K\gamma_0}{\sum_j |D_j|}, \tag{4.5}$$

where the constant was chosen to be $K = 10^4$. The dispersion curve is evaluated via D_j – a set of dispersion points at wavelengths λ_j where $\lambda_j = (1440 + [j-1]) \times 14$ nm and $j = 1, 2..15$.

The material chosen for the fibre design was an in house tellurite. This is the same as the TZNL tellurite glass mentioned in Chapter 3 ($73{\cdot}TeO_2$ — $20{\cdot}ZnO$ — $5{\cdot}Na_2O$ — $2{\cdot}La_2O_3$). This glass was chosen mainly due to the fact that it has quite a high nonlinear index of n_2, of 5.9×10^{-19} m^2 [28, 195] – an order of magnitude higher that that for fused silica [209]. Additionally this is a mature glass, in terms of fibre fabrication, and thus its behaviour under fabrication conditions is understood better [9, 156, 167].

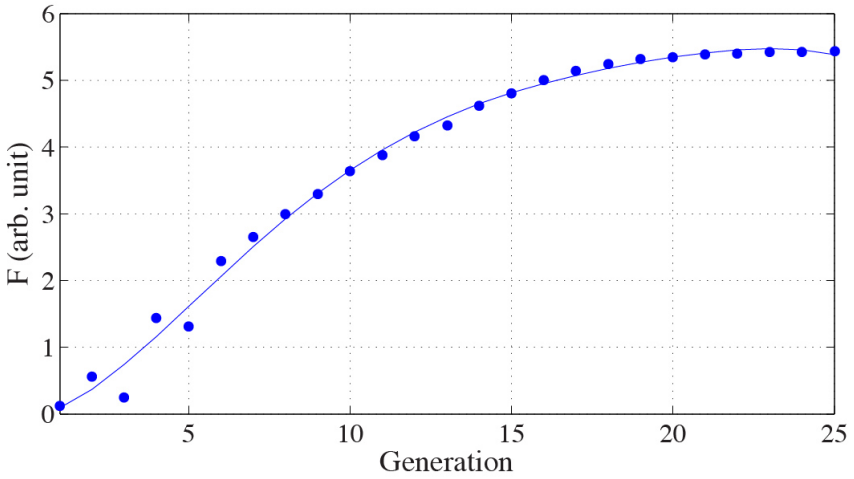

FIGURE 4.8: Evolution of mean fitness for tellurite HWW. After an initial fluctuation in the mean fitness, it steadily increases before converging at around the 21st generation.

The genetic algorithm was then started with an initial population of 1000 parameter sets – each one being a randomly generated based on the structure shown in Figure 4.6. To ensure that the output designs could were within reasonable fabrication capabilities, limits were set on each parameter. For example the lower and upper limits on R3 were 0.5 µm and 5 µm, respectively. As this parameter determines the radius of the suspended core region anything smaller than 0.5 µm would be impossible to fabricate; similarly anything larger than 5 µm would have too low a nonlinearity to be useful.

In addition to these limits, an additional condition was imposed that forced R1 to be equal to R2 – this ensures that each set of inner holes is the same distance away from the centre of the fibre. This is not ideal as it results in fewer degrees of freedom and, consequently, ability to fine tune the dispersion profile. However it significantly reduces the possibility of the genetic algorithm generating a design that would require a die that was too complex, or even impossible to fabricate. Having the sets of holes too close together in the radial direction could, for example, make the design infeasible (more information on die design and how it relates to fibre fabrication can be found in Chapter 6).

Parameter	Value
r1	171 nm
r2	224 nm
r1	813 nm
R2	813 nm
R3	1.09 µm
R4	2.30 µm

TABLE 4.1: Fibre parameters for the 23rd generation.

The evolution of the population fitness is shown in Figure 4.8. We see the average population fitness start to saturate at around the 21st generation. The algorithm was then stopped shortly after this point and the structure with the highest fitness in the 23rd generation was evaluated. The fibre parameters for this generation are shown in Table 4.1 while the geometry is shown in Figure 4.9.

The evaluated dispersion and nonlinearity are shown in Figure 4.10. It shows that the genetic algorithm has produced a structure with extremely low dispersion over a broad band – the dispersion only varies from -2.87 ps^{-1}nm^{-1}km^{-1} to 0.29 ps^{-1}nm^{-1}km^{-1} over

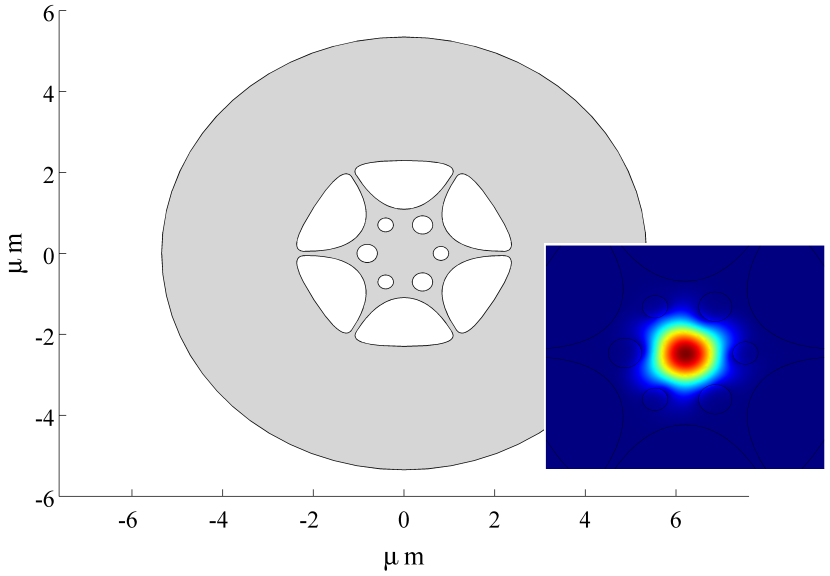

FIGURE 4.9: The geometry of HWW fibre designed in tellurite for multicasting. The shape of the fundamental mode at 1550 nm is shown in the figure inset. This geometry corresponds to the fibre parameters in Table 4.1.

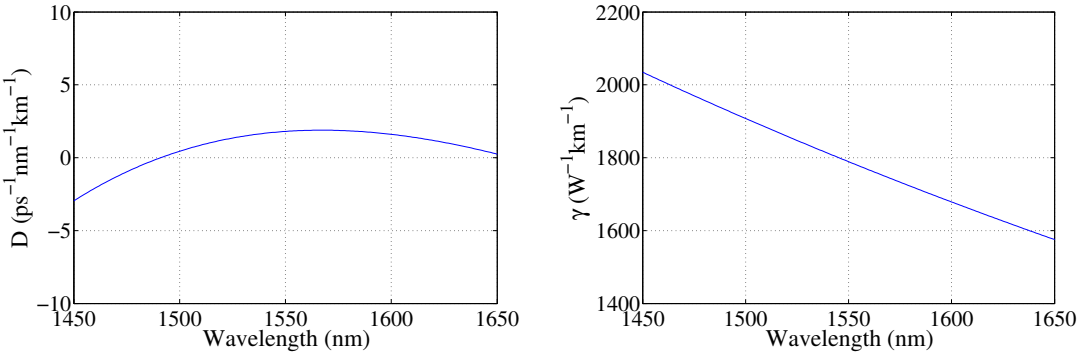

FIGURE 4.10: Dispersion and nonlinearity for the tellurite HWW design shown in Figure 4.9. At 1550 nm the nonlinear coefficient of this fibre design $\gamma = 1789$ W^{-1}km^{-1}, while the dispersion $D = 1.8$ ps^{-1}nm^{-1}km^{-1} and the dispersion slope (evaluated from 1540 nm to 1560 nm) is 0.010 ps^{-1}nm^{-2}km^{-1}

the wavelength rage from 1450 to 1650 nm. The resulting fibre design also has a high nonlinearity, with $\gamma = 1789$ W^{-1}km^{-1} at 1550 nm.

This fibre design in modelled in Chapter 4, where it is numerically shown to be capable of multicasting signals over such a broad band.

4.5.4 Bismuth HWW for PSA

The design process for the fibre for phase sensitive amplification was similar to the one used in Section 4.5.3 in the design of the HWW for multicasting. However, some

Parameter	Value
r1	120 nm
r2	120 nm
R1	619 nm
R2	619 nm
R3	810 nm
R4	1.66 µm

TABLE 4.2: Fibre parameters for the 20^{th} generation.

significant changes were made. The first of these was changing the substrate from the in-house tellurite glass to a commercially available Asahi bismuth-oxide glasses, BIAB061. While this glass has a lower nonlinear refractive index than the tellurite ($n_2 = 3.2 \times 10^{-19}$ m^{2}W^{-1} [117]) it is known to have good mechanical and thermal stability which aids the fabrication process. Indeed bismuth oxide glasses have been used extensively for the fabrication of microstructured optical fibres [117, 133].

The second change was equalising the size of the inner holes by introducing an additional limit of forcing r1 and r2 to be the same. Again this results in a loss of some degrees of freedom and to achieve fine dispersion control, we must consider independently varying r1, r2, R1 and R2 i.e., two sets of inner holes, each with a different radius and distance away from the centre. However, such a design presents significant fabrication challenges. Consequently there is a trade off between ease of fabrication and dispersion control. Given that the operating bandwidth for PSA is narrower than that for multicasting, the required dispersion profile could still be obtained with just one set of inner hole sizes. Thus making this trade off between ease of fabrication and fine dispersion control worthwhile.

After implementing these changes into the program the algorithm was restarted with an initial population of 1000 randomly generated versions of the base design. The limits imposed were the same and the fitness function only changed slightly to narrow the wavelength range from 1500 nm to 1600 nm, i.e. $\lambda_j = (1500 + [j-1]) \times 14$ nm with $j = 1, 2..15$. The evolution of the fitness in each generation is shown in Figure 4.11. It shows a sharper rise in the average fitness of the population but, again, the fitness saturates after a certain number of generations; in this case this happens at around the 15^{th} generation.

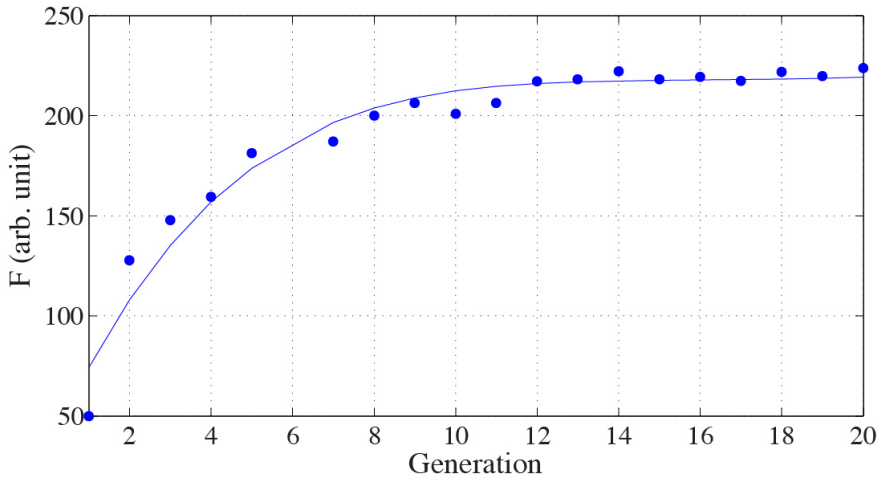

FIGURE 4.11: Evolution of mean fitness for bismuth HWW. After an initial fluctuation in the mean fitness it increases steadily before converging at around the 15^{th} generation.

The algorithm was consequently stopped at the 20^{th} generation and, as before, the member of the population in that generation with the highest fitness was extracted and evaluated. The resulting parameter set is shown in Table 4.2

Convergence of the parameter set is verified by observing the parameter regions in the R1/R3 : R3 plane. The plots in Figure 4.12 show the parameter space for R1 and R3 shrinking towards an optimal region as the genetic algorithm evolves through successive generations.

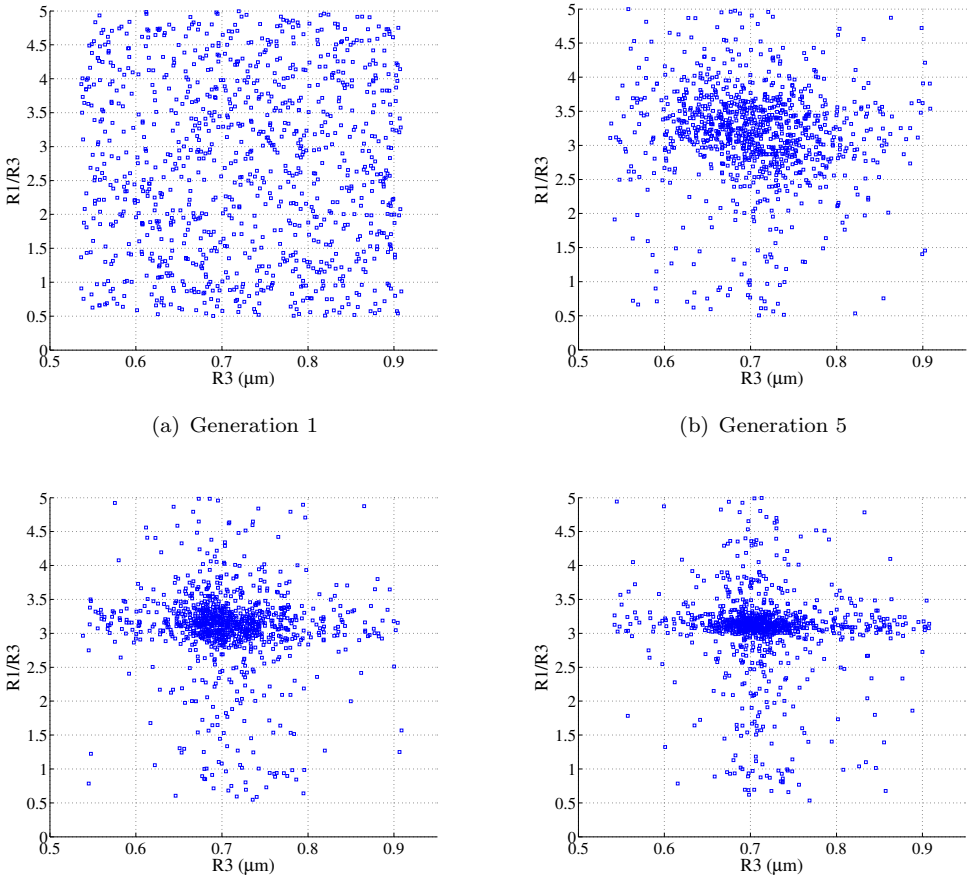

(a) Generation 1

(b) Generation 5

(c) Generation 10

(d) Generation 15)

FIGURE 4.12: Convergence of population parameters R1 and R3

The dispersion and nonlinearity for this structure is shown in Figure 4.14. This fibre has a dispersion value $D = 0.14$ ps^{-1}nm^{-1}km^{-1} and nonlinear coefficient $\gamma = 1099$ W^{-1}km^{-1}, respectively at the telecoms wavelength of 1550 nm. The dispersion slope for this fibre design is higher than that obtained for the Te HWW due to the extra limitations imposed on the optimisation procedure. However, since the PSA application is over a much narrower bandwidth, the desired result may still be achieved. Simulations were carried out to demonstrate this and their results are presented in Chapter 5.

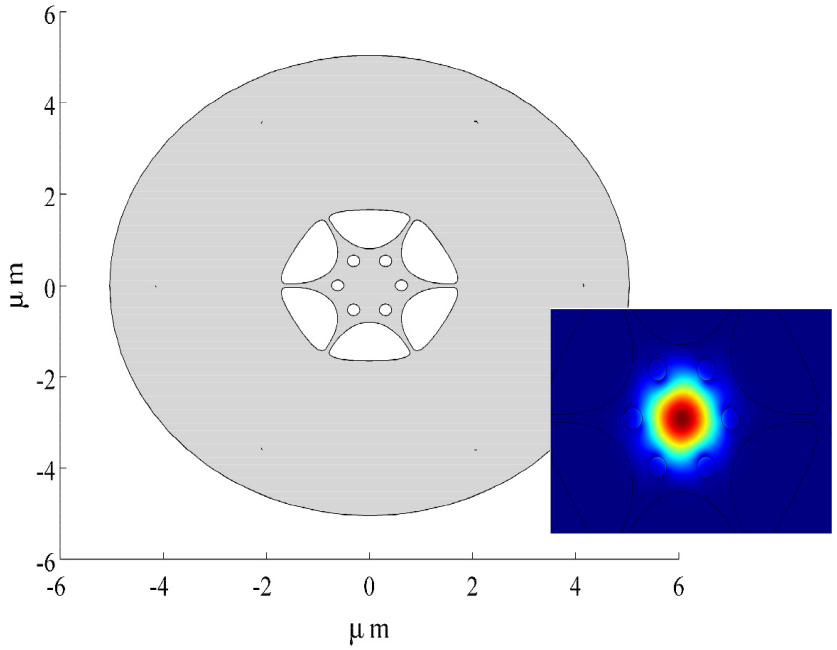

FIGURE 4.13: The geometry of HWW fibre designed in bismuth for PSA. The shape of the fundamental mode at 1550 nm is shown in the figure inset. This geometry corresponds to the fibre parameters in Table 4.2.

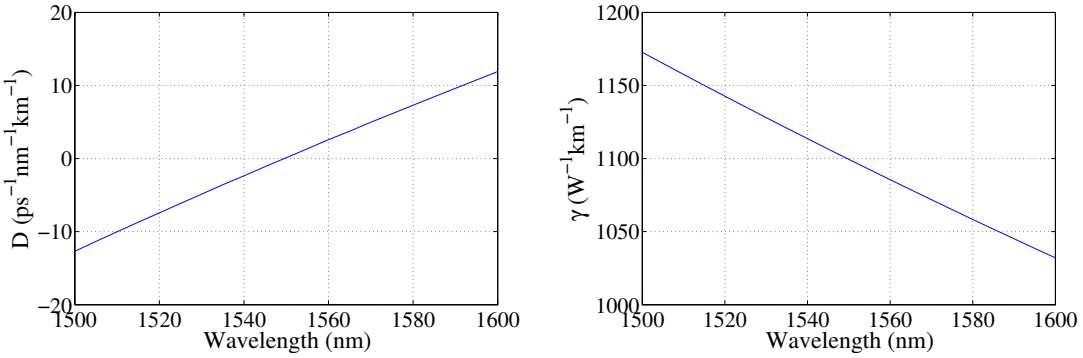

FIGURE 4.14: Dispersion and nonlinearity for bismuth HWW shown in Figure 4.13. At 1550 nm the nonlinear coefficient of this fibre $\gamma = 1099$ W^{-1}km^{-1}, while the dispersion $D = 0.14$ ps^{-1}nm^{-1}km^{-1} and the dispersion slope is 0.246 ps^{-1}nm^{-2}km^{-1}

.

4.6 Evaluation of optimisation procedure

The power of this genetic algorithm optimisation technique is seen by comparing the parametric gain g, as a function of pump separation, for the dispersion engineered MOFs designed here with commercially available highly nonlinear fibres. In Figure 4.15 below shows the gain for the following types of fibre:

(a) commercially available silica HNLF with flattened dispersion and ZDW at 1550 nm;

(b) bismuth step index fibre with a core diameter of 3.6 µm so that the zero dispersion wavelength is at 1550 nm (the same as the optimised HWW fibres)

(c) tellurite step index fibre with a core diameter of 3.8 µm so that the zero dispersion wavelength is at 1550 nm (the same as the optimised HWW fibres)

(d) the same as (b) above but for its nonlinear coefficient, which has been artificially raised to match that of the designed bismuth MOF.

(e) the bismuth HWW designed for PSA, shown in Figure 4.13

(f) the tellurite HWW designed for multicasting, shown in Figure 4.9

For similar values of pump power, the gain per length gets successively higher and broader as we move from the silica fibre to the soft glass fibres, with the best performance being that of the dispersion engineered HWW fibres. By just maintaining the ZDW and increasing the γ value through the use of a material with a higher intrinsic nonlinearity the gain, per length, in (b) and (c) are already orders of magnitude higher and covers a broader band, relative to that in (a).

The best gain has been achieved by combining dispersion flattening with high nonlinearity through the use of microstructure – as done with the optimised MOF designs presented here. The gain in this case [i.e. (e) and (f)] is even significantly better that in (d) where the nonlinear coefficient of the bismuth-air step index fibre has been artificially increased. This highlights the benefits of using soft glass based designs, both in terms of high material nonlinearity and the ability to specifically tailor and optimise the dispersion profile through the use of microstructure.

To achieve similar gain in a conventional silica HNLF one would require significantly higher pump powers or longer lengths, compared to the dispersion tailored, soft glass MOF. Generally, if the total power into the fibre is to be kept at a few Watts the required length of silica HNLF is of the order of a few 100 metres. In addition to this, the operating bandwidth, which is determined by the pump separation, of a Silica based HNLF is lower, irrespective of length. This is due to the fact that the region over which g is nonzero and real is narrower, as seen in Figure 4.15.

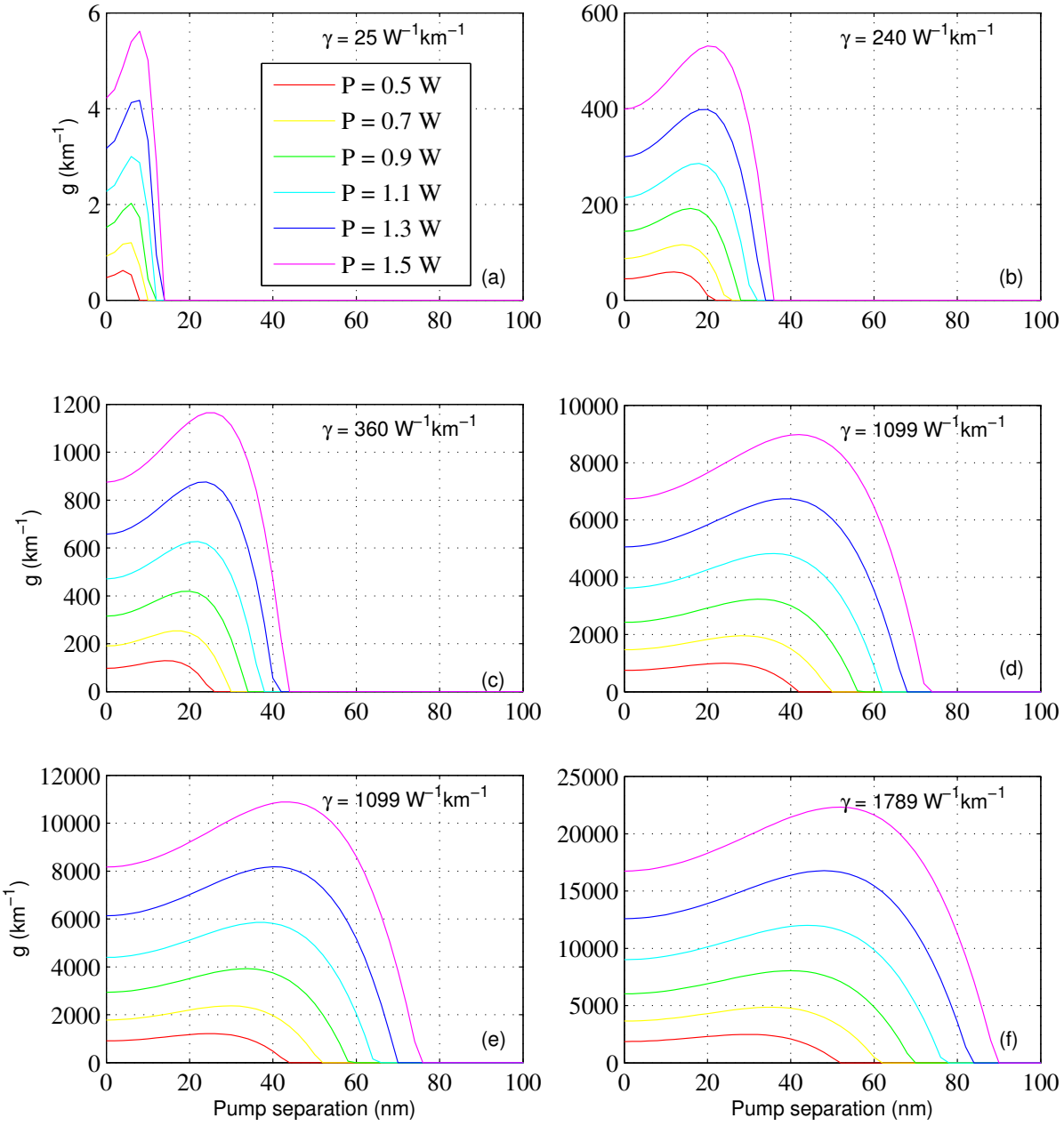

FIGURE 4.15: Gain bandwidth for dispersion engineered fibre MOF compared to other highly nonlinear fibres. In the figures above P represents the power in either pump and the gain is defined as in Equation 2.73. In all plots the ZDW is at 1550 nm.

4.7 Simplified germanate HWW

The complex HWW structure allows for fine tuning of the dispersion profile due to the varied degrees of freedom offered by having two sets of holes (the ring of smaller inner holes and the ring of larger outer holes). Having an inner ring of holes also aids in the confinement of the mode and thus increases the nonlinearity of the fibre. However, during

fabrication trials with the GPNL5 germanate glass the surface tension was discovered to be too high to allow a microstructured fibre design of this type (with both inner holes and outer holes, of varying size) to be drawn without a complex pressurisation setup (see Section 6.5 for details of these results).

Thus, a simplified design, without any inner holes, was also considered. The properties of this design are mostly determined by the radius of the suspended core region and the size of the outer holes. Consequently the design is more robust as it would have higher tolerances to deviations of fibre parameters from the ideal structure.

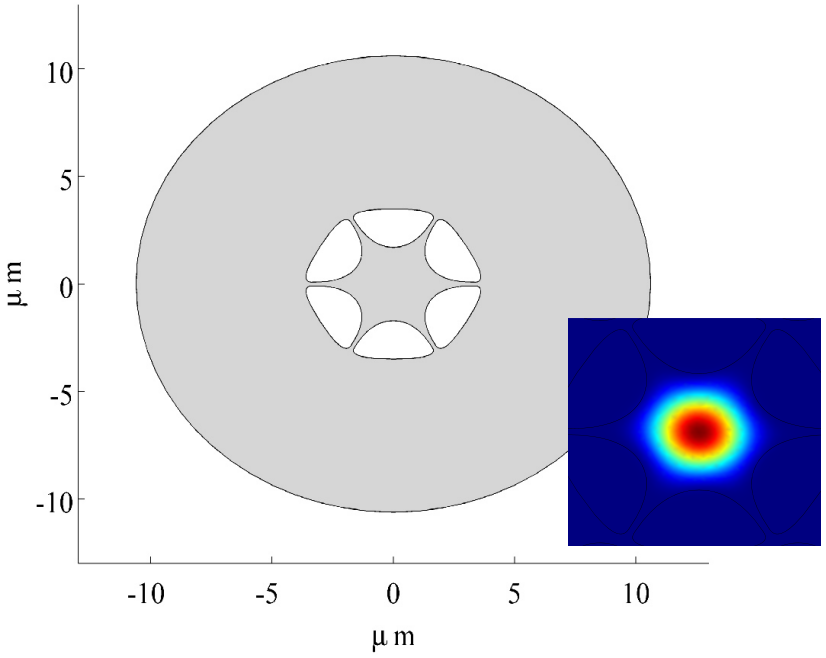

FIGURE 4.16: The geometry of the HWW with no inner holes at a core radius of 3.4 µm. This geometry was obtained by taking the HWW design shown in Figure 4.13, removing the inner holes and scaling the core radius to move the ZDW to 1.55 µm. The shape of the fundamental mode at 1550 nm is shown in the figure inset.

For this simplified HWW fibre design one of the novel germanate glasses described in Section 3.5, the GPNL5 glass, was chosen. The choice of glass is in line with the main reason behind considering this simplified design – enabling fabrication of a fibre that is more robust than those considered thus far. This is due to the fact that these germanate glasses possess many of the favourable properties of tellurite but are more mechanically and thermally stable [142, 150].

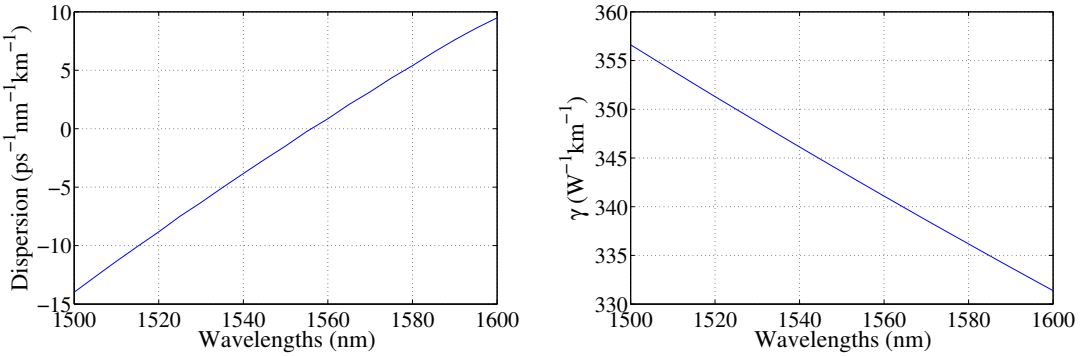

FIGURE 4.17: Dispersion and nonlinearity for the simplified germanate HWW, with no inner holes and a core diameter of 3.4 µm (as shown in Figure 4.16). At 1550 nm the nonlinear coefficient of this fibre $\gamma = 344$ W^{-1}km^{-1}, while the dispersion $D = -1.47$ ps^{-1}nm^{-1}km^{-1} and the dispersion slope is 0.237 ps^{-1}nm^{-2}km^{-1}

The benefits of genetic algorithm optimisation procedure for this simplified HWW design are limited, as the parameter set is relatively small. Therefore, to determine the optimal fibre parameters, the initial structure chosen was that shown in Figure 4.13 but with its inner holes removed. This geometry from this parameter set was then scaled by a set of constant values and the dispersion and nonlinearity were evaluated each time. These results are shown in Figure 4.18, where the dispersion and dispersion slope at 1550 nm have been plotted as a function of the scaled core radius (i.e. R3).

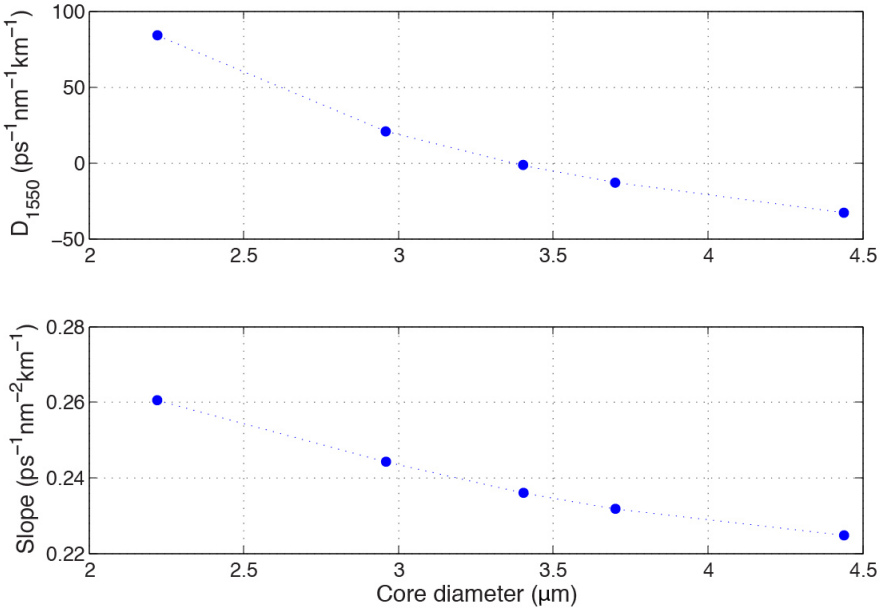

FIGURE 4.18: Evaluation of the dispersion at 1550 nm and the dispersion slope for a germanate HWW with no inner holes. A core diameter of 3.4 µm gives the best result

The results show that, at a core diameter of 3.4 µm, a ZDW of 1550 nm may be obtained with a dispersion slope of 0.24 $ps^{-1}nm^{-2}km^{-1}$. The geometry is shown in Figure 4.16. The dispersion and nonlinearity for this geometry is shown in Figure 4.18

We see that by moving to this simplified structure the core diameter is relatively much larger than the fibres obtained via the genetic algorithm optimisation. This larger core region, along with the lack of inner holes to confine the mode, result in a relatively lower effective area and thus nonlinearity. However, it is worth noting that this simplified structure still has a favourable dispersion profile (albeit over a narrower band) and a nonlinearity of $\gamma = 344\ W^{-1}km^{-1}$ at 1550 nm, which is still an order of magnitude higher than commercial silica HNLF. Thus it still has much potential for use in nonlinear telecommunications applications.

4.8 Conclusion

This chapter has described how the two most important fibre properties for telecommunications applications, namely the dispersion and the nonlinearity, are affected by the fibre geometry. Section 4.4 describes some of the types of fibre geometries commonly used to engineer these fibre properties. Following this, Section 4.5 discusses the process used in this in this research to obtain the fibre designs for the applications outlined in Chapter 2. This process, a genetic optimisation algorithm, is shown to generate novel fibre designs with low, flat dispersion and high nonlinearity. A simplified structure has also been studied and is described in Section 4.7 – this structure is based on the optimised designs, but reduced in complexity to aid fabrication.

Further evaluation of these designs is done in Chapter 5 where a pulse propagation method is used to simulate the nonlinear process for which the fibre was designed. These simulations are used to judge the gain performance of the fibre designs before beginning fabrication trials.

Chapter 5

Modelling of fibre designs

5.1 Introduction

This chapter describes the pulse propagation modelling of the hexagonal wagon wheel fibre designs presented in Chapter 4; namely the tellurite based HWW design for multicasting and the bismuth oxide based HWW design for phase sensitive amplification.

The results presented here were obtained by the use of a pulse propagation model to simulate the behaviour of an optical wave travelling along the length of the fibre. For the tellurite HWW the modelling showed that the fibre is able to multicast a signal from 1-to-16 copies – where each copy has a bandwidth of 40 Gb/s and thus enables processing of a signal at 640 Gb/s. For the bismuth fibre design, a high bit rate, noisy DPSK signal at 640 Gb/s was simulated and the numerical model was used to demonstrate that this signal could have its phase noise squeezed significantly by the designed fibre.

Analysis has also been done on the effect of structural variances on the performance of both the tellurite and bismuth fibre designs. When fabricating microstructured fibres a certain amount of structural variance is inevitable. Thus, modelling these effects is necessary to develop an understanding of allowable fabrication tolerances.

This chapter begins with an overview of the pulse propagation modelling technique in Section 5.2. The modelling for each fibre design is then presented – the tellurite HWW is discussed in Section 5.3 and the bismuth HWW in Section 5.4. Each fibre section has its own summary however an overall conclusion of the results is provided at the end.

5.2 Pulse propagation model

A pulse propagation model (PPM) is a numerical tool that is used to predict the evolution of an input pulse (or set of pulses) within a waveguide of known optical properties. It takes in the propagation characteristics calculated by the FEM model and simulates the propagation of an optical wave through the fibre. A PPM is extremely valuable for the design of optical fibres for nonlinear applications as it enables one to simulate the application for which the fibre is intended. This validation of the design is an essential prerequisite for fibre fabrication.

In a pulse propagation model, the functional form of the input must be specified along with the equations governing its propagation within the waveguide. This equation is then solved in a stepwise manner and used to quantify how the input pulse propagates, culminating with the final output from the waveguide. For optical fibres this governing equation is the nonlinear Schrödinger equation (NSE) for nonlinear, dispersive media [210, 211], as shown in Equation 2.48. Specifying the parameters of the NSE requires knowledge of the optical properties of the fibre, such as dispersion, loss and nonlinearity which must therefore be evaluated first by using a process such as the finite element modelling technique described earlier.

Considerable insight into nonlinear optical processes such as FWM can be gained via the use of a PPM, as the stepwise nature of the model can be used to quantify both the spectral and temporal evolution of a given waveform within a fibre and how the process is affected by the optical properties of the fibre. This can be used to refine the fibre design and, as mentioned earlier, validate designs before commencing the fibre fabrication process, which is generally relatively more expensive and time consuming.

The PPM used in this work was a split-step Fourier pulse propagation model of the nonlinear Schrödinger equation. This program was originally developed by my colleague Wen Qi Zhang as part of his research into supercontinuum generation in the mid infrared [207]. This program has now been released for public use [208]. I adapted his program to work with the dispersion and nonlinearity of the fibre designs developed in Chapter 4, under input conditions that simulate the application for which the fibres were designed.

This numerical simulation method is used instead of just solving the simplified coupled four wave equations as it allows us to more closely simulate real conditions. Pump

depletion and cascaded four wave mixing, for instance, are included in the PPM and, as shown later in Section 5.4, this allows us to consider the effect of saturation in phase sensitive amplification.

The form of the NSE (in the time domain) that governs the propagation model used in this research is shown in Equation 5.1, for a pulse with envelope A. This equation may be derived in a similar fashion to the simpler pulse propagation relation shown in Equation 2.48, however a more general form must be used for the optical susceptibility and higher order terms are retained from the Taylor expansion of β [34].

$$\begin{aligned}\frac{\partial A}{\partial z} =& -\frac{\alpha}{2}A + \sum_{k\geqslant 2}\frac{i^{k+1}}{k}\beta^{(k)}\frac{\partial^k A}{\partial T^k} \\ &+ i\gamma\left[1 + i\tau_{shock}\frac{\partial}{\partial T}\right] \\ &\times\left[A\int R(T')|A(z,T-T')|^2 dT'\right].\end{aligned} \tag{5.1}$$

Note that we have moved to the reference frame of the pulse, i.e. $T = t - z/v_g$, where v_g is the group velocity.

Equation 5.1 is a generalised form of the NSE that covers all the effects that determine the propagation of an optical wave through a waveguide: the first term on the right hand side includes the effect of loss thorough the absorption coefficient α; the second term gives us the effect of dispersion through $\beta^{(k)}$ (the coefficients of the Taylor series expansion of the propagation constant $\beta(\omega)$ around the frequency ω_0); the third term handles all the nonlinear effects and includes the optical shock time, defined below [34].

$$\tau_{shock} = \frac{1}{\omega_0} - \frac{1}{n_{eff}(\omega_0)}\frac{\partial n_{eff}(\omega)}{\partial\omega}\bigg|_{\omega_0} - \frac{1}{A_{eff}(\omega_0)}\frac{\partial A_{eff}(\omega)}{\partial\omega}\bigg|_{\omega_0}, \tag{5.2}$$

where n_{eff} is the effective mode index (as defined in Equation 2.32), A_{eff} is the effective area of the mode (as defined in Equation 2.34) and ω_0 is the angular frequency about which the pulse is centred. The nonlinear response function $R(t)$ contained in Equation (5.2) is given by [34].

$$R(t) = (1 - f_R)\delta(t) + f_R h_R(t). \tag{5.3}$$

The δ-function in the first term of Equation (5.3) represents the instantaneous dielectric response. This is responsible for all Kerr type effects such as self and cross phase modulation, along with four wave mixing. The second term represents the delayed Raman response of the ions in the glass. It is evaluated using the Raman fraction f_R and the Raman response function $h_R(t)$. The Raman response function, which depends on the material used, describes the delayed temporal response of the nonlinearity, while The Raman fraction f_R represents the fractional amount of the nonlinear polarisation that arises from this Raman response [34].

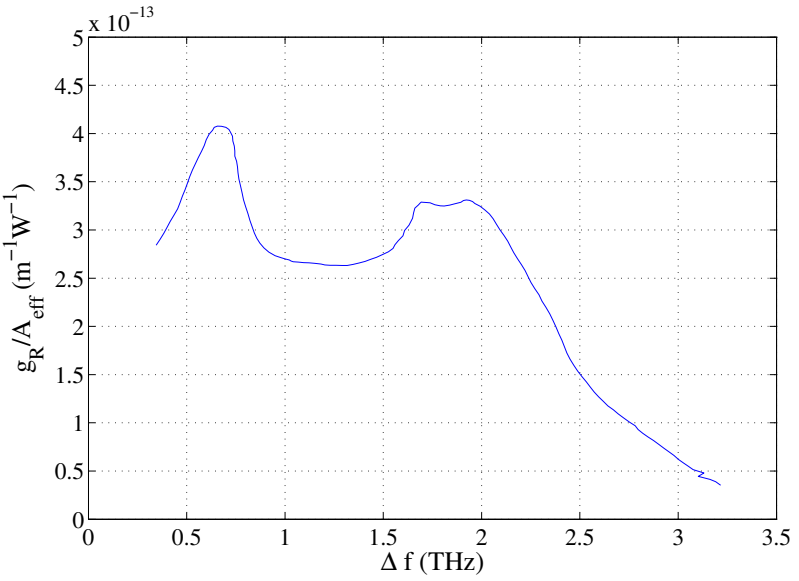

FIGURE 5.1: Raman gain for BiAB061 glass. This data is reproduced from [6] which is, to the best of our knowledge, the only known measurement of Raman gain for bismuth oxide glasses.

For bismuth oxide glasses such as the one considered here in the fibre design for PSA (see Section 4.5.4) the Raman gain may be evaluated using the Raman response function in Reference [6] – giving a Raman gain coefficient per unit effective area g_R/A_{eff} as a function of frequency shift Δf as shown in FIgure 5.1, with two peaks of approximately 0.013 $\mathrm{W^{-1}m^{-1}}$ (at $\Delta f = 0.64$ THz) and 0.011 $\mathrm{W^{-1}m^{-1}}$ (at $\Delta f = 1.9$ THz); and goes to zero for frequency shifts larger than 3.2 THz. Thus, given the short fibre length, relatively low pump power and, most importantly, the fact that the pump-signal separation (29 nm = 3.7 THz) is larger than the Raman gain bandwidth of the first

pump (at 1521 nm), Raman effects have not been considered in the simulations based on this glass.

For the tellurite glass considered in the design for multicasting (see Section 4.5.3) the Raman gain was evaluated using the data from Reference [7] – where the authors reported on TZN glass of composition $70{\cdot}TeO_2$ — $20{\cdot}ZnO$ — $10{\cdot}Na_2O$. This glass is very similar to the TZNL glass used in this research that has composition $73{\cdot}TeO_2$ — $20{\cdot}ZnO$ — $5{\cdot}Na_2O$ — $2{\cdot}La_2O_3$ and thus the TZNL glass can be expected to have a very similar Raman gain profile.

This Raman gain data (shown in Figure 5.2) shows that for the tellurite, unlike the Bismuth, the Raman gain bandwidth is relatively large. The gain spectrum, in terms of just the gain coefficient g_R, has three prominent peaks – one of approximately 5.5×10^{-13} m/W (at $\Delta f = 13$ THz) and two peaks of 8.6×10^{-13} m/W (at $\Delta f = 20.5$ Thz and $\Delta f = 22$ THz).

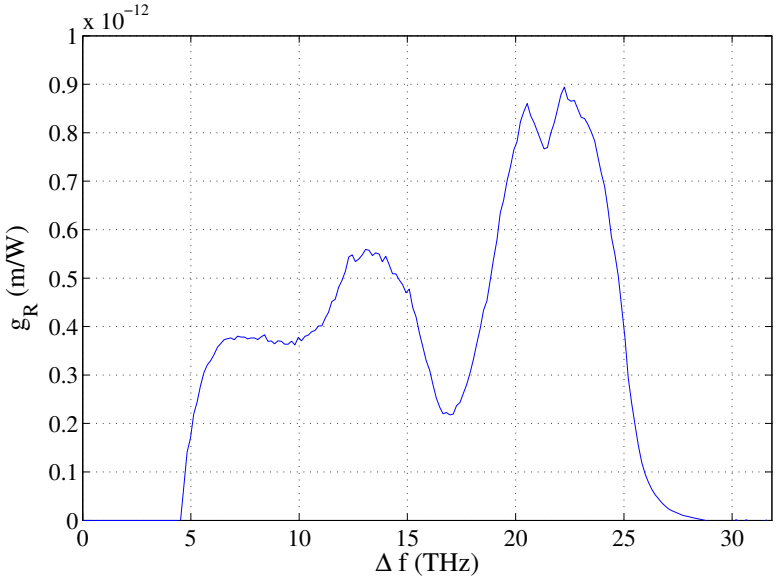

FIGURE 5.2: Raman gain for TZN glass of composition $70{\cdot}TeO_2$ — $20{\cdot}ZnO$ — $10{\cdot}Na_2O$ from Reference [7]. This glass has a very similar composition to the TZNL glass ($73{\cdot}TeO_2$ — $20{\cdot}ZnO$ — $5{\cdot}Na_2O$ — $2{\cdot}La_2O_3$) considered in this work.

The breadth of the Raman gain for the tellurite glass, being non zero from approximately 5 THz to 25 THz, means that it must be included in the multicasting simulations as signal copies are generated in an approximately 25 Thz band (from approximately 1450 nm to 1650 nm) centred around the signal (at 1550 nm). To do this the Raman fraction f_R and the Raman response function $h_R(t)$ given in Equation 5.3 must first be calculated. The value of the gain fraction f_R was calculated to be 0.064 – the details of this calculation

can be found in Reference [197]; it essentially uses the Kramers-Kronig relations and the relationship between the complex nonlinear refractive index and Raman gain given in Reference [212] to obtain an expression for f_R in terms of the complex nonlinear index.

This value is comparatively much lower than that of silica, which is 0.18 [212]. However the total Raman response (which is the product $\gamma f_r h_R(t)$) is still significant due to the fact that γ is much higher in tellurite because of its higher nonlinear refractive index ($5.9 \times 10^{-19}\mathrm{m}^2\mathrm{W}^{-1}$ for tellurite versus $2.4 \times 10^{-20}\mathrm{m}^2\mathrm{W}^{-1}$ for silica).

Once all the relevant terms for the NSE have been defined, namely the input pulse, loss, dispersion, nonlinearity and Raman fraction, the PPM proceeds via the 'split step' method. The split step method derives its name from the basic premise by which it operates: the initial equation (which does not have an analytical solution) is first split into components that do; each component is then solved individually, stepped forward by a small amount in the direction of propagation and then recombined. The process then repeats for as many steps as is required. The key assumption is that, if the step is very small, each component can be treated independently and propagating the solution only adds a numeric error that is proportional to the size of the step taken (and can be neglected if the step size is small enough).

In this case the initial equation is the NSE defined in Equation 5.1. It can be split into a component that is linear in A and another that is nonlinear and rewritten, using the formalism in Reference [34], as

$$\frac{\partial A}{\partial z} = (\widehat{D} + \widehat{N})A, \tag{5.4}$$

where $\widehat{D}$ is the operator responsible for the linear component and $\widehat{N}$ is the nonlinear operator. Physically, $\widehat{D}$ includes the effects of loss and dispersion and $\widehat{N}$, as its name suggests, accounts for all the nonlinear effects on the pulse. They are given by

$$\widehat{D} = \frac{\alpha}{2}A + \sum_{k\geqslant 2} \frac{i^{k+1}}{k}\beta^{(k)}\frac{\partial^k A}{\partial t^k}, \tag{5.5}$$

$$\widehat{N} = i\gamma\left[1 + i\tau_{shock}\frac{\partial}{\partial T}\right]\left[A\int R(T')|A(z, T-T')|^2 dT'\right]. \tag{5.6}$$

We then assume that, if the pulse propagates according to Equation 5.4 over a small distance h (in the direction of the z axis), the two operators can be assumed to act independently. We may therefore set $\widehat{D} = 0$ in Equation 5.4 and solve for $\widehat{N}$; and similarly set $\widehat{N} = 0$ and solve for $\widehat{D}$. Thus we arrive at an approximate solution given by

$$A(z+h,T) \approx e^{h\widehat{D}} e^{h\widehat{N}} A(z,T). \tag{5.7}$$

The exponential term in Equation 5.7 involving $\widehat{N}$ can be evaluated directly from Equation 5.6; the term involving $\widehat{D}$ however is computed in the Fourier domain using the relationship

$$e^{h\widehat{D}} A(z,T) = \mathscr{F}^{-1}(e^{h\widehat{D}(-i\omega)} \mathscr{F}[A(z,T)]), \tag{5.8}$$

where $\mathscr{F}$ and $\mathscr{F}^{-1}$ denote the forward and inverse Fourier transform, respectively; and ω is the angular frequency. $\widehat{D}(-i\omega)$ is evaluated from Equation 5.5 by replacing $\delta/\delta T$ by $-i\omega$.

In practice these Fourier transforms are evaluated using the fast Fourier transform algorithm (FFT) [213], which has been developed to run extremely fast on modern computers and thus allows us evaluate the split step solution over a number of small steps. The use of a small step size is essential to making accurate predictions as the error of the split step method is of the order $\frac{1}{2}h^2[\widehat{D},\widehat{N}]$. This is derived by taking the dominant term derived from evaluating the Baker–Hausdorff formula [214], up to the second order, for the two noncommutating operators $\widehat{D}$ and $\widehat{N}$. $[\widehat{D},\widehat{N}]$ represents the commutator, given by

$$[\widehat{D},\widehat{N}] = \widehat{D}\widehat{N} - \widehat{N}\widehat{D}. \tag{5.9}$$

The size of the step used in the simulations must however be balanced with computational load. In these simulations a step size of 10 µm was found to provide accurate results in a reasonable time frame when modelling fibres over lengths in the order of 10 cm to 1 m.

In addition to the step size, when using this sort of split step Fourier algorithm, one must also be careful of the size of the time window used in the computation. The FFT algorithm must be bounded within a predefined time window and if this is not large enough, numerical artefacts may be introduced into the Fourier spectrum. In these simulations care was taken to ensure that the time window was large enough such that only a negligible amount of the pulse, if any, was present at the edge of the window.

It should be noted that the split step Fourier method is but one of a set of numerical methods that may be used to solve the NSE. Other solutions have been proposed that employ a finite difference methods that could also have been used to solve Equation 5.1 [215]. However the split step Fourier method was used in this pulse propagation algorithm as it is a long standing technique that is well understood and has previously been applied to a variety of optics problems of a similar nature [211].

5.3 Tellurite HWW for for multicasting

This section details the results of the PPM carried out on the tellurite HWW design introduced in Section 4.5.3. This fibre was designed to have a broad flat dispersion, to be able to multicast a high bandwidth signal by replicating it into multiple, lower bandwidth tributaries for parallel processing. The dispersion and nonlinearity for this fibre were first calculated using a FEM model of the fibre cross section (see Section 4.5.3 for details). These results, shown in Figure 5.3, are key inputs to the PPM program, along with the details of the input wave. The complete details and results of these simulations are discussed in the following section.

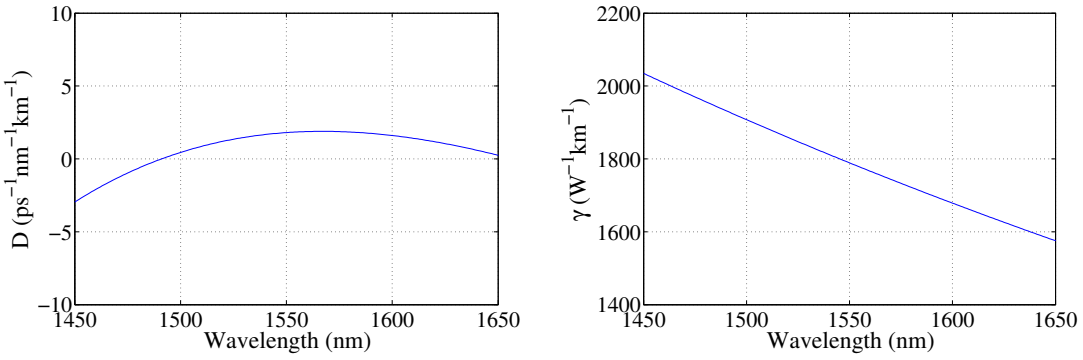

FIGURE 5.3: Dispersion and nonlinearity for the tellurite HWW design modelled for multicasting (see Figure 4.9 for the fibre geometry).

5.3.1 Simulation results

The pulse propagation was modelled with similar pump powers to those used in Reference [37], where two CW pumps with 1.2 W of power each were used to multicast a 40 Gb/s into 8 copies and this perform 320 Gb/s multicasting. To demonstrate the potential of this fibre for broadband multicasting, the pulse propagation model was run with a pair of slightly lower power CW pumps with 1W at 1535 nm and 1565 nm; and a low power input signal of 10 mW at the standard telecommunications wavelength of 1550 nm. The PPM was evaluated using a step size of 10 µm, with 2^{16} points used when calculating the FFTs.

The pump wavelengths were chosen such that there would be enough room in the spectrum around these pump wavelengths to fit high bandwidth input signals. These initial powers would be easily achievable with by using an EDFA as a preamplifying stage. The fibre loss in the simulation was set to 2 dB/m – this value was set based on the fact that unstructured fibres made with this TZNL glass have been measured with losses of 1 to 2 dB/m [9, 156].

The evolution of the spectrum is seen in Figure 5.4 which shows the spectrum at a few points down the fibre length – just after the start of the simulation (Figure 5.4(a)), after 10 cm of propagation (Figure 5.4(b)), after 25 cm of propagation (Figure 5.4(c)), and finally at 48 cm of propagation (Figure 5.4(d)). These plots show the evolution of the spectrum as the simulation progresses along the modelled fibre length. It shows that after just 48 cm of fibre the 16 required signal copies have been produced. The variation in peak power of the multicast signals, termed the noise ripple, is also reasonable at less than 5 dB across the spectrum. This noise ripple must be kept to a minimum so ensure that the signal to noise ratio is consistent across the multicast signals.

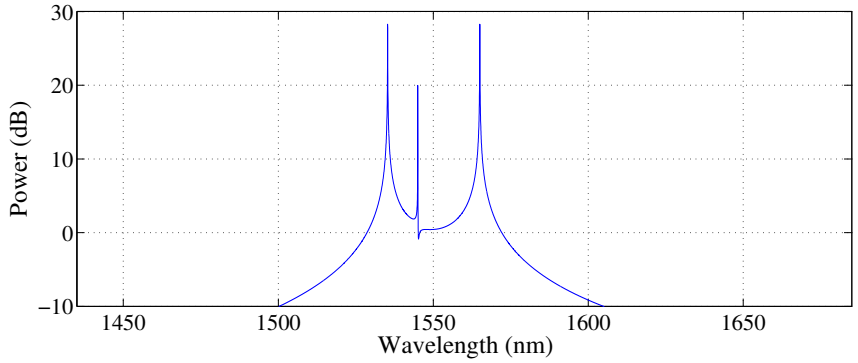

(a) Propagation length = 1 cm

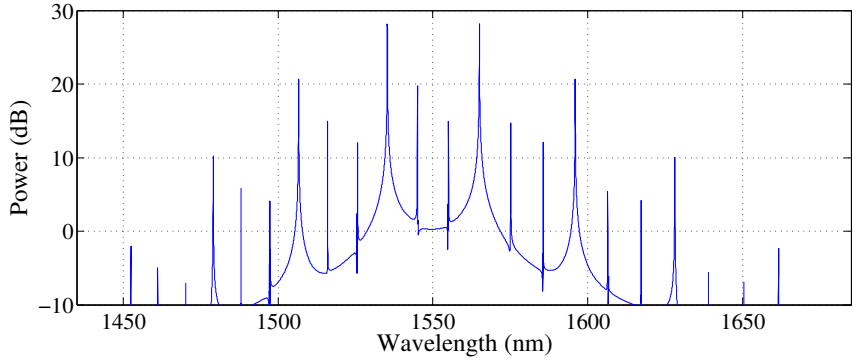

(b) Propagation length = 10 cm

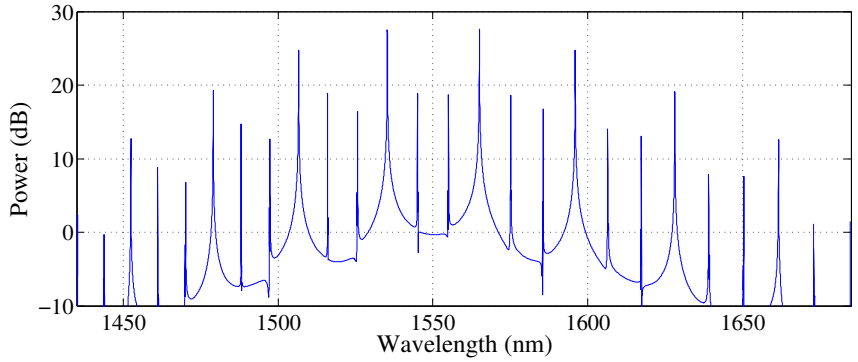

(c) Propagation length = 25 cm

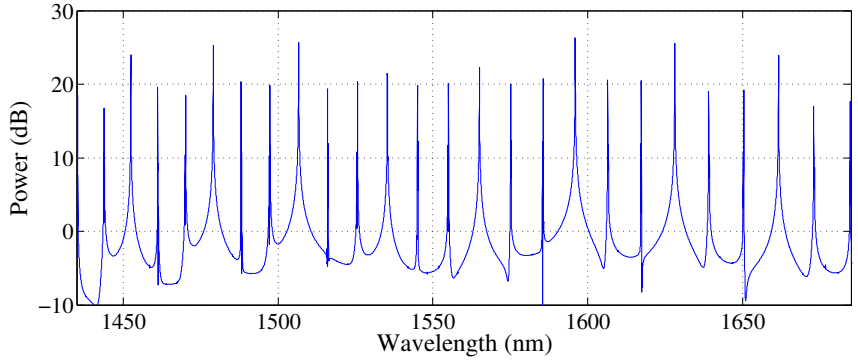

(d) Propagation length = 48 cm

FIGURE 5.4: Power spectrum at various fibre lengths in the propagation model. The cascaded FWM process has already started by 10 cm. At 48 cm, 16 signal copies have been generated with < 5 dB noise ripple.

5.3.2 Analysis of structural deviations

We have seen that the tellurite fibre design obtained via the genetic algorithm has very favourable dispersion and nonlinearity – allowing for the 1-to-16 multicasting required to process a 640 Gb/s signal in less than 0.5 m of fibre. However, with any microstructured design, some structural variation from the ideal geometry can be expected to occur during fabrication. This includes distortions to the shape of the holes (generally form circular to elliptical), partial closure of small holes relative to large ones and scaling of the geometry to be larger, or smaller than intended. With this HWW design in particular, the maintenance of the size of the inner holes, at 171 nm and 224 nm, presents a significant fabrication challenge (refer to Table 4.1 for the complete parameter set).

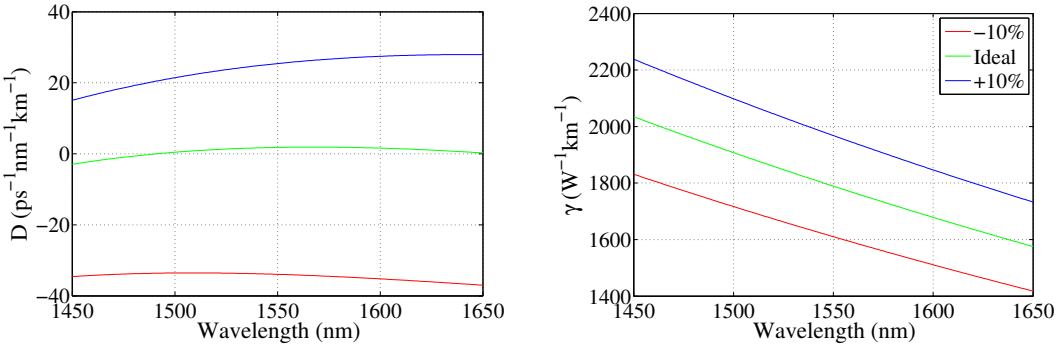

(a) Dispersion (b) Nonlinearity

FIGURE 5.5: The effect, on dispersion and nonlinearity, of scaling the fibre design.

Figure 5.5 shows the effect, on dispersion and nonlinearity, of uniformly scaling the ideal fibre design by +10% and −10% – a relatively simple distortion of the structure. These scale factors were chosen as fabrication of fibres similar to this design indicate that fabrication distortion does indeed lead to a final structure where the key structural parameters are scaled by approximately ±10%, relative to the ideal design [216].

We see quite a significant change in the dispersion where it has moved to become completely normal for the −10% case and completely anomalous for the +10% case. The dispersion value at 1550 nm changes from 1.8 ps^{-1}nm^{-1}km^{-1} to 25.4 ps^{-1}nm^{-1}km^{-1} for the +10% and −33.9 ps^{-1}nm^{-1}km^{-1} for the −10% case. It is worth noting however that the dispersion slope (evaluated from 1540 nm to 1560 nm) is still relatively flat, especially for the −10% case where it is −0.018 ps^{-1}nm^{-2}km^{-1} compared to the ideal case which is 0.010 ps^{-1}nm^{-2}km^{-1} (the dispersion slope for the +10% case is 0.059 ps^{-1}nm^{-2}km^{-1}).

Nevertheless, this change in dispersion is still large and suggests that the dispersion is very sensitive to fibre geometry.

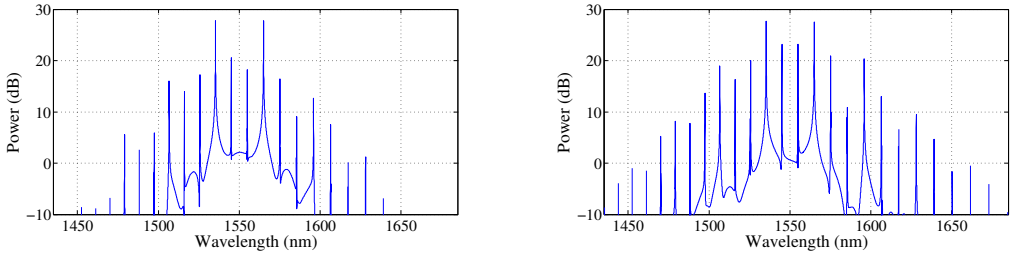

(a) −10% case (b) +10% case

FIGURE 5.6: Power spectrum at 48 cm for the non ideal fibre cases. This spectrum has much poorer signal equalisation compared to the spectrum for the ideal case at the same length [Figure 5.4(c)].

The pulse propagation results for these non ideal fibre scenarios are shown in Figure 5.6. The same input conditions were used as before and the simulation was run for the same fibre length (48 cm). However at the 48 cm mark for these simulations the amplitude of the FWM generated idlers is not even across the spectrum – the difference in power between the signal copies at the edge of the spectrum, compared with those at the centre of the spectrum is up to 20 dB. This level of noise ripple in the spectrum is too high for it to be usable for practical multicasting.

Some improvement to the noise ripple may be obtained by allowing more gain to accumulate over a fibre length longer than 48 cm. However, this improvement is slight and does not compensate for the change in the dispersion profile in the non ideal fibre geometries that results in the FWM gain (as defined by Equation 2.73) being narrower and not as flat as the ideal case. Consequently the gain for the signal copies at the edge of the spectrum is significantly lower than that for those at the centre, resulting in unequal pump powers.

5.3.3 Summary of Tellurite HWW modelling

The tellurite fibre design shows great potential for high bandwidth FWM based applications such as multicasting a 640 Gb/s signal. The dispersion is near zero at 1550 nm and flat over an extremely broad bandwidth of 200 nm. In addition to this the nonlinearity is also extremely high, with a nonlinearity of $\gamma = 1789$ $W^{-1}km^{-1}$ at 1550 nm.

However, the flat, broad dispersion curve of this fibre design is obtained by having two inner sets of inner holes in the suspended core region which provide fine dispersion control over a broad band. However, as these holes alternate in size and are significantly subwavelength with radii of 171 nm and 224 nm, the fabrication of such a structure is challenging. Furthermore, modelling of expected fabrication variances shows a large deviation from the ideal state for a relatively small $\pm 10\%$ scaling of fibre geometry. The change in dispersion is so high that the noise ripple of the multicast signals from the scaled geometries is over 20 dB and thus too large for practical use. Thus, for the next design of a HWW fibre, fabrication constraints such as equalising the size of the inner holes were included into the genetic algorithm.

5.4 Bismuth HWW for phase sensitive amplification

This section describes results of the pulse propagation model of the bismuth HWW fibre designed for phase sensitive amplification. The details of this design can be found in section Section 4.5.4. Compared to the tellurite HWW design, the spectral region for which low dispersion is required is narrower – due to the fact that the operating bandwidth for PSA is much lower than that for multicasting. This eases the design and fabrication requirements on the fibre as the dispersion control is applied over a narrower band.

As before, the dispersion and nonlinearity were evaluated using a FEM model of the fibre cross section (see Section 4.5.4 for details). This information, shown in Figure 5.7, was then used in the PPM. The details of this simulation, along with its results, are presented below.

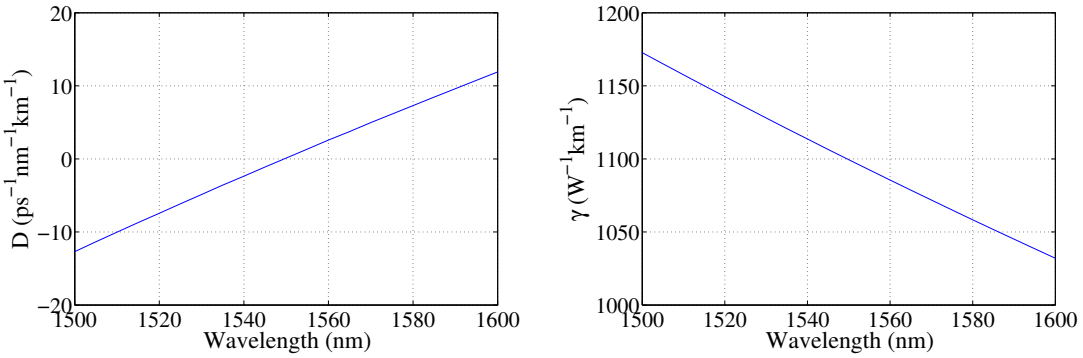

FIGURE 5.7: Dispersion and nonlinearity for bismuth HWW design modelled for PSA (see Figure 4.13 for the fibre geometry).

5.4.1 Simulation results

To test the fibre design from Section 4.5.4 the model needs to demonstrate a reduction in both amplitude and phase noise for a noisy input signal. As this fibre was designed to operate in next generation telecommunications devices, noise suppression must be shown at high bit rates, such as 640 Gb/s. As with the multicasting simulations, The PPM was evaluated using a step size of 10 µm, and 2^{16} points were used to calculate the FFTs.

To reduce the amplitude noise, the amplifier must operate in a regime where the signal gain is saturated [217], i.e. where the output power does not increase for further increases

in the input signal power. This gain saturation happens mainly due to depletion of the pump energy when the fibre is operating close to its maximum gain [217]. Once the gain is saturated, further amplification will serve to equalise the amplitudes of the pulse train by amplifying them all up to the saturation point. Thus by operating parametric amplifiers in the saturation regime, one may limit or squeeze the amplitude of a train of input pulses.

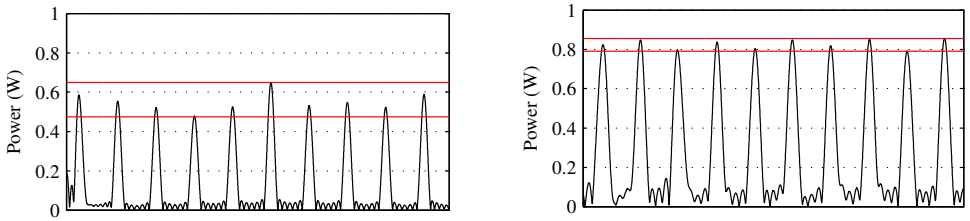

(a) Input signal (b) Output

FIGURE 5.8: Simultaneous reduction in amplitude noise ripple and amplification for a train of 640 Gb/s pulses. The red bars show the spread in amplitude noise.

The noise suppression effect of operating in the gain saturation regime was first studied in semiconductor optical amplifiers (SOAs) [218, 219] before being demonstrated in fibre parametric optical amplifiers (FOPAs) [220]. Since four wave mixing based amplification also preserves phase, gain saturation is particularly useful for performance improvement of DPSK signals [221, 222] as it counteracts the phase-to-amplitude noise conversion aspect of the transfer function.

The effect of saturation is seen in Figure 5.8 which shows good power equalisation of the output pulses. For the input, a train of 640 Gb/s pulses was defined with equal pulse widths and pulse separation of 78.1 ps. The simulated pump power and fibre length were 0.8 W (in each pump) and 53 cm, respectively. The fibre loss was set to be 2 dB/m.

The effect of saturation on amplitude suppression may be quantified by defining a ripple factor in the amplitude noise as $P_r = \Delta P / P_{RMS}$, where ΔP is the difference in power between the lowest and highest signals and P_{RMS} is the root mean square power. We then see that the amplitude noise ripple is reduced by 7.9 dB while the RMS power is amplified by 2.6 dB.

The four wave mixing scheme to achieve phase squeezing considered in this work is similar to that in Reference [93], where the signal and idler are degenerate at 1550 nm and the two pumps are placed symmetrically apart (in frequency). In this FWM scheme

the pump wavelengths were set to $\lambda_{P1} = 1521.1$ nm and $\lambda_{P2} = 1580.0$ nm. Having such a large pump to pump separation minimises unwanted interference between the two pumps and allows for high bandwidth signals. The fibre loss was again set to be 2 dB/m. The model was then run on a train of noisy 640 Gb/s DPSK type input pulses which were defined, as earlier, to have equal width and separation of 78.1 ps. Noise was introduced into both the phase and the amplitude through a random number generator such that it would produce a broad scatter of points (when plotted on a polar plot, as in Figure 5.9) similar to those obtained after transmission of DPSK pulses in a real system.

The results, seen in Figure 5.9, show the phase noise being progressively squeezed as the pulses propagate along the modelled fibre. Maximum squeezing was found to occur at a length of 53 cm – after this point the fibre loss starts to dominate and the signal amplitude degrades. At this point however significant squeezing of the phase noise has been achieved. Phase noise of approximately 90° has been reduced to just over 20° with a small amplitude gain of 0.7 dB and without a significant penalty in amplitude noise, which rises by 0.5 dB from a noise ripple of 1.6 dB in the input signal to 2.1 dB in the phase squeezed output.

This level of squeezing is comparable to what has currently been achieved experimentally at bit rates of 40 Gb/s, but is demonstrated here for an ultrafast, broadband input signal at 640 Gb/s. Note that the rotation in absolute phase of the signals due to the build up of linear phase as the pulses propagate down the fibre is not important for differentially encoded formats like DPSK. In any case, the absolute phase can be rotated by changing the pump phases appropriately.

5.4.2 Analysis of structural deviations

By designing a MOF to have high gain within a relatively short length it can tolerate both the effect of variations in the zero dispersion wavelength due to structural fluctuations along the fibre length and the inevitable deviations from the ideal structure that happen during fabrication.

Figure 5.10 shows the variations in fibre dispersion and nonlinearity for deviations from the ideal structure. These structures have been numerically altered from the ideal case

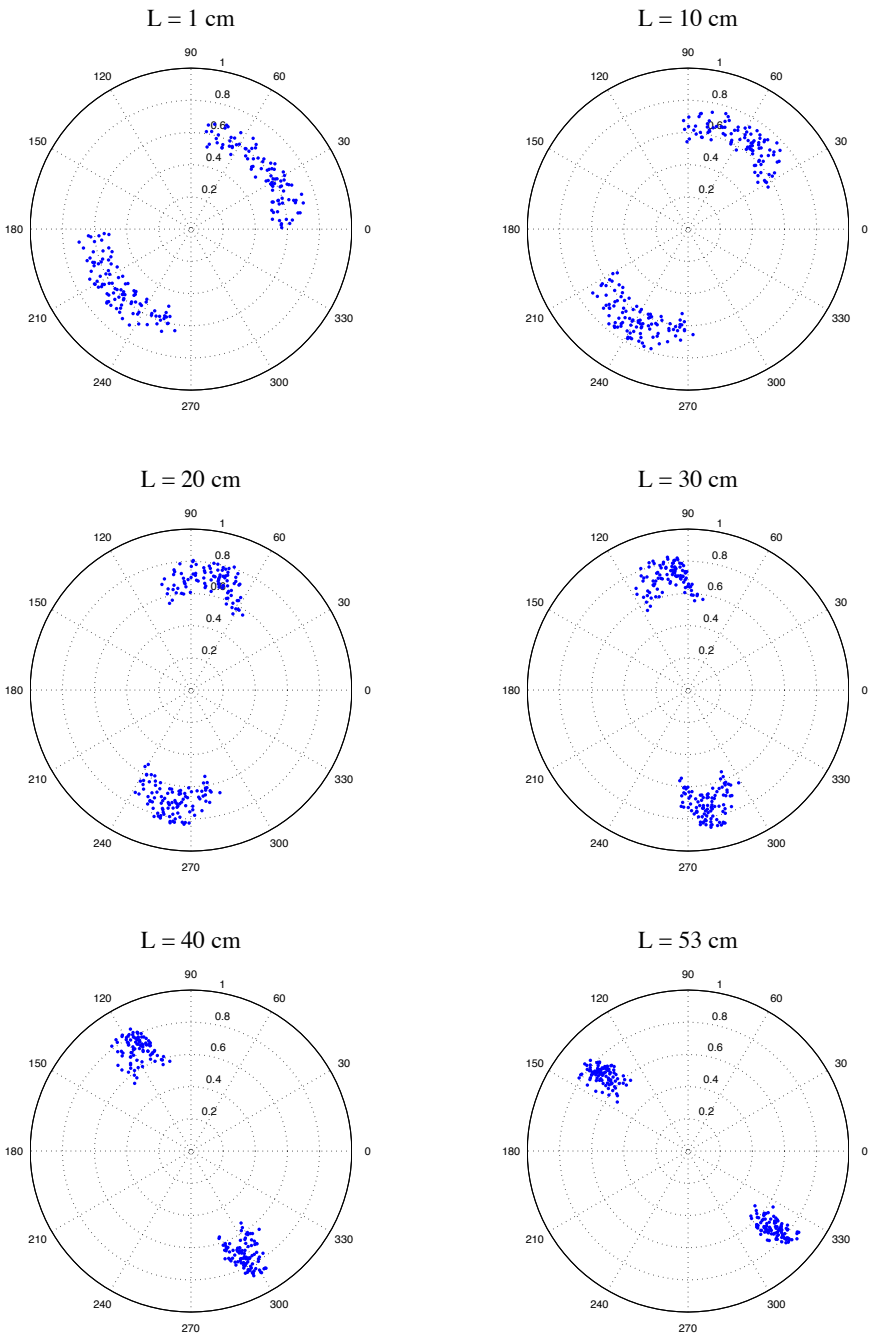

FIGURE 5.9: Squeezing performance for 640 Gb/s pulses at different propagation distances – from near the start of the model (fibre length $L = 1$ cm, top left), in steps of 10 cm to the end of the model ($L = 53$ cm, bottom right). The initial signal had approximately 90° of noise, which is squeezed to less than 20° after 53 cm of propagation. The input signal for this simulation was set to 0.35 W, while each pump was set to 0.8 W.

by uniformly stretching/contracting the fibre parameters by -10%, $+10\%$ and $+20\%$, relative to the ideal case (the ideal structure has also been included for comparison).

The most significant change is seen in the -10% case where the zero dispersion wavelength

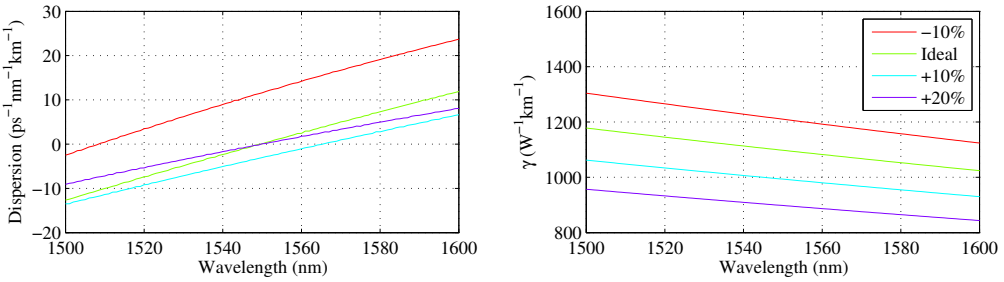

(a) Dispersion (b) Nonlinearity

FIGURE 5.10: The effect, on dispersion and nonlinearity, of scaling the fibre design.

moves to a much shorter wavelength, relative to the ideal case. For the other cases, the fluctuation in the dispersion is not as pronounced. The change in the nonlinearity is as expected – as the structure gets smaller γ increases due to the mode being more confined; whereas an increase in size leads to less confinement and a lower γ.

As dispersion and nonlinearity curves, by themselves, do not represent PSA the phase responses for these structures is also shown in Figure 5.11. The phase response here is defined as the gain of the input signal as a function of its initial phase. As is typical for phase sensitive amplification, the phase responses show the gain periodically oscillating with phase where the input signal phases for which the gain is highest are separated from those for which the gain is lowest by $\pi/2$. Ideally, one would want this gain discrimination to be as large as possible as it determines how 'tightly' the phase noise is squeezed.

We see that as the performance of the fibre design suffers considerably for a change in the structure of -10%. However, the results also show that the fibre performance in the 100% to 120% range is quite similar. In some instances, such as for the $+10\%$ case (shown in the bottom left of Figure 5.11), the squeezing is slightly improved when compared to the ideal case (shown in the top right of Figure 5.11), albeit with less amplitude gain. Given this trade off, the ideal design is still the best case. However the similar performance shown in plots (b), (c) and (d) of Figure 5.11 indicate that the high nonlinearity of this fibre allows us to tolerate fluctuations in the dispersion at the signal wavelength quite well, provided that D remains sufficiently small and normal.

This indicates that good fabrication tolerance may be achieved by aiming for a structure that is slightly larger than the optimal design. Note that, for comparison, these simulations were all done with the same values of pump and signal power and phase. By

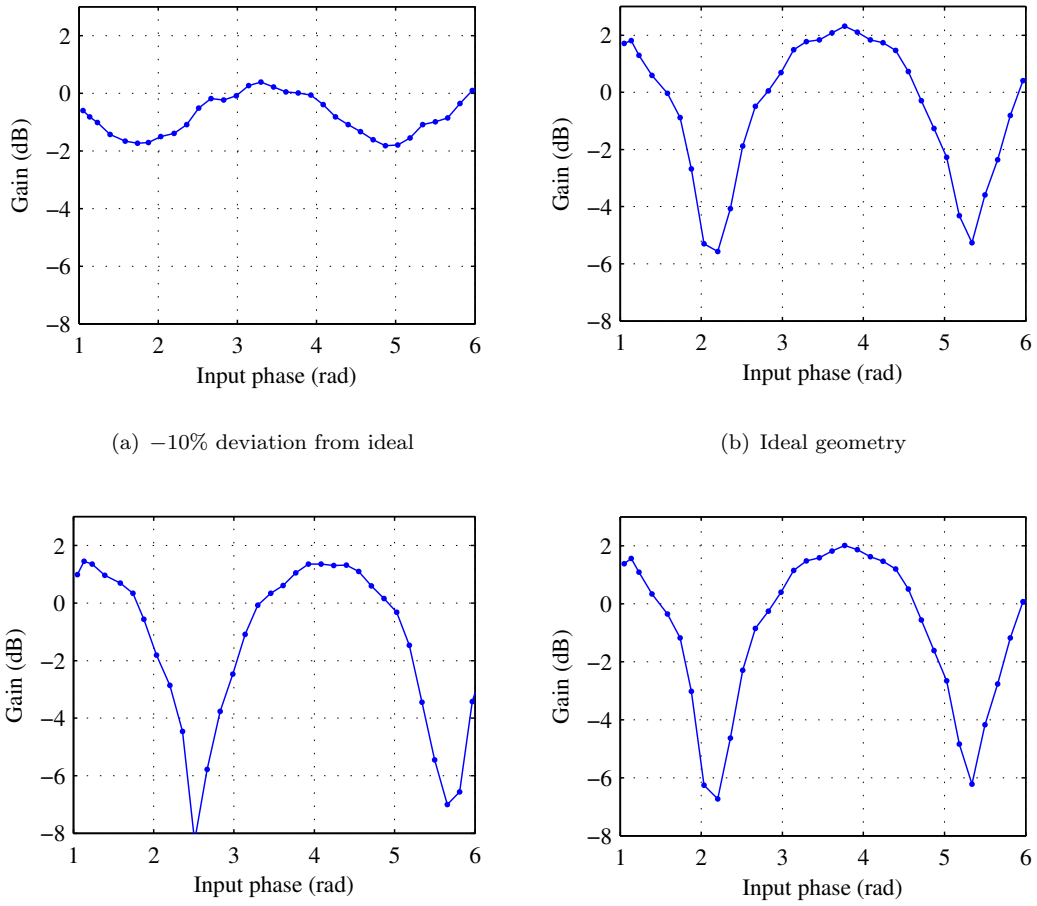

(a) −10% deviation from ideal

(b) Ideal geometry

(c) +10% deviation from ideal

(d) +20% deviation from ideal

FIGURE 5.11: Phase response for deviations from the ideal fibre structure: −10% deviation from ideal structure (top left), ideal structure (top right), +10% deviation from ideal structure (bottom left), +20% deviation from ideal structure (bottom right)

optimising these parameters one may improve the performance of a non ideal structure even further, to bring it closer to the response of the ideal fibre.

5.4.3 Summary of Bismuth HWW modelling

The modelling analysis of the bismuth HWW fibre indicates that it could be used to perform broadband phase sensitive amplification for high speed telecommunication networks, operating at speeds up to 640 Gb/s. The fibre design has a high gain and short operating length. Analysis of performance when subjected to geometric variations that are expected during fabrication show that changes in the dispersion profile can be compensated for by the high nonlinearity.

It is worth highlighting the fact that the fibre length used in these simulations is only 53 cm – two orders of magnitude lower than the lengths generally used in silica HNLF based PSA devices. This is useful for building compact devices with low latency. Such a fibre may also be used to simultaneously perform phase and amplitude amplification without the need to suppress the Stimulated Brillouin Scattering, since the Brillouin coefficient for Bismuth oxide based nonlinear fibres has been shown to be an order of magnitude less than a silica based HNLF [223].

5.5 Conclusion

Modelling of the genetic algorithm optimised HWW fibres first shown in Chapter 4 shows that these fibres may indeed be used to form the basis of a high bandwidth all optical device. The fibre designs were modelled using input powers similar to those used in the literature to perform low bandwidth operation in silica fibres. However, in both cases, they were able to demonstrate much higher bandwidth operation, over much shorter lengths.

With the tellurite HWW design, the 1-to-16 multicasting required to process a 640 Gb/s signal was shown to be possible with just under 0.5 m of fibre. However this structure was also shown to be very sensitive to deviations from the ideal parameter set. Consequently, it would be difficult to reliably fabricate a multicasting device using this fibre design.

The modelling results for the bismuth HWW design were more promising. The fabrication constraints applied to the genetic algorithm optimisation procedure in the design stag resulted in a fibre that is more tolerant of fabrication deviances. The results from Section 5.4.2 show that a certain amount of dispersion variability may be sufficiently compensated for by the high fibre nonlinearity. Consequently this fibre design is the more practical of the two, albeit with less favourable dispersion and nonlinearity.

The results from the attempted fabrication of these fibre designs is discussed in Chapter 6 that follows.

Chapter 6

Fibre fabrication

6.1 Introduction

This chapter describes the soft glass fibre fabrication work that was done as part of this research. The bulk of the work presented in this chapter revolves around the fabrication of the hexagonal wagon wheel fibres designed and modelled in the preceding chapters (Chapter 4 for design and Chapter 5 for modelling). Preliminary work done on the fabrication of some other all solid composite fibres made from tellurite and chalcogenide is also presented.

As the results presented throughout this chapter have been obtained via the extrusion technique, some background on this fabrication technique is first given in Section 6.2. Section 6.4 onwards covers fabrication trials of the HWW fibre. Ultimately, the required fibre structure was not achieved but significant progress was made, especially towards the simplified germanate HWW structure presented in Section 4.7. This work on the germanate glass fibre is discussed in Sections 6.5 and 6.6.

While the final fibre structure falls short of the required parameters in the design, the novel nature of the glass involved meant that there were many useful outcomes from this research. These learnings are summarised in the concluding remarks in Section 6.7

6.2 Background

The fibre fabrication process begins with a billet of glass, made by combining a set of raw ingredients in a glass melting oven as described in Chapter 3. Turning this glass billet into a microstructured fibre is a complex process with many intermediate steps. The two methods most commonly used for this process are the 'stack and draw' technique [16, 188] and the extrusion technique [2]. Another method that is sometimes used is the casting method – this is somewhat less flexible than either stack and draw or extrusion (in terms of the structures it can produce), however it has been used to fabricate microstructured chalcogenide fibres through the use of a structured mould [224].

The casting technique is applied to the glass while it is still in a liquid state. The molten glass is cast into a mould and then allowed to cool. Once cool, the mould is removed, leaving the glass behind. If the mould is structured then this structure will be imprinted onto the glass – this is the technique used in Reference [224] to fabricate microstructured chalcogenide fibre, where the cast was dissolved away to leave a structured glass billet which could be drawn into fibre. A variation of the casting technique, rotational casting, can also be used in the fabrication of concentric glass structures. When fabricating fibres using this method the cladding glass is first poured into a preheated mould which is then rapidly swung into a horizontal position and then rotated at high speed (typically ≥ 3000 revs/min) until the glass has cooled [225, 226]. The core glass is then cast into the centre of this tube to create the preform.

The stack and draw technique consists of first drawing a glass tube into a number of capillaries. These capillaries are then stacked together in a jacket tube, around a central glass rod (that corresponds to the core region in the final fibre), with the geometry of the stack determining the final fibre structure. This technique is extremely useful when fabricating MOFs such as those with a hexagonal array of holes (see Section 4.4.1.2) however it is limited by the fact the final fibre structure must match that of the assembled capillary stack. Thus for the complex HWW fibres designed here, where the geometry consists of noncircular hole arrangements, the stack and draw technique cannot be used.

The extrusion technique on the other hand is more flexible as the preform is obtained by extruding the billet through a metal die. The preform structure is then only limited

by what can be machined into the metal of the die. This enables an range of complex geometries to be fabricated in the final fibre, as shown in Figure 6.1.

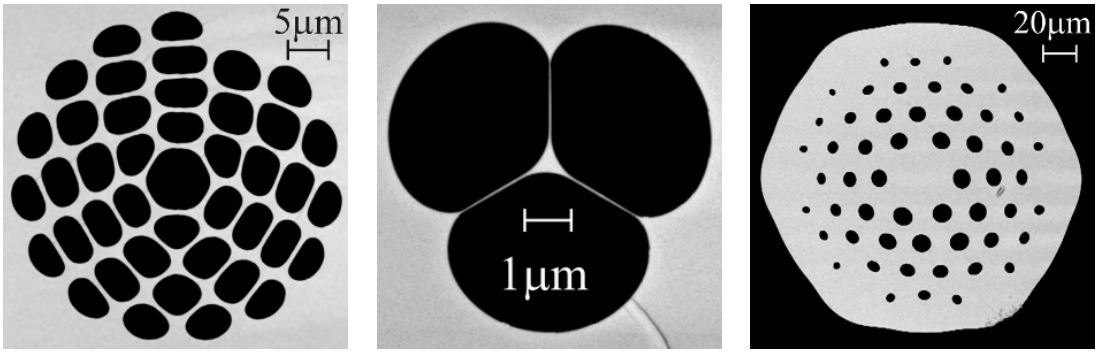

(a)) (b) (c)

FIGURE 6.1: Examples of various microstructured fibre geometries fabricated at the Institute for Photonics and Advanced Sensing, University of Adelaide. The fibre in (a) is a photonic band gap fibre; (b) is a suspended core fibre (alternatively known as a 'wagon wheel' fibre); (c) is a large mode area fibre.

Before the start of any extrusion, there is a certain amount of preparation that must be done to ensure optimal results. The first step in this is careful polishing of the glass billet to ensure that it is smooth on all sides. This is done through the use of a slowly rotating lapping plate and polishing pads. The billet is first roughly polished with an abrasive paper to ensure that the surfaces are level, and that the billet proportions (such as diameter) are as required. The process then moves through finer grades of abrasion, eventually finishing with a soft pad and a slurry of 1 µm grade particles that results in an extremely fine, optical grade finish.

Once the billet has been polished to a suitable quality it is thoroughly cleaned, along with the die, to ensure that all surfaces are free of any dust or grease. This cleaning process includes washing the items with water, detergent[1] and alcohol and placing it in an ultrasonic bath for around 20 minutes to ensure that any fine particles are dislodged.

The polishing and cleaning process is important for several reasons: it prevents foreign particles from contaminating the final preform and fibre and thus increasing the optical loss; a smooth glass surface against the metal during extrusion minimises the chances of air being trapped in between the scratches in the glass and the metal and thus being drawn out into air bubbles in the preform; excessive roughness, or even deep scratches

[1]If the glass composition is such that it will react with the detergent, this step is omitted and the glass is cleaned with just water and alcohol.

in the billet, can also lead to poor internal surfaces in the preform and fibre which contribute to the loss.

Once the glass and die have been adequately prepared the extrusion is ready to begin. The first step in this process is to heat the bulk glass billet up to a point where it softens. Once the glass is at the required temperature, a controlled ram is used to force it through the die. This results in an extruded preform whose transverse profile reflects the inverse of the die structure. Therefore, complex geometry can be introduced into the glass by appropriately designing and fabricating the die structure.

The success of the extrusion depends on the management of two key parameters: the extrusion temperature and ram speed. The extrusion temperature determines how soft the glass will be as it is pushed through the die, i.e. it determines the glass viscosity. Differences of a few degrees are sufficient to produce significantly different extrusion results so precise control of this temperature is crucial to the success of the extrusion. The ram speed is also important as it determines how quickly the glass will flow through the die, and consequently, the pressure applied (on both the glass and the die) and the amount of time the glass will spend absorbing heat as it passes through the hot zone.

The correct values for extrusion temperature and ram speed vary significantly depending on both the glass used and the design of the die. Incorrectly specifying these values by, for instance, setting the ram speed too high or the temperature too low can cause an extremely high pressure within the die enclosure that can lead to catastrophic results, such as the breaking of the die. The extrusion may also fail if the glass is not sufficiently fused coming out of the die exit due to either passing through the die too quickly or by not being hot enough; or if the preform is tapered due to the glass moving too slowly and thus remaining too hot for too long – both cases being a consequence of incorrectly set values for extrusion temperature and ram speed. However, knowing which values to set these parameters at is nontrivial as it requires prerequisite knowledge of glass properties (such as transition temperature and viscosity) and some prior experience with the specific glass and die design. It is therefore not uncommon, when extruding a new glass and die combination, to require a number of trials to obtain the best extrusion parameters.

In our extrusion setup the glass and die is placed into a stainless steel body, which is then inserted into a furnace. The ram sits above the furnace and is set to push on the top

of the billet via a circular plate placed just above the glass. This plate simultaneously protects the glass from the rough surface of the piston and allows the piston to be recovered from the body post extrusion (by preventing it from adhering to the softened glass during the extrusion). Once the apparatus has been heated up to the appropriate temperature (a process that takes a few hours, with the exact time depending on the glass), the temperature is fixed for the rest of the extrusion and the ram speed is set to a constant value to start the extrusion. An electronic feedback loop is used to adjust both the temperature of the furnace and the force of the ram accordingly. This is shown schematically in Figure 6.2

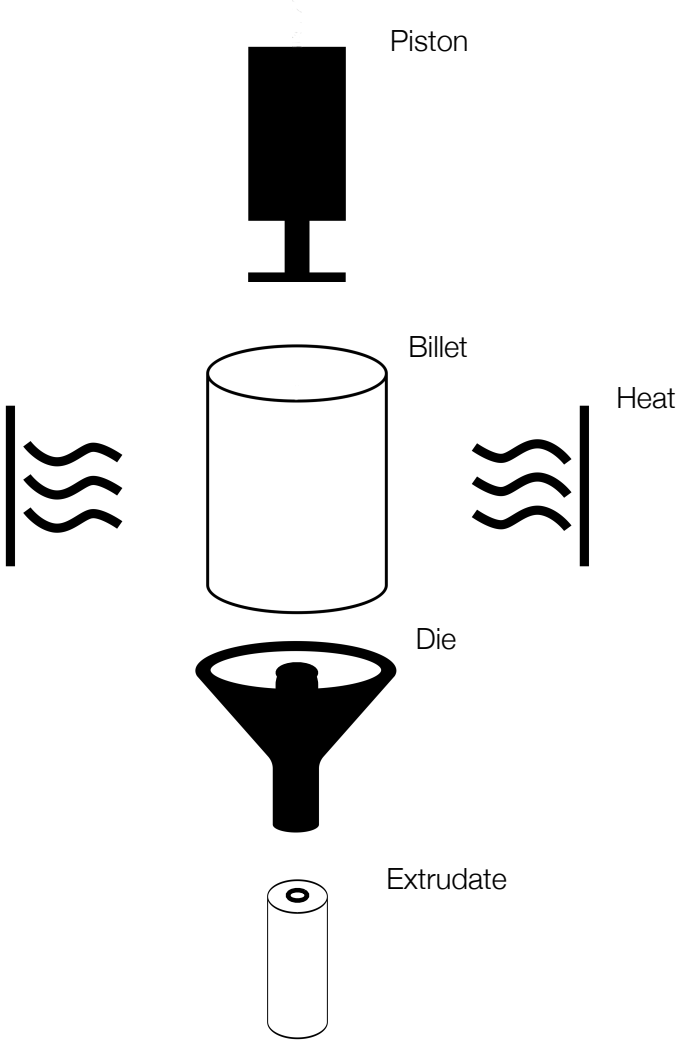

FIGURE 6.2: A schematic of the extrusion process. The billet is placed in a metal body within a chamber (not pictured) where it is heated to a point where the glass softens. Pressure is then applied via a piston acting on the top of the glass to force the glass through a die. The result is an extrudate which has the inverse shape of the die – for example, as pictured here, if the glass is extruded through a die with a single central pin the extrudate will take the shape of a tube.

The resulting preform is then drawn down into a cane – usually a millimetre or so in diameter. This is done by vertically mounting the preform at one end and applying heat just above the other end until that section begins to soften, taper and draw down under its own weight – an event referred to as 'the drop', represented schematically in Figure 6.3. Once the glass has dropped down to an appropriate level, the glass bulb is cleaved off the end and a tractor wheel is then lightly applied to the remaining cane. This is shown schematically in Figure 6.4. This allows the operator to keep pulling the cane out of the preform and control the draw speed. Control of the draw speed is important, as the draw speed is inversely proportional to the square of the cane diameter – the diameter of the cane is thus controlled via the draw speed. As the cane is drawn, sections are cut off every 20 to 30 cm or so to allow room under the tower for more cane to be drawn.

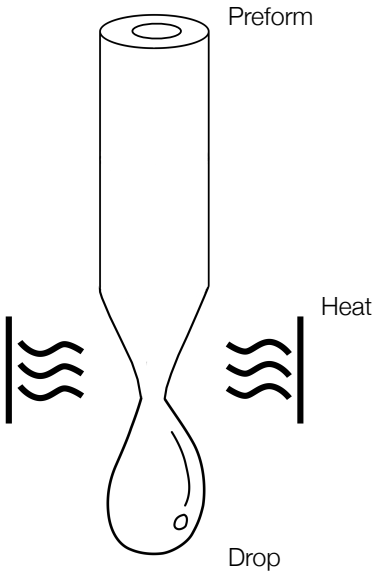

FIGURE 6.3: To start the fibre draw or caning process, heat is applied to the bottom of the preform such that a section starts to soften. The weight of the glass beneath the softened section then starts to pull the glass through under gravity forming what is known as the drop. The drop is allowed to continue under its own weight until a suitably long section has been drawn out. If a cane is to be drawn this section is then softly clamped between rollers to continue drawing out the glass (see Figure 6.4), otherwise the end is fixed to a rolling fibre drum which pulls the glass through.

Once the cane has been obtained it is inserted into an glass tube known as a 'jacket'. The jacket is obtained by extruding another glass billet through a simple die to form a tube. Once the cane is integrated into the jacket, this essentially results in a second preform

with much smaller hole sizes than the first. This is important for small, subwavelength features (such as the inner holes in the HWW fibres) as it allows us to get the correct dimensions in the fibre. Drawing down to a fibre with subwavelength holes in a single step is not possible as it would require the outer diameter of the fibre to be much smaller than the minimum it needs to be to have enough mechanical strength to be spooled onto a drum without breaking – this outer diameter minimum is generally approximately 100 µm (the exact value depends on the fragility of the glass used) [1].

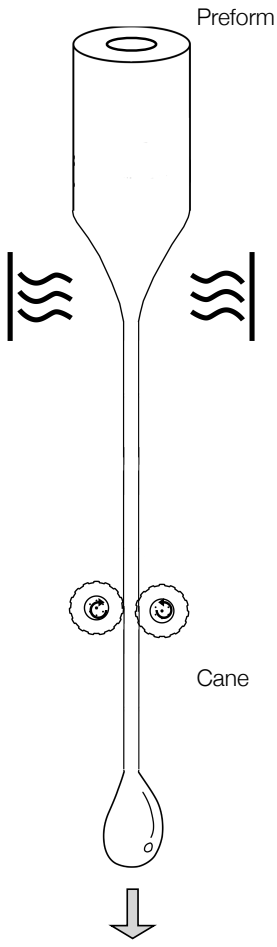

FIGURE 6.4: Once the drop has formed and drawn down some cane, tractor wheels are applied to the side to enable more cane to be drawn. Sections of cane are cleaved off below the rolling wheels once they are long enough and the process continues until all the glass from the preform has been drawn out. The fibre drawing process is very similar to this schematic where instead of pulling the glass via the rollers the (much narrower) fibre end is attached to a rolling drum that pulls the glass through as it rotates.

The process of inserting the cane into the jacket to form a glass assembly for fibre drawing is usually referred to as the rod–in–tube technique.

The jacketed cane is then drawn down to fibre, in a fashion very similar to that used for drawing the cane. The main difference in the fibre draw is that the traction wheels are no longer present and the material is pulled instead by a rotating drum. As the drop happens the descending end is clamped on this drum, which is located at the bottom of the draw tower. The drum is then set to rotate at a controllable rate, specified by the operator. As the drum rotates, material is continually drawn from the preform into a fibre whose diameter may be anywhere from 100 µm to 300 µm. During the draw this fibre diameter is controlled by the rotating speed of the drum – the faster it rotates the quicker the glass will be drawn out of the preform and the narrower the fibre will be; and vice versa. The diameter of the fibre is also measured by the tower as it is being drawn, which allows the drum speed to be adjusted dynamically to achieve the desired fibre diameter.

During both the caning and fibre drawing stages the amount of hole inflation is regulated by the pressure of the gas within. Control of this pressure is achieved through one of two methods: self pressurisation or active pressurisation. Self pressurisation is when the pressure within the holes builds up naturally due to the restriction of glass flow out of the preform caused by the tapering of the glass as it is pulled through the draw. This is quite a complex process that is generally difficult to describe theoretically. Previous work has shown that an analytical theory may be used for the simple case of a capillary [227], however this model may not readily be extended to the drawing of microstructured fibres, where the geometry is complex. In the past, self pressurisation has been the preferred way to draw microstructured fibres, largely due to the difficulty of actively controlling the pressure of the gas during the draw. Improvements in fibre drawing technology have now made it easier to control pressure during the draw and thus draw fibres under active pressurisation.

Active pressurisation, as the name suggests, involves actively increasing the gas pressure within the holes of the preform or cane. This is done by attaching the exposed top end of the preform, via a seal, to a controlled source which can be used to pump gas in with variable pressure. This method allows additional control of the fibre process but it introduces challenges due to its inherent sensitivity. With self pressurisation, for instance, it is not possible to lose control of the fibre draw to the extent that the final fibre is over inflated however this can easily happen when using active pressurisation. These issues are discussed in further detail in Section 6.6.

The fibre draw operator must control all the following variables to obtain the desired structure in the final fibre: the draw temperature, the pressure of the gas in the holes of the preform, the rate at which the preform is fed into the hot zone (see Figure 6.3) and the speed at which the cane or fibre is drawn. As the process is inherently sensitive to small fluctuations in any of these parameters, fibre drawing requires a considerable amount of expertise. Consequently the fibre draws were always done with a dedicated technician operating the draw tower. I was on hand at all times to assist as required and do spot analyses of the drawn fibre as it emerged to ensure that it had the required structure.

6.3 Preliminary work – composite fibre fabrication

This section documents some preliminary fabrication work on composite fibres done as part of this research. This preliminary work explored the use of two highly nonlinear glasses, namely chalcogenide and tellurite, in a composite, all solid fibre design.

As discussed in Section 4.4.2, the all solid design (where different glasses are used in the core and the cladding) may be used to engineer the zero dispersion wavelength of the fibre via the core radius and cladding composition. Using such a geometry with an extremely nonlinear glass such as chalcogenide for the core can thus be used to fabricate a highly nonlinear fibre with zero dispersion at 1.55 µm.

6.3.1 Background and motivation

The extreme nonlinearity of chalcogenide glasses (as discussed in Section 3.4.1) makes them a favourable choice for nonlinearity based applications. For this preliminary work the commercially available IG5 chalcogenide glass was used. The composition for this IG5 glass (sometimes also refereed to as AMTIR-3) is 28·Ge — 12·Sb — 60·Se [228] and it has a high nonlinear refractive index of 400×10^{-19} m^2W^{-1} [29].

While this glass has favourable nonlinear properties at 1.55 µm, its material dispersion is strongly normal in this wavelength region. The approach considered to counter this material dispersion was to introduce a tellurite cladding around the chalcogenide and consequently introduce a waveguide dispersion to match the material dispersion of the

IG5. Figure 6.5 shows how using a tellurite cladding and setting the core diameter appropriately can be used to create a composite fibre with zero dispersion at 1.55 µm.

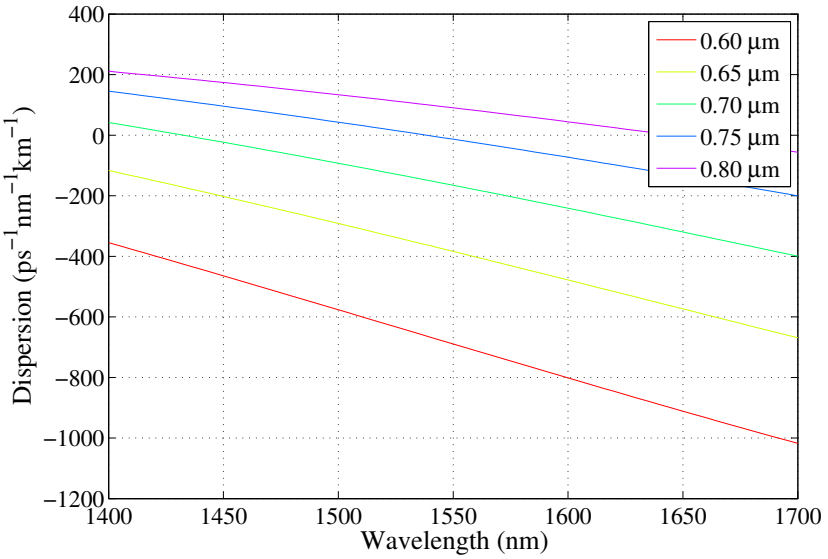

FIGURE 6.5: Dispersion variation of chalcogenide and tellurite composite fibre with core diameter. The graph shows that a ZDW of 1550 nm can be obtained for a core diameter around 0.75 µm.

6.3.2 Results and discussion

This initial choice was to fabricate this fibre via the rod–in–tube method. The chalcogenide glass was first extruded into a rod and then combined it with a tube created of tellurite. The combination of the two results in a rod–in–tube assembly that can then be drawn down into fibre.

The chalcogenide rod was created by extruding a cylindrical IG5 billet with a 30 mm outer diameter through a die with a 1 mm circular aperture. This resulted in a long, slightly tapered rod with an outer diameter ranging from 1.05 mm to 1.12 mm. This long rod was then cleaved into smaller lengths, as shown in Figure 6.6.

The increase in outer diameter of the rod relative to the die exit is due to die swell – a phenomenon where friction between the die exit and the glass results in distorting swell of the glass as it leaves the die [229, 230]

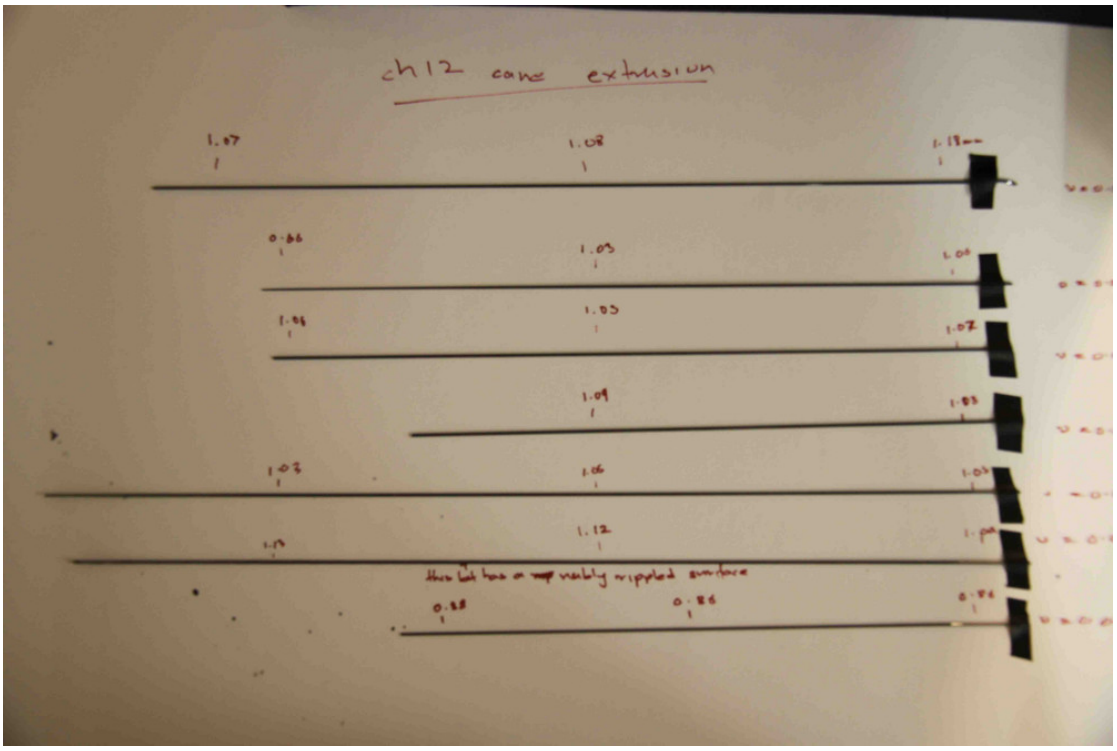

FIGURE 6.6: Chalcogenide rods obtained after extruding the glass through a 1 mm rod die.

The tellurite tube was created by extruding a large TZNL[2] billet with a 50 mm outer diameter through a tube die with a 1.5 mm internal diameter and a 10 mm outer diameter. Tapering of the tube (under its own weight) resulted in a final glass tube with an outer diameter ranging from 8.5 cm to 9.3 cm and an inner diameter ranging from 1.05 mm to 1.31 mm. The internal diameter of the tube was calculated from a high resolution photograph of the tube cross section, which was scaled by the measured outer diameter. The scale factor is determined by measuring the number of pixels in the photograph that correspond to the known outer diameter of the tube.

After fabrication, both the rod and the tube were annealed and then cleaned. The cleaning procedure consisted of first immersing the glass in isopropanol and then placing the immersed glass in an ultrasonic bath for 15 minutes. The glass was then flushed once more with the isopropanol before placing the rod in the tube to form a rod–in–tube assembly for fibre drawing.

The assembly was then drawn under a vacuum seal to produce a fibre with an outer diameter of approximately 160 µm. As this was only a preliminary draw this diameter

[2]Recall that this is a Na-Zn-L tellurite glass with composition $73{\cdot}TeO_2$ — $20{\cdot}ZnO$ — $5{\cdot}Na_2O$ — $2{\cdot}La_2O_3$, introduced in Chapter 3

was chosen purely to obtain a stable draw, as opposed to targeting a specific value for dispersion engineering.

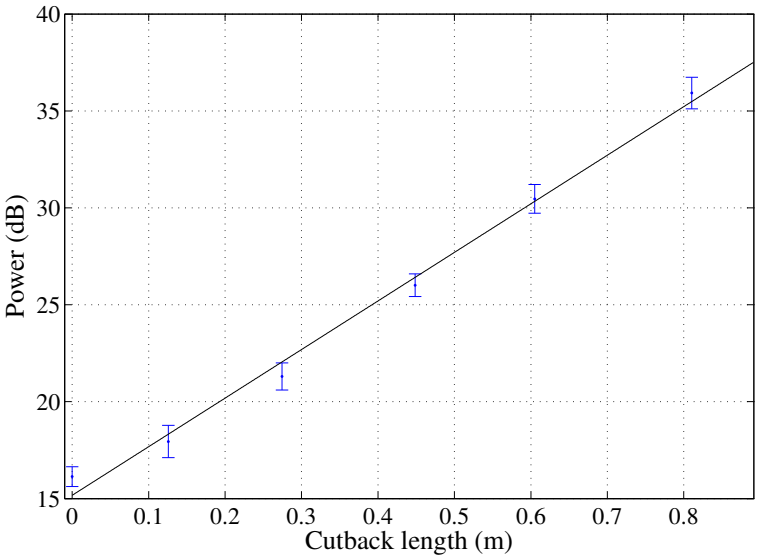

FIGURE 6.7: The measured loss for the chalcogenide–tellurite composite fibre fabricated via the rod–in–tube technique. The loss for this fibre was measured to be 25.1 ± 1.0 dB/m for a core diameter of 9.1 ± 0.4 µm at 1.55 µm.

Once the fibre was fabricated, its loss was measured using the standard cutback technique, where the loss per unit length is calculated by measuring the power over a series of cutbacks from an initial length (this technique is described in more detail in Chapter 7). The results, seen in Figure 6.7, show that this fibre had a high loss of 25.1 ± 1.0 dB/m at 1.55 µm. While this loss value is high, it should be noted that, based on the transmission data and refractive index given in the product data sheet for this glass [228], the bulk loss at 3 µm is approximately 20 dB/m and can be expected to be higher at 1.55 µm[3]. This suggests that the material loss for this glass at near to mid-IR wavelengths, including 1.55 µm, is already quite high. However, the actual bulk transmission for this glass at 1.55 µm was unable to be measured due to the lack of a suitable spectrometer at the time.

The core diameter of the fibre section used in the cutback measurement was also measured, by placing sections from the cleaved fibre ends under a calibrated optical microscope to measure the diameter of the core region. The average core diameter from

[3]This assumption is based on the fact that the bulk loss for another commercially available glasses with a very similar composition, AMTIR-1, is higher at at 1.55 µm than 3 µm [231]

this measurements was calculated to be 9.1 ± 0.4 µm, which corresponds to a large mode area.

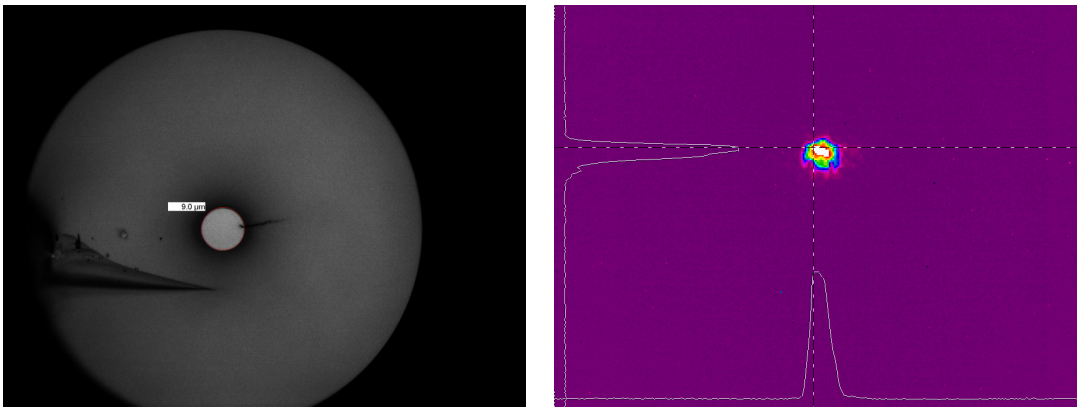

(a) Optical microscope image (b) IR camera view of core guidance

FIGURE 6.8: The core diameter of the composite fibre was measured using an image such as (a) from a calibrated optical microscope. The guidance in the core was confirmed by imaging the output face of the fibre onto an IR camera to produce an image such as that in (b).

Closer inspection of the fibre cross section under a scanning electron microscope revealed another possible reason for the high measured loss: a poor quality interface between the core and cladding glasses. The SEM images from a some of fibre cross sections, seen in Figure 6.9, show a number of voids at the interface of the core and the cladding. These images are representative of the rest of the analysed cross sectional samples, all of which show the same features. These bubble shaped voids would cause high scattering losses at the interface between the core and the cladding, adding to the total fibre loss.

These voids were most likely caused by grooves or scratches on either the outer surface of the rod or the inner surface of the tube. Scratches may be introduced into the surface during the extrusion stage via imperfections on the die surfaces. However, this is unlikely due to the high level of care and cleaning done on the surfaces in preparation for extrusion. The more likely scenario is these scratches occur during the assembly of the rod–in–tube preform. Although care is taken during this stage it is inevitable that there will be some level of abrasion between surfaces which could lead to scratches that then manifest as voids in the final fibre. When fabricating microstructured fibres via extrusion this is not generally an issue as the core region is physically separated from the edge of the cane, however for MOFs fabricated via stack and draw and especially for an all solid, step index type geometry the quality of the interface is crucial to maintaining good guidance.

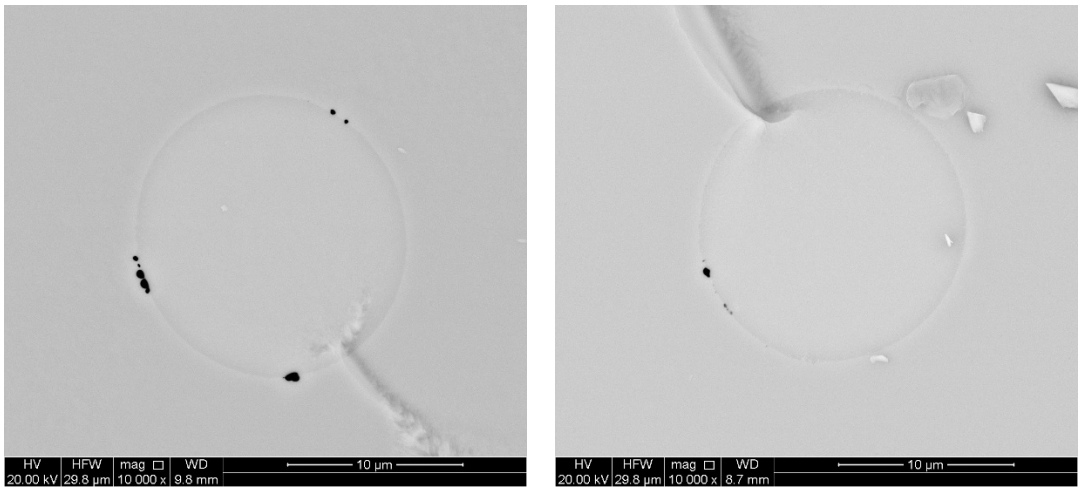

(a) (b)

FIGURE 6.9: SEM images showing defects at the core–cladding interface of the composite chalcogenide–tellurite fibre.

The voids at the surface interface could also have been caused by incomplete wetting between the two glasses during the fibre drawing stage – if the fusion of the core and cladding glass at the interface is incomplete due to the materials not being able to wet to each other, it could result in gaps such as those observed. Another possible reason is the evaporation of gases from either the core or cladding glass leading to bubbles at the interface between the two glasses.

Since the rod–in–tube technique could not guarantee a smooth interface between the core and cladding regions, the billet stack technique was used for the next fabrication trial. With this method the glass billets are vertically stacked on top of each other and then the stack is extruded through a regular rod die. The interface between the two materials is formed as the glass flows through the die in a 'soft' state and is thus less susceptible to mechanical scratching.

As the composite flows through the die the glass stacked at the bottom (closest to the die) becomes the outer cladding, while the glass at the top remains as the core. This is due to the friction between the glass and the die at the die wall, which results in an parabolic radial distribution of glass flow velocity through the die. This velocity profile, as a function of radial distance, is given by

$$v = \frac{\Delta p}{4nl}(R^2 - r^2), \tag{6.1}$$

where r is the radial coordinate, R is the radius of the die aperture, Δp is the pressure difference between the glass at the die entrance and exit, l is the length of the die and η is the glass viscosity. This equation is derived from the Hagen-Poiseuille law for viscous fluid flow through a capillary, assuming a stagnant layer adjacent to the die wall [232].

Consequently the glass flowing through the centre of the die does so at a faster rate that the glass that is closer to the die wall. This enables the glass at the top to effectively push against the glass at the bottom, which flows around it to create a concentric layer. In this work the stack only consisted of two glass billets, however the billet stack method can be used with multiple glasses to create a perform with multiple coaxial rings of glass [196]. This is represented schematically in Figure 6.10.

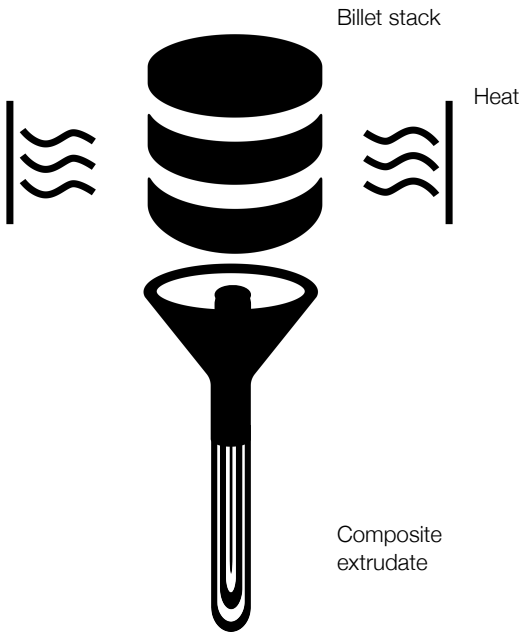

FIGURE 6.10: A schematic of the billet stack extrusion process. Individual glass billets are vertically stacked and then extruded together. The resulting preform is a composite structure with alternating layers of glass.

Two composite preforms were extruded using this technique: one with an 10.5 mm outer diameter and another with a 5.5 mm outer diameter. Cross sectional analysis of these preforms showed that, as expected, the preform started with a section that was mostly tellurite, with a small chalcogenide core, before gradually transitioning into a section that was mostly chalcogenide. Figure 6.11 shows cross sectional samples taken from each end of the large preform that demonstrate this.

While composite preforms were fabricated using this technique, these preforms were very fragile – especially as the outer diameter decreased. Indeed no usable cane could

(a) Start of preform (b) End of preform

FIGURE 6.11: Cross sectional samples of composite preform created by a billet stack extrusion. We see the amount of the core material (chalcogenide) increasing through the preform. Note the cracks through the glass seen in (a). These seem to indicate physical stresses in the preform.

be fabricated as, upon removing the extruded preform from the die body, it broke into pieces that were too short to to be inserted into another tube. This is likely due to physical stresses introduced into the material as a consequence of their differing physical characteristics. For instance, the thermal expansion coefficient for the IG5 chalcogenide is quoted as $14.3 \times 10^{-6}/K$ while that of a tellurite composition very similar to the TZNL has been measured to be $18.8 \times 10^{-6}/K$ [233].We see some evidence of physical stresses in the glass in Figure 6.11(a), albeit exacerbated by the cleaving procedure.

6.3.3 Summary

The preceding sections document fabrication trials of a composite glass fibre, consisting of a chalcogenide core and a tellurite cladding. This work was motivated by theoretical modelling which showed that, by choosing an appropriate core index, a chalcogenide and tellurite composite fibre could be fabricated with a zero dispersion wavelength at 1.55 µm. This could have potential for narrow bandwidth telecommunications applications due to the extremely high nonlinearity of the chalcogenide.

Fabrication was attempted first via the rod–in–tube method and while this was used to successfully fabricate a fibre, it was found to have a high loss due to voids at the core–cladding interface. This prompted us to use the billet stacking method to have a smoother interface between the two glasses. However the preforms produced by the billet stack extrusions were found to be mechanically unstable, possibly due to stresses in the glass.

This line of work was abandoned at this point, however some promise was shown by the fact that a composite fibre was fabricated and this fibre was shown to guide light at 1.55 µm, albeit with high loss. Significant improvements to this could be made by, for instance, changing the composition of the glasses used slightly to better marry their physical properties. Other glasses could also be used as the cladding to further tune the dispersion.

6.4 Tellurite HWW fabrication trials

The fabrication for the hexagonal wagon wheel was first attempted in tellurite, however the design chosen for fabrication was the HWW geometry designed for PSA described in Section 4.5.4 (refer to Figure 4.13); instead of the HWW geometry designed for multicasting described in Section 4.5.3 (refer to Figure 4.9). The primary reason for choosing to fabricate the geometry from Figure 4.13 over that in Figure 4.9 was the size of the inner holes, i.e. those in the suspended core region of the HWW design. The fibre geometry designed for multicasting consists of two sets of inner holes, with radii of 171 nm and 224 nm, and modelling of structural variances suggested that the design was extremely sensitive to the simplest expected fabrication deviations (see Section 5.3.2 or details). Consequently, it was decided that this geometry could not be reasonably fabricated within required tolerances and the geometry designed for PSA in Figure 4.13 was a better investment of effort instead – the inner holes in this fibre design are all the same size, with a radius of 120 nm, and the modelling results of structural deviations on this design showed better tolerance of geometric variations (see Section 5.4.2 for details).

Although the HWW geometry for PSA was originally designed in a bismuth oxide glass, a stable source of this glass was unavailable at the time as it stemmed from an earlier collaboration with the supplier which had been completed by the time these fabrication trials started. However the material dispersions for the tellurite and bismuth are very similar thus, with some slight modifications to the structure designed in Section 4.5.4, a similar dispersion profile could be obtained by using tellurite as the glass substrate.

It was therefore decided to attempt to fabricate the HWW fibre in tellurite glass. While this meant the fibre would have less mechanical stability, due to the tellurite glass

having a lower transition temperature than the bismuth oxide glass, it would have a higher nonlinearity due to the higher nonlinear index of the tellurite.

6.4.1 First iteration

For the first iteration a relatively large target preform outer diameter of 15 mm was chosen. Generally preforms are around 10 mm in diameter but this larger size was chosen to have a high ratio between the core diameter (i.e. R3) and the outer diameter of the preform. The higher this ratio is, the higher the eventual fibre diameter can be while still having the required core size.

6.4.1.1 Die design – v1

The die consisted of two parts – a die plate and a jacket. The die plate contains the inverse of the structure required in the preform. Thus, as the glass is extruded through it, the required structure is longitudinally imprinted into the glass. The die jacket, which the plate fits into, constrains the outer edges of the glass flow and determines the radius of the preform as it exits the die. These two parts are fitted together to make up the die. Figure 6.12 shows photographs of these two parts.

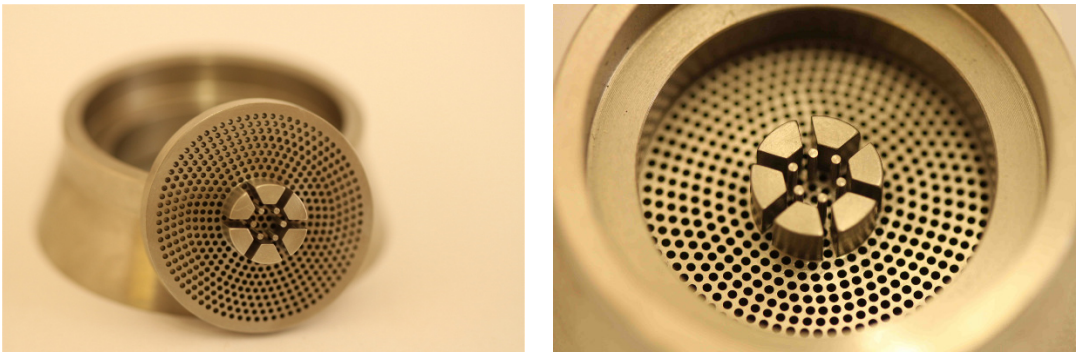

(a) Separated die components

(b) Exit of die with fitted components

FIGURE 6.12: The die plate and jacket used in the v1 design.

When viewed from top down the die resembles a sieve with a number of 'feed holes'. These holes allow the glass to flow through the die, with the idea being that the glass strands would fuse as they emerge on the other side and then solidify into the preform after passing out the die exit and cooling down. A set of metal pins is used to block the glass flow in certain sections – these regions then become voids in the preform that

correspond to the holes in the fibre design. This design is shown in Figure 6.13, where black has been used to represent the feed holes for glass flow and red sections represent the metal pins used to create the holes.

Other die designs, with a more complex arrangement of metal components, could also have been used [207] but this sieve plate based design was chosen mainly because it minimises the glass volume held in the die. This glass is unrecoverable as it does not exit the die and solidifies within it at the end of the extrusion, thus requiring a larger billet volume.

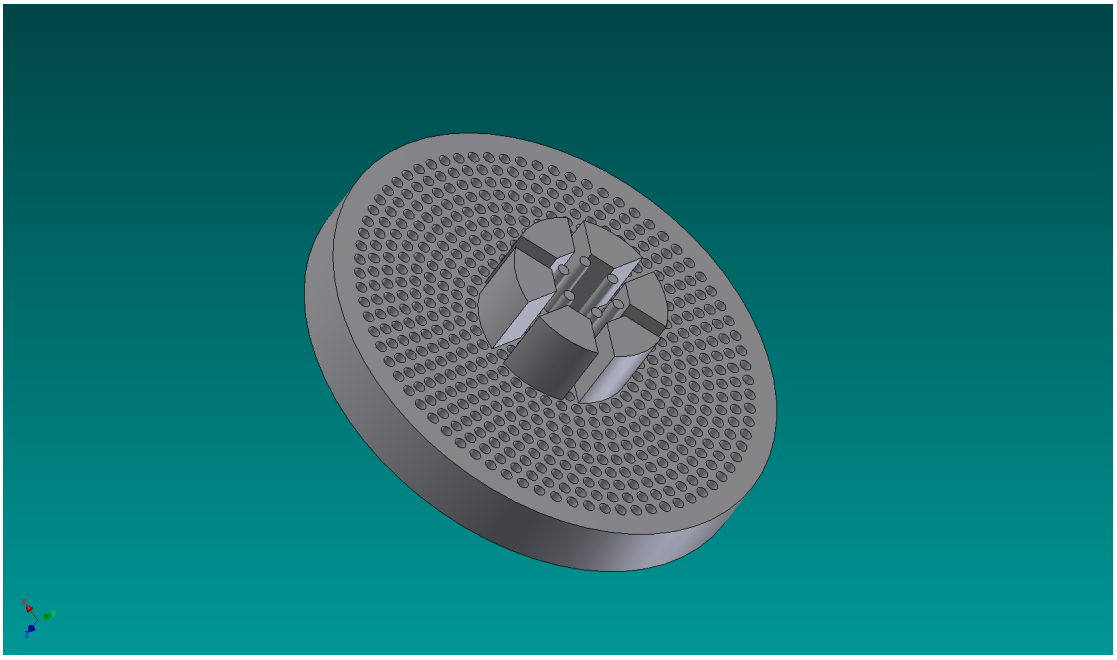

FIGURE 6.13: The die design for the sieve plate, which consists of six cylindrical pins for the inner hoes and six wedge shaped pins for the outer holes.

6.4.1.2 Extrusion results

The results of the tellurite extrusions are detailed in the following sections. In all cases the La10 composition of the tellurite was used (see Chapter 3) to fabricate the glass billets. These billets were then polished to a smooth surface on all sides using a 1 µm grade polishing powder.

Te-126

This was the first attempt at extruding a preform for a hexagonal wagon wheel fibre in this research, and also the first time a HWW geometry of this type (i.e. tailored

for dispersion engineering around 1.55 µm) had been attempted in this glass. Based on previous extrusions of MOFs with this glass, the extrusion was carried out at a temperature of 360 °C and a ram speed of 0.02 mm/min. Unfortunately, the outcome of the extrusion was not a success as the preform glass did not fuse sufficiently upon exiting the die, possibly due to either the extrusion temperature being too low or the ram speed being too high. The problem was most pronounced at the start and outer edges of the preform where individual glass strands could be observed. This can be seen in the photographs of the preform, shown in Figure 6.14.

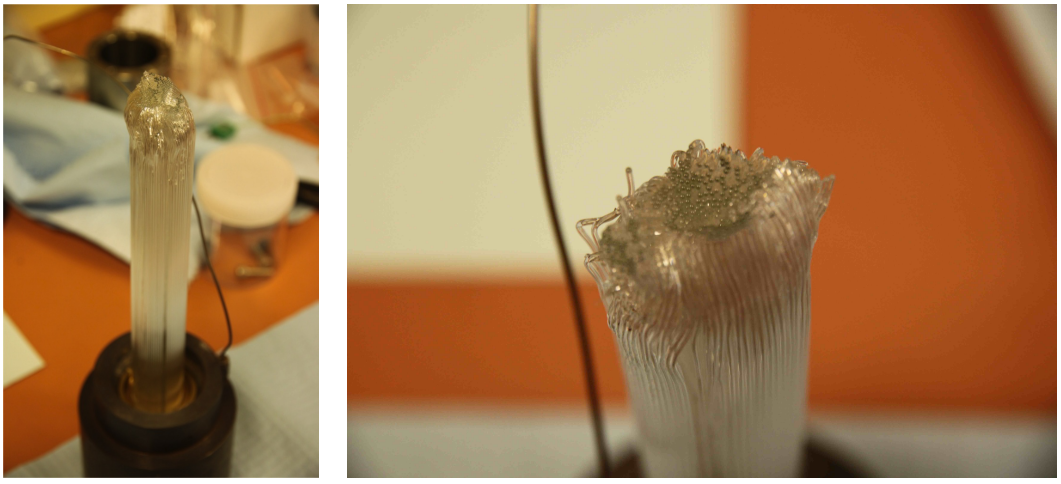

(a) (b)

FIGURE 6.14: The preform obtained from the Te-126 extrusion. Unfused glass strands around the outer part of the preform are observed along the length of the preform in (a), and at the start of the preform in (b).

Cross sectional samples of the preform, shown in Figure 6.15, revealed that, although the preform was largely unfused, partial fusion of glass did occur in the core region. In this part of the preform the glass, while not fusing into a solid block, had nonetheless partially coalesced. The analysis of the core region also revealed another problem with the preform: the inner holes had drifted outwards, towards the edge of the suspended core region. This suggests an issue with the glass flow in the core region, where the direction of the flow is moving partially outwards from the core and thus pushing the holes out as well.

Since the preform from this extrusion was not fused, further progress towards fibre fabrication, such as caning, was not possible.

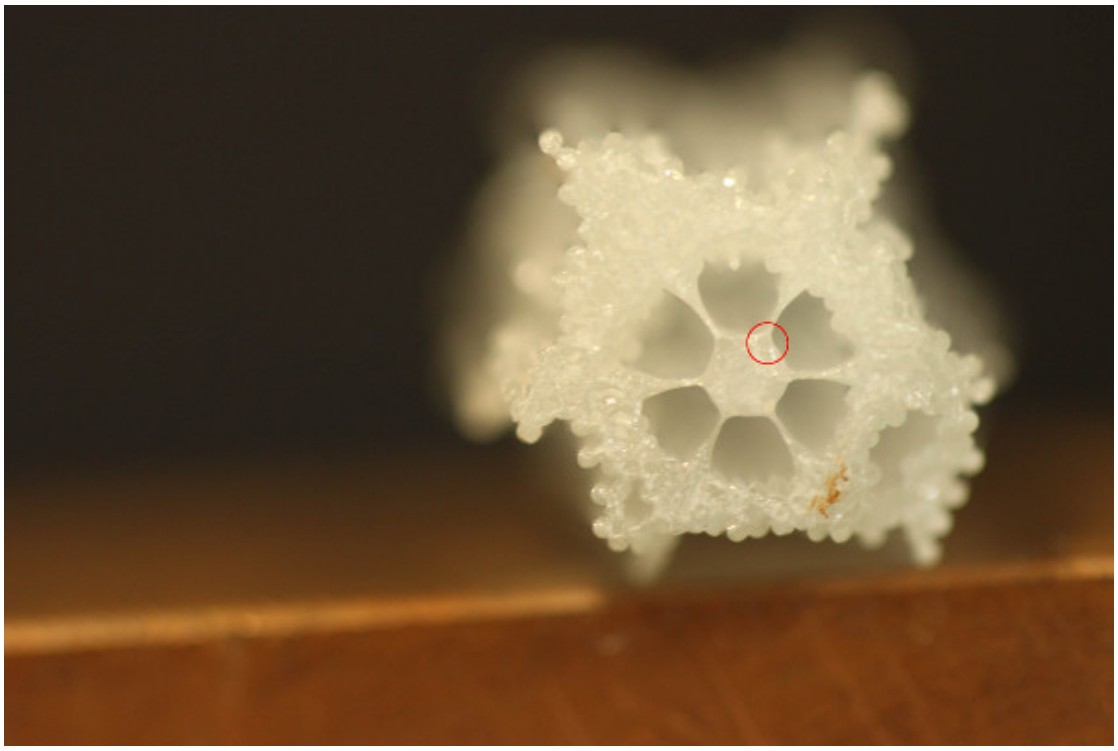

FIGURE 6.15: Cross-section from the Te-126 extrusion result. This extrusion was not successful due to the clear lack of fusion in the glass, and the distortion of the inner holes. The red circle highlights one of the inner holes, which has drifted out toward the edge of the core region.

The lack of fusion in this preform suggests that the glass flowing through the die was either too cold, and therefore not soft enough to fuse properly; or that it moved through the die too quickly and cooled before complete fusion could take place. For the next extrusion, the conditions were modified to facilitate more glass fusion in the preform.

Te-127

The main conclusion from the previous extrusion was that the incomplete fusion observed in the preform was due the glass not having sufficient time to fuse upon exiting the die. To resolve this, the extrusion temperature would have to be increased or the ram speed decreased. Increasing the temperature increases the heat within the glass, making it softer and thus aiding fusion, however it also increases the chances of crystallisation within the glass. The choice was therefore made maintain the extrusion temperature at 360 °C but reduce the ram speed from 0.02 mm/min to 0.01 mm/min, thereby facilitating fusion by allowing the glass more time in the hot zone.

The results of this attempt are shown in Figure 6.16. We see that, in spite of the very slow ram speed, the preform is much the same, i.e. mostly unfused except around the

(a) (b)

FIGURE 6.16: Preform obtained from second tellurite extrusion (Te-127). The preform is again mostly unfused with some partial fusion around the core region.

core region. As this extrusion was done at close to the upper limit for temperature (for this glass) and lower limit for ram speed, this suggested a fundamental issue with the die design. The die design was therefore revisited to improve the glass flow though the die for the next fabrication trial. This second iteration of the die is discussed in the following section.

6.4.2 Second iteration

The results from the previous extrusion trials suggest that the reason the glass did not fuse in the outer regions had to do with the v1 design of the die and the way the glass flowed through it. Based on these results and analysis of the die it was concluded that the flaw in the design was the relatively large amount of feed holes in the outer region, compared to the inner region. In this outer region the glass does not 'see' much metal, compared to the inner region with the metal pins. Consequently the friction for the glass flowing through the outer region is significantly lower than that for the inner region. This results in the glass outside the core region flowing too fast, without sufficient time to fuse. Fusion in the inner region is also aided by the fact that the glass in this region is exposed to more metal and will therefore be hotter due to the heat from the die.

As most of the glass flow is also in these outer regions it effectively pulls the whole of the preform through the die too quickly. This results in the glass of the inner region of the preform not spending enough time in the hot zone, thus explaining why this region was only partially fused.

To test this hypothesis the die from the Te-127 extrusion was recovered and modified, before the next trial. This modified version of the die, labelled v1.1, is described below.

6.4.2.1 Die design – v1.1

To reduce the flow of glass in the outer region of the die many of the feed holes from the v1 die used in the Te-127 extrusion were blocked, on both sides of the die. On the die entrance side it stops the glass from flowing into these regions, while on the die exit side it effectively brings the outer wall closer. These modifications are shown in Figure 6.17.

(a) (b)

FIGURE 6.17: The v1.1 die. This die was made by taking the v1 die (pictured in Figure 6.12) and adding some modifications to block some of the outer feed holes and thus reduce the amount of glass flow in this region.

By reducing the rings of outer feed holes from nine to just two, the feed holes in the v1.1 die were all close to a metal surface – the glass strands from the inner ring were close to the outer surface of the wedge shaped metal pins while those from the outer ring were close to the metal of the new die wall. Compared to the v1 design, the v1.1 die was expected to facilitate fusion better as much more of the glass would 'see' metal and therefore flow through more slowly, allowing sufficient time for the preform to fuse. The idea behind this recycled, modified die was to enable this hypothesis to be tested in a relatively quick and cheap manner, compared to fabricating a brand new die.

6.4.2.2 Extrusion results

Te-128

This extrusion was carried out with the v1.1 die, under the same conditions as Te-127, i.e. an extrusion temperature of 360 °C and a ram speed of 0.01 mm/min.

The results of this extrusion confirmed the hypothesis that the cause of the unfused glass in the preform was the lack of metal surfaces in the outer regions. The preform from this extrusion came out completely fused, albeit with low glass quality due to being run through an already used die. Figure 6.18 shows a cross section of the preform obtained from this extrusion.

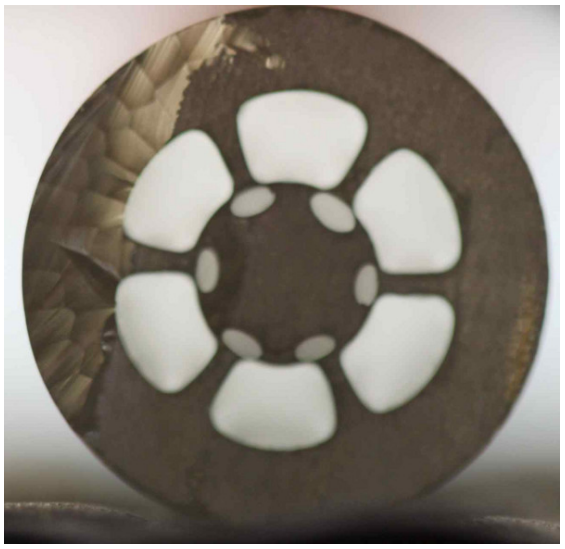

FIGURE 6.18: Results from Te-128 extrusion showing the preform fused into a solid block.

While the fusion problem had been solved with the modifications to the die design the secondary problem of the inner holes being deformed still remained. Figure 6.18 shows that the inner holes had been deformed from the intended circular shape and had again drifted out towards the edge of the suspended core region. This suggested that the glass flow from the core was being pulled outward, towards the edge of the suspended core region, and thus also moving the holes in the same direction. Further revisions were made to the die design to compensate for this (see Section 6.5.1.1).

Even though this preform had a low glass quality due to the die being recycled from the Te-127 extrusion, it was caned to observe the effect of this caning procedure on the inner holes. The resulting cane is shown in Figure 6.19. It shows that, as suspected, the inner holes have moved out even further. In some cases the holes had even moved into the struts, causing them to break.

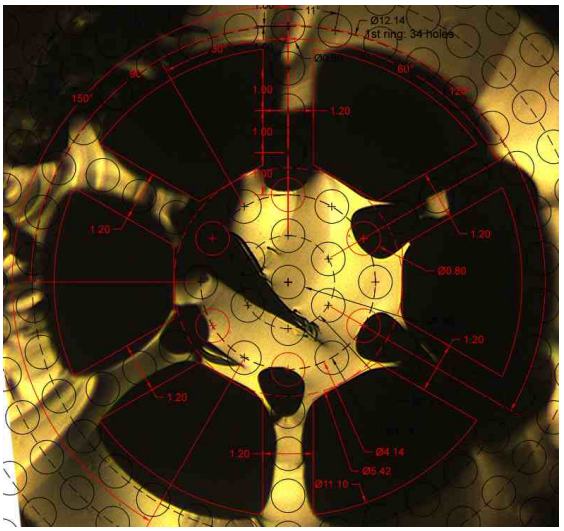

FIGURE 6.19: The cane obtained from the Te-128 preform. While the shape of the core is close to the design, some of the inner holes have drifted out into the struts.

Extrusion	Die design	T (°C)	v (mm/min)	Result
Te-126	v1	360	0.02	Preform was largely unfused.
Te-127	v1	360	0.01	Slower ram speed did not solve problem of glass not fusing.
Te-128	v1.1	360	0.01	Modified die design resulted in fused preform. However inner holes were displaced. Caning of preform pushed inner holes out further, causing breakage of struts in some instances

TABLE 6.1: Summary of results from tellurite HWW fabrication trials. The columns labelled T and v refer to the extrusion temperature and ram speed, respectively.

6.4.3 Summary of tellurite HWW extrusions

Three fibre fabrication attempts of the HWW fibre design were made with the tellurite glass, however none of them resulted in a preform from which fibre could be drawn. The results of these extrusions are summarised in Table 6.1.

For the first two extrusions, Te-127 and Te-128, the v1 die design was used and preform did not come out fused, even though the ram speed was slowed from 0.02 mm/min in Te-127 to 0.01 mm/min in Te-128 to allow the glass more time to fuse during the extrusion. The die was then modified to reduce the amount of outer feed holes and the next extrusion with this modified v1.1 die did result in a fused preform. However, as

most of the die was recycled from the previous extrusion, the quality of this preform was too poor to continue on to fibre drawing.

Whilst unsuccessful, useful insight was drawn from these extrusions – the large number of outer feed holes in the v1 die, relative to the inner feed holes, resulted in too much glass flow in the outer regions of the die. This, in turn, was causing the glass to be pulled through the die too quickly, and with insufficient heat. Consequently, for the next set of fabrication trials, the die would need to minimise regions where the glass would flow without 'seeing' metal. This would help maintain uniform friction and thus flow velocity for the glass strands across the die, and ensure that this glass had enough contact with hot metal to absorb sufficient heat.

The next set of fabrication trials is presented in the following section.

6.5 Germanate HWW fabrication trials

After the unsuccessful attempts at fibre fabrication with the v1 and v1.1 die designs the die design was again revisited. This period also coincided with the development of the GPNL5 germanate glass described in Section 3.5 and consequently, the decision was made to switch from the tellurite glass to the germanate glass. The germanate glass has better mechanical properties than the tellurite but also possesses many of the favourable properties of tellurite such as high nonlinearity and good transmission in the near infrared.

6.5.1 First iteration

6.5.1.1 Die design – v2

For this version of the die major changes were made, to accommodate the material dispersion of the germanate glass (calculated from the refractive index measurements of this glass, described in Section 3.5.3) and to solve the issues observed in the tellurite extrusions. The major changes were as follows:

- The number of outer feed holes was significantly reduced to just two rings. This follows from the partial success observed with the Te-128 extrusion through the modified v1.1 die

- The inner edges of the wedge shaped metal pins were changed from sharp edges to rounded edges (see Figure 6.20). These edges correspond to the region where the glass from the core flows into that of the struts. As the flow of the glass naturally tends towards forming a rounded edge, changing the pin to facilitate this shape should ease the pressure of the flow. This should result in less 'pull' on the inner holes as the glass flows through the die, making them less likely to drift outwards.

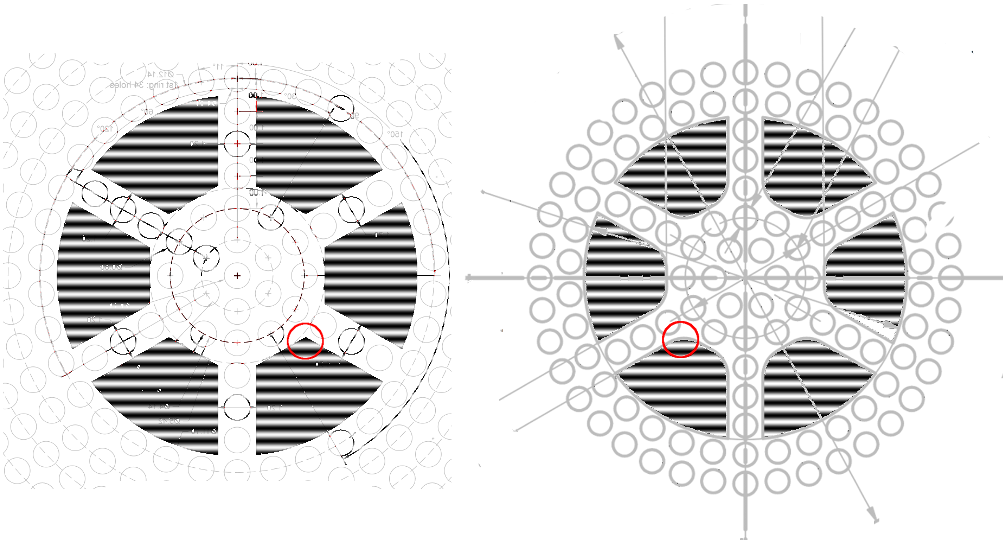

FIGURE 6.20: Change in shape of outer pins from the v1.1 die (left) to the v2 die. The red circles highlight the inner edges of one of the outer pins showing how it changed from a sharp edge on the v1.1 die (left) to a rounded edge on the v2 die (right).

Photographs of this new (v2) die design are shown in Figure 6.21.

6.5.1.2 Extrusions

Ge-15

The first of the HWW extrusion trials with the GPNL5 germanate glass was a partial success. The preform was indeed fused however the problem of the inner holes being distorted and drifting was not entirely solved. A cross section of the preform (Figure 6.23) reveals the holes to be elliptical in shape and closer to the edge of the core region than desired. However the drift is not as bad as with the Te-128 extrusion.

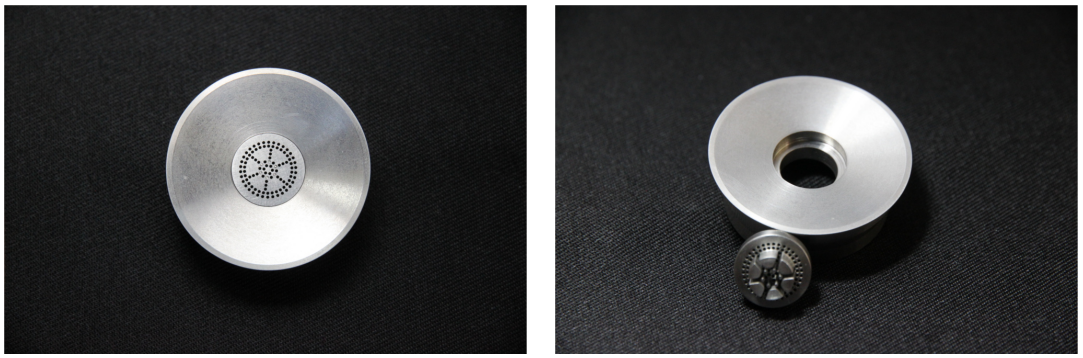

(a) (b)

FIGURE 6.21: The v2 design of the die. This major revision to the design has a much smaller die plate due to the reduced number of outer feed holes.

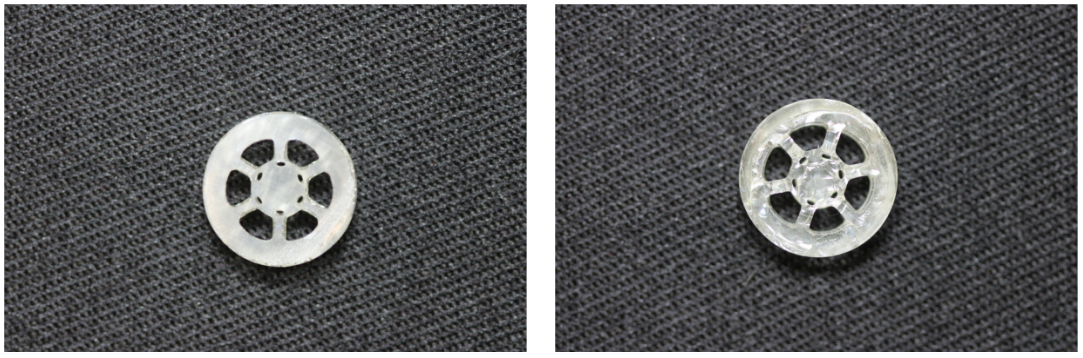

(a) (b)

FIGURE 6.22: Results from Ge-15 extrusion

Even though the holes were deformed, this preform was caned so that a fibre draw could be attempted. Upon caning, an interesting observation was made – the inner holes had collapsed in on themselves and disappeared from the cane altogether. The outer holes had also contracted a little bit. Figure 6.23 shows a cross section of the cane taken after the draw – it is immediately obvious from this image that the inner holes are missing from the geometry.

This suggested that the surface tension of the germanate glass at the caning temperature is higher than that of the tellurite [234] and that self pressurisation may not be sufficient to draw this fibre.

6.5.2 Second iteration – the simplified HWW

Section 4.7 introduced the simplified version of the HWW structure in germanate. The work on developing this simplified design, with no inner holes, was motivated by the

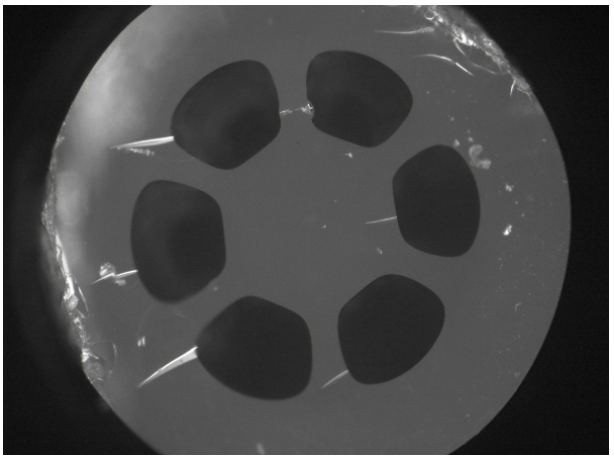

FIGURE 6.23: Cross section of Ge-15 cane showing no inner holes

realisation from the Ge-15 trial that the surface tension of the GPNL5 glass was too high for a structured preform in this glass to be drawn into fibre using self pressurisation. Opening out the preform requires active pressurisation, however as the inner holes of the preform are sized differently to the outer holes, a complex active pressurisation setup is required – one that is able to apply different pressures to different regions of the fibre. As such a setup was not available, a simplified fibre design was pursued instead.

It should be noted that in future work on developing HWW fibre designs, the surface tension of the intended glass should be taken into account at the start of the design procedure so that the inner microstructure, and thus the ability to finely control the dispersion, can be maintained. The future work section (Section 9.1) at the end of this thesis discusses this in more detail

6.5.2.1 Die design – v3

Using the fibre core radius and outer holes for dispersion control instead of the inner holes (which were not included in this design) means the inner set of metal pins are no longer required in the die. This necessitates a change in the die design from the v2 model shown earlier. Along with the removal of the inner pins, the wedge shaped pins for the outer holes were also made larger (relative to the diameter of the die exit). This has the additional effect of making the core diameter relatively smaller, which makes it easier to scale it down to the required dimensions in the fibre. This v3 design in shown in Figure 6.24.

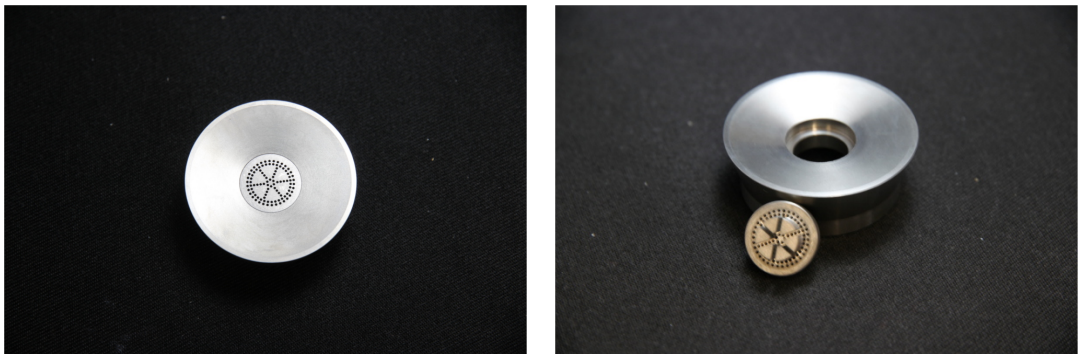

(a) (b)

FIGURE 6.24: The v3 version of the die design for the simplified germanate HWW

6.5.2.2 Extrusions

Ge-21

The preform resulting from this extrusion was the closest of all the HWW extrusions to the original design. This is partly due to the simplified design and partly due to the application of all the knowledge and expertise gleaned from the previous trials. The difficulty of computationally modelling glass flow through complex extrusion dies [230], due to the fact that this requires a three dimensional modelling technique, means that the process mainly relies on empirical knowledge and practical expertise. It is therefore not uncommon to require a number of trials, as documented here, before achieving even a moderately successful fabrication outcome.

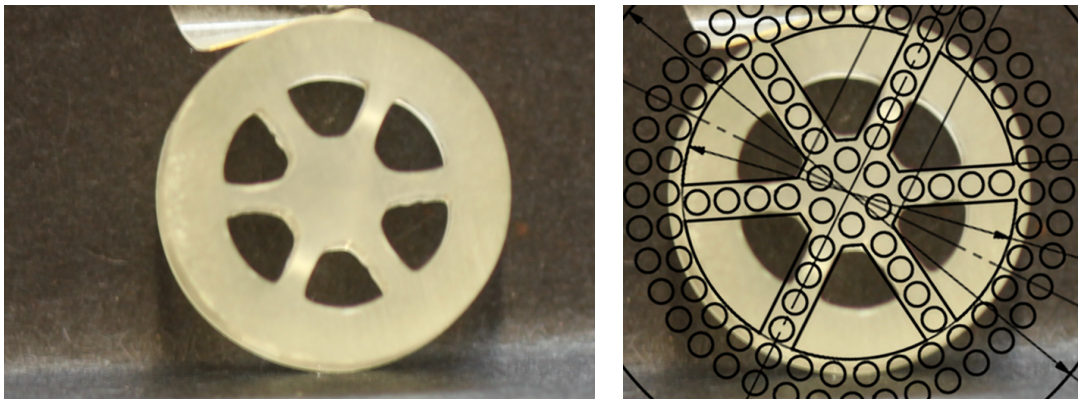

(a) (b)

FIGURE 6.25: Results of Ge-21 extrusion. A cross section of the preform is shown in (a) and again in (b) with the die structure overlaid

Figure 6.25 shows a cross section of the preform on the left, with the die design overlaid on the right. By overlaying the intended design with the final result it can be seen that the core region matches the design quite well, however the outer holes are significantly smaller than they should be. These small outer holes also result in the the outer wall of the preform being thicker and closer to the core region than expected. This is further evidence of the high surface tension present in this glass. Indeed the surface tension of the GPL5 germanate glass, which has a very similar composition to the GPNL5 used in this fabrication work (see Table 3.3 for composition details), was later measured by a colleague to be 0.24 N/m – significantly higher than 0.16 N/m surface tension value measured for tellurite [234].

This high surface tension would likely shrink the holes even further in the caning step, and successively more so in the fibre drawing step. Such a fibre is likely to suffer from hole collapse in the draw, or require significant applied pressure to keep the holes open. To mitigate this and keep the holes as large as possible in the cane, the caning was performed with active pressurisation. The applied pressure was increased in steps of 5 mbar (from the initial state of no applied pressure) until sufficient hole expansion was observed in the cane. The best results were achieved with an applied pressure of 35 mbar, as shown in Figure 6.26(c).

The results in Figure 6.26 show that the holes open out significantly with increasing applied pressure. The geometry of the cane in Figure 6.26(a) closely resembles that of Figure 6.23 (done under self pressurisation).

6.5.3 Summary of germanate HWW extrusions

Two extrusion attempts were made with the germanate glass. These results are summarised in Table 6.2.

Extrusion	Die design	T (°C)	v (mm/min)	Result
Ge-15	v2	528	0.036	Partial success as preform was fused but inner holes were still distorted.
Ge-21	v3	534	0.036	Simplified preform was extruded by abandoning the inner holes.

TABLE 6.2: Summary of results from germanate HWW fabrication trials. The columns labelled T and v refer to the extrusion temperature and ram speed, respectively.

(a) 0 mbar (b) 25 mbar

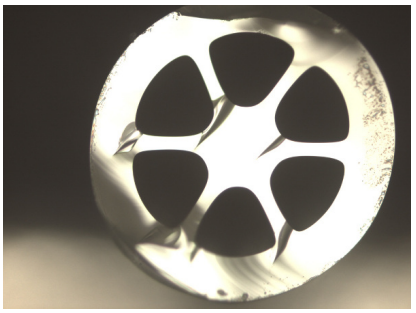

(c) 35 mbar

FIGURE 6.26: The effect of active pressure on the caning of the Ge-21 preform. The applied pressure was increased from 0 mbar to 35 mbar to open out the holes.

The first, which used the v2 die design, was a partial success – the preform came out fused however the inner holes were still distorted and too close to the edge of the core region. When this preform was caned however these inner holes disappeared, and the area of outer holes (as a fraction of the total cross section) was significantly smaller in the cane compared to the preform. This suggested that the surface tension of the germanate glass was higher than expected – it was confirmed in a later experiment that the surface tension of the lead germanate glass was indeed significantly higher than that of tellurite [234].

For the second extrusion the simplified v3 die design was used, where the inner pins were removed and the outer ones were made larger to combat the surface tension. This did away with the inner holes and led to a preform whose structure was closer than the previous trials to that expected from the die design. This preform was caned under active pressurisation to ensure the outer holes stayed open.

The canes obtained from the Ge-21 preform were then used in HWW fibre fabrication trials. This is described in Section 6.6 that follows.

6.6 Fibre draws

Since a satisfactory preform was not obtained with the tellurite glass, the fibre draws were attempted with the germanate preforms from the Ge-15 and Ge-21 trials. As described earlier in Section 6.2, the canes were first jacketed with a tube extruded from the same glass – as shown in Figure 6.27.

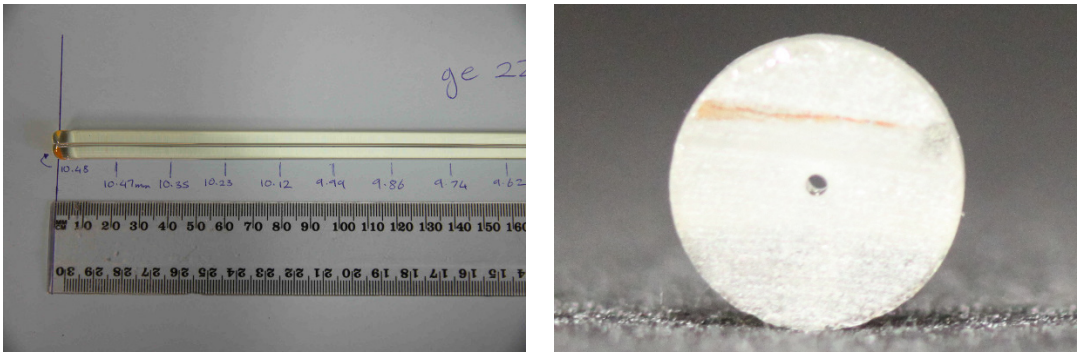

(a) (b)

FIGURE 6.27: Example of a tube extrusion. The cross section shown in (b) has an outer diameter of 10.4 mm and an inner diameter of 0.8 mm.

When extruding the tube it is important to match the inner diameter of the tube with the outer diameter of the cane. The inner diameter of the tube must be set to get a reasonably snug fit with the cane. If this fit is too loose there is a risk the cane may not expand enough into the space and thus compromise the fibre structure. If a vacuum is used in the fibre draw, the issue of cane fit is not a problem as the tube can be easily collapsed onto the cane by the vacuum. However this means that active pressurisation cannot be used as our fibre draw tower was not equipped to actively pressurise the cane, while simultaneously applying a vacuum between the cane and the tube.

6.6.1 Initial trials – self pressurisation

The first fibre draw trials were performed under self pressurisation using the cane from the Ge-15 extrusion. These attempts did not succeed due to severe hole collapse during the draw. The end result was essentially a bare fire, i.e. a fibre with no internal structure. The failure of the holes to open out at all during the draw is further indication that the surface tension of this glass is too high to be drawn under self pressurisation, for this

hole size. However, as drawing under self pressurisation is easier to control this was the method initially attempted.

As this germanate glass had not previously been used to fabricate a microstructured fibre with active pressurisation, it was first necessary to develop an understanding of how the glass responds to pressure during the draw. This study is discussed in the following section.

6.6.2 Inflation trials

To examine the effect of pressure, inflation trials were conducted on two of the germanate glasses – the GPL and GPNL5 compositions. The aim of this study was to quantify the inflation of the glass, as a function of applied pressure.

To begin the trial a tube was fabricated and its inner and external diameters were measured. The external diameter is measured using a set of callipers and the internal diameter is then calculated from a scaled, high resolution image of the tube cross section. As the internal diameters can be between 0.7 to 1.1 mm in size, this is the most accurate way to measure them.

After the tube dimensions have been measured it is mounted on the drawing tower as per a normal fibre draw. In this instance however, instead of a fibre the result of the draw will be a capillary. By performing the same set of measurements on the capillary diameters (with an optical microscope) a simple inflation ratio, I, may be defined as below

$$I = \frac{ID_c/ODc}{ID_t/OD_t}, \tag{6.2}$$

where ID is the internal diameter, OD is the external diameter and the subscripts c and t refer to the capillary and tube, respectively.

For both glasses the fibre draw was started with no pressure, allowed to stabilise to the point where the fibre diameter remained consistent for over a minute, and then the active pressure was turned on. The pressure was increased from 0 mbar in steps to 5, 10 20 and 30 mbar. After each step in pressure the draw was allowed to stabilise and

then run for a further 10 to 15 metres to create a band corresponding to that value of applied pressure. At the end of the fibre draw a set of ten evenly spaced cuts were made along each band to build up a set of values for ID_c and OD_c. Finally, the average of these values, along with the ratio for the tube was used to calculate the inflation ratios.

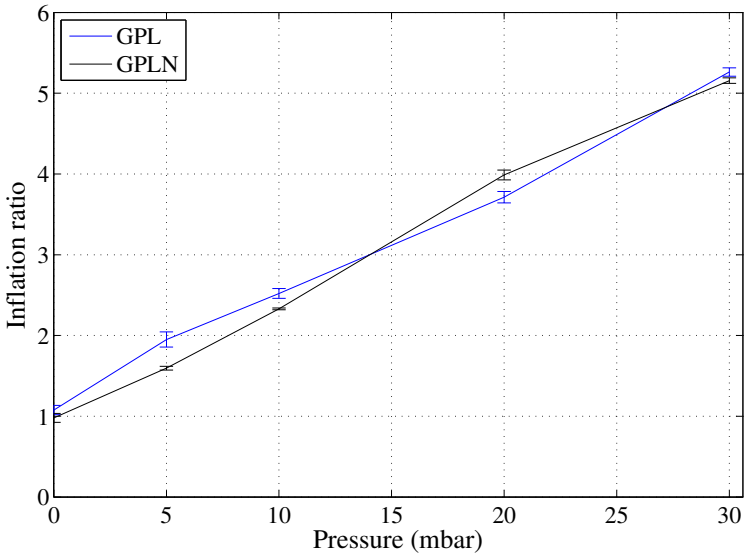

FIGURE 6.28: Inflation ratio (as defined in Equation 6.2) plotted as a function of applied pressure for GPL (blue) and GPNL5 (black) capillaries.

The results of the inflation trials is shown in Figure 6.28. It shows that the glass responds smoothly and predictably to applied pressure – a high inflation ratio of just over 5 can be achieved by increasing the pressure up to 30 mbar. This result was encouraging as it demonstrated that the high surface tension of the glass could be countered and significant hole inflation could be achieved with applied pressure.

6.6.3 Active pressurisation trials

The data gathered from the inflation study demonstrated that, with sufficient pressure, the intrinsically high surface tension of the germanate glass could be overcome. This data was used to proceed with active pressurisation in the subsequent draws for this fibre. The aim of these trials was to fabricate the simplified HWW structure introduced in Section 4.7.

Initially, the fibre draws were not very successful. The active pressurisation process requires very precise control of fibre draw parameters, such as applied pressure and

draw speed, throughout the process and, in the initial attempts, the right values for these parameters were not found. This resulted in fibres where the pressure was either too high or too low., resulting in over or under inflation of the cane into the jacket. Figure 6.29 shows some examples of this.

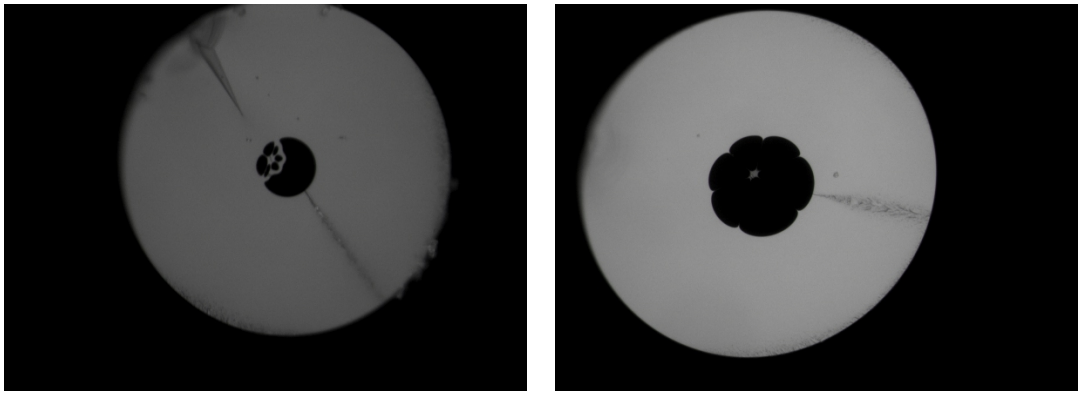

(a) (b)

FIGURE 6.29: The effect of pressure and temperature on fibre inflation. For the fibre shown in (a) the pressure is too low and consequently the cane has not fully inflated into the space of the tube. In (b) the pressure is too high leading to some of the holes blowing out.

It is also important to note that the correct pressure to use depends on the temperature of the glass. For a given value of applied pressure, the inflation of the holes in the fibre will increase as a function of glass temperature. This glass temperature is impossible to measure with the setup used and must be judged based on the temperature of the furnace. However for a given furnace temperature the glass temperature will increase based on the size of the preform – for instance, a 13 mm diameter preform will have its edges closer to the furnace than a 10 mm one and (due to its larger volume of heat conducting glass) will absorb more heat.

Another factor that needs to be considered is the fit of the cane into the tube. If this fit is too loose the amount of pressure required to inflate the cane out into this space needs to be quite high. This is undesirable as the higher the applied pressure, the more sensitive the process becomes to fluctuations in temperature and pressure. Ideally the applied pressure should be as low as possible – just high enough to inflate the holes out to the size required. This can also be thought of as staying as close to the self pressurisation case as possible.

After a number of unsuccessful attempts enough empirical data was built up to be able to determine a set of draw parameters good enough to result in a structured HWW fibre. This enabled a fibre draw of the first HWW structure in this germanate glass, using the preform from the Ge-15 extrusion. The result of this first success is shown in Figure 6.30, where an applied pressure of 30 mbar was used to achieve the required hole inflation. The images show that the cane was successfully inflated into the jacket.

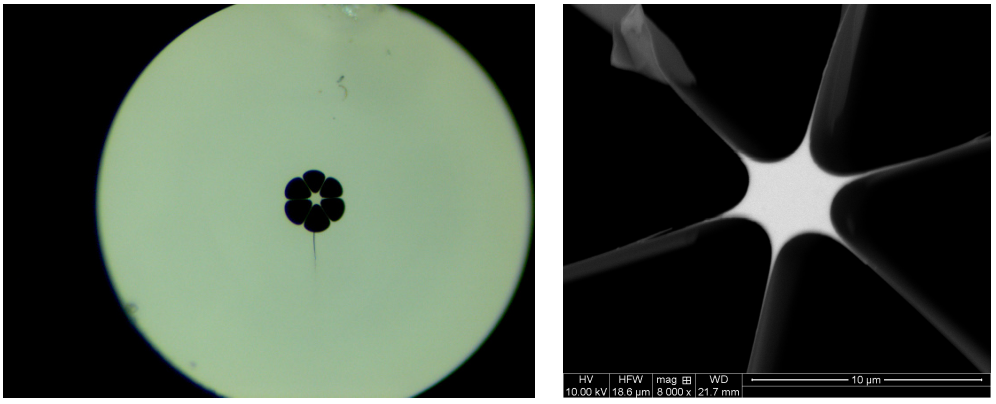

(a) (b)

FIGURE 6.30: Ge-f19 draw – the first successful HWW fibre draw using the GPNL5 germanate glass. The image in (a) is from an optical microscope while (b) shown a scanning electron micrograph (SEM) image of the core region.

While this result was heartening, the fibre draw has room for improvement. One of the issues with the draw was that the preform used was relatively short and consequently only a few metres of fibre could be fabricated from it. Close inspection of the SEM image of the fibre in Figure 6.30(b) also reveals the core to be slightly asymmetric. This makes the fibre birefringent and distorts the dispersion profile.

Following on from this result, the next trial sought to reproduce the successes of the Ge-f19 draw but with a longer preform and with less distortion of the core. Canes were chosen from the Ge-21 extrusion that had the largest holes and the most symmetry, with the expectation that these properties would be reflected in the fibre draw. The use of a cane with larger holes did indeed reduce the amount of pressure required from 30 mbar to 27 mbar. The structure was also more symmetric, although not entirely so. Images from this draw are shown in Figure 6.31.

The result in Figure 6.31 is the closest version of the ideal simplified HWW fibre. To have the right dispersion profile a core diameter of 3.4 µm is required, however the actual

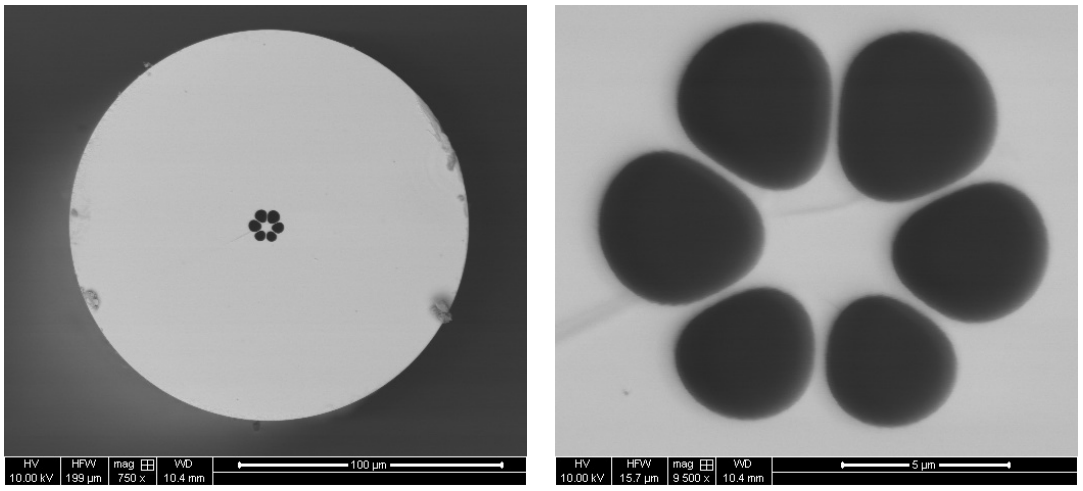

(a) (b)

FIGURE 6.31: Ge-f23 draw – SEM images of second successful HWW fibre draw. This structure is more symmetric than the previous one.

core diameter measured is 3.9 µm. Further work is therefore required to obtain the ideal result however, due to the time constraints of this research, this result was not attained.

The loss of this fibre was measured to be 10.8 ± 1.3 dB/m (this experiment is detailed in Section 7.4) – a high value given that the unstructured fibres in this glass have losses of less than 2 dB/m at 1.55 µm (see Section 3.5.5.1). However it should be noted that, as this fibre is only the second fibre with this structure that has ever been fabricated in this glass its loss may be improved significantly by improving the fibre fabrication procedure in further trials. Previous experience within the group has indeed shown this to be the case for extruded fibres in other glasses, such as fluoride [235], lead silicate [236, 237] and tellurite [156].

6.7 Conclusion

This chapter details the fabrication work performed during the course of this research.

Preliminary work investigated the use of tellurite and chalcogenide to fabricate composite fibres, where the core diameter refractive index of the cladding region may be used to control dispersion and nonlinearity. Both the rod–in–tube technique and the billet stack technique were used in preform fabrication with the preform from the rod–in–tube successfully drawn down into guiding fibre, albeit with high loss.

From Sections 6.4 onwards, this chapter describes the work done on fabricating HWW fibres to operate at telecommunications wavelengths. When this work was initially set out the end goal was to fabricate a HWW fibre with flattened dispersion, as discussed in the design chapter (Chapter 4). Due to unanticipated difficulties in the fabrication and unavailability of material, fabrication of the tellurite and bismuth oxide based designs that featured inner holes was not possible. However, several key learnings were made from those attempts. The most important among them is the position of the inner ring of holes, relative to the edge of the suspended core region. If these holes are too close to the edge, the flow of the glass tends to push them out further, thus distorting the structure. Future designs will have to incorporate a factor into the fitness function that takes this into account.

While fabrication of a HWW structure featuring inner holes was not achieved, significant progress was made towards fabrication of the simplified germanate HWW from Section 4.7. The fabrication trials revealed the high surface tension present in this glass, making holes contract in both the extrusion and drawing stages. Combating this required the use of active pressurisation which led to the manifestation of asymmetries in the cane that were exacerbated in the fibre.

The best way to tackle this would be to start off with even bigger holes in the preform – holes big enough so that minimal, if any, pressure (< 20 mbar) needs to be applied in the caning stage. This will reduce, or even eliminate, asymmetries in the cane and have a flow on effect on the fibre structure. Ideally the fibre could then be drawn with a low applied pressure. This also requires that the cane fit into the jacket be as tight as possible, to ensure that it inflates out into the space.

It is also worth noting that the high surface tension of the germanate glass means that fabricating an HWW fibre in this glass that contains inner holes requires an active pressurisation setup that is able to differentially apply pressure to certain regions of the fibre – the pressure applied in the inner holes needs to be different to that applied on the outer holes to obtain the required geometry. This is due to the fact that the inner holes would require a high applied pressure for the same amount of inflation (due to their smaller diameter) and if the same pressure was applied to the outer holes it would cause the fibre to blow out.

In the end though, many of the fabrication challenges, invariably posed by a novel glass, were overcome and HWW fibre was fabricated in the germanate glass. This core diameter of this fibre, at 3.9 µm, was larger than the 3.4 µm required for it to have a ZDW at 1550 nm (refer to Figure 4.17), but it represents and important step in the fabrication of such fibres. It is the first generation of such a fibre and the first instance of a microstructured fibre being drawn under active pressurisation with this glass. It is hoped that this work may serve as a basis from which the many fabrication learnings may be extended into developing HWW fibres that are closer to the intended design, or even other microstructured fibres in this glass.

The characterisation of the fibres and materials developed in this research is presented in Chapter 7 that follows, including a measurement of the loss of the germanate HWW fabricated in the Ge-f23 trial. Chapter 7 also details the measurement of dispersion and nonlinearity for suspended core fibres made from tellurite and germanate, respectively.

Chapter 7

Fibre characterisation

7.1 Introduction

This chapter describes a number of fibre characterisation experiments that were performed as part of this research. These characterisation experiments include measurements of dispersion, nonlinearity and loss of various fibres. As these properties are crucial to the design of nonlinear fibres for telecommunications applications, measuring them and comparing to simulation results is an important validation of the modelling process.

The experimental results presented in this chapter are as follows: a measurement of the dispersion of a tellurite suspended core fibre is presented in Section 7.2 and compared to modelling results. Section 7.3 covers the measurement of the nonlinear coefficient for a germanate suspended core fibre. This measurement, carried out via the so called Boskovic method [166], is performed on the novel GPNL5 germanate glass first presented in Section 3.5 and is used to derive the nonlinear index of this glass. The results show that it compares favourably with other nonlinear glasses, such as tellurite, and is thus a promising candidate for nonlinear fibre devices. Finally, Section 7.4 details a measurement of the optical loss for the Ge-f23 germanate fibre (shown in Figure 6.31; fabrication details are in Section 6.6).

7.2 Dispersion measurement

Given the role of the dispersion profile in determining the gain for four wave mixing, it is important to be able to characterise this property in optical fibres designed and fabricated for FWM applications.

When characterising the dispersion for both designed and newly fabricated fibres, the typical approach is to take a high resolution image of the fibre cross section and use a the finite element method to model the optical properties of the fibre and calculate the dispersion (see Section 4.3 for details). For fibre designs, the cross sectional geometry is drawn directly using the COMSOL® modelling software in conjunction with MATLAB® (as in Figure 4.1); whereas for fabricated fibres, an SEM micrograph of the fibre cross section is imported into COMSOL® and used to create the geometry.

Evaluating the dispersion profile for MOFs via a model of the fibre cross section is typically much quicker and less complex than experimentally measuring it. For novel fibres in particular, where the fabrication process is not very mature, the loss may be too high for an experimental measurement to be performed with adequate accuracy. However, to verify this characterisation procedure, the dispersion for a tellurite and bismuth suspended core fibre was experimentally measured and used to validate the results from the model of the geometry. These experiments are described in the following sections.

7.2.1 Background

The techniques for measuring chromatic dispersion in optical fibres fall into one of the following categories: the time of flight method [238], the phase shift method [239] and the interferometric method [240, 241]. Of these three, the time of flight and phase shift methods are widely used in the characterisation of conventional silica optical fibres [242].

The time of flight method essentially measures the time that a pulse spends 'in flight', along a length of optical fibre, and compares it to a reference signal to calculate the delay on the pulse imposed by the glass. A tunable laser (or a set of lasers at fixed wavelengths) is used to send a set of short, periodically spaced pulses down the fibre, for a set of wavelengths. The time between when the pulse was injected to when it exits the

fibre is recorded as the delay τ By making this measurement for several wavelengths a result for the relative group delay, as a function of wavelength is obtained. Differentiating this result and using the fibre length L according to Equation 7.1 then produces the dispersion for the fibre.

$$D = \frac{\delta}{\delta\lambda}\left(\frac{\tau}{L}\right). \tag{7.1}$$

While this technique is widely used it is limited to very long lengths of fibre (hundreds of meters, typically) due to the fact that the optical path must be long enough for the delay between consecutive pulses to be distinguishable. In addition to this, the spectral resolution and bandwidth of this technique is limited by the spectral properties of the laser used in the experiment. The high stability and pulse rise times required to obtain accurate results typically limit the optical source to narrow band, high fidelity lasers.

The phase shift technique is similar to the time of flight method, in that it also measures a delay. However this measurement is made on phase difference, instead of time delay. The input signal is amplitude modulated and at the output end of the fibre the relative phase shifts between different wavelengths, extracted via a monochromator, are measured. The delay, and hence dispersion, may then be calculated from this result.

An immediate advantage that the phase shift technique has over the time of light technique is the ability to make a high resolution measurement of dispersion of over a broad spectral range. However this technique still requires a relatively long length of fibre (a few metres at least), to observe sufficient phase shift.

When working with soft glass microstructured fibres the operating length is generally too short to use either the time of flight or phase shift method. The interferometric method, on the other hand, requires a metre of fibre at most and may easily be done with 10-20 cm lengths of fibre. This makes it an ideal method for measuring the dispersion of our fibres.

In this technique the interferometer is set up into a Mach-Zender configuration where the light is split into two arms (one where the beam travels in air, while the other contains the fibre under test) before being recombined and analysed with an OSA. The air arm is of variable path length so that the light travelling down that arm can be phase

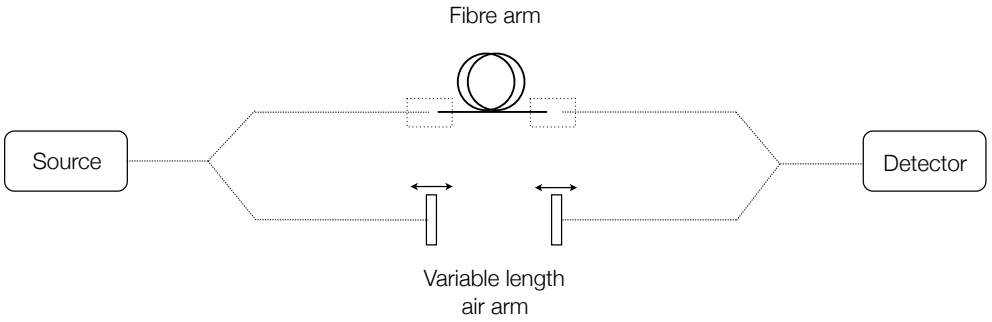

FIGURE 7.1: Experimental setup used when measuring the dispersion of a fibre via the interferometric method. The interferometer is setup into a Mach-Zender configuration, with the test fibre being placed in the fibre arm and the variable length air arm used to match the optical path length.

matched to the light in the fibre arm. A schematic of this measurement setup is shown in Figure 7.1.

The intensity at the output may then be written as [240]

$$I_{out} = |Ef + Ea|^2 = |Ef|^2 + |Ea|^2 + 2|E_f||E_a|cos(\phi(\omega)), \tag{7.2}$$

where E_f and E_a denote the electric field amplitudes in the fibre and air arm, respectively, and the phase difference $\phi(\omega)$ is given by:

$$\phi(\omega) = \beta_f l_f - \beta_a l_a, \tag{7.3}$$

where β refers to the propagation constant, l is the path length and the subscripts f and a denote the fibre and air arms, respectively. By replacing $\beta_a l_a$ with $\frac{\omega l_a}{c}$ and expanding $\phi(\omega)$ in a Taylor series about an arbitrary frequency ω_0, we arrive at the expression below:

$$\begin{aligned}\phi(\omega) = \beta_f(\omega_0)l_f - \frac{\omega_0 l_a}{c} + \left(\beta_f^{(1)}(\omega_0)l_f - \frac{l_a}{c}\right)(\omega - \omega_0) \\ + \frac{1}{2}\cdot\beta_f^{(2)}(\omega_0)l_f(\omega-\omega_0)^2 + \frac{1}{6}\cdot\beta_f^{(3)}(\omega_0)l_f(\omega-\omega_0)^3 + ...\end{aligned} \tag{7.4}$$

where $\beta_f^{(n)}$ represents the n^{th} order partial derivative of the fibre propagation constant, i.e. $\beta_f^{(n)} = \frac{\delta^n \beta}{\delta \omega^n}$

Equation 7.4 may be simplified into the form below:

$$\begin{aligned}\phi(\omega) = \phi_0 + [\tau(\omega_0) - T_0](\omega - \omega_0) \\ + \frac{1}{2} \cdot \beta_f^{(2)}(\omega_0) l_f (\omega - \omega_0)^2 + \frac{1}{6} \cdot \beta_f^{(3)}(\omega_0) l_f (\omega - \omega_0)^3 + ...\end{aligned} \tag{7.5}$$

where we have introduced the term ϕ_0, the delay (due to first order dispersion) in the fibre arm $\tau(\omega_0)$ and the delay in the air arm T_0. These terms are defined as follows:

$$\phi_0 = \beta_f(\omega_0) l_f - \frac{\omega_0 l_a}{c}, \tag{7.6}$$

$$\tau(\omega_0) = \beta_f^{(1)}(\omega_0) l_f, \tag{7.7}$$

$$T_0 = \frac{l_a}{c}. \tag{7.8}$$

When the delay in the air arm is equal to that of the fibre arm (i.e. $\tau(\omega_0) = T_0$), the second term in Equation 7.5 disappears, leaving us with the following expression:

$$\phi(\omega) = \phi_0 + \frac{1}{2} \cdot \beta_f^{(2)}(\omega_0) l_f (\omega - \omega_0)^2 + \frac{1}{6} \cdot \beta_f^{(3)}(\omega_0) l_f (\omega - \omega_0)^3 + ... \tag{7.9}$$

If we ignore the contribution from the $\beta_f^{(3)}$ term onwards (by assuming that $\beta_f^{(3)}$ and higher order dispersion terms are much smaller than $\beta_f^{(2)}$) we see that the interference pattern produced by Equation 7.9 will be symmetric about the central angular frequency ω_0. At this central frequency the delay in each of the interferometer arms is the same and thus the delay in the fibre arm may be obtained by equating it to the known delay in the air arm. By doing this for multiple wavelengths and using the relationship in Equation 7.1 the dispersion parameter D may be calculated for the given fibre.

Measuring the dispersion this way, while simpler, is not ideal as it is limited to wavelengths away from the zero dispersion wavelength. As D approaches zero so do does $\beta_f^{(2)}$ and thus the assumption that higher order β_f terms may be ignored as they are significantly smaller is no longer valid. This method was used initially to test and 'sanity check' the experimental setup at wavelengths where the fibre was expected to be highly dispersive. Once this was established the data analysis methodology was changed to instead evaluate the phase difference in a more direct fashion: by fitting an equation of the form given in Equation 7.2 to the interferogram obtained when the two arms are path matched. This allows for better measurement of the dispersion around the ZDW.

The interferogram fit was evaluated using a combination of the genetic algorithm curve fitting technique (see Section 4.5.2 for an overview of genetic algorithm based optimisation) and the nonlinear least squares method [243] – with the fitting function code provided by the optimisation toolbox package in MATLAB®[1]. Due to the highly oscillatory nature of the data it was difficult, in most cases, to determine appropriate initial guess values for the nonlinear least squares fitting function to be able to return a suitable fit to the experimental data. The genetic algorithm was therefore used to supplement this process – taking the initial guess values (determined based on a manually entered guess of the dispersion range for a given interferogram) and refining it before beginning the nonlinear least squares fit. The program exited the genetic algorithm if the relative fitness improvement from generation to generation was less than 0.001% after a maximum of 8 successive generations (the genetic algorithm was also set to time out at 3 minutes). The 'genes' from the member of the population with the highest fitness were then used as the guess values for the nonlinear least squares fit.

The genetic algorithm could have been used as the sole fitting method, however this would have been too slow. By using a combination of fitting techniques the program was able to evaluate a suitable fit to the experimental data in approximately 1 to 2 minutes for each interferogram.

Once the fitting of the experimental data was complete, the phase difference at the central wavelength of the interferogram was then used to determine the time delay (as a function of wavelength) via Equations 7.6 and 7.7; this time delay term was then differentiated as in Equation 7.1 to obtain the fibre dispersion.

[1]More details on the fitting functions provided in this software package may be found at http://www.mathworks.com.au/products/global-optimization/

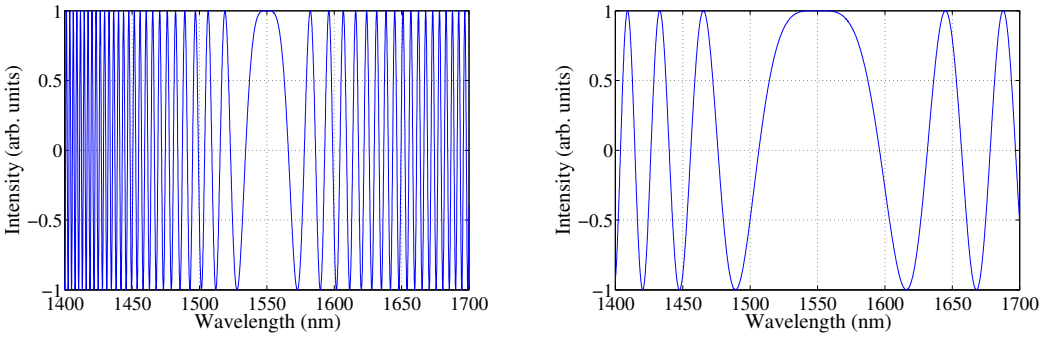

(a) (b)

FIGURE 7.2: Example of interferogram obtained for an imaginary 0.2 m fibre, path length matched at a central wavelength of 1550 nm. Figure (a) shows the case of a relatively high normal dispersion ($D = -80$ ps^{-1}nm^{-1}km^{-1})while Figure (b) corresponds to a relatively low normal dispersion ($D = -10$ ps^{-1}nm^{-1}km^{-1}). The greater number of fringes available when the dispersion is high makes the error of the fit lower.

However the relative accuracy of the measurement near the ZDW is still lower than for wavelengths further way due to the fact that the density of fringes in the interferogram is proportional to the absolute value of the dispersion, as seen in Figure 7.2. A denser fringe pattern provides more peaks for fitting and thus the oscillating cosine term in Equation 7.2 that contains the phase delay may be determined with a higher degree of confidence.

7.2.2 Experimental details

The optical source used in the experiment was a commercially available supercontinuum generator (KOHERAS SuperK™Compact) with a broad bandwidth, spanning from 500 nm to just over 1750 nm. The fibre output of this white light source was free space coupled out via a microscope objective before being split by a beam splitting cube to form the two arms of the interferometer – one of which contains the test fibre, while the other is free space and of adjustable path length.

In the fibre arm of the interferometer light was coupled into and out of the fibre via a set of lenses. At each end of the fibre, the lens and fibre end are placed on a nanostage that allows for three dimensional translation of the lens, relative to the fibre end. The fibre end was held stationary while the nanometre axis gauges on the stage are used move the lens and adjust the position of the focussed beam spot until light was optimally coupled

into the core of the fibre. Meanwhile, in the free space arm of the interferometer, a set of mirrors on a linearly translatable rail was used to vary the path length.

Light from the two arms was combined via another beam splitter before being coupled back from free space into a conventional silica fibre (SMF-28) which directs the light into an optical spectrum analyser (OSA). This apparatus is shown in Figure 7.3.

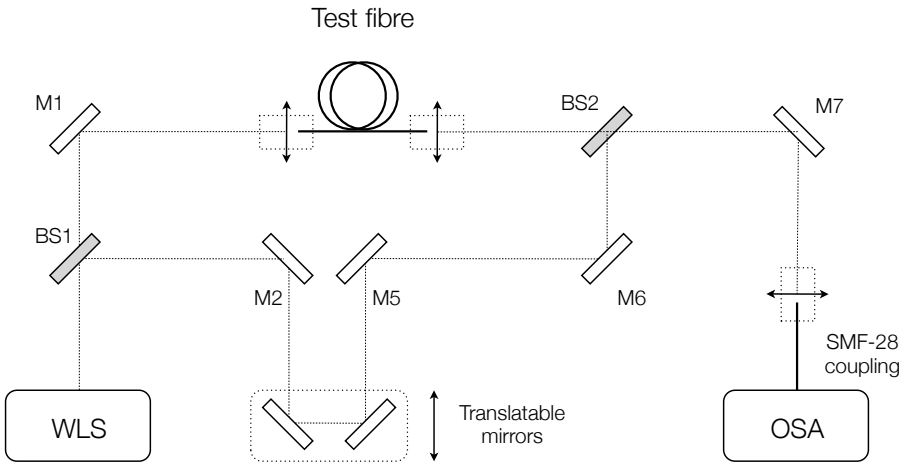

FIGURE 7.3: Experimental setup for interferometric measurement. In the diagram above WLS refers to the white light source; OSA to the optical spectrum analyser; M1 to M7 are mirrors; and BS1 and BS2 are 50:50 beam splitters. The dotted lines show the path of the beam.

Once the light has successfully been coupled into and out of the test fibre in that arm of the interferometer, the optical path in the free space arm must be adjusted until it equals that of the fibre arm. This was done by using a mechanical micrometer screw on the rail on which the translatable mirrors are mounted. These allow for the path to be adjusted on a micron scale. However, since it would be extremely cumbersome to adjust the optical path entirely via the micrometer the path length of the fibre arm is first measured to determine the approximate length required of the free space arm, to path match it with the fibre arm. The mirrors are then positioned at a value a few centimetres below this and adjusted upwards in small increments until the paths are matched.

At this point an interferogram can be seen on the OSA. Further adjustments of the path are then used to move the position of the central peak in the spectrum and thus generate a set of data from which the dispersion can be calculated.

Given the sensitive nature of this experiment the OSA must be capable of analysing and displaying the spectrum in real time – a monochromator based approach is too slow to pick up the interferogram in time, making it extremely difficult to find the path matched point. Consequently, in these experiments, a Ocean Optics USB2000 spectrometer that displayed the spectrum in real time was used. This spectrometer had a detection range from 350 nm to 1100 nm.

Once the measurement was complete the fibre end used in the experiment was cleaved off and a SEM image of its cross section was taken. This image was then imported into the finite element model and the dispersion was calculated for comparison with the experimental result.

7.2.3 Results

As mentioned above, the first step in measuring the dispersion is matching the optical paths of the two arms of the interferometer and then obtaining the interferogram. Figure 7.4 shows an interferogram obtained for the bismuth suspended core fibre.

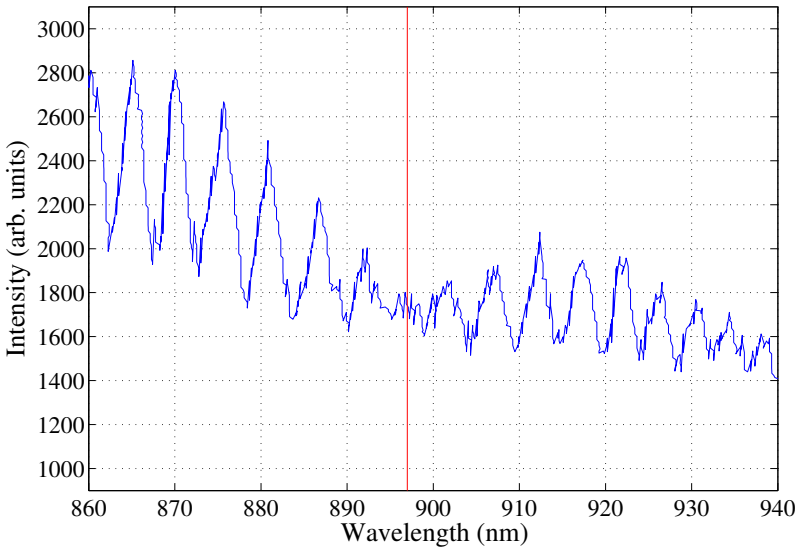

FIGURE 7.4: Interferogram obtained for the bismuth suspended core fibre. The central peak in this spectrum is at approximately 897 nm, as highlighted by the vertical red line.

The path length of the free space arm was then adjusted to move the central peak of the spectrum, with the results saved at each stage to build up a set of interferogram

measurements. Each of these measurements was then used to calculate a value for the dispersion parameter D, at the central wavelength of the interferogram.

The results of the dispersion calculation are shown in Figure 7.5 where the dispersion D has been plotted as a function of wavelength for two suspended core fibres, one fabricated with bismuth and the other with tellurite. We see good agreement between the calculated dispersion (solid black line) and experimentally measured values (blue points) – most of the experimentally measured data points are within 15% of the calculated values.

The results for the tellurite fibre in particular show that the agreement between measured and calculated dispersion is better when the magnitude of the dispersion is higher. However, this is not observed to the same extent in the graph for the bismuth fibre – most likely due to the higher concentration of data points measured for the tellurite fibre in the highly dispersive region.

This relative inaccuracy of the measurement near the ZDW is expected, since the interferogram broadens out as the dispersion approaches zero (as shown in Figure 7.2). This reduces the number of peaks in the measured spectrum and consequently reduces the confidence in the fit. A possible improvement to this technique (when measuring dispersion values close to zero) would be to insert a dispersive element (whose dispersion is well known) into the fibre arm to ensure that the magnitude of the net dispersion in that arm is of a sufficiently high value. This would increase the number of peaks in the spectrum (thus improving the confidence of the fit) and the known dispersion value can be subtracted off to obtain the fibre dispersion.

In addition to errors arising from the fitting procedure, the measured dispersion values may also differ from the values calculated from the fibre SEM due to variations in structural parameters (like core diameter) along the fibre length. The model assumes the geometry is fixed along the fibre length, whereas in reality there is always some structural variation – which is effectively averaged out in the measured dispersion value.

7.2.4 Summary of dispersion measurements

The dispersion has been measured for two microstructured fibres: one fabricated in bismuth and the other in tellurite; both were of the suspended core type geometry. The results, for both fibres, are shown to be in good agreement with the modelled dispersion

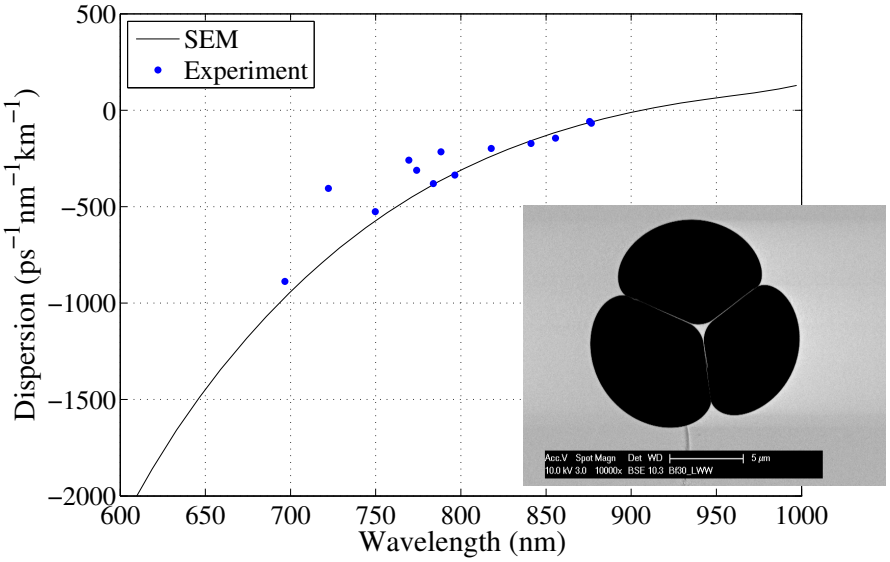

(a) Bismuth fibre

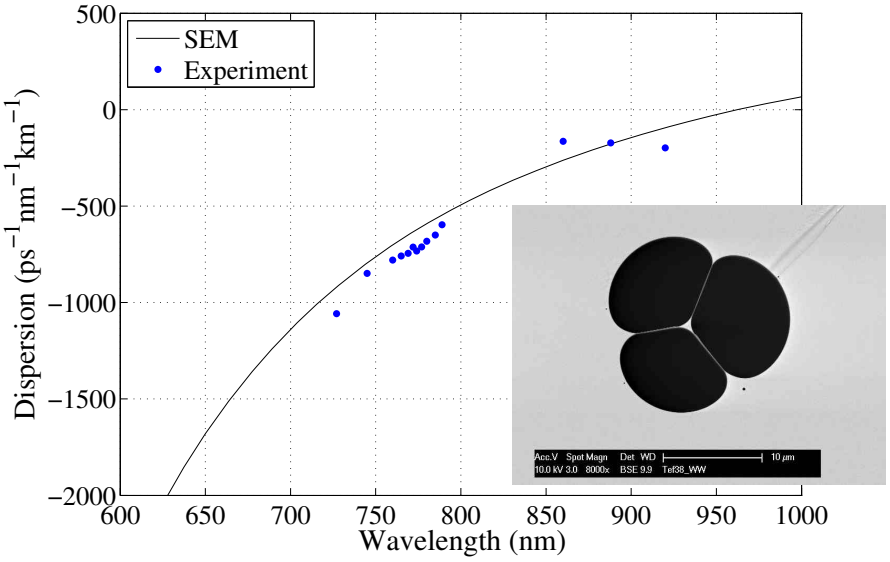

(b) Tellurite fibre

FIGURE 7.5: Dispersion results for (a) bismuth and (b) tellurite suspended core fibres. The solid line shows the dispersion as evaluated by modelling a SEM image of the fibre geometry (shown in the insets of each figure) while the dots correspond to experimentally measured points.

curves, with most of the data points within 15% of the value calculated from the SEM of the fibre geometry.

These measurements validate the modelling technique used to evaluate the dispersion of fibre design geometries, however more work is needed to both increase the accuracy of the experiment and extend the measurement range further out into the infrared. The

accuracy of the measurement could, for instance, be increased by using a beam splitter that sends more of the input beam into the fibre arm relative to the air arm instead of the 50:50 beam splitter used in this experiment (BS1 in Figure 7.3). This would compensate for the fact that the loss in the fibre arm is relatively much higher than in the air arm (where there is virtually no loss) and improve the signal to noise ratio of the interferogram. The measurement range of this experiment is limited by the long wavelength edge of the real time spectrometer (1100 nm) and may be increased by using a different real time spectrometer (such as the Ocean Optics NIRQuest series which can extend out to 2.6 µm [244]).

7.3 Nonlinearity measurement

As mentioned in Chapter 4, knowledge of the fibre nonlinearity (along with its dispersion profile) is extremely important in guiding the design of optical fibres for telecommunication applications. For four wave mixing applications, such as those studied in this work, the nonlinear coefficient γ is needed to evaluate the gain parameter in Equation 2.73. The nonlinear coefficient can also be used to measure the nonlinear refractive index (via Equation 2.33), thus making its measurement also useful for glass characterisation.

The following sections describe how the nonlinear coefficient was measured for a commercially available silica HNLF and a suspended core fibre fabricated in the GPNL5 lead germanate glass, introduced in Section 3.5. The measurement of γ for this novel germanate fibre was used to characterise the nonlinear refractive index of the glass (see Section for 3.5.4 more details).

7.3.1 Background

Several methods exist for measuring the nonlinear coefficient γ of an optical fibre, defined in Equation 2.33. They are generally either interferometric, or directly utilise nonlinear effects such as self phase modulation, cross phase modulation or four wave mixing.

When interferometric methods are used, the interferometer is set up to measure the nonlinear phase shift, i.e. the phase shift that results from the Kerr induced effect on the refractive index [111]). This may be written as

$$\phi = \gamma L_{eff} P, \tag{7.10}$$

where γ is the nonlinear coefficient, L_{eff} is the effective length and P is the average optical power. The effective length in this equation is the same as that defined in Equation 3.6. By measuring the phase shift for a given set of optical powers, on a fibre of known length and loss, the nonlinear coefficient may be calculated using Equation 7.10 above.

Various experimental configurations have been used in the literature to achieve this, including a Michelson interferometer [245], Mach-Zender interferometer [246] and a Sagnac interferometer [247]. In general these interferometric schemes are quite sensitive to environmental perturbations and experimental conditions. However work has been done with a 'self-aligning' interferometer [248] that uses a Faraday mirror to suppress the effect of environmental perturbations on the experiment.

The method used to determine nonlinearity in non interferometric experimental setups depends on the specific nonlinear effect being used. For instance, the spectral broadening on short optical pulses caused by either SPM [249] or XPM [250] can be used to measure γ. However this requires both an assumption or knowledge of the pulse shape and complex deconvolution to infer γ from the broadened pulses.

This experiment used the measurement technique first presented by Boskovic *et. al.* [166]. This method essentially measures the SPM induced phase shift on the beat signal of a pair of high power CW waves. The two closely separated waves at frequencies f_{P1} and f_{P2} are injected into the fibre to generate two FWM side bands at frequencies of $f_{S1} = 2f_{P2} - f_{P1}$ and $f_{S2} = 2f_{P1} - f_{P2}$. The relative intensity of the side bands compared to the pump is then used to measure the phase shift.

This is done using the shape of the spectrum – an example of which is shown in Figure 7.6. The Fourier transform of the electric field propagating down the fibre can be used to express the ratio of the side bands to pump intensities as [166]

$$\frac{I_{P1}}{I_{S1}} = \frac{J_0^2(\phi/2) + J_1^2(\phi/2)}{J_1^2(\phi/2) + J_2^2(\phi/2)}, \tag{7.11}$$

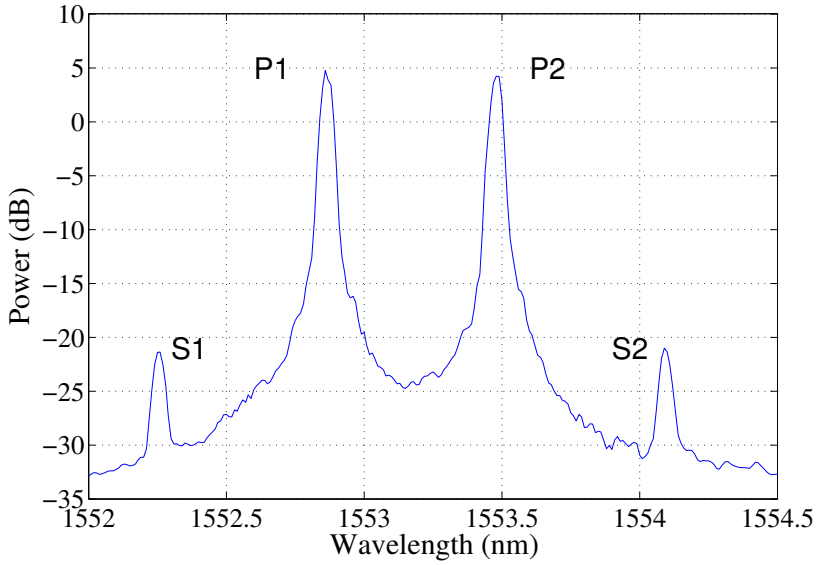

FIGURE 7.6: An example of a FWM spectrum that may be used to calculate the SMP induced phase shift and consequently the fibre nonlinearity. The pump waves that comprise the beat signal are labelled $P1$ and $P2$, while the FWM side bands are labelled $S1$ and $S2$.

where I_{P1} and I_{S1} are the intensities of the first pair of signal and side band, respectively. J_n are n$^{\text{th}}$ order Bessel functions and ϕ is the SPM induced nonlinear phase shift. By measuring the relative intensities of the signal and side band, the phase shift may be calculated by solving Equation 7.11. Note that as the left hand side of Equation 7.11 is a ratio of intensities the FWM spectrum may be measured in arbitrary units.

From this phase shift the nonlinear coefficient can be calculated using the following equation [166]

$$\phi = \frac{2\omega_0 n_2}{cA_{eff}} L_{eff} \overline{P} = 2\gamma L_{eff} \overline{P}, \tag{7.12}$$

where ω_0 and $\overline{P}$ are the central frequency and average power, respectively, of the beat signal; n_2 is the nonlinear refractive index; γ is the nonlinear coefficient; L_{eff} is the effective length of the fibre; and A_{eff} is the effective area of the mode propagating within the fibre. The effective area is the same as that defined in Equation 2.34, while the effective length is defined in Equation 3.6, in terms of the fibre length and the absorption coefficient. The fibre loss must therefore be known, to calculate γ via this technique.

Once the nonlinearity has been measured, it may then be used to calculate the nonlinear refractive index index via Equation 7.12. This method was used to characterise the nonlinearity of the GPNL5 germanate glass. These measurements are described in the following sections.

7.3.2 Experimental details

The experimental setup that was used to perform the measurement is shown in Figure 7.7. The input signal is made up of two laser beams from distributed feedback diode lasers operating at approximately 1.55 µm, with approximately ±5 nm of tunability around the central wavelength. The polarisation of the beams was adjusted via inline polarisation controllers to align the polarisation of the input beam to the principal axis of the test fibre. The polarisers also ensured that the two beams were identically polarised and of equal intensity.

The polarised beams were then amplified via an EDFA before being coupled into the test fibre. For this experiment the input power used was in the range from 500 mW to 1 W. The light is coupled into and out of the fibre via lenses and a free space segment. The lens L1 collimates the light coming out of the EDFA, which is then coupled into the test fibre through L2. Similarly L3 collimates the light coming out of the test fibre, which is then coupled back into the SMF-28 fibre leading into the OSA by the lens L4.

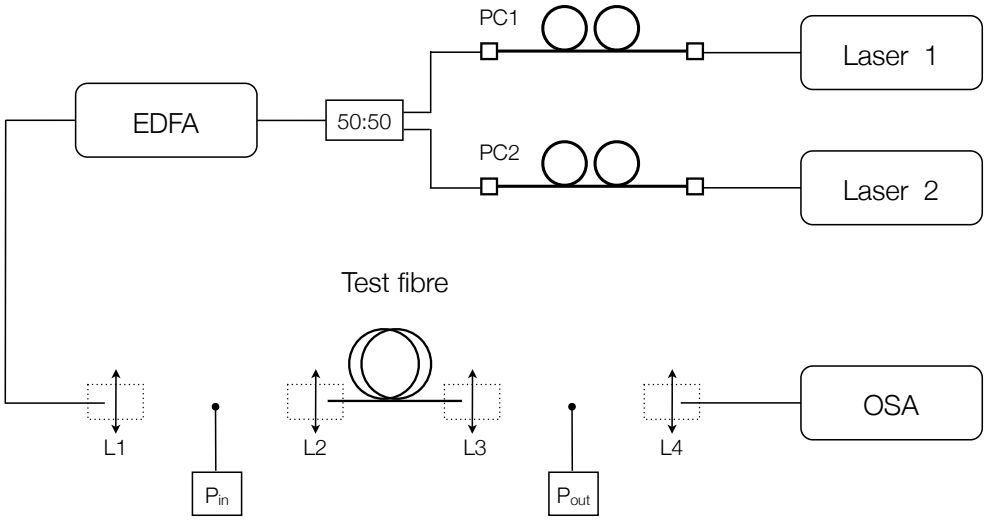

FIGURE 7.7: Experimental setup for nonlinearity measurement. In the diagram above EDFA refers to the erbium doped fibre amplifier; OSA to the optical spectrum analyser; PC1, PC2 are polarisation controllers; and L1, L2, L3, L4 are coupling lenses.

The power at both the input and output ends of the fibre was measured by placing a power meter in the free space segment next to the respective fibre end – for the input power this is the segment between L1 and L2 and for the output power it is the one between L3 and L4, as shown in the diagram above.

The measurement result does not explicitly depend on the frequency separation of the pump waves however, one of the key assumptions made in the derivation of Equation 7.11 is that the dispersion across the spectrum is the same. Therefore, by keeping the separation between the pumps to a few nanometres, the difference in dispersion across the spectrum is minimised. The stability of the spectrum is also improved by keeping the pump waves close together.

7.3.3 Results

The experiment was performed on two test fibres: the first was a commercially available silica nonlinear fibre (HNLF) manufactured by Corning; the second was a suspended core fibre made from the GPNL5 glass first introduced in Section 3.5. The first measurement was made on the HNLF fibre as the nonlinear coefficient for this fibre is provided by the manufacturer and thus it could be used to test that the setup could indeed accurately measure γ.

The nonlinear fibre used in this instance was a microstructured, high nonlinearity fibre with a manufacturer quoted length of 302 m, loss of 0.16 dB/m and nonlinear coefficient of 11 $\mathrm{W^{-1}km^{-1}}$. The fibre spool was placed in between the coupling lenses and light was coupled into the fibre using the lenses L2 and L3, whose numerical apertures matched that of the fibre.

The output spectrum was measured for a range of input powers, as shown in Figure 7.8. These spectra were then used to measure the intensity ratio between the pump peak and corresponding side band and calculate the nonlinear phase shift by solving the corresponding Bessel function, given by Equation 7.11.

Figure 7.9 shows the calculated phase shift for each output power. The slope of this line was used to extract the value for γ, as per Equation 7.12. For this fibre the nonlinearity was calculated to be $\gamma = 10.3 \pm 0.2$ $\mathrm{W^{-1}km^{-1}}$. This is quite close to the quoted value

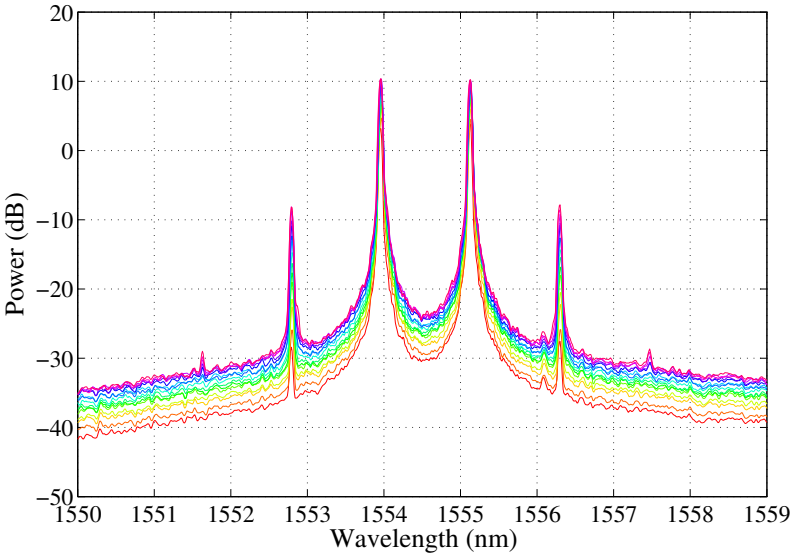

FIGURE 7.8: FWM spectrum for silica HNLF, with power specified as a dB ratio with an arbitrary reference. The pump peaks are visible at 1554 nm and 1555 nm while primary side bands are visible at 1553 nm and 1556 nm. For higher powers, a second set of side bands starts to appear at 1552.5 nm and 1557.5 nm. Note that, for clarity, the average power for each spectrum has not been labelled on this graph; these values are found on the x axis in Figure 7.9.

by the manufacturer of 11 $W^{-1}km^{-1}$ and thus shows that the experiment is able to accurately measure the fibre nonlinearity.

After measuring the nonlinearity for the HNLF, the test fibre was changed to be the germanate suspended core fibre. This fibre was made from the novel GPNL5 glass described in Section 3.5. Figure 7.10 shows SEM images of the fibre cross section.

Light was again coupled into this fibre using the same setup as before (albeit with difference lenses at L3 and L4 due to the smaller core and thus higher numerical aperture) and the output spectra were recorded by the OSA for various pump powers. These results are shown in Figure 7.11

As before, the spectra were then used to calculate the phase shift as a function of average power. These values are plotted in Figure 7.12.

For the silica HNLF, the loss of the fibre was known and the value for γ could thus be extracted from the phase shift curve with no additional measurements. For the germanate suspended core fibre however, this quantity was unknown so there was an extra step in the experimental procedure – performing a cutback loss measurement on the test fibre (see Section 7.4.1 for more information on this procedure).

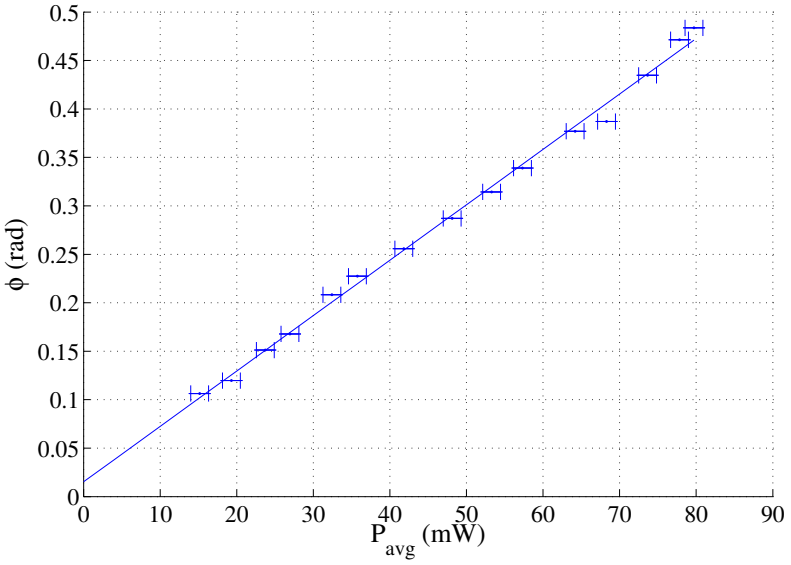

FIGURE 7.9: Phase shift measurement for silica HNLF. For this fibre length and loss were quoted by the manufacturer to be 302 m and 0.16 dB/m, respectively. This results in a nonlinearity value of $\gamma = 10.3 \pm 128$ W^{-1}km^{-1}. Note that the error bars for ϕ are too small to be seen on this graph.

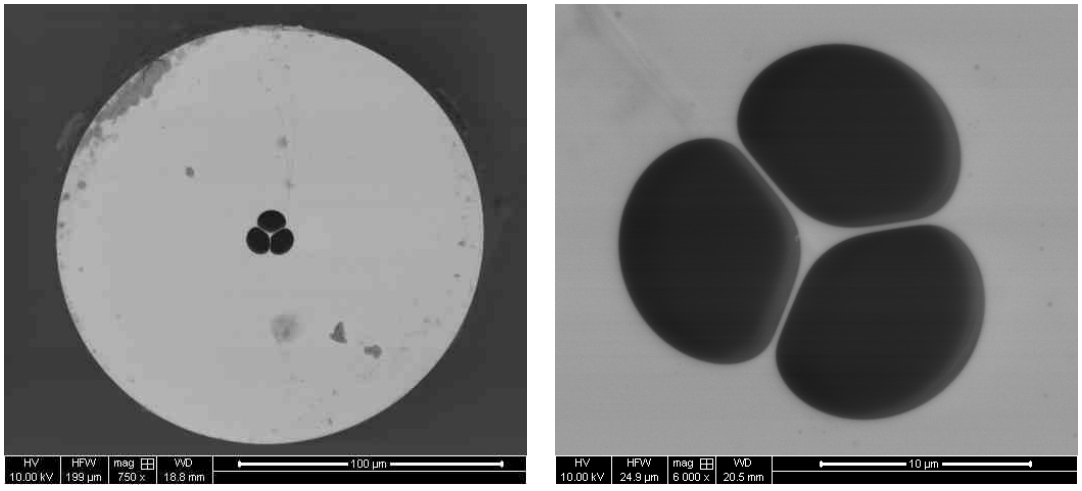

(a)) (b)

FIGURE 7.10: SEM images of GPNL5 suspended core fibre cross section. This fibre was used to measure the nonlinear index of this glass, via a nonlinearity measurement.

The loss, in this case, was measured to be 8.0±0.8 dB/m. Using this value with the slope of Figure 7.12 and Equation 7.12 gives a nonlinearity value of $\gamma = 1177 \pm 128$ W^{-1}km^{-1} for this germanate fibre. This value is significantly higher than that of the silica fibre and comparable to similar fibres made from other high index soft glasses such as tellurite.

Once the nonlinearity for the fibre had been measured, the tip was cleaved off and imaged with a SEM to obtain a scaled cross section of the fibre sample (the images produced

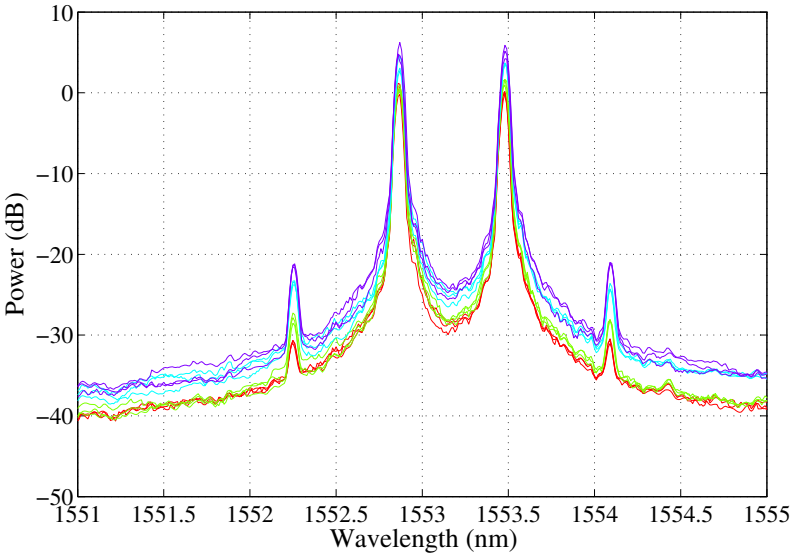

FIGURE 7.11: FWM spectrum for germanate suspended core fibre, with power specified as a dB ratio with an arbitrary reference. The pump peaks are visible at 1552.8 nm and 1553.5 nm while the side bands are visible at 1552.2 nm and 1554.1 nm. Note that, for clarity, the average power for each spectrum has not been labelled on this graph; these values are found on the x axis in Figure 7.12.

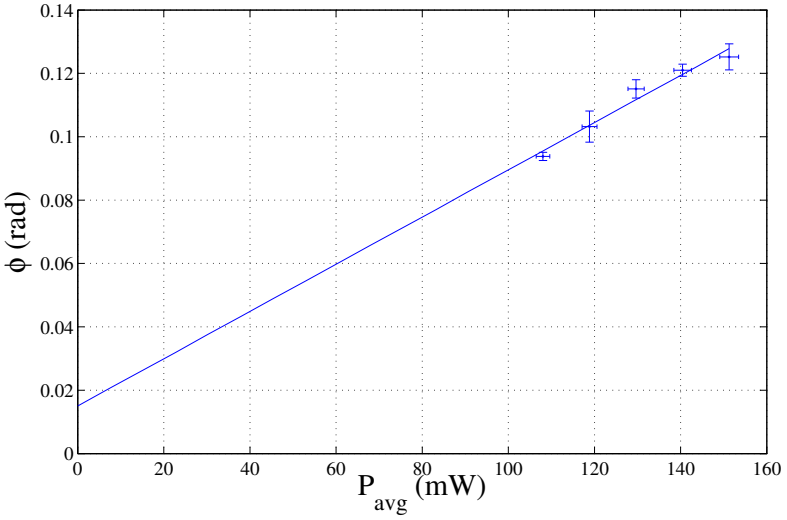

FIGURE 7.12: Phase shift measurement for germanate suspended core fibre. For this fibre, the length was measured to be 56.6 cm and the loss, α, to be 8.0 ± 0.8 dB/m. This results in a nonlinearity value of $\gamma = 1177 \pm 128$ W^{-1}km^{-1}.

were similar to Figure 7.10(b)). By then inserting this image into a finite element model the effective area of the fundamental mode, A_{eff}, was calculated. By then rearranging Equation 2.33 and using the values for γ and A_{eff} the nonlinear refractive index of this glass was calculated to be $n_2 = 56 \pm 6 \times 10^{-20}$ m^{2}W^{-1}. This value for n_2 agrees with previous measurements of the nonlinear refractive index for lead germanates by Hall *et.*

al. [148]; its significance has been discussed in Section 3.5.4.

7.3.4 Summary of nonlinearity measurements

The Boskovic method of using FWM to measure nonlinearity was used to to measure γ for a known silica HNLF and a new lead germanate suspended core fibre. The γ measurement for the silica fibre agrees well with the manufacturer quoted value, thereby validating the accuracy of the experiment. The γ measurement for the germanate fibre was used to measure the nonlinear refractive index of the glass – a measurement that agrees well with values found in the literature for similar glasses. This measurement also plays an important role in characterising these novel germanate glasses, showing that they have a high nonlinearity and thus have significant potential for use in nonlinear telecommunications devices.

7.4 Ge HWW loss measurement

This section details the loss measurement on the simplified hexagonal wagon wheel fibre fabricated in Ge-f23 fibre draw, shown in Figure 6.31. Recall that this was the second ever successful fabrication of a HWW fibre with the germanate glass. With such preliminary fibres, determining guidance and measuring the loss is the first characterisation stage. For this fibre the loss was measured using the cutback technique.

7.4.1 Background

The cutback technique is a widely used means of measuring the loss in optical fibres. The output power is measured through a fibre of a long initial length which is then cut back to successively shorter lengths with the power measured each time. When making one of these cutbacks, both the new output power and the length of fibre cut off are measured – resulting in a dataset that tracks power as a function of fibre length. These measurements may then be used to evaluate the fibre loss by starting with the relation

$$P(z) = P_{in}e^{-\alpha z}, \tag{7.13}$$

where P_{in} is the power coupled into the input end of the fibre, α is the loss coefficient and $P(z)$ is the power at the propagation length z. Taking the natural logarithm of each side gives

$$\ln[P(z)] = \ln P_{in} - \alpha z, \tag{7.14}$$

which is a linear function of propagation distance z with slope equal to the fibre loss coefficient $-\alpha$.

The major advantage of using the cutback method is that, since the cutbacks are made from the output end of the fibre, the coupling efficiency can be assumed to be constant throughout the experiment. However care must therefore be taken to ensure that the initial coupling is robust and that it is not disturbed when making the cutbacks. It is also important to ensure that, when cleaving the fibre to make a cutback, the quality of the cleave is consistent across cutbacks. The effect of cleave quality may be averaged out by making multiple cleaves for a given cutback length. The light source must also be stable and not fluctuate in power over the course of the measurement, as this would result in variations in P_{in} which would lead to errors in the final result.

The initial fibre length used in the measurement must be as long as possible – a longer fibre allows more cutback measurements to be taken, which increases the number of data points in Equation 7.14 and thus the accuracy in determining the slope. Due to the relatively high losses of microstructured optical fibres (compared to silica fibres) the fibre length must be short enough to have adequate power at the output (to make a reliable measurement) but long enough to be able to make enough cutbacks to confidently calculate the loss. Consequently balancing these criteria, for microstructured optical fibres, usually requires initial lengths of 1 to 5 meters depending on the loss of the fibre.

7.4.2 Experimental details

The experimental setup used is shown in Figure 7.13. The light source used was a DFB laser operating at 1.55 µm. Light from this source was collimated out and then coupled into the test fibre. At the output end of the fibre the light was collimated out again. An OSA was used initially to maximise the coupling into the test fibre as it has better

sensitivity than the power meter. For the rest of the measurement the output and input powers were measured via power meters at the positions shown on the diagram.

Care was taken with each cutback to ensure that the coupling into the fibre was not disturbed, and that light was coupled out onto the power meter with maximum efficiency.

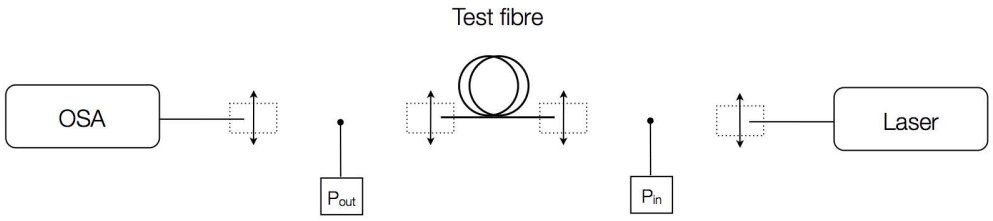

FIGURE 7.13: Experimental setup for loss measurement. The points marked P_{in} and P_{out} show where the input and output powers were measured.

7.4.3 Results

This results of the loss measurement are shown in Figure 7.14. The linear fit through the points gives a loss of 10.8 ± 1.3 dB/m for the loss of the fibre. This is obviously quite a high value, especially given that the unstructured fibres in this glass have losses of less than 2 dB/m at 1.55 µm (see Section 3.5.5.1). However, this fibre is only the second fibre with this structure that has ever been fabricated in this glass. The loss of the structured fibre may be reduced quite significantly, to match the less than 2 dB/m loss of the unstructured fibres, by improving the fibre fabrication procedure. Previous experience within the group has indeed shown this with fluoride glass based microstructured fibres [235].

We also see some scatter between some of the points and the linear fit, larger than the error bars for power. This indicates that the loss of this fibre varies somewhat along its length – again, this is due to the preliminary nature of this fibre and not a fundamental issue with the material or structure. This variation will likely also be reduced, by more fabrication iterations.

7.4.4 Summary of germanate HWW loss measurements

The loss of the Ge-f23 HWW was measured to be 10.8 ± 1.3 dB/m – a high value that is due to the preliminary nature of this fibre, given that this particular geometry

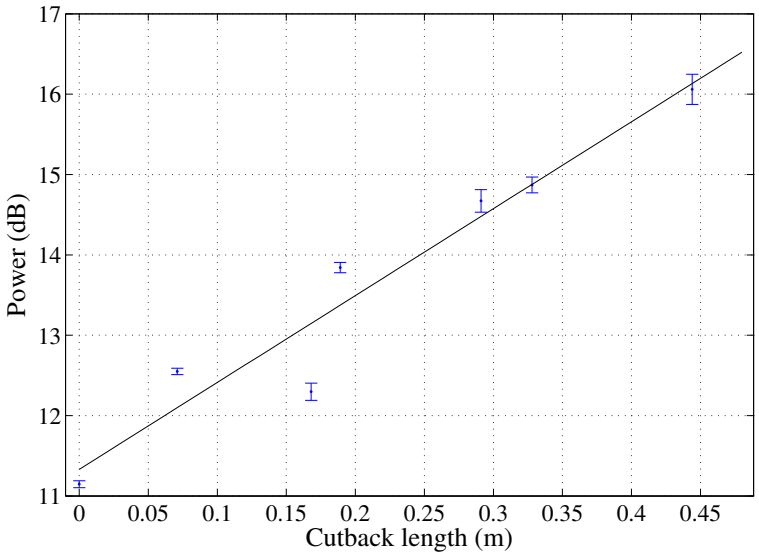

FIGURE 7.14: Loss curve for Ge-f23 HWW fibre, with power specified as a dB ratio with an arbitrary reference. The black line represents a linear fit of the data; its slope gives the loss as 10.8 ± 1.3 dB/m

had not been previously fabricated in this glass. Further iterations of the fabrication procedure are expected to be able to significantly reduce this number. Unfortunately the time frame of this research was not able to accommodate this, however this presents an interesting opportunity for further work.

7.5 Conclusion

This chapter has presented results on some fundamental fibre characterisation experiments. Results have been presented that show that the dispersion and nonlinearity for fibres has been accurately measured, and that these values agree well with simulations. This validates much of the modelling work done in earlier chapters which showed the potential for dispersion engineering in soft glass microstructured fibres for use in telecommunication applications.

In the next chapter, some further experimental work is presented, where HWW fibres fabricated in SF57 were used to generate dispersive waves using a Raman generated soliton. These experiments demonstrate how microstructured soft glass optical fibres may be used to convert a signal at infrared wavelengths to much shorter wavelengths via the generation of dispersive waves.

Chapter 8

Dispersive wave generation

8.1 Introduction

This chapter covers work done in collaboration with the research group led by Prof. Jay Sharping the University of California, Merced. This collaboration presented an opportunity to experimentally study nonlinear effects in dispersion engineered hexagonal wagon wheel fibres and demonstrate how these fibres may be used to generate new wavelengths via nonlinear effects. The planned experiments hoped to show four wave mixing and the generation of dispersive waves to demonstrate how dispersion engineered fibres can be used to generate frequency shifted waves in the IR region. Ideal fibres were not available for these experiments as this opportunity arose about halfway through this research project, and thus the combination of the zero dispersion wavelength of the fibre used in the experiments (calculated to be at 1614 nm; refer to Figure 8.4) and available laser wavelengths did not yield significant FWM results. However the experiments on dispersive waves did show significant frequency shifts of 250 nm to 400 nm using relatively low pump power of 100 W a short fibre length in the order of cm.

Although the physics behind this phenomenon and the results obtained are not in themselves novel, they are presented herein as these experiments still demonstrate how these fibres may be used to generate new wavelengths via nonlinear effects. Additionally the experiments were also used to validate the beam propagation model by comparing the simulations to experimental data. This comparison is an important validation of

the modelling technique, and thus an important check for the design and fabrication process.

This chapter is organised as follows: background information on the nature of solitons and specifically, how the dynamics of these unique pulses are related to the generation of dispersive waves is presented in Section 8.2. Section 8.3 describes the experimental setup used to generate solitons and then observe dispersive waves, followed by the results of the experiment in Section 8.4. These results show that dispersive waves are generated at wavelengths approximately 230 nm to 380 nm shorter than the Raman pump. To understand this process better and confirm that energy was indeed being dispersed from the soliton to shorter wavelengths the experimental data is analysed and tied back to theory and simulations in Section 8.5. The findings from this chapter are summarised in Section 8.6.

8.2 Background

The generation of dispersive waves is an interesting phenomenon that occurs in optical fibres when pulses that approximately match optical solitons are coupled into the fibre. This phenomenon (also known as nonsolitonic or Cherenkov radiation) is a consequence of soliton dynamics that arises due to combination of nonlinear and dispersive effects within the fibre. Dispersive waves are generated at wavelengths much shorter than the soliton wavelength and are thus a useful method of generating new frequencies of light. Analysis of the generation mechanism for wide band supercontinuum has also shown that dispersive wave generation may serve as a seeding process, resulting in extremely broad spectra, spanning many octaves from the ultraviolet all the way to the infrared [251–253].

In general, the term ‘soliton’ refers to a wave that maintains (or periodically recovers) its shape as it traverses through the medium. In optical media the stability of these solitons (which are solutions to the NSE) is due to the balancing of the pulse broadening caused by the nonlinear Kerr effect with the pulse compression caused by anomalous dispersion. The simplest instance of this is the fundamental soliton – where, for hyperbolic secant shaped pulses of certain widths, the broadening induced by nonlinearity is exactly cancelled out by the narrowing effect of anomalous dispersion such that the pulse travels

with constant temporal shape down the fibre. It is also possible to have higher order solitons where the pulse does not maintain a constant shape but rather, at periodic intervals (determined by the soliton order), the pulse recovers shape to match its initial form.

Dispersive waves emerge from solitons due to the remarkable stability of these waves. For a pulse to be a soliton, the pulse parameters must be such that the pulse narrowing effect of anomalous dispersion is balanced by the broadening effect of nonlinearity, either exactly (for a fundamental soliton) or periodically (for higher order solitons). What is remarkable is that, even if a pulse only approximately matches this soliton (or if an exact soliton solution is slightly perturbed) it will still evolve to match the closest soliton order that approximates its shape (see Section 8.2 for a theoretical description of this process). This behaviour has been studied analytically using perturbation theory [254, 255] and has also been seen experimentally [256]. As the pulse shape changes to match that of the soliton any excess energy (i.e. the energy that does not go into the soliton) is shed and this manifests as the dispersive wave. The closeness of the pulse shape to that of the ideal soliton determines how much energy is shed away into the dispersive wave – the better the match, the lesser the amount of energy in the dispersive wave (and vice versa). In addition to this, any further perturbations to the pulse (caused by, for example, changes in loss or dispersion along the fibre length) will result in more energy being transferred to the dispersive wave.

The wavelength at which the dispersive wave is produced depends on the dispersion profile of the fibre. For energy to be transferred to the dispersive wave in the normal dispersion regime, it must be phase matched with the soliton in the anomalous regime. This is known as the resonance condition and can be used to predict where dispersive waves may be generated (see Section 8.2.2 for more detail).

Thus, by engineering the dispersion profile of a microstructured optical fibre, one may use dispersive wave generation as a means to transfer energy from a femtosecond pump pulse to a desired shorter wavelength. This is useful for creating blue and ultraviolet pulses which have many applications in spectroscopy and sensing. Additionally dispersive waves may be used to translate the tunability of a infrared source to shorter wavelengths, in the visible and ultraviolet regions of the spectrum.

The transfer of soliton energy into dispersive waves also has implications for telecommunications systems where solitons are used to transfer information. The idea behind using solitons to increase the performance of high speed telecommunications networks was first proposed in 1973 [14, 257], as a way to overcome the limit imposed by dispersion on signal bandwidth. Unless the dispersion is constant over the signal band, the signal will distort (due to different spectral components travelling at at different speeds) – this is especially true for high speed networks with broad signal bandwidth. However, as solitons maintain their shape through propagation, they are essentially impervious to dispersion related distortion and thus may be used to increase both the performance and capacity of optical networks. Consequently, loss of pulse energy into dispersive waves is undesirable as it lowers the peak power of the pulse, forcing it to broaden to satisfy the soliton condition [34]

8.2.1 Solitons

As dispersive waves originate due to the pulse dynamics of a soliton propagating within a fibre, a theoretical description of this process first requires an understanding of the characteristics of a soliton. In particular, its form within an optical medium such as a fibre.

The first observation of a soliton actually dates back to 19$^{\text{th}}$ century Britain when, in 1834, a Scottish scientist by the name of Scott Russell made a serendipitous discovery while studying the motion of water in a canal. He was observing a boat being drawn along the canal by a pair of horses when it suddenly stopped. This motion caused the wave that was previously being dragged along behind the boat to build up into a 'state of violent agitation' and then continue to propagate down the waterway. Russell noted that the solitary wave maintained its shape and moved rapidly along the water as a large solitary wave for a few kilometres. In a report published many years later he would come to describe this phenomenon as a 'wave of translation' [258].

Since that time these waves have come to be known simply as solitons and have been discovered and studied extensively in many branches of physics and mathematics [259, 260], including optics [261, 262]. Optical solitons broadly fall into two categories: temporal solitons and spatial solitons. For temporal solitons the pulse maintains either a constant or periodic shape as it propagates over time; while for spatial solitons it is the transverse

profile of the beam that is either constant or periodic (due to a balance of the optical Kerr effect and diffraction) [263]. Temporal solitons can also either classed as bright or dark based on their intensity profile: bright solitons are just regular pulses (i.e. bumps in intensity) whereas dark solitons refer to pulses of optical 'darkness' (i.e. dips in intensity) that may exist within a wave [264, 265]. In the context of this work, bright temporal solitons are what is of interest and henceforth the term soliton refers to these.

The analytical form of the soliton is derived from the nonlinear Schrödinger equation (given earlier in Equation 5.1) using the inverse scattering method [266]. There are, in general, an infinite number of soliton solutions to the NSE. However, to summarise the features of these solitons, it is sufficient to consider a pulse with initial form (i.e. at propagation distance $z = 0$) given by [34]

$$U(0, T) = N \operatorname{sech}(T), \tag{8.1}$$

where the parameter T refers to the (retarded) time frame of the pulse, given by the relation

$$T = t - \frac{z}{v_g(\omega_0)}, \tag{8.2}$$

where ω_0 is the central pulse frequency and $v_g(\omega_0)$ is the group velocity of the pulse – physically, this time parameter T is a measure of time from the pulse centre.

N is an integer that specifies the order of the soliton (which relates to the number of poles in the direct scattering problem used to solve the NSE for the soliton). It is given by

$$N^2 = \gamma \frac{P_0 T_0^2}{|\beta^{(2)}(\omega_0)|}, \tag{8.3}$$

where P_0 the initial peak power, T_0 is the initial pulse width, γ is the nonlinear coefficient and $\beta^{(2)}(\omega)$ is the second order derivative of the propagation constant $\beta(\omega)$.

For the fundamental soliton $N = 1$ and it increases in integer values for higher order solitons ($N = 2$ for the second order soliton, $N = 3$ for the third order soliton and so

on). This soliton order specifies the relationship between pulse width and amplitude via Equation 8.3 – to launch a soliton of order N, the pulse parameters on the right hand side of this equation must evaluate to the value of the soliton order required; alternatively, for a given set of pulse parameters the soliton order is given by the solution to this equation.

As noted earlier, a remarkable property of solitons is that even if the pulse shape only approximately matches that of a soliton (i.e. N does not exactly evaluate to an integer) it will still evolve to match the soliton order that corresponds to the integer closest to the value of N. Indeed numerical pulse propagation based on the NSE can be used to show that a pulse of the form given in Equation 8.1 with $0.5 < N < 1.5$ will eventually form a fundamental soliton [34]. This also applies generally to all soliton orders, i.e. for any integer value of N, a pulse with $(N - 0.5) < N < (N + 0.5)$ will evolve to a soliton of order N. This behaviour may be explained using perturbation theory [254, 255] and has also been seen experimentally [256].

Physically, the formation of solitons in optical fibres occurs due to a combination of anomalous dispersion and Kerr nonlinearity acting on the pulse. For a fundamental soliton the pulse broadening due to the nonlinearity is countered by the pulse contraction caused by the anomalous dispersion in such a way that the pulse propagates with a constant shape. For higher order solitons the interplay between nonlinearity and dispersion is oscillatory – the pulse broadens, then contracts before broadening again in a repeating pattern that has a fixed period, determined by the soliton order.

8.2.2 Dispersive wave generation

If a pulse with a hyperbolic secant shape matching Equation 8.1 and pulse parameters such that $N > 1$ is launched into an optical fibre, it will propagate as a higher order soliton – which is an unstable, degenerate solution of the NSE [267]. Once the higher order soliton forms, it is perturbed by a combination of dispersion and the nonlinear response, which leads to an effect known as self steepening (or the self frequency shift) of the soliton [268, 269]. Since the higher order soliton solution is not stable in the presence of perturbations [270, 271], a process known as soliton fission then occurs. During soliton fission the soliton of order N first decays into an order $N-1$ soliton and a fundamental soliton. This process then continues for the remaining higher order solitons

until the initial soliton of order N has split a set N fundamental solitons. Essentially, self steepening breaks the degeneracy within the higher order soliton, releasing it from the bound state to its constituent fundamental solitons [34, 267].

Dispersive waves are generated during this soliton fission process and also arise from further perturbations to the fundamental solitons – they essentially manifest due to the energy that leaks from the perturbed solitons. The wavelength at which these dispersive waves are generated may be predicted analytically by solving the nonlinear Schrödinger equation. This process is summarised here using the results and formalism presented in References [272, 273].

In the presence of perturbations, the NSE may be written as

$$i\frac{\partial U}{\partial z} + \frac{1}{2}\frac{\partial^2 U}{\partial T^2} + |U|^2 U = \epsilon \widehat{P}(U), \tag{8.4}$$

where the perturbative operator $\widehat{P}$ has been included in the right hand side, along with the parameter ϵ which determines the magnitude of the perturbation – for solitons to exist, this parameter must be below a certain threshold [274]. Note that in Equation 8.4 T again refers to the reference frame of the pulse as in Equation 8.2.

The general solution to Equation 8.4 is of the form

$$U(z,T) = A(z)\,\mathrm{sech}[A(z)(T - q(z))]\exp[i\phi(z) - i\delta T], \tag{8.5}$$

where parameters have been introduced that correspond to physical pulse parameters such as pulse amplitude A, frequency δ, peak position q and phase ϕ. These parameters may be solved by using a variety of perturbation techniques [1] that result in a set of four ordinary differential equations – one for each parameter. The details of these derivations include quite complex mathematics and is beyond the scope of this work, however details may be found in References [272, 273, 275].

If the perturbation is assumed to be due to the effect of the third order dispersion, the perturbative term in Equation 8.4 becomes

[1] Methods for solving the perturbed NSE include the adiabatic perturbation method, the perturbed inverse scattering method, the Lie-transform method and the variational method [273]

$$\widehat{P} = i\frac{\partial^3}{\partial T^3}. \tag{8.6}$$

This relation, coupled with the ordinary differential equations for the pulse parameters may then be used to obtain an expression for the soliton wave number; while the wave number of the dispersive wave is found by substituting the form of a linear dispersive wave, $\exp[i(k_{DW}z + \omega t]$, into Equation 8.4 and neglecting the nonlinear term (again details may be found in References [272, 273, 275]). The phase terms for the soliton and linear dispersive waves may be equated to obtain the phase matching condition which gives [272, 276]

$$\beta(\omega_S) - \beta(\omega_{DW}) = \frac{\omega_S}{v_{g,s}} - (1 - f_R)\gamma P_S - \frac{\omega_{DW}}{v_{g,s}} = 0, \tag{8.7}$$

where ω_{DW} is the central angular frequency of the dispersive wave, ω_S is that of the soliton, β is the propagation constant, $v_{g,s}$ is the group velocity at the soliton frequency, γ is the nonlinear coefficient, P_S is the soliton peak power and f_R is the Raman fraction (which accounts for the fractional contribution of the Raman response). This relation may be used to predict the wavelength at which dispersive waves are generated.

In the absence of perturbations the right hand side of Equation 8.4 is simply zero and the general solution may be written as

$$U(z, T) = A\,\mathrm{sech}(AT)\exp(ik_S z), \tag{8.8}$$

where the z dependence of the pulse amplitude has been dropped as the pulse amplitude remains constant. The wave number of this soliton is $k_S = A^2/2$ [272]; while a dispersive wave of the form $\exp[i(k_{DW}z + \omega t]$ has a wave number $k_{DW} = -\frac{1}{2}\omega^2$ [272] – as $k_{DW} < 0$ and $k_S > 0$ the soliton can never be phase matched to the dispersive wave and is therefore stable. The effect of perturbations is to add an $O(\epsilon)$ term to the linear wave number that allows the dispersive wave to be phase matched to the soliton – thus enabling energy from the soliton to be transferred to radiation at ω_{DW}

While Equation 8.7 is an useful analytical predictor of where dispersive waves may be generated, it only includes the effect of dispersive perturbations, up to third order. It is

really only valid when soliton fission is the governing decay process for the initial higher order soliton. As the soliton power increases, higher order $\beta^{(n)}$ terms and nonlinearity have an increasing effect, which changes the wavelength of the dispersive wave.

Higher order dispersion, for instance, has the effect of red-shifting the dispersive waves to longer wavelengths [252]. On the other hand, it has also been shown that nonlinear effects such as cross phase modulation result in a blue shift. Where dispersive waves are part of the supercontinuum seeding precess, this has the effect of extending out the spectrum into shorter wavelengths [252, 277].

A surer means of predicting the location of the dispersive waves is to solve the NSE numerically as this takes into account higher order dispersion and nonlinear effects. In Section 8.4 this numerical investigation is performed and the results are compared to those obtained experimentally.

8.3 Experimental details

The experimental setup consisted of two parts – a 500 m length SMF silica fibre and the nonlinear microstructured fibre. The silica fibre was used to generate a soliton pulse using stimulated Raman scattering, which was then injected into the MOF and used to generate dispersive waves. A diagram of the experimental setup is shown in Figure 8.1

The soliton is generated in the silica fibre via the stimulated Raman scattering (SRS) phenomenon [176] – where the interaction of the strong pump wave with the vibrational modes of medium scatters photons into a frequency down shifted Stokes wave. The Stokes wave then continues to propagate down the fibre and may be used for many applications, notably spectroscopy [169–171] and in the making of Raman lasers [172, 173] and amplifiers [174, 175].

The wavelength at which the Stokes wave is formed depends on the Raman gain spectrum of the medium [278, 279] which is given by the Raman gain coefficient, plotted as a function of frequency shift (relative to the pump). This spectrum determines the frequencies for which the gain of the Stokes wave is highest. We may describe the evolution of the Stokes wave and pump wave by

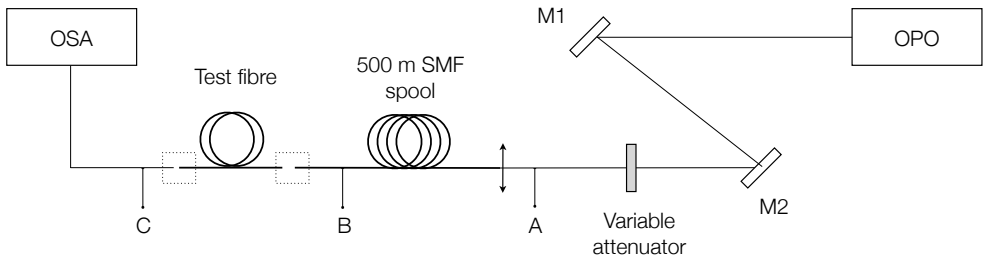

FIGURE 8.1: Experimental setup for dispersive wave generation. An OPO was used to pump a 500 m length of silica SMF to generate a Raman soliton which was then injected into a soft glass MOF test fibre to generate dispersive waves. The OPO beam is coupled into the SMF at the point A, the Raman soliton is coupled into the test fibre at the point B and the final spectra with the dispersive waves are measured by coupling the light into an OSA at point C.

$$\frac{dI_s}{dz} = g_R I_s I_p - \alpha_s I_s, \tag{8.9}$$

$$\frac{dI_p}{dz} = -\frac{\lambda_s}{\lambda_p} g_R I_p I_s - \alpha_p I_p, \tag{8.10}$$

where I_p, I_s and α_p, α_s refer to the intensity and loss at the pump and Stokes wavelengths (the subscripts p and s denote the pump and Stokes waves, respectively), g_R is the Raman gain coefficient and z is the propagation axis. The terms containing α in the equations above account for the fibre losses and pump depletion, which reduces the energy available to be transferred to the Stokes wave. In addition to this, any remaining energy not transferred to the Stokes is lost as phonons into the fibre – this manifests as heat within the fibre and may even cause damage [176].

The resulting Raman gain spectrum looks like that in Figure 8.2, which shows the well known Raman gain for fused silica glass (this data was obtained from Reference [8]). Spontaneous Raman scattering occurs across the bandwidth of the spectrum (approximately 40 Thz in this case). However, since the gain is highest for those photons near the peak of g_R, the intensity rises exponentially at this point, once the Raman threshold has been reached [34, 176].

For an input pump pulse in the anomalous dispersion regime of the fibre the generated Raman pulse can, under the right conditions, continue to propagate along the fibre as a fundamental soliton. For this to occur the propagation distance at which the Raman pulse forms must also be approximately the point at which the pump pulse has

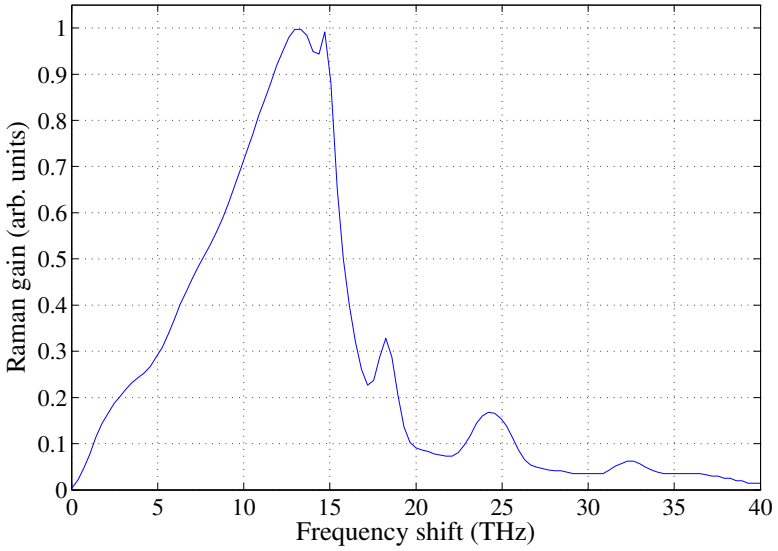

FIGURE 8.2: Raman gain spectrum for fused silica, normalised to the maximum gain [8]. Note that the pump and Stokes are polarised along the same axis for this measurement and thus this represents the maximum Raman gain possible for this material.

been compressed (by the anomalous dispersion) to its minimum temporal width – in such a scenario almost all the energy from the Raman pulse may be transferred to the fundamental soliton [34]. In quantitative terms, this condition is said to be met when the dispersive length of the fibre L_D is approximately equal to the walk off length L_W; these parameters being defined as

$$L_D = \frac{T_0^2}{|\beta_p^{(2)}|}, \tag{8.11}$$

$$L_W = \frac{T_0}{|d|}, \tag{8.12}$$

where T_0 is the initial width of the pump pulse, $\beta_p^{(2)}$ is the second order derivative of the pump propagation constant (evaluated at the pump frequency) and d accounts for the difference in the group velocity of the pump $v_{g,p}$ and the group velocity of the Raman pulse $v_{g,r}$ by the relation

$$d = v_{g,p} - v_{g,r}. \tag{8.13}$$

For the condition $L_D \approx L_W$ to be met, the input pump pulses must be of a certain width, determined by the dispersion of the fibre – for silica, this is approximately a few 100 fs [34]. Thus, by pumping the fibre with pulses of the appropriate width, the SRS effect may be used as a method to generate high powered solitons.

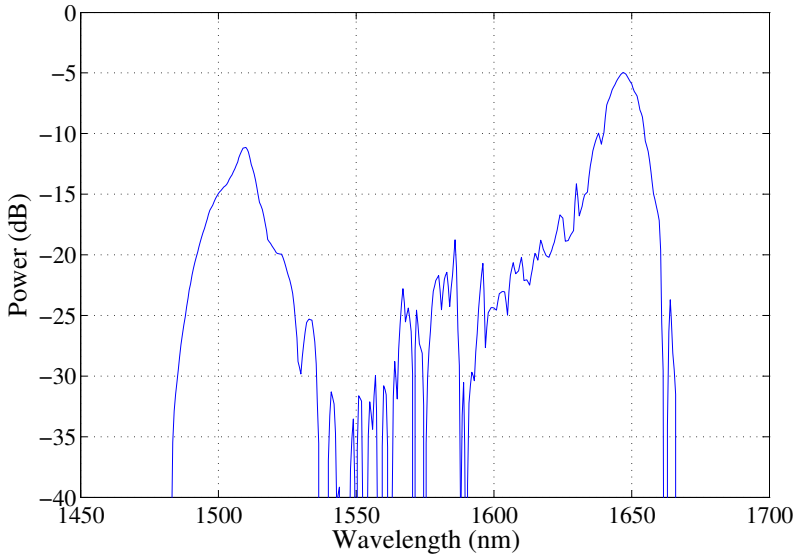

FIGURE 8.3: The spectrum obtained from the SMF spool, i.e. measured at the point B in Figure 8.1, with power specified as a dB ratio with an arbitrary reference. The generated Raman soliton is seen at approximately 1650 nm. This soliton (along with the residual pump) was used as input to the MOF to generate dispersive waves.

In this experiment, the silica fibre was pumped by the output from a laser driven optical parametric oscillator (OPO), which produces a 300 fs pulse train at 80 Hz with an average power of 100 mW and a central wavelength that may be tuned from 1100 nm to 1700 nm. The width of these pulses is ideal for the generation of Raman solitons so the pump wavelength was set to 1550 nm (which is in the anomalous GVD region for SMF fibre) and used to generate a Raman soliton at around 1650 nm.

The wavelength of the Raman soliton was tuned by moving the pump wavelength, however this also affected the pump power within the fibre as it changed the effectiveness of the coupling of the pump into the fibre. Consequently each time the pump wavelength was tuned both the pump power and wavelength changed – both parameters affect the wavelength of the soliton as increasing pump power results in more intrapulse Raman scattering [280, 281] – a form of self induced SRS. In this case, the pump pulse broadens (in frequency) initially and the long wavelength side of the spectrum acts as a seed for Raman amplification, drawing energy from the blue tail of the spectrum. As the pulse

continues to propagate down the fibre energy is continually funnelled from the short wavelength side to the long wavelength side via the Raman shift, thus moving it to longer wavelengths. This is referred to as the soliton self frequency shift [268, 282, 283]. The combination of intrapulse Raman scattering and the soliton self frequency shift have proven to be a extremely useful method by which to generate tunable lasers with narrow temporal width pulse trains [284–287]. The work of Hartig and Schmidt in Reference [285] is particularly notable as they demonstrate a Raman laser pumped by a high power dye laser and tunable without gaps over an extremely broad wavelength range of 0.7 µm to 7 µm.

In this experiment, the Raman soliton was tuned within the silica fibre over a range of approximately 1650 nm to 1750 nm (some of this soliton tuning is shown in in Figure 8.5). This soliton pulse was then used as input into a hexagonal wagon wheel type MOF and used to generate dispersive waves.

The HWW fibre used in this experiment was originally fabricated by a colleague, Wen Qi Zhang, for coherent supercontinuum generation in the infrared [197, 207]. This fibre was made with commercially available SF57 glass and is shown in Figure 8.4 along with its dispersion profile.

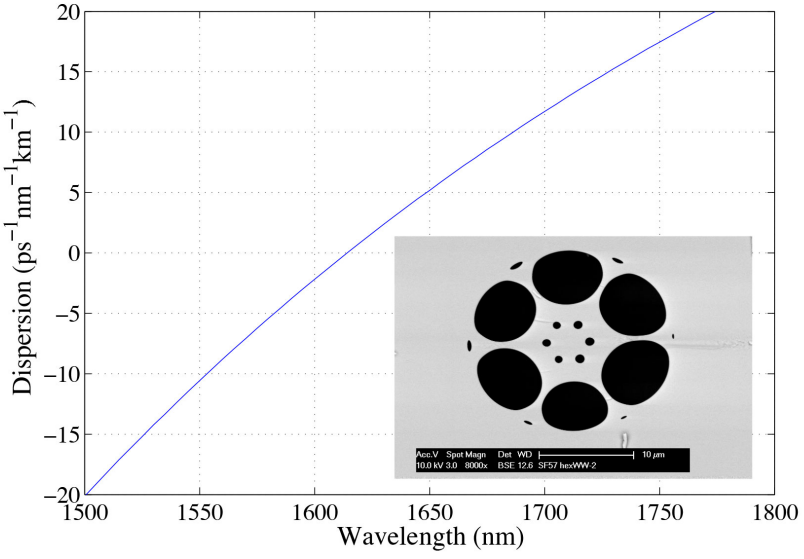

FIGURE 8.4: The dispersion profile of the SF57 HWW fibre used in the experiment. The zero dispersion wavelength is at 1614 nm. The inset shows a cross section of the fibre core region.

The dispersion curve in Figure 8.4 shows that this fibre has a zero dispersion wavelength of 1614 nm, which means the Raman solitons generated in the silica MOF would all be in

the anomalous dispersion regime of the fibre and would thus propagate as higher order solitons in the MOF.

8.4 Results

As described earlier, the experiment consisted of two stages. In the first stage a Raman soliton was generated in a 500 m length of SMF fibre by pumping the fibre with a 300 fs pulse from an OPO; while in the second stage the Raman soliton was coupled into a SF57 MOF to generate dispersive waves.

Results from the first stage of the experimental setup (i.e. at the point marked B in Figure 8.1,) are shown in Figure 8.5. This figure shows that the central wavelength of the soliton could be tuned by varying the pump wavelength from the OPO [2]. Indeed the wavelength of the soliton is extremely sensitive to the position of the pump peak – changes in the pump peak over a range of less than 3 nm, are sufficient to tune the Raman soliton over a 50 nm range. Further tuning of the Raman soliton, into longer IR wavelengths would have been possible, however this experiment was limited to wavelengths less than 1768 nm due to the detection limit of the spectrum analyser.

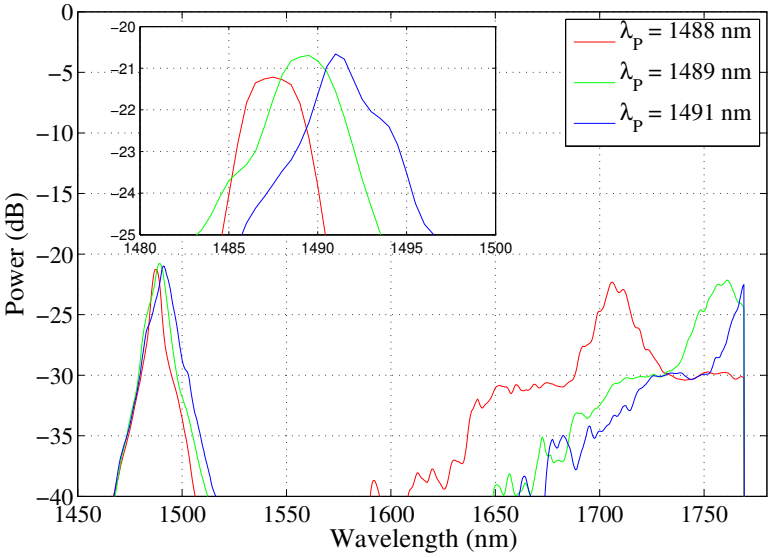

FIGURE 8.5: The effect of varying both pump power and wavelength (simultaneously) on the position of the Raman soliton, with power specified as a dB ratio with an arbitrary reference. The inset shows a zoomed-in version of the pump peak, highlighting how relatively small changes to the pump wavelength λ_P and power were used to tune the soliton peak over a 50 nm range. The cut-off in the spectrum at 1768 nm is due to the detection limit of the OSA.

Once successful generation of the Raman soliton was observed, the light was coupled into the MOF. The wavelength of the Raman soliton was then varied and the spectrum

[2] as changing the OPO wavelength also affects the coupling into the SMF simultaneous variation of the pump wavelength and power was unavoidable

from the output of the MOF was measured each time via the OSA (this spectrum is measured at the point labelled C in Figure 8.1). The results are shown in Figure 8.6. It shows the Raman soliton in the wavelength range from 1680 nm to 1780 nm and the generated dispersive waves in the 1350 nm to 1450 nm region. The residue of the pump is also observed at around 1560 nm. Ideally the pump residue would have been filtered from the spectrum before the light was coupled into the MOF stage but, due to equipment constraints at the time of making these measurements, an appropriate filter was not available.

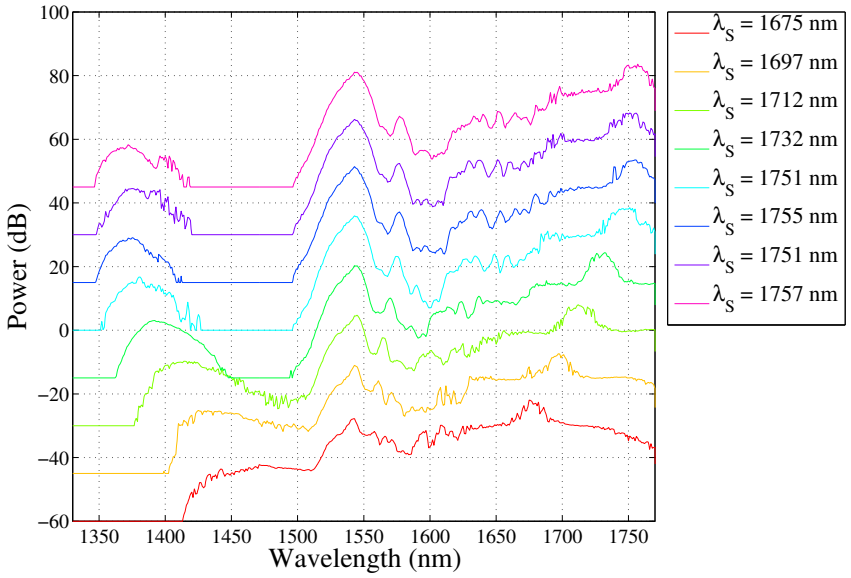

FIGURE 8.6: Results from the experiment showing dispersive waves generated in the soft glass MOF in the wavelength region from 1350 nm to 1450 nm when pumped with solitons in the 1680 nm to 1780 nm range. The spectral power is specified as a dB ratio with an arbitrary reference. The central peak of the soliton λ_S is given in the legend. The residue of the OPO pump that was used to generate the soliton is also seen at around 1560 nm, as equipment to filter this residue was unavailable at the time.

These spectra in Figure 8.6 show clear signs of soliton dynamics – we see that, as the soliton moves to longer wavelengths, the generated dispersive waves move to shorter wavelengths, as expected.

To better understand the nonlinear effects occurring within the MOF the propagation of the Raman soliton was simulated using the generalised NSE. This pulse propagation algorithm is the same one used to obtain the results shown in Chapter 5 (see Section 5.2 for details on the pulse propagation model).

8.5 Comparison to theory and simulations

When analysing these results for dispersive waves, a first point of comparison is the resonance condition given in Equation 8.7. This equation may be used to analytically predict the position of dispersive waves, given a set of pump waves and fibre dispersion. However, as mentioned earlier, simplifications (such as no 4^{th} order or higher dispersion) were made in deriving this relation. A full pulse propagation model of the NSE, on the other hand, may be expected to provide better agreement with experimental results since it includes many of the effects not considered in the analytical description (such as higher order dispersion).

To effectively model the soliton dynamics within the MOF using the pulse propagation model the input conditions to the fibre must first be determined, i.e. the central wavelength, pulse width and peak power of the soliton at the fibre input.

Due to the fact that the SMF was butt-coupled into the soft glass MOF measuring these soliton parameters directly was not possible – doing so would require recoupling the SMF to the MOF each time. This recoupling would result in a different coupling coefficient (between the SMF and the MOF) each time and thus render the results incomparable.

The soliton parameters were instead approximated by first calibrating the output spectra from the MOF, using this to quantify the power of the soliton at the output end of the fibre, and then working back using the (previously measured) fibre loss and length to calculate the input power.

The OSA was calibrated using an IR power meter and the output spectrum from the SMF stage (i.e. at point B in Figure 8.1). This spectrum, shown in Figure 8.7, was measured at the start of the experiment, before the SMF was first butt-coupled into the MOF. Any of the output spectra from the MOF could also have been used for calibration, but since they have much lower average power they result in less accurate readings on both the power meter and, to a lesser extent, on the OSA.

The process of calculating the soliton parameters was as follows.

1. The energy of the spectrum is calculated using the measured average power and the known value of the OPO pulse repetition rate.

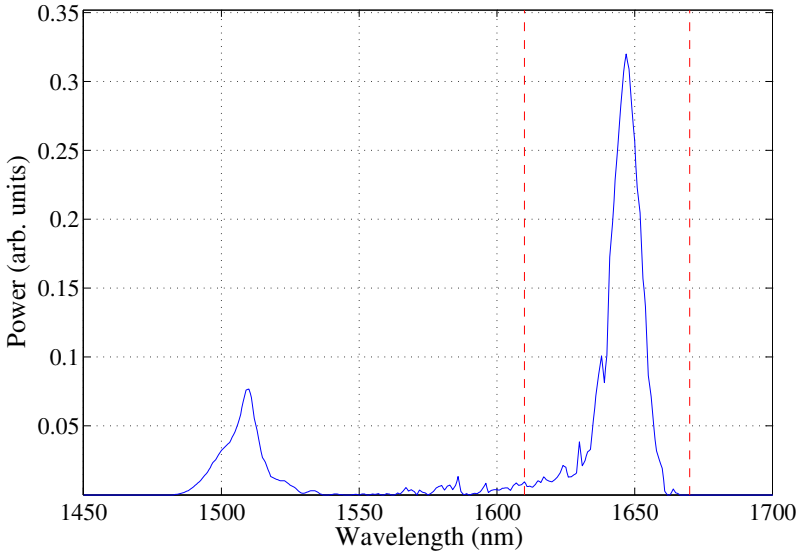

FIGURE 8.7: The power spectrum measured after the SMF. The red dotted lines indicate the spectral edges of the soliton.

2. The energy of the soliton is calculated by integrating the area of the spectrum corresponding to the soliton and comparing it to the total integral.

3. The temporal width of the soliton is calculated by fitting a fundamental soliton form to the soliton spectrum and performing a Fourier transform of the fitted sech^2 pulse to the time domain.

4. The peak power of the soliton is then evaluated by integrating the fitted soliton from the previous step such that it matches the soliton energy calculated in step 2.

For example, applying the procedure above to the calibration curve in Figure 8.7 yields the following results: The power reading for this spectrum is 36 mW which, coupled with the 75 MHz repetition rate of the OPO source, gives an average power of 480 pJ per pulse, across the spectrum. The region of the spectrum corresponding to the soliton (demarcated by the vertical dashed lines in Figure 8.7) is 75% of the total integral, which implies that the average power of each soliton pulse is 360 pJ. Fitting a sech^2 pulse to the soliton spectrum (as demonstrated in Figure 8.8) and transforming to the time domain then gives a full width at half maximum value for the soliton of 131 fs. Finally integrating this to give a pulse with 360 pJ of energy gives a peak power of approximately 1330 W.

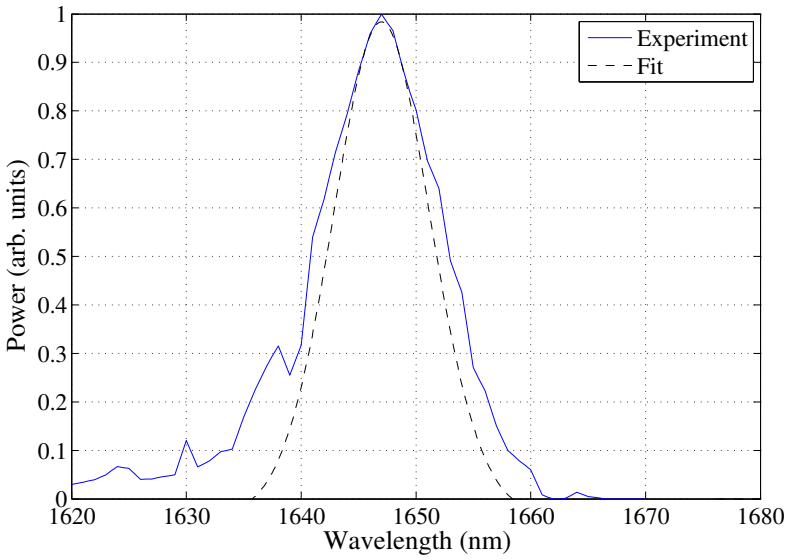

FIGURE 8.8: Normalised soliton spectrum along with the theoretical pulse fit used to calculate the pulse width. The fitted pulse may be transformed back to the time domain to obtain the pulse width, calculated to be 131 fs for this pulse.

The procedure described above was applied to each of the spectra from Figure 8.6 to calculate the peak power and width of the soliton at the output end of the MOF. The peak power at the input end of the fibre was then calculated by using Equation 4.2 and the known values for the fibre length and loss – 27 cm and 4.5 dB/m, respectively. These results are summarised in Table 8.1, which also gives the values for the central wavelength for the soliton and dispersive wave peaks, extracted from the spectra.

		Soliton			Dispersive wave
Peak (nm)	Energy (pJ)	$P_{avg,out}$ (µW)	$P_{peak,out}$ (W)	$P_{peak,in}$ (W)	Peak (nm)
1675	12.54	0.940	84.37	111.6	1441
1697	13.36	1.002	89.86	118.9	1420
1712	12.98	0.974	87.31	115.5	1402
1732	13.58	1.018	91.32	120.8	1392
1751	13.25	0.994	89.10	117.9	1381
1755	13.54	1.017	91.08	120.5	1375
1751	10.37	0.777	69.72	92.22	1379
1757	12.84	0.963	86.33	114.2	1372

TABLE 8.1: This table shows the measured peak wavelength for the soliton (first column) and dispersive wave (last column) for the experimental dataset shown in Figure 8.6. The table also shows the calculated power values for the soliton. These values for the input peak power, $P_{peak,in}$, were used in a pulse propagation model to match numerical data to the experiment.

The calculated values for soliton wavelength and peak power shown in Table 8.1 were used to build an input pulse profile that could then be fed into the pulse propagation algorithm. This modelling exercise was used to confirm that the short wavelength peaks in the experimentally observed spectra were indeed dispersive waves generated by the soliton. Along with the input pulse profile, the other major inputs to this model were the fibre dispersion, nonlinearity, length and loss.

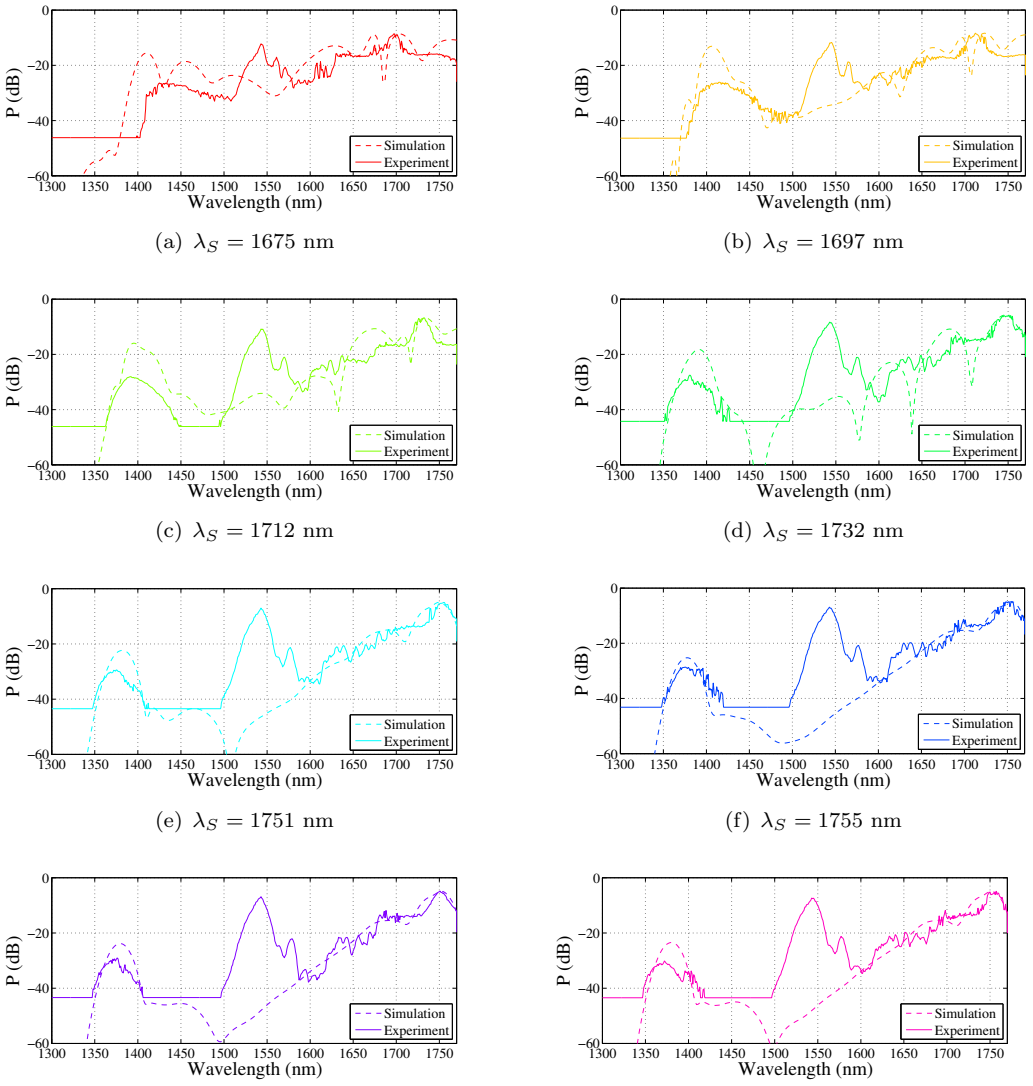

(a) $\lambda_S = 1675$ nm (b) $\lambda_S = 1697$ nm

(c) $\lambda_S = 1712$ nm (d) $\lambda_S = 1732$ nm

(e) $\lambda_S = 1751$ nm (f) $\lambda_S = 1755$ nm

(g) $\lambda_S = 1751$ nm (h) $\lambda_S = 1757$ nm

FIGURE 8.9: Comparison of experimental spectra to simulations. For each soliton wavelength λ_S the corresponding spectrum from Figure 8.6 is overlaid with a spectrum obtained by running a pulse propagation model for a soliton at the same wavelength, with the input pulse parameters from Table 8.1.

The resulting data is shown in Figure 8.9. Each subfigure contains an experimentally measured spectrum from Figure 8.4 overlaid with a simulated spectrum, where the central wavelength of the soliton used in the simulation was set to match that of the experiment and the peak power was set based on the calculated values in Table 8.1. For example, Figure 8.9(a) contains the red curve from Figure 8.6, overlaid with a spectrum obtained by simulating the propagation of a soliton at $\lambda_S = 1675$ nm with a peak power of 111.6 W.

Note that the spectra from the simulations do not have a peak in the 1550 nm to 1560 nm

region corresponding to the residual pump (from the SMF stage of the experiment), as the input to the simulation contained only the soliton.

We see from this figure that there is good agreement between the wavelength of the dispersive wave peaks of the numerical curves and the experimental curves, especially for longer soliton wavelengths. However the power of the dispersive waves seem to be higher in the simulation curves, compared to the experimentally observed curve. This is possibly due to the approximations used in calculating the peak power of the soliton. As a suitable broad band source was unavailable at the time of making these measurements, the loss of the fibre in the simulations is set to a constant value of 4.5 dB/m across the spectrum, based on a spot measurement of the loss at approximately 1560 nm. This is of course not exactly representative of the loss experienced by the dispersive waves in the experiment. Due to the relatively short length of fibre used in this experiment a cutback experiment to measure the actual fibre loss was not possible – this data may further improve the agreement between experiment and simulation, by providing more accurate values to the model inputs.

In addition to matching individual soliton wavelengths from Figure 8.6, simulations were also run for a range of evenly spaced soliton wavelengths, with a peak power of 114 W – which is the average of the soliton input peak powers in Table 8.1. This enabled us to construct a curve of predicted dispersive wave peak wavelengths, as a function of the soliton wavelength, based on the numerical model.

In Figure 8.10 the experimental data is plotted with both predictive curves – the analytical one obtained from Equation 8.7 and the numerical one obtained via numerical modelling of the NSE within the fibre. In obtaining the analytical curve $f_R = 0.2$ was assumed for the Raman fraction of the SF57 [288] glass. We see that there is much better agreement between the numerical curve and the experimental data. As mentioned before, this is expected as this model takes into account factors like higher order dispersion that the simplified analytical model cannot.

8.6 Conclusion

This chapter presented a detailed study of the generation of dispersive waves in dispersion engineered microstructured optical fibres. The results show that the use of a

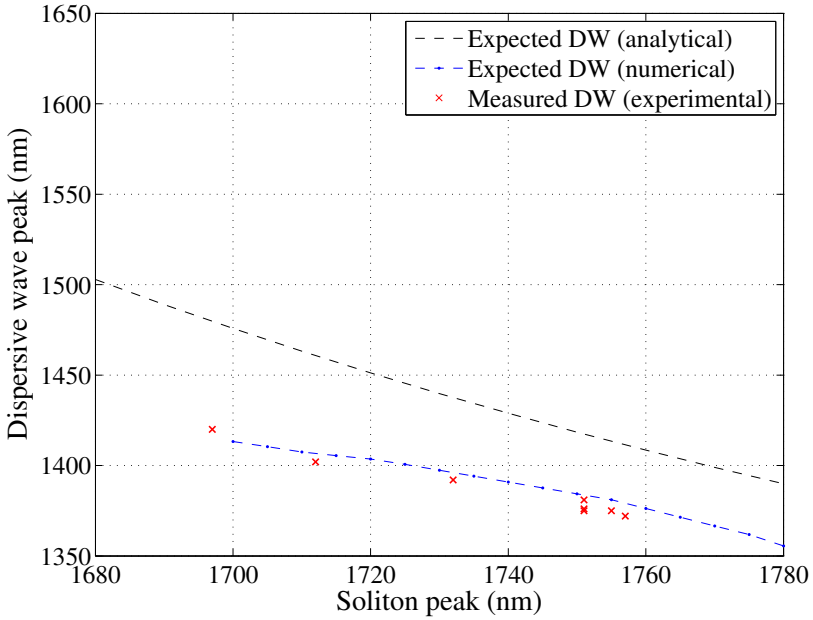

FIGURE 8.10: Comparison of the dispersive wave peaks observed experimentally, to those predicted by Equation 8.7 (black line) and those from a numerical model of the NSE (blue line).

soliton shaped pulse with a peak power of just over 100 W is sufficient to generate dispersive waves at much shorter wavelengths. In these experiments soliton pulses in the wavelength range from approximately 1680 nm to 1780 nm were used to generate dispersive waves between 1350 nm to 1450 nm. As the soliton peak moved towards longer wavelengths the dispersive wave peak was observed to move towards shorter wavelengths, leading to approximate wavelength shifts of 230 nm to 380 nm. This was done using a SF57 soft glass fibre of only 27 cm in length which was engineered to have anomalous dispersion in the near infrared region.

The relatively low pump power of just over 100 W, along with the wide shift of 250 nm to 400 nm and short fibre length of 27 cm further demonstrate the potential these glasses have for nonlinear device applications. It is worthwhile to note that the fibre used in these experiments was not specifically designed for this purpose.

Chapter 9

Conclusion

The research documented in this thesis explored the use of the enhanced optical nonlinearity and dispersion engineering possible in soft glass microstructured fibres as a basis for developing devices for broadband telecommunications applications at 1.55 µm. Two applications were considered in this research, namely multicasting and phase sensitive amplification – both of which are signal processing applications that are important to the realisation of all optical networks. This work studied how combining the inherently high material nonlinearity of soft glasses with a tailored dispersion profile, achieved by using a genetic algorithm to optimise the microstructured fibre geometry, can enable a fibre design with a high gain prevalent over a very broad band. Modelling of these fibre designs suggested that these fibres could be used to perform the multicasting and phase sensitive amplification signal processing applications at the extremely high bit rate of 640 Gb/s – speeds that are expected to become common in next generation communication networks.

The main aims of this work were to improve the understanding of how dispersion engineering in soft glasses, using a genetic algorithm optimisation method, can be used to develop a tailored fibre design for each application; and progress the development of the designed soft glass fibre for potential use in a nonlinear telecommunications device.

Significant progress has been made towards the ultimate aims of this project, notably.

- The development of a novel tellurite fibre design with a high nonlinearity of 1789 $W^{-1}km^{-1}$ at 1550 nm and a low dispersion profile – where the dispersion

only varies from -2.87 $ps^{-1}nm^{-1}km^{-1}$ to 0.29 $ps^{-1}nm^{-1}km^{-1}$ over the wavelength rage from 1450 to 1650 nm.

- The development of a novel bismuth fibre design with high nonlinearity of 1099 $W^{-1}km^{-1}$ at 1550 nm and low dispersion of 0.14 $ps^{-1}nm^{-1}km^{-1}$ at 1550 nm. Computational modelling of this fibre design was used to demonstrate the capability of this fibre to achieve broadband PSA of high bandwidth signals at 1550 nm.

- The measurement of fibre dispersion that correlates well with modelled values, demonstrating the accuracy of the modelling technique.

- The fabrication and characterisation of a novel set of germanate glasses for nonlinear applications. The measurement of the nonlinear index of this glass, in particular, is significant as little data exists in the literature on the measurement of the nonlinearity of such glasses.

- The fabrication of a hexagonal wagon wheel fibre in germanate glass – the first time such a fibre design has been fabricated in this novel material.

- Dispersive wave generation, with an approximately 230 nm to 380 nm wavelength shift, in a microstructured fibre similar to the designs developed here. This shows the potential for signal regeneration in these fibres.

Considerable progress was made in the development of nonlinear fibre designs with broad parametric gain bandwidth. These fibre designs were obtained using a hybrid, hexagonal wagon wheel fibre design which was optimised via a genetic algorithm. This optimisation procedure allowed for extremely fine tuning of the dispersion which, coupled with the high nonlinear index of the substrate glass used in the design, led to fibre designs with extremely broad characteristics.

Significant progress was also made in the development and characterisation of a novel nonlinear glass – namely lead germanate glasses that, when compared with other infrared transmitting high index glasses (such as tellurites), stand out for having the desirable properties of low phonon energy and high refractive index and nonlinearity without compromising on fibre stability. The measurement of the nonlinearity of is particularly important as relatively little information on the nonlinear properties of this glass family exits in the literature.

While the successful fabrication of the fibre designs produced in the early stages of this research was not achieved, valuable insight was gained into the fabrication process for such designs. Some progress was made with the fabrication of a simplified HWW structure in the novel germanate glass. But the fabrication of the optimised structure in either the tellurite fibre for multicasting or the bismuth fibre for PSA ultimately, unsuccessful. For the original bismuth based fibre design for PSA unanticipated issues with the supplier of the bismuth oxide glass meant that the fabrication strategy for this design had to be altered to use tellurite instead.

The main reason for being unable to fabricate the HWW fibre design in tellurite was an inability to produce a preform with a suitable structure to be drawn down into fibre. The initial preforms were not fused properly and had structural deformations that resulted in the inner holes not being in the correct position. The issue of glass fusion was rectified through an altered die design and a change to the extrusion conditions, however the issue of the inner hole deformation remained.

Even when the fabrication process moved on to use the germanate glasses the issue of the inner holes drifting from their intended positions during the extrusion remained. This suggests a flaw in the die design that was causing the glass flow during extrusion to push these holes towards the edge of the suspended core region. This is currently being investigated and provides scope for some future work (discussed in the following section).

In addition to the achievements made in fibre design and development of materials, important experimental work was also done in this research. This included characterisation of key optical properties such as the measurement of nonlinearity in a germanate fibre (a first for this particular germanate composition and one of the few direct measurements overall of the nonlinear refractive index in germanate glasses) and the measurement of dispersion in a tellurite fibre. In addition to this, nonlinear effects in HWW fibres were characterised by generating dispersive waves for the first time in a SF57 HWW that had been fabricated previously. The data from this experiment was shown to have good agreement with modelling data, thereby indicating confidence in the modelling process.

9.1 Future work

Considerable progress was made during this work towards the development of nonlinear fibres for broadband telecommunications applications. However there remains potential for future work, based on the results presented herein.

Further fabrication trials are needed to resolve the deformation of the inner hole arrangement observed in the HWW fabrication trials (Sections 6.4 and 6.5). This process could be aided by computational modelling of the glass flow dynamics through the die structure. One possible solution would be to increase the distance between the inner holes and the edge of the suspended core region to allow for more glass to flow around the pins in the die that correspond to the inner holes. The current design has more glass flow on the inside of these pins, which could be the reason for the holes drifting out. This would of course change the design of the fibre and would thus mandate a change in the design and optimisation procedure to, for example, stipulate a minimum distance between the inner holes and the edge of the suspended core region.

The fibre drawing attempts of the germanate fibre (Section 6.6) revealed a high surface tension in this glass. Further work needs to be done to accurately quantify how this high surface tension affects the fibre draw parameters. The fabrication process for these glasses may also need to be altered in order to have larger holes in the preform and cane – this may mitigate hole collapse during the fibre draw and allow for the fibres to be drawn under self pressurisation.

The dispersion measurement experiments on the bismuth and tellurite suspended core fibres (Section 7.2) demonstrated a setup that could be used to accurately measure the dispersion for such microstructured fibres. However the accuracy of some experimental points were low, mainly due to the high signal to noise ratio of the interferogram obtained at these wavelengths. This experimental setup could be improved by replacing the 50:50 input beam splitter with, for instance, a 90:10 beam splitter that would send 90% of the beam to the fibre arm, which has a significantly higher loss than the air arm. This would allow for more light to be present at the output of the interferometer, improving the visibility and signal to noise ratio of the interferogram and thus also improving the accuracy of the fitting procedure that is used to calculate the dispersion. This measurement could also be extended to more complex MOFs.

References

[1] Heike Ebendorff-Heidepriem, Stephen C. Warren-Smith, and Tanya M. Monro. Suspended nanowires: fabrication, design and characterization of fibers with nanoscale cores. *Optics Express*, 17(4):2646–2657, February 2009. ISSN 1094-4087. doi: 10.1364/OE.17.002646. URL http://www.opticsexpress.org/abstract.cfm?URI=oe-17-4-2646.

[2] Heike Ebendorff-Heidepriem and Tanya M. Monro. Extrusion of complex preforms for microstructured optical fibers. *Optics Express*, 15(23):15086–15092, November 2007. ISSN 1094-4087. doi: 10.1364/OE.15.015086. URL http://www.opticsexpress.org/abstract.cfm?URI=oe-15-23-15086.

[3] Arun K Varshneya. *Fundamentals of inorganic glasses*. Gulf Professional Publishing, 1994.

[4] J.A. Woolam Co. Inc. Spectroscopic Ellipsometry Tutorial Ellipsometry Measurements - J.A. Woollam Co. URL http://www.jawoollam.com/tutorial_4.html.

[5] Tanya M. Monro and Heike Ebendorff-Heidepriem. Progress in microstructured optical fibres. *Annual Review of Materials Research*, 36(1):467–495, August 2006. ISSN 1531-7331. doi: 10.1146/annurev.matsci.36.111904.135316. URL http://www.annualreviews.org/doi/abs/10.1146/annurev.matsci.36.111904.135316?journalCode=matsci.

[6] C Cantini, K Abedin, G Saachi, F Pasquale, and F Kubota. Measurement of Raman Gain Coefficient in Bismuth-Based Single ModeOptical Fibres. In *Tenth Optoelectronics and Communications Conference Technical digest*, pages 234–235, 2005.

[7] M. D. O'Donnell, K. Richardson, R. Stolen, A. B. Seddon, D. Furniss, V. K. Tikhomirov, C. Rivero, M. Ramme, R. Stegeman, G. Stegeman, M. Couzi, and T. Cardinal. Tellurite and Fluorotellurite Glasses for Fiberoptic Raman Amplifiers: Glass Characterization, Optical Properties, Raman Gain, Preliminary Fiberization, and Fiber Characterization. *Journal of the American Ceramic Society*, 90(5):1448–1457, May 2007. ISSN 0002-7820. doi: 10.1111/j.1551-2916.2007.01574.x. URL http://doi.wiley.com/10.1111/j.1551-2916.2007.01574.x.

[8] Q. Lin and Govind P. Agrawal. Raman response function for silica fibers. *Optics Letters*, 31(21):3086, 2006. ISSN 0146-9592. doi: 10.1364/OL.31.003086. URL http://ol.osa.org/abstract.cfm?URI=ol-31-21-3086.

[9] Michael R. Oermann, Heike Ebendorff-Heidepriem, Yahua Li, Tze-Cheung Foo, and Tanya M. Monro. Index matching between passive and active tellurite glasses for use in microstructured fiber lasers: Erbium doped lanthanum-tellurite glass. *Optics Express*, 17(18):15578–15584, August 2009. ISSN 1094-4087. doi: 10.1364/OE.17.015578. URL http://www.opticsexpress.org/abstract.cfm?URI=oe-17-18-15578.

[10] K.C. Kao and G.A. Hockham. Dielectric-fibre surface waveguides for optical frequencies. *Proceedings of the Institution of Electrical Engineers*, 113(7):1151, July 1966. ISSN 00203270. doi: 10.1049/piee.1966.0189. URL http://digital-library.theiet.org/content/journals/10.1049/piee.1966.0189.

[11] F. P. Kapron. Radiation losses in glass optical waveguides. *Applied Physics Letters*, 17(10): 423, October 1970. ISSN 00036951. doi: 10.1063/1.1653255. URL http://scitation.aip.org/content/aip/journal/apl/17/10/10.1063/1.1653255.

[12] T. Miya, Y. Terunuma, T. Hosaka, and T. Miyashita. Ultimate low-loss single-mode fibre at 1.55 μm. *Electronics Letters*, 15(4):106, February 1979. ISSN 00135194. doi: 10.1049/el:19790077. URL http://digital-library.theiet.org/content/journals/10.1049/el_19790077.

[13] Nobel Media AB 2014. The 2009 Nobel Prize in Physics - Press Release, 2009. URL http://www.nobelprize.org/nobel_prizes/physics/laureates/2009/press.html.

[14] Akira Hasegawa. Transmission of stationary nonlinear optical pulses in dispersive dielectric fibers. I. Anomalous dispersion. *Applied Physics Letters*, 23(3):142, October 1973. ISSN 00036951. doi: 10.1063/1.1654836. URL http://scitation.aip.org/content/aip/journal/apl/23/3/10.1063/1.1654836.

[15] M.N. Islam. Raman amplifiers for telecommunications. *IEEE Journal of Selected Topics in Quantum Electronics*, 8(3):548–559, May 2002. ISSN 1077-260X. doi: 10.1109/JSTQE.2002.1016358. URL http://ieeexplore.ieee.org/articleDetails.jsp?arnumber=1016358.

[16] Philip Russell. Photonic crystal fibers. *Science*, 299(5605):358—-362, 2003. URL http://www.jstor.org/stable/3833378.

[17] Stojan Radic, David J. Moss, and Benjamin J. Eggleton. *Optical Fiber Telecommunications V A*. Elsevier, 2008. ISBN 9780123741714. doi: 10.1016/B978-0-12-374171-4.00020-4. URL http://www.sciencedirect.com/science/article/pii/B9780123741714000204.

[18] W. Belardi, K. Furusawa, P. Petropoulos, Z. Yusoff, T.M. Monro, and D.J. Richardson. Four-wave mixing based 10-Gb/s tunable wavelength conversion using a holey fiber with a high SBS threshold. *IEEE Photonics Technology Letters*, 15(3):440–442, March 2003. ISSN 1041-1135. doi: 10.1109/LPT.2002.807928. URL http://ieeexplore.ieee.org/articleDetails.jsp?arnumber=1182784.

[19] K.K. Chow, C. Shu, and A. Bjarklev. Polarization-insensitive widely tunable wavelength converter based on four-wave mixing in a dispersion-flattened nonlinear photonic Crystal fiber. *IEEE Photonics Technology Letters*, 17(3):624–626, March 2005. ISSN 1041-1135. doi: 10.1109/LPT.2004.840929. URL http://ieeexplore.ieee.org/articleDetails.jsp?arnumber=1396035.

[20] S. Radic, C.J. McKinstrie, R.M. Jopson, J.C. Centanni, and A.R. Chraplyvy. All-optical regeneration in one- and two-pump parametric amplifiers using highly nonlinear optical fiber. *IEEE Photonics Technology Letters*, 15(7):957–959, July 2003. ISSN 1041-1135. doi: 10.1109/LPT.2003.813444. URL http://ieeexplore.ieee.org/articleDetails.jsp?arnumber=1206774.

[21] Martin Rochette, Justin L. Blows, and Benjamin J. Eggleton. 3R optical regeneration: an all-optical solution with BER improvement. *Optics Express*, 14(14):6414, 2006. ISSN 1094-4087. doi: 10.1364/OE.14.006414. URL http://www.opticsexpress.org/abstract.cfm?URI=oe-14-14-6414.

[22] Masaki Asobe. Nonlinear Optical Properties of Chalcogenide Glass Fibers and Their Application to All-Optical Switching. *Optical Fiber Technology*, 3(2):142–148, April 1997. ISSN 10685200. doi: 10.1006/ofte.1997.0214. URL http://www.sciencedirect.com/science/article/pii/S1068520097902145.

[23] K. J. Blow, N. J. Doran, and B. K. Nayar. Experimental demonstration of optical soliton switching in an all-fiber nonlinear Sagnac interferometer. *Optics Letters*, 14(14):754, July 1989. ISSN 0146-9592. doi: 10.1364/OL.14.000754. URL http://ol.osa.org/abstract.cfm?URI=ol-14-14-754.

[24] Stojan Radic and Colin J McKINSTRIE. Optical amplification and signal processing in highly nonlinear optical fiber. *IEICE transactions on electronics*, 88(5):859–869, 2005.

[25] Ju Han Lee, Kazuro Kikuchi, Tatsuo Nagashima, Tomoharu Hasegawa, Seiki Ohara, and Naoki Sugimoto. All fiber-based 160-Gbit/s add/drop multiplexer incorporating a 1-m-long Bismuth Oxide-based ultra-high nonlinearity fiber. *Optics Express*, 13(18):6864, 2005. ISSN 1094-4087. doi: 10.1364/OPEX.13.006864. URL http://www.opticsexpress.org/abstract.cfm?URI=oe-13-18-6864.

[26] Hans-Georg Weber, Reinhold Ludwig, Sebastian Ferber, Carsten Schmidt-Langhorst, Marcel Kroh, Vincent Marembert, Christof Boerner, and Colja Schubert. Ultrahigh-Speed OTDM-Transmission Technology. *Journal of Lightwave Technology*, 24(12):4616–4627, December 2006. ISSN 0733-8724. doi: 10.1109/JLT.2006.885784. URL http://ieeexplore.ieee.org/articleDetails.jsp?arnumber=4063441.

[27] Gregory Raybon, Peter J. Winzer, Andrew A. Adamiecki, Alan H. Gnauck, Agnieszka Konczykowska, Filipe Jorge, Jean-Yves Dupuy, Larry L. Buhl, Christopher R. Doerr, Roger Delbue, and Peter J. Pupalaikis. All-ETDM 80-Gbaud (160-Gb/s) QPSK Generation and Coherent Detection. *IEEE Photonics Technology Letters*, 23(22):1667–1669, November 2011. ISSN 1041-1135. doi: 10.1109/LPT.2011.2166111. URL http://ieeexplore.ieee.org/articleDetails.jsp?arnumber=6045313.

[28] K. S. Kim, R. H. Stolen, W. A. Reed, and K. W. Quoi. Measurement of the nonlinear index of silica-core and dispersion-shifted fibers. *Optics Letters*, 19(4):257, February 1994. ISSN 0146-9592. doi: 10.1364/OL.19.000257. URL http://ol.osa.org/abstract.cfm?URI=ol-19-4-257.

[29] M. Olivier, J.C. Tchahame, P. Němec, M. Chauvet, V. Besse, C. Cassagne, G. Boudebs, G. Renversez, R. Boidin, E. Baudet, and V. Nazabal. Structure, nonlinear properties, and photosensitivity of (GeSe_2)_100-x(Sb_2Se_3)_x glasses. *Optical Materials Express*, 4(3):525, February 2014. ISSN 2159-3930. doi: 10.1364/OME.4.000525. URL http://www.opticsinfobase.org/ome/abstract.cfm?URI=ome-4-3-525.

[30] Jonathan C Knight. Photonic crystal fibres. *Nature*, 424(6950):847–51, August 2003. ISSN 1476-4687. doi: 10.1038/nature01940. URL http://www.nature.com.proxy.library.adelaide.edu.au/nature/journal/v424/n6950/full/nature01940.html.

[31] V.V. Ravi Kumar, A. George, W. Reeves, J. Knight, P. Russell, F. Omenetto, and A. Taylor. Extruded soft glass photonic crystal fiber for ultrabroad supercontinuum generation. *Optics Express*, 10(25):1520, December 2002. ISSN 1094-4087. doi: 10.1364/OE.10.001520. URL http://www.opticsexpress.org/abstract.cfm?URI=oe-10-25-1520.

[32] H. Tilanka Munasinghe, Anja Winterstein-Beckmann, Christian Schiele, Danilo Manzani, Lothar Wondraczek, Shahraam Afshar V., Tanya M. Monro, and Heike Ebendorff-Heidepriem. Lead-germanate glasses and fibers: a practical alternative to tellurite for nonlinear fiber applications. *Optical Materials Express*, 3(9):1488, August 2013. ISSN 2159-3930. doi: 10.1364/OME.3.001488. URL http://www.opticsinfobase.org/ome/abstract.cfm?URI=ome-3-9-1488.

[33] H. Tilanka Munasinghe, Shahraam V Afshar, and Tanya M Monro. Highly Nonlinear and Dispersion-Flattened Fiber Design for Ultrafast Phase-Sensitive Amplification. *Journal*

of Lightwave Technology, 30(21):3440–3447, 2012. doi: 10.1109/JLT.2012.2215307. URL http://ieeexplore.ieee.org/xpl/articleDetails.jsp?arnumber=6286974.

[34] Govind P Agrawal. *Nonlinear fiber optics*. Springer, 2000.

[35] A.W. Snyder and J. Love. *Optical Waveguide Theory*, volume 1983. Springer, 1983. ISBN 0412099500. URL http://books.google.com/books?hl=en&lr=&id=gIQB_hzB0SMC&pgis=1.

[36] Camille-Sophie Brès, Nikola Alic, Alan H. Gnauck, Robert M. Jopson, and Stojan Radic. Multicast Parametric Synchronous Sampling. *IEEE Photonics Technology Letters*, 20(14): 1222–1224, July 2008. ISSN 1041-1135. doi: 10.1109/LPT.2008.925503. URL http://ieeexplore.ieee.org/lpdocs/epic03/wrapper.htm?arnumber=4544847.

[37] Camille-Sophie Brès, A.O.J. Wiberg, B.P.-P. Kuo, J.M. Chavez-Boggio, C.F. Marki, N. Alic, and S. Radic. Optical Demultiplexing of 320 Gb/s to 8 X 40 Gb/s in Single Parametric Gate. *Journal of Lightwave Technology*, 28(4):434–442, February 2010. ISSN 0733-8724. doi: 10.1109/JLT.2009.2034874. URL http://ieeexplore.ieee.org/articleDetails.jsp?arnumber=5290021.

[38] C McKinstrie and S Radic. Phase-sensitive amplification in a fiber. *Optics express*, 12(20): 4973–9, October 2004. ISSN 1094-4087. URL http://www.ncbi.nlm.nih.gov/pubmed/19484051.

[39] John A. Buck. Fundamentals of Optical Fibers, 2nd Edition. *Fundamentals of Optical Fibers, 2nd Edition, by John A. Buck, pp. 352. ISBN 0-471-22191-0. Wiley-VCH , April 2004.*, -1, April 2004. URL http://adsabs.harvard.edu/abs/2004fof..book.....B.

[40] H Tilanka Munasinghe, Wen Qi Zhang, Nikola Alic, Camille-sophie Bres, Stojan Radic, Tanya M Monro, and Shahraam Afshar V. Design of a Tellurite Microstructured Optical Fibre for Self-Seeded Multicasting for Ultra-Fast Signal Processing. In *Proceedings of the Australasian Conference on Optics, Lasers and Spectroscopy and Australian Conference on Optical Fibre Technology in association with the International Workshop on Dissipative Solitons*, pages 280–281, 2009. URL http://digital.library.adelaide.edu.au/dspace/handle/2440/57712.

[41] H Tilanka Munasinghe, Tanya M Monro, and Shahraam V Afshar. The effect of subwavelength guidance on mode propagation and dispersion in high index optical waveguides. In *2010 Conference on Optoelectronic and Microelectronic Materials and Devices*, pages 75—-76, Canberra, Australia, 2010. doi: 10.1109/COMMAD.2010.5699787.

[42] H. Tilanka Munasinghe, Shahraam V Afshar, and Tanya M Monro. Highly nonlinear, low dispersion fibres for telecommunications applications. *. . . on Optical Fibre . . .*, 57:4–5, 2010. URL http://digital.library.adelaide.edu.au/dspace/handle/2440/63657.

[43] H. Tilanka Munasinghe, Shahraam Afshar V., David J. Richardson, and Tanya M. Monro. Nonlinear fibre design for broadband phase sensitive amplification. In *Proceedings of the International Quantum Electronics Conference and Conference on Lasers and Electro-Optics Pacific Rim 2011*, page C702. Optical Society of America, August 2011. URL http://www.opticsinfobase.org/abstract.cfm?URI=CLEOPR-2011-C702.

[44] Leily Kiani, Tilanka Munasinghe, Wen Qi Zhang, Shahraam Afshar, and Jay Sharping. Linear and nonlinear properties in soft glass optical fibers for device applications. *Bulletin of the American Physical Society*, Volume 57,, February 2012. URL http://meetings.aps.org/link/BAPS.2012.MAR.S1.9.

[45] Alan E. Willner, Salman Khaleghi, Mohammad Reza Chitgarha, and Omer Faruk Yilmaz. All-Optical Signal Processing. *Journal of Lightwave Technology*, 32(4):660–680, February 2014. ISSN 0733-8724. doi: 10.1109/JLT.2013.2287219. URL http://ieeexplore.ieee.org/articleDetails.jsp?arnumber=6648413.

[46] Khurram K. Qureshi, H Y. Tam, W H. Chung, P K. Wai, and N Sugimoto. All Optical On-Off Switching Using Bismuth-Based Highly Nonlinear Fiber. In *Conference on Lasers and Electro-Optics*, page CMAA2. Optical Society of America, May 2006. URL http://www.osapublishing.org/abstract.cfm?uri=CLEO-2006-CMAA2.

[47] Zhiqiang Nie, Huaibin Zheng, Yanpeng Zhang, Yan Zhao, Cuicui Zuo, Changbiao Li, Hong Chang, and Min Xiao. Experimental demonstration of optical switching and routing via four-wave mixing spatial shift. *Optics express*, 18(2):899–905, January 2010. ISSN 1094-4087. doi: 10.1364/OE.18.000899. URL http://www.osapublishing.org/viewmedia.cfm?uri=oe-18-2-899&seq=0&html=true.

[48] Ana Pejkic, Ron R Nissim, Evgeny Myslivets, Andreas O J Wiberg, Nikola Alic, and Stojan Radic. All-optical switching in a highly efficient parametric fiber mixer: design study. *Optics express*, 22(19):23512–27, September 2014. ISSN 1094-4087. doi: 10.1364/OE.22.023512. URL http://www.osapublishing.org/viewmedia.cfm?uri=oe-22-19-23512&seq=0&html=true.

[49] Reza Salem, Mark A. Foster, Amy C. Turner, David F. Geraghty, Michal Lipson, and Alexander L. Gaeta. Signal regeneration using low-power four-wave mixing on silicon chip. *Nature Photonics*, 2(1):35–38, December 2007. ISSN 1749-4885. doi: 10.1038/nphoton.2007.249. URL http://dx.doi.org/10.1038/nphoton.2007.249.

[50] C J McKinstrie and D S Cargill. Simultaneous frequency conversion, regeneration and reshaping of optical signals. *Optics express*, 20(7):6881–6, March 2012. ISSN 1094-4087. doi: 10.1364/OE.20.006881. URL http://www.osapublishing.org/viewmedia.cfm?uri=oe-20-7-6881&seq=0&html=true.

[51] Mohamed A. Ettabib, Liam Jones, Joseph Kakande, Radan Slavík, Francesca Parmigiani, Xian Feng, Francesco Poletti, Giorgio M. Ponzo, Jindan Shi, Marco N. Petrovich, Wei H. Loh, Periklis Petropoulos, and David J. Richardson. Phase sensitive amplification in a highly nonlinear lead-silicate fiber. *Optics Express*, 20(2):1629–1634, January 2012. ISSN 1094-4087. doi: 10.1364/OE.20.001629. URL http://www.opticsexpress.org/abstract.cfm?URI=oe-20-2-1629.

[52] Tobias Roethlingshoefer, Thomas Richter, Colja Schubert, Georgy Onishchukov, Bernhard Schmauss, and Gerd Leuchs. All-optical phase-preserving multilevel amplitude regeneration. *Optics express*, 22(22):27077–85, November 2014. ISSN 1094-4087. doi: 10.1364/OE.22.027077. URL http://www.osapublishing.org/viewmedia.cfm?uri=oe-22-22-27077&seq=0&html=true.

[53] J Schröder, T D Vo, Y Paquot, and B J Eggleton. Breaking the Tbit/s Barrier: Higher Bandwidth Optical Processing. *Optics and Photonics News*, 23(3):32–37, 2012.

[54] D Marcuse. Pulse distortion in single-mode fibers. *Applied optics*, 19(10):1653–60, May 1980. ISSN 0003-6935. doi: 10.1364/AO.19.001653. URL http://ao.osa.org/abstract.cfm?URI=ao-19-10-1653.

[55] M. J. Potasek, Govind P. Agrawal, and S. C. Pinault. Analytic and numerical study of pulse broadening in nonlinear dispersive optical fibers. *Journal of the Optical Society of America B*, 3(2):205, February 1986. ISSN 0740-3224. doi: 10.1364/JOSAB.3.000205. URL http://josab.osa.org/abstract.cfm?URI=josab-3-2-205.

[56] Mary R. Phillips and Daniel M. Ott. Crosstalk Due to Optical Fiber Nonlinearities in WDM CATV Lightwave Systems. *J. Lightwave Technol.*, 17(10):1782–, 1999. URL http://jlt.osa.org/abstract.cfm?URI=jlt-17-10-1782.

[57] J. Zhou, M.J. O'Mahony, and S.D. Walker. Analysis of optical crosstalk effects in multi-wavelength switched networks. *IEEE Photonics Technology Letters*, 6(2):302–305, February 1994. ISSN 1041-1135. doi: 10.1109/68.275457. URL http://ieeexplore.ieee.org/articleDetails.jsp?arnumber=275457.

[58] Claude Elwood Shannon. A mathematical theory of communication. *ACM SIGMOBILE Mobile Computing and Communications Review*, 5(1):3–55, 2001.

[59] J. Tang. The Shannon channel capacity of dispersion-free nonlinear optical fiber transmission. *Journal of Lightwave Technology*, 19(8):1104–1109, 2001. ISSN 07338724. doi: 10.1109/50.939789. URL http://ieeexplore.ieee.org/articleDetails.jsp?arnumber=939789.

[60] R.H. Stolen. Nonlinearity in fiber transmission. *Proceedings of the IEEE*, 68(10):1232–1236, October 1980. ISSN 0018-9219. doi: 10.1109/PROC.1980.11837. URL http://ieeexplore.ieee.org/articleDetails.jsp?arnumber=1456106.

[61] P P Mitra and J B Stark. Nonlinear limits to the information capacity of optical fibre communications. *Nature*, 411(6841):1027–30, June 2001. ISSN 0028-0836. doi: 10.1038/35082518. URL http://dx.doi.org/10.1038/35082518.

[62] Robert W Boyd. *Nonlinear optics*. Academic press, 2003.

[63] Anatoly Efimov, Antoinette Taylor, Fiorenzo Omenetto, Jonathan Knight, William Wadsworth, and Philip Russell. Phase-matched third harmonic generation in microstructured fibers. *Optics Express*, 11(20):2567, October 2003. ISSN 1094-4087. doi: 10.1364/OE.11.002567. URL http://www.opticsexpress.org/abstract.cfm?URI=oe-11-20-2567.

[64] Shahraam Afshar V. and Tanya M. Monro. A full vectorial model for pulse propagation in emerging waveguides with subwavelength structures part I: Kerr nonlinearity. *Optics Express*, 17(4):2298, February 2009. ISSN 1094-4087. doi: 10.1364/OE.17.002298. URL http://www.opticsexpress.org/abstract.cfm?URI=oe-17-4-2298.

[65] Shahraam Afshar V., Wen Qi Zhang, Heike Ebendorff-Heidepriem, and Tanya M. Monro. Small core optical waveguides are more nonlinear than expected: experimental confirmation. *Optics Letters*, 34(22):3577, November 2009. ISSN 0146-9592. doi: 10.1364/OL.34.003577. URL http://ol.osa.org/abstract.cfm?URI=ol-34-22-3577.

[66] E. Ciaramella and S. Trillo. All-optical signal reshaping via four-wave mixing in optical fibers. *IEEE Photonics Technology Letters*, 12(7):849–851, July 2000. ISSN 1041-1135. doi: 10.1109/68.853523. URL http://ieeexplore.ieee.org/articleDetails.jsp?arnumber=853523.

[67] M. Onishi, T. Okuno, T. Kashiwada, S. Ishikawa, N. Akasaka, and M. Nishimura. Highly Nonlinear Dispersion-Shifted Fibers and Their Application to Broadband Wavelength Converter. *Optical Fiber Technology*, 4(2):204–214, April 1998. ISSN 10685200. doi: 10.1006/ofte.1998.0248. URL http://dx.doi.org/10.1006/ofte.1998.0248.

[68] Stéphane Coen, Alvin Hing Lun Chau, Rainer Leonhardt, John D. Harvey, Jonathan C. Knight, William J. Wadsworth, and Philip St. J. Russell. Supercontinuum generation by stimulated Raman scattering and parametric four-wave mixing in photonic crystal

fibers. *Journal of the Optical Society of America B*, 19(4):753, April 2002. ISSN 0740-3224. doi: 10.1364/JOSAB.19.000753. URL http://josab.osa.org/abstract.cfm?URI=josab-19-4-753.

[69] Young-Geun Han, Thi Van Anh Tran, and Sang Bae Lee. Wavelength-spacing tunable multiwavelength erbium-doped fiber laser based on four-wave mixing of dispersion-shifted fiber. *Optics Letters*, 31(6):697, March 2006. ISSN 0146-9592. doi: 10.1364/OL.31.000697. URL http://ol.osa.org/abstract.cfm?URI=ol-31-6-697.

[70] C. Lu. Self-stabilizing effect of four-wave mixing and its applications on multiwavelength erbium-doped fiber lasers. *IEEE Photonics Technology Letters*, 17(12):2541–2543, December 2005. ISSN 1041-1135. doi: 10.1109/LPT.2005.858075. URL http://ieeexplore.ieee.org/articleDetails.jsp?arnumber=1542142.

[71] Yijiang Chen. Four-wave mixing in optical fibers: exact solution. *Journal of the Optical Society of America B*, 6(11):1986, November 1989. ISSN 0740-3224. doi: 10.1364/JOSAB.6.001986. URL http://www.osapublishing.org/viewmedia.cfm?uri=josab-6-11-1986&seq=0&html=true.

[72] IEEE. IEEE Standard for Information technology– Local and metropolitan area networks– Specific requirements– Part 3: CSMA/CD Access Method and Physical Layer Specifications Amendment 4: Media Access Control Parameters, Physical Layers, and Management Paramet, 2010.

[73] Ju Han Lee, Takuo Tanemura, Kazuro Kikuchi, Tatsuo Nagashima, Tomoharu Hasegawa, Seiki Ohara, and Naoki Sugimoto. Use of 1-mBi2O3 nonlinear fiber for 160-Gbit/s optical time-division demultiplexing based on polarization rotation and a wavelength shift induced by cross-phase modulation. *Optics Letters*, 30(11):1267, June 2005. ISSN 0146-9592. doi: 10.1364/OL.30.001267. URL http://www.osapublishing.org/viewmedia.cfm?uri=ol-30-11-1267&seq=0&html=true.

[74] Koji Igarashi, Kazuhiro Katoh, Kazuro Kikuchi, Tatsuo Nagashima, Tomoharu Hasegawa, Seiki Ohara, and Naoki Sugimoto. 160-Gbit/s Optical Time-Division Demultiplexing Based on Cross-Phase Modulation in a 2-m-Long Dispersion-Shifted Bi¡sub¿2¡/sub¿O¡sub¿3 ¡/sub¿Photonic Crystal Fiber. In *Photonic Applications Systems Technologies Conference*, page JTuC3. Optical Society of America, May 2007. URL http://www.osapublishing.org/abstract.cfm?uri=PhAST-2007-JTuC3.

[75] Mark D. Pelusi, Vahid G. Ta'eed, Michael R. Lamont, Steve Madden, Duk Y. Choi, Barry Luther-Davies, and Benjamin J. Eggleton. Ultra-High Nonlinear Chalcogenide Planar Waveguide for Four-Wave Mixing Based Time-Division Demultiplexing of a 160 Gb/s Optical Signal. In *Nonlinear Photonics*, page NTuA1, Washington, D.C., September 2007.

OSA. doi: 10.1364/NP.2007.NTuA1. URL http://www.osapublishing.org/abstract.cfm?uri=NP-2007-NTuA1.

[76] R.K. Pankaj. Wavelength requirements for multicasting in all-optical networks. *IEEE/ACM Transactions on Networking*, 7(3):414–424, June 1999. ISSN 10636692. doi: 10.1109/90.779211. URL http://ieeexplore.ieee.org/lpdocs/epic03/wrapper.htm?arnumber=779211.

[77] Xiang Liu and S. Chandrasekhar. Beyond 1-Tb/s superchannel transmission. In *IEEE Photonic Society 24th Annual Meeting*, pages 893–894. IEEE, October 2011. ISBN 978-1-4244-8939-8. doi: 10.1109/PHO.2011.6110846. URL http://ieeexplore.ieee.org/lpdocs/epic03/wrapper.htm?arnumber=6110846.

[78] Yuanxiang Chen, Juhao Li, Paikun Zhu, Yingying Xu, Yongqi He, and Zhangyuan Chen. Experimental Demonstration of 1.2-Tb/s Optical PDM SCFDM Superchannel Multicasting by HNLF. *IEEE Photonics Journal*, 5(5):7902007–7902007, October 2013. ISSN 1943-0655. doi: 10.1109/JPHOT.2013.2280534. URL http://ieeexplore.ieee.org/lpdocs/epic03/wrapper.htm?arnumber=6588889.

[79] A. Bogris and D. Syvridis. RZ-DPSK signal regeneration based on dual-pump phase-sensitive amplification in fibers. *IEEE Photonics Technology Letters*, 18(20):2144–2146, October 2006. ISSN 1041-1135. doi: 10.1109/LPT.2006.883890. URL http://ieeexplore.ieee.org/lpdocs/epic03/wrapper.htm?arnumber=1705512.

[80] K Croussore, I Kim, Y Han, C Kim, G Li, and S Radic. Demonstration of phase-regeneration of DPSK signals based on phase-sensitive amplification. *Optics Express*, 13 (11):3945–3950, 2005. ISSN 1094-4087.

[81] A Mecozzi, W L Kath, P Kumar, and C G Goedde. Long-term storage of a soliton bit stream by use of phase-sensitive amplification. *Optics letters*, 19(24):2050–2052, 1994. ISSN 1539-4794.

[82] R D Li, P Kumar, and W L Kath. Dispersion compensation with phase-sensitive optical amplifiers. *Lightwave Technology, Journal of*, 12(3):541–549, 1994. ISSN 0733-8724.

[83] A H Gnauck and P J Winzer. Optical phase-shift-keyed transmission. *Lightwave Technology, Journal of*, 23(1):115–130, 2005.

[84] M Rohde, C Caspar, N Heimes, M Konitzer, E J Bachus, and N Hanik. Robustness of DPSK direct detection transmission format in standard fibre WDM systems. *Electronics Letters*, 36(17):1483–1484, 2000.

[85] H A Haus and J A Mullen. Quantum noise in linear amplifiers. *Physical Review*, 128(5): 2407–2413, 1962. ISSN 0031-899X.

[86] Adonis Bogris, Dimitris Syvridis, and Costas Efstathiou. Noise Properties of Degenerate Dual Pump Phase Sensitive Amplifiers. *Journal of Lightwave Technology*, 28(8):1209–1217, April 2010. ISSN 0733-8724. doi: 10.1109/JLT.2010.2044016. URL http://ieeexplore.ieee.org/lpdocs/epic03/wrapper.htm?arnumber=5423993.

[87] Carlton Caves. Quantum limits on noise in linear amplifiers. *Physical Review D*, 26 (8):1817–1839, October 1982. ISSN 0556-2821. doi: 10.1103/PhysRevD.26.1817. URL http://link.aps.org/doi/10.1103/PhysRevD.26.1817.

[88] Z Tong, C Lundström, P A Andrekson, C J McKinstrie, M Karlsson, D J Blessing, E Tipsuwannakul, B J Puttnam, H Toda, and L Grüner-Nielsen. Towards ultrasensitive optical links enabled by low-noise phase-sensitive amplifiers. *Nature Photonics*, 5(7):430–436, 2011.

[89] Kevin Croussore, Cheolhwan Kim, and Guifang Li. All-optical regeneration of differential phase-shift keying signals based on phase-sensitive amplification. *Optics letters*, 29(20): 2357–9, October 2004. ISSN 0146-9592. URL http://www.ncbi.nlm.nih.gov/pubmed/15532266.

[90] Kevin Croussore, Inwoong Kim, Cheolhwan Kim, Yan Han, and Guifang Li. Phase-and-amplitude regeneration of differential phase-shift keyed signals using a phase-sensitive amplifier. *Optics express*, 14(6):2085–94, March 2006. ISSN 1094-4087. URL http://www.ncbi.nlm.nih.gov/pubmed/19503540.

[91] K Croussore and G Li. Amplitude regeneration of RZ-DPSK signals based on four-wave mixing in fibre. *Electronics Letters*, 43(3):1–2, 2007. doi: 10.1049/el.

[92] Xiaosheng Xiao and Ping Shum. Four-wave mixing-based phase sensitive amplification with pulsed signal input. *Proceedings of the 2008 International Conference on Advanced Infocomm Technology - ICAIT '08*, pages 1–4, 2008. doi: 10.1145/1509315.1509384. URL http://portal.acm.org/citation.cfm?doid=1509315.1509384.

[93] J Kakande, C Lundström, P A Andrekson, Z Tong, M Karlsson, P Petropoulos, F Parmigiani, and D J Richardson. Detailed characterization of a fiber-optic parametric amplifier in phase-sensitive and phase-insensitive operation. *Optics Express*, 18(5):4130–4137, 2010. ISSN 1094-4087.

[94] R Slavík, F Parmigiani, J Kakande, C Lundström, M Sjödin, P A Andrekson, R Weerasuriya, S Sygletos, A D Ellis, L Grüner-Nielsen, and Others. All-optical phase and amplitude regenerator for next-generation telecommunications systems. *Nature Photonics*, 2010.

[95] Richard Neo, Jochen Schröder, Yvan Paquot, Duk-Yong Choi, Steve Madden, Barry Luther-Davies, and Benjamin J Eggleton. Phase-sensitive amplification of light in a

$\chi(3)$ photonic chip using a dispersion engineered chalcogenide ridge waveguide. *Optics express*, 21(7):7926–33, April 2013. ISSN 1094-4087. doi: 10.1364/OE.21.007926. URL http://www.opticsexpress.org/abstract.cfm?URI=oe-21-7-7926.

[96] Yanbing Zhang, Jochen Schröder, Chad Husko, Simon Lefrancois, Duk-Yong Choi, Steve Madden, Barry Luther-Davies, and Benjamin J. Eggleton. Pump-degenerate phase-sensitive amplification in chalcogenide waveguides. *Journal of the Optical Society of America B*, 31(4):780, March 2014. ISSN 0740-3224. doi: 10.1364/JOSAB.31.000780. URL http://www.osapublishing.org/viewmedia.cfm?uri=josab-31-4-780&seq=0&html=true.

[97] Y. Zhang, C. Husko, J. Schröder, S. Lefrancois, I. Rey, T. Krauss, and B. J. Eggleton. Record 11 dB Phase Sensitive Amplification in Sub-millimeter Silicon Waveguides. In *Conference on Lasers and Electro-Optics/Pacific Rim*, page PD1b_3. Optical Society of America, June 2013. URL http://www.osapublishing.org/abstract.cfm?uri=CLEOPR-2013-PD1b_3.

[98] Francesco Da Ros, Dragana Vukovic, Andrzej Gajda, Kjeld Dalgaard, Lars Zimmermann, Bernd Tillack, Michael Galili, Klaus Petermann, and Christophe Peucheret. Phase regeneration of DPSK signals in a silicon waveguide with reverse-biased p-i-n junction. *Optics express*, 22(5):5029–36, March 2014. ISSN 1094-4087. doi: 10.1364/OE.22.005029. URL http://www.osapublishing.org/viewmedia.cfm?uri=oe-22-5-5029&seq=0&html=true.

[99] T Umeki, O Tadanaga, M Asobe, Y Miyamoto, and H Takenouchi. First demonstration of high-order QAM signal amplification in PPLN-based phase sensitive amplifier. *Optics express*, 22(3):2473–82, February 2014. ISSN 1094-4087. doi: 10.1364/OE.22.002473. URL http://www.opticsexpress.org/abstract.cfm?URI=oe-22-3-2473.

[100] Takeshi Umeki, Takushi Kazama, Osamu Tadanaga, Koji Enbutsu, Masaki Asobe, Yutaka Miyamoto, and Hirokazu Takenouchi. PDM Signal Amplification Using PPLN-Based Polarization-Independent Phase-Sensitive Amplifier. *Journal of Lightwave Technology*, 33 (7):1326–1332, April 2015. URL http://www.osapublishing.org/abstract.cfm?uri=jlt-33-7-1326.

[101] Yan Meng, Junzi Lian, Songnian Fu, Ming Tang, P. Shum, and Deming Liu. All-Optical DPSK Regenerative One-to-Nine Wavelength Multicasting Using Dual-Pump Degenerate Phase Sensitive Amplifier. *Journal of Lightwave Technology*, 32(15):2605–2612, August 2014. URL http://www.osapublishing.org/abstract.cfm?uri=jlt-32-15-2605.

[102] DF Walls. Squeezed states of light. *Nature*, 306(5939):141–146, 1983. ISSN 0028-0836. URL http://physics.princeton.edu/~mcdonald/examples/QM/walls_nature_306_141_83.pdf.

[103] Horace P. Yuen. Two-photon coherent states of the radiation field. *Physical Review A*, 13(6):2226–2243, 1976. ISSN 1094-1622. URL http://link.aps.org/doi/10.1103/PhysRevA.13.2226.

[104] Horace P. Yuen and Jeffrey H. Shapiro. Generation and detection of two-photon coherent states in degenerate four-wave mixing. *Optics Letters*, 4(10):334, October 1979. ISSN 0146-9592. doi: 10.1364/OL.4.000334. URL http://ol.osa.org/abstract.cfm?URI=ol-4-10-334.

[105] Yun Zhang, Hai Wang, Xiaoying Li, Jietai Jing, Changde Xie, and Kunchi Peng. Experimental generation of bright two-mode quadrature squeezed light from a narrow-band nondegenerate optical parametric amplifier. *Physical Review A*, 62(2):023813, July 2000. ISSN 1050-2947. doi: 10.1103/PhysRevA.62.023813. URL http://link.aps.org/doi/10.1103/PhysRevA.62.023813.

[106] R. Slusher, L. Hollberg, B. Yurke, J. Mertz, and J. Valley. Observation of Squeezed States Generated by Four-Wave Mixing in an Optical Cavity. *Physical Review Letters*, 55(22): 2409–2412, November 1985. ISSN 0031-9007. doi: 10.1103/PhysRevLett.55.2409. URL http://link.aps.org/doi/10.1103/PhysRevLett.55.2409.

[107] Arthur Q. Tool. Relation between inelastic deformability and thermal expansion of glass in its annealing range. *Journal of the American Ceramic Society*, 29(9):240–253, September 1946. ISSN 0002-7820. doi: 10.1111/j.1151-2916.1946.tb11592.x. URL http://doi.wiley.com/10.1111/j.1151-2916.1946.tb11592.x.

[108] Prashanth Badrinarayanan, Wei Zheng, Qingxiu Li, and Sindee L. Simon. The glass transition temperature versus the fictive temperature. *Journal of Non-Crystalline Solids*, 353(26):2603–2612, August 2007. ISSN 00223093. doi: 10.1016/j.jnoncrysol.2007.04.025. URL http://www.sciencedirect.com/science/article/pii/S0022309307004103.

[109] Alan D McNaught. *Compendium of chemical terminology*, volume 1669. Blackwell Science Oxford, 1997.

[110] J T Littleton. The softening point of glass. *J. Soc. Glass Technol*, 24:176, 1940.

[111] R.H. Stolen. Optical Kerr effect in glass waveguide. *Applied Physics Letters*, 22(6):294, March 1973. ISSN 00036951. doi: 10.1063/1.1654644. URL http://ieeexplore.ieee.org/articleDetails.jsp?arnumber=4843864.

[112] Hidetoshi Onodera, Ikuo Awai, and Jun-ichi Ikenoue. Refractive-index measurement of bulk materials: prism coupling method. *Applied optics*, 22(8):1194–1197, 1983.

[113] Howard R. Lillie. Viscosity-time-temperature relations in glass at annealing temperatures. *Journal of the American Ceramic Society*, 16(1-12):619–631, October 2006. ISSN 00027820. doi: 10.1111/j.1151-2916.1933.tb19269.x. URL http://doi.wiley.com/10.1111/j.1151-2916.1933.tb19269.x.

[114] B. T. Kolomiets and V. P. Pishlo. Softening temperatures of some chalcogenide glasses. *Glass and Ceramics*, 20(8):413–415, August 1963. ISSN 0361-7610. doi: 10.1007/BF00689641. URL http://link.springer.com/10.1007/BF00689641.

[115] I. H. Malitson. Interspecimen Comparison of the Refractive Index of Fused Silica. *Journal of the Optical Society of America*, 55(10):1205, October 1965. ISSN 0030-3941. doi: 10.1364/JOSA.55.001205. URL http://www.opticsinfobase.org/abstract.cfm?URI=josa-55-10-1205.

[116] Robert C. Miller. Optical second harmonic generation in piezoelectric crystals. *Applied Physics Letters*, 5(1):17, November 1964. ISSN 00036951. doi: 10.1063/1.1754022. URL http://scitation.aip.org/content/aip/journal/apl/5/1/10.1063/1.1754022.

[117] H. Ebendorff-Heidepriem, P. Petropoulos, S. Asimakis, V. Finazzi, R. C. Moore, K. Frampton, F. Koizumi, D. J. Richardson, and T. M. Monro. Bismuth glass holey fibers with high nonlinearity. *Optics Express*, 12(21):5082, October 2004. ISSN 1094-4087. doi: 10.1364/OPEX.12.005082. URL http://www.opticsinfobase.org/viewmedia.cfm?uri=oe-12-21-5082&seq=0&html=true.

[118] Xian Feng, Francesco Poletti, Angela Camerlingo, Francesca Parmigiani, Periklis Petropoulos, Peter Horak, Giorgio M. Ponzo, Marco Petrovich, Jindan Shi, Wei H. Loh, and David J. Richardson. Dispersion controlled highly nonlinear fibers for all-optical processing at telecoms wavelengths. *Optical Fiber Technology*, 16(6):378–391, December 2010. ISSN 10685200. doi: 10.1016/j.yofte.2010.09.014. URL http://dx.doi.org/10.1016/j.yofte.2010.09.014.

[119] William Houlder Zachariasen. The atomic arrangement in glass. *Journal of the American Chemical Society*, 54(10):3841–3851, 1932.

[120] A Zakery and S R Elliott. Optical properties and applications of chalcogenide glasses: a review. *Journal of Non-Crystalline Solids*, 330(1):1–12, 2003.

[121] J. M. Harbold, F. Ö. Ilday, F. W. Wise, J. S. Sanghera, V. Q. Nguyen, L. B. Shaw, and I. D. Aggarwal. Highly nonlinear As-S-Se glasses for all-optical switching. *Optics*

Letters, 27(2):119, January 2002. ISSN 0146-9592. doi: 10.1364/OL.27.000119. URL http://ol.osa.org/abstract.cfm?URI=ol-27-2-119.

[122] A.B. Seddon. Chalcogenide glasses: a review of their preparation, properties and applications. *Journal of Non-Crystalline Solids*, 184:44–50, May 1995. ISSN 00223093. doi: 10.1016/0022-3093(94)00686-5. URL http://www.sciencedirect.com/science/article/pii/0022309394006865.

[123] Guangming Tao, Soroush Shabahang, Esmaeil-Hooman Banaei, Joshua J. Kaufman, and Ayman F. Abouraddy. One-step Multi-material Preform Extrusion for Robust Chalcogenide Glass Optical Fibers and Tapers. In *Conference on Lasers and Electro-Optics 2012*, page CM1N.6, Washington, D.C., 2012. OSA. ISBN 978-1-55752-943-5. doi: 10.1364/CLEO_SI.2012.CM1N.6. URL http://www.opticsinfobase.org/abstract.cfm?URI=CLEO_SI-2012-CM1N.6.

[124] J Troles, Q Coulombier, G Canat, M Duhant, W Renard, P Toupin, L Calvez, G Renversez, F Smektala, M El Amraoui, J L Adam, T Chartier, D Mechin, and L Brilland. Low loss microstructured chalcogenide fibers for large non linear effects at 1995 nm. *Optics express*, 18(25):26647–54, December 2010. ISSN 1094-4087. doi: 10.1364/OE.18.026647. URL http://www.opticsexpress.org/abstract.cfm?URI=oe-18-25-26647.

[125] C. Quémard, F. Smektala, V. Couderc, A. Barthélémy, and J. Lucas. Chalcogenide glasses with high non linear optical properties for telecommunications. *Journal of Physics and Chemistry of Solids*, 62(8):1435–1440, August 2001. ISSN 00223697. doi: 10.1016/S0022-3697(01)00059-2. URL http://dx.doi.org/10.1016/S0022-3697(01)00059-2.

[126] Dong-Il Yeom, Eric C. Mägi, Michael R. Lamont, Libin Fu, and Benjamin J. Eggleton. Low-Threshold Supercontinuum Generation in Dispersion Engineered Highly Nonlinear Chalcogenide Fiber Nanowires - OSA Technical Digest (CD). In *Optical Fiber Communication Conference/National Fiber Optic Engineers Conference*, page OTuB5. Optical Society of America, February 2008. URL http://www.opticsinfobase.org/abstract.cfm?URI=OFC-2008-OTuB5.

[127] J. Troles, F. Smektala, L. Brillant, P. Houizot, F. Desevedavy, G. Boudebs, T. Chartier, and N. Traynor. Preparation of Chalcogenide Step-Index and Micro-Structured Fiber for Telecommunication. In *2006 International Conference on Transparent Optical Networks*, volume 2, pages 112–115. IEEE, June 2006. ISBN 1-4244-0235-2. doi: 10.1109/ICTON.2006.248351. URL http://ieeexplore.ieee.org/articleDetails.jsp?arnumber=4013747.

[128] M. Asobe, T. Kanamori, and K. Kubodera. Ultrafast all-optical switching using highly nonlinear chalcogenide glass fiber. *IEEE Photonics Technology Letters*, 4(4):362–365, April

1992. ISSN 1041-1135. doi: 10.1109/68.127214. URL http://ieeexplore.ieee.org/articleDetails.jsp?arnumber=127214.

[129] Steve Madden, Duk-Yong Choi, Douglas Bulla, Andrei V Rode, Barry Luther-Davies, Vahid G Ta'eed, Mark Pelusi, Benjamin J Eggleton, and Others. Long, low loss etched As2S3 chalcogenide waveguides for all-optical signal regeneration. *Made available in DSpace on 2010-12-20T06: 04: 14Z (GMT). No. of bitstreams: 1 Madden_Long2007. pdf: 270318 bytes, checksum: b64016ecea99cda2d1376c85480d8cbf (MD5) Previous issue date: 2009-06-03T03: 38: 03Z*, 2009.

[130] Michael Galili, Jing Xu, Hans C H Mulvad, Leif K Oxenlowe, Anders T Clausen, Palle Jeppesen, Barry Luther-Davies, Steve Madden, Andrei V Rode, Duk-Yong Choi, and Others. Breakthrough switching speed with an all-optical chalcogenide glass chip: 640 Gbit/s demultiplexing. *Made available in DSpace on 2010-12-20T06: 04: 54Z (GMT). No. of bitstreams: 1 Galili_Breakthrough. pdf: 328806 bytes, checksum: 38afe2def9e0593d868a53357ceccf23 (MD5) Previous issue date: 2009-10-20T00: 33: 15Z*, 2009.

[131] S Asimakis, P Petropoulos, F Poletti, J Y Y Leong, R C Moore, K E Frampton, X Feng, W H Loh, and D J Richardson. Towards efficient and broadband four-wave-mixing using short-length dispersion tailored lead silicate holey fibers. *Optics Express*, 15(2):596–601, 2007.

[132] Angela Camerlingo, Xian Feng, Francesco Poletti, Giorgio M. Ponzo, Francesca Parmigiani, Peter Horak, Marco N. Petrovich, Periklis Petropoulos, Wei H. Loh, and David J. Richardson. Near-zero dispersion, highly nonlinear lead-silicate W-type fiber for applications at 155μm. *Optics Express*, 18(15):15747, July 2010. ISSN 1094-4087. doi: 10.1364/OE.18.015747. URL http://www.opticsexpress.org/abstract.cfm?URI=oe-18-15-15747.

[133] K. Kikuchi, K. Taira, and N. Sugimoto. Highly nonlinear bismuth oxide-based glass fibres for all-optical signal processing. *Electronics Letters*, 38(4):166, February 2002. ISSN 00135194. doi: 10.1049/el:20020135. URL http://ieeexplore.ieee.org/articleDetails.jsp?arnumber=986844.

[134] Yutaka Kuroiwa, Naoki Sugimoto, Katsuhiro Ochiai, Seiki Ohara, Yasuji Fukasawa, Setsuro Ito, Setsuhisa Tanabe, and Teiichi Hanada. Fusion Spliceable and High Efficient Bi2O3-based EDF for Short-length and Broadband Application Pumped at 1480 nm. - 2001 OSA Technical Digest Series. In *Optical Fiber Communication Conference and International Conference on Quantum Information*, page TuI5. Optical Society of America, March 2001. URL http://www.opticsinfobase.org/abstract.cfm?URI=OFC-2001-TuI5.

[135] J. S. Wang, E.M. Vogel, and E. Snitzer. Tellurite glass: a new candidate for fiber devices. *Optical Materials*, 3(3):187–203, 1994. URL http://www.sciencedirect.com.proxy.library.adelaide.edu.au/science/article/pii/0925346794900043.

[136] Billy Richards, Yuen Tsang, David Binks, Joris Lousteau, and Animesh Jha. Efficient ˜2 μm Tmˆ3+-doped tellurite fiber laser. *Optics Letters*, 33(4):402–404, February 2008. ISSN 0146-9592. doi: 10.1364/OL.33.000402. URL http://ol.osa.org/abstract.cfm?URI=ol-33-4-402.

[137] A. Mori, Y. Ohishi, and S. Sudo. Erbium-doped tellurite glass fibre laser and amplifier. *Electronics Letters*, 33(10):863–864, 1997.

[138] A. Mori, H. Masuda, K. Shikano, and M. Shimizu. Ultra-wide-band tellurite-based fiber raman amplifier. *Journal of Lightwave Technology*, 21(5):1300–1306, May 2003. ISSN 0733-8724. doi: 10.1109/JLT.2003.810917. URL http://ieeexplore.ieee.org/xpls/abs_all.jsp?arnumber=1213585'escapeXml='false'/>.

[139] P. Domachuk, N. A. Wolchover, M. Cronin-Golomb, A. Wang, A. K. George, C. M. B. Cordeiro, J. C. Knight, and F. G. Omenetto. Over 4000 nm bandwidth of mid-IR supercontinuum generation in sub-centimeter segments of highly nonlinear tellurite PCFs. *Optics Express*, 16(10):7161–7168, May 2008. ISSN 1094-4087. doi: 10.1364/OE.16.007161. URL http://www.opticsinfobase.org/viewmedia.cfm?uri=oe-16-10-7161&seq=0&html=true.

[140] Meisong Liao, Weiqing Gao, Zhongchao Duan, Xin Yan, Takenobu Suzuki, and Yasutake Ohishi. Directly draw highly nonlinear tellurite microstructured fiber with diameter varying sharply in a short fiber length. *Optics Express*, 20(2):1141–1150, January 2012. ISSN 1094-4087. doi: 10.1364/OE.20.001141. URL http://dx.doi.org/10.1364/OE.20.001141.

[141] Yasutake Ohishi, Atsushi Mori, Makoto Yamada, Hirotaka Ono, Yoshiki Nishida, and Kiyoshi Oikawa. Gain characteristics of tellurite-based erbium-doped fiber amplifiers for 1.5-m broadband amplification. *Optics Letters*, 23(4):274, February 1998. ISSN 0146-9592. doi: 10.1364/OL.23.000274. URL http://ol.osa.org/abstract.cfm?URI=ol-23-4-274.

[142] Heike Ebendorff-Heidepriem, C. Schiele, A. Winterstein, L. Wondraczek, David George Lancaster, David John Ottaway, and Tanya Mary Monro. New germanate glasses for infrared fibre applications. In *Proceedings of the 37th Australian Conference on Optical Fibre Technology*, page paper no. 518.00, Sydney, Australia, 2013. URL http://digital.library.adelaide.edu.au/dspace/handle/2440/75100.

[143] Jianfeng Wu, Zhidong Yao, Jie Zong, and Shibin Jiang. Highly efficient high-power thulium-doped germanate glass fiber laser. *Optics Letters*, 32(6):638–640, March 2007. ISSN 0146-9592. doi: 10.1364/OL.32.000638. URL http://ol.osa.org/abstract.cfm?URI=ol-32-6-638.

[144] H. Hundertmark, S. Rammler, T. Wilken, R. Holzwarth, T. W. Hänsch, and P. S. Russell. Octave-spanning supercontinuum generated in SF6-glass PCF by a 1060 nm mode-locked fibre laser delivering 20 pJ per pulse. *Optics Express*, 17(3):1919, January 2009. ISSN 1094-4087. doi: 10.1364/OE.17.001919. URL http://www.opticsexpress.org/abstract.cfm?URI=oe-17-3-1919.

[145] S. Friberg and P. Smith. Nonlinear optical glasses for ultrafast optical switches. *IEEE Journal of Quantum Electronics*, 23(12):2089–2094, December 1987. ISSN 0018-9197. doi: 10.1109/JQE.1987.1073278. URL http://ieeexplore.ieee.org/xpls/abs_all.jsp?arnumber=1073278'escapeXml='false'/>.

[146] Francesca Parmigiani, Symeon Asimakis, Naoki Sugimoto, Fumihito Koizumi, Periklis Petropoulos, and David J. Richardson. 2R regenerator based on a 2-m-long highly nonlinear bismuth oxide fiber. *Optics Express*, 14(12):5038, 2006. ISSN 1094-4087. doi: 10.1364/OE.14.005038. URL http://www.opticsexpress.org/abstract.cfm?URI=oe-14-12-5038.

[147] Sean Manning. Personal communication. *Defence Science and Technology Organisation (DSTO), Salisbury, Australia*, 2013.

[148] D. W. Hall, M. A. Newhouse, N. F. Borrelli, W. H. Dumbaugh, and D. L. Weidman. Nonlinear optical susceptibilities of high-index glasses. *Applied Physics Letters*, 54 (14):1293–1295, April 1989. ISSN 00036951. doi: 10.1063/1.100697. URL http://ieeexplore.ieee.org/xpls/abs_all.jsp?arnumber=4858544'escapeXml='false'/>http://ieeexplore.ieee.org/xpl/articleDetails.jsp?arnumber=4858544.

[149] F Smektala, C Quemard, L Leneindre, J Lucas, A Barthélémy, and C De Angelis. Chalcogenide glasses with large non-linear refractive indices. *Journal of Non-Crystalline Solids*, 239(1-3):139–142, October 1998. ISSN 00223093. doi: 10.1016/S0022-3093(98)00730-3. URL http://www.sciencedirect.com/science/article/pii/S0022309398007303.

[150] Xin Jiang, Joris Lousteau, and Animesh Jha. The Structural, Thermal, and Optical Analyses of Multicomponent Germanium Oxide Glasses for Engineering Mid-Infrared Fiber Chemical Sensing. *Journal of the American Ceramic Society*, 93(10):3259–3266, October 2010. ISSN 00027820. doi: 10.1111/j.1551-2916.2010.03913.x. URL http://doi.wiley.com/10.1111/j.1551-2916.2010.03913.x.

[151] Xin Jiang, Joris Lousteau, Billy Richards, and Animesh Jha. Investigation on germanium oxide-based glasses for infrared optical fibre development. *Optical Materials*, 31(11):1701–1706, September 2009. ISSN 09253467. doi: 10.1016/j.optmat.2009.04.011. URL http://dx.doi.org/10.1016/j.optmat.2009.04.011.

[152] A. Winterstein, S. Manning, H. Ebendorff-Heidepriem, and L. Wondraczek. Luminescence from bismuth-germanate glasses and its manipulation through oxidants. *Optical Materials Express*, 2(10):1320–1328, August 2012. ISSN 2159-3930. doi: 10.1364/OME.2.001320. URL http://www.opticsinfobase.org/ome/abstract.cfm?URI=ome-2-10-1320.

[153] Xin Jiang, Joris Lousteau, Shaoxiong Shen, and Animesh Jha. Fluorogermanate glass with reduced content of OH-groups for infrared fiber optics. *Journal of Non-Crystalline Solids*, 355(37-42):2015–2019, October 2009. ISSN 00223093. doi: 10.1016/j.jnoncrysol.2009.04.069. URL http://www.sciencedirect.com/science/article/pii/S0022309309004190.

[154] Aoxiang Lin, Aleksandr Ryasnyanskiy, and Jean Toulouse. Fabrication and characterization of a water-free mid-infrared fluorotellurite glass. *Optics Letters*, 36(5):740–742, March 2011. ISSN 1539-4794. URL http://www.ncbi.nlm.nih.gov/pubmed/21368967.

[155] M. F. Churbanov, A. N. Moiseev, A. V. Chilyasov, V. V. Dorofeev, I. A. Kraev, M. M. Lipatova, T. V. Kotereva, E. M. Dianov, V. G. Plotnichenko, and E. B. Kryukova. Production of high-purity TeO2-ZnO and TeO2-WO3 glasses with the reduced content of OH-groups. *Journal of Optoelectronics and Advanced Materials*, 9(10):3229–3234, 2007. ISSN 1454-4164. URL http://cat.inist.fr/?aModele=afficheN&cpsidt=19165402.

[156] Heike Ebendorff-Heidepriem, Kevin Kuan, Michael R. Oermann, Kenton Knight, and Tanya M. Monro. Extruded tellurite glass and fibers with low OH content for mid-infrared applications. *Optical Materials Express*, 2(4):432–442, March 2012. ISSN 2159-3930. doi: 10.1364/OME.2.000432. URL http://www.opticsinfobase.org/viewmedia.cfm?uri=ome-2-4-432&seq=0&html=true.

[157] Meisong Liao, Chitrarekha Chaudhari, Guanshi Qin, Xin Yan, Takenobu Suzuki, and Yasutake Ohishi. Tellurite microstructure fibers with small hexagonal core for supercontinuum generation. *Optics Express*, 17(14):12174–12182, July 2009. ISSN 1094-4087. doi: 10.1364/OE.17.012174. URL http://www.opticsexpress.org/abstract.cfm?URI=oe-17-14-12174.

[158] Jiafang Bei, Tanya Mary Monro, Alexander Hemming, and Heike Ebendorff-Heidepriem. Reduction of scattering loss in fluoroindate glass fibers. *Optical Materials Express*, 3(9):1285–1301, 2013.

[159] Warner Vogel. *Glass chemistry*. Springer-Verlag, 1994.

[160] John A Woollam, Blaine Johs, Craig M Herzinger, James Hilfiker, Ron Synowicki, and Corey L Bungay. Overview of variable angle spectroscopic ellipsometry (VASE), part I: basic theory and typical applications. *SPIE, CR72*, pages 3–28, 1999.

[161] Carl A. Fenstermaker and Frank L. McCrackin. Errors arising from surface roughness in ellipsometric measurement of the refractive index of a surface. *Surface Science*, 16 (null):85–96, August 1969. ISSN 00396028. doi: 10.1016/0039-6028(69)90007-7. URL http://dx.doi.org/10.1016/0039-6028(69)90007-7.

[162] Blaine Johs and C. M. Herzinger. Quantifying the accuracy of ellipsometer systems. *physica status solidi (c)*, 5(5):1031–1035, May 2008. ISSN 16101634. doi: 10.1002/pssc.200777755. URL http://doi.wiley.com/10.1002/pssc.200777755.

[163] G.E. Jellison. Data analysis for spectroscopic ellipsometry. *Thin Solid Films*, 234(1-2):416–422, October 1993. ISSN 00406090. doi: 10.1016/0040-6090(93)90298-4. URL http://dx.doi.org/10.1016/0040-6090(93)90298-4.

[164] Harland Tompkins and Eugene A Irene. *Handbook of Ellipsometry(Google eBook)*. William Andrew, 2005. ISBN 0815517475. URL http://books.google.com/books?hl=en&lr=&id=6PQf1fSzHHEC&pgis=1.

[165] V Dimitrov and T Komatsu. An interpretation of optical properties of oxides and oxide glasses in terms of the electronic ion polarizability and average single bond strength. *Journal of the University of Chemical Technology and Metallurgy*, 45(3):219–250, 2010.

[166] A. Boskovic, S. V. Chernikov, J. R. Taylor, L. Gruner-Nielsen, and O. A. Levring. Direct continuous-wave measurement of n_2 in various types of telecommunication fiber at 155 m. *Optics Letters*, 21(24):1966–1968, December 1996. ISSN 0146-9592. doi: 10.1364/OL.21.001966. URL http://ol.osa.org/abstract.cfm?URI=ol-21-24-1966.

[167] Sean Manning, Heike Ebendorff-Heidepriem, and Tanya M. Monro. Ternary tellurite glasses for the fabrication of nonlinear optical fibres. *Optical Materials Express*, 2(2):140–152, January 2012. ISSN 2159-3930. doi: 10.1364/OME.2.000140. URL http://www.opticsinfobase.org/ome/abstract.cfm?URI=ome-2-2-140.

[168] P. Petropoulos, Heike Ebendorff-Heidepriem, V. Finazzi, R.C. Moore, K. Frampton, D.J. Richardson, and T.M. Monro. Highly nonlinear and anomalously dispersive lead silicate glass holey fibers. *Optics Express*, 11(26):3568–3573, December 2003. ISSN 1094-4087. doi: 10.1364/OE.11.003568. URL http://www.opticsexpress.org/abstract.cfm?URI=oe-11-26-3568.

[169] Din Ping Tsai, Andreas Othonos, Martin Moskovits, and Deepak Uttamchandani. Raman spectroscopy using a fiber optic probe with subwavelength aperture. *Applied Physics Letters*, 64(14):1768, April 1994. ISSN 00036951. doi: 10.1063/1.111802. URL http://ieeexplore.ieee.org/articleDetails.jsp?arnumber=4882729.

[170] F. Tuinstra and J.L. Koenig. Characterization of Graphite Fiber Surfaces with Raman Spectroscopy. *Journal of Composite Materials*, 4(4):492–499, October 1970. doi: 10.1177/002199837000400405. URL http://jcm.sagepub.com/content/4/4/492.short.

[171] Jason T. Motz, Martin Hunter, Luis H. Galindo, Joseph A. Gardecki, John R. Kramer, Ramachandra R. Dasari, and Michael S. Feld. Optical Fiber Probe for Biomedical Raman Spectroscopy. *Applied Optics*, 43(3):542, 2004. ISSN 0003-6935. doi: 10.1364/AO.43.000542. URL http://ao.osa.org/abstract.cfm?URI=ao-43-3-542.

[172] Yan Feng, Luke R Taylor, and Domenico Bonaccini Calia. 150 W highly-efficient Raman fiber laser. *Optics express*, 17(26):23678–83, December 2009. ISSN 1094-4087. doi: 10.1364/OE.17.023678. URL http://www.opticsexpress.org/abstract.cfm?URI=oe-17-26-23678.

[173] Haisheng Rong, Richard Jones, Ansheng Liu, Oded Cohen, Dani Hak, Alexander Fang, and Mario Paniccia. A continuous-wave Raman silicon laser. *Nature*, 433(7027):725–8, February 2005. ISSN 1476-4687. doi: 10.1038/nature03346. URL http://dx.doi.org/10.1038/nature03346.

[174] Yan Feng, Luke R Taylor, and Domenico Bonaccini Calia. 25 W Raman-fiber-amplifier-based 589 nm laser for laser guide star. *Optics express*, 17(21):19021–6, October 2009. ISSN 1094-4087. doi: 10.1364/OE.17.019021. URL http://www.opticsexpress.org/abstract.cfm?URI=oe-17-21-19021.

[175] H. Kidorf, K. Rottwitt, M. Nissov, M. Ma, and E. Rabarijaona. Pump interactions in a 100-nm bandwidth Raman amplifier. *IEEE Photonics Technology Letters*, 11(5):530–532, May 1999. ISSN 1041-1135. doi: 10.1109/68.759388. URL http://ieeexplore.ieee.org/articleDetails.jsp?arnumber=759388.

[176] R G Smith. Optical power handling capacity of low loss optical fibers as determined by stimulated Raman and brillouin scattering. *Applied optics*, 11(11):2489–94, November 1972. ISSN 0003-6935. doi: 10.1364/AO.11.002489. URL http://ao.osa.org/abstract.cfm?URI=ao-11-11-2489.

[177] J. Wang, J. R. Lincoln, W. S. Brocklesby, R. S. Deol, C. J. Mackechnie, A. Pearson, A. C. Tropper, D. C. Hanna, and D. N. Payne. Fabrication and optical properties of lead-germanate glasses and a new class of optical fibers doped with Tm3+. *Journal of*

Applied Physics, 73(12):8066–8075, June 1993. ISSN 00218979. doi: 10.1063/1.353922. URL http://link.aip.org/link/?JAPIAU/73/8066/1.

[178] V.N. Sigaev, I. Gregora, P. Pernice, B. Champagnon, E.N. Smelyanskaya, A. Aronne, and P.D. Sarkisov. Structure of lead germanate glasses by Raman spectroscopy. *Journal of Non-Crystalline Solids*, 279(2-3):136–144, February 2001. ISSN 00223093. doi: 10.1016/S0022-3093(00)00410-5. URL http://dx.doi.org/10.1016/S0022-3093(00)00410-5.

[179] M Dussauze, A Giannoudakos, L Velli, C P E Varsamis, M Kompitsas, and E I Kamitsos. Structure and optical properties of amorphous lead-germanate films developed by pulsed-laser deposition. *The Journal of Chemical Physics*, 127(3):034704, July 2007. ISSN 0021-9606. doi: 10.1063/1.2752503. URL http://link.aip.org/link/?JCPSA6/127/034704/1.

[180] W.A. Gambling, H. Matsumura, and C.M. Ragdale. Mode dispersion, material dispersion and profile dispersion in graded-index single-mode fibres. *IEE Journal on Microwaves, Optics and Acoustics*, 3(6):239, November 1979. ISSN 03086976. doi: 10.1049/ij-moa.1979.0051. URL http://ieeexplore.ieee.org/articleDetails.jsp?arnumber=4807654.

[181] T. P. White, R. C. McPhedran, C. M. de Sterke, L. C. Botten, and M. J. Steel. Confinement losses in microstructured optical fibers. *Optics Letters*, 26(21):1660, November 2001. ISSN 0146-9592. doi: 10.1364/OL.26.001660. URL http://ol.osa.org/abstract.cfm?URI=ol-26-21-1660.

[182] B. M. A. Rahman, F. A. Fernandez, and J. B. Davies. Review of finite element methods for microwave and optical waveguides. *IEEE Proceedings*, 79:1442–1448, October 1991. ISSN 1107-1115. URL http://adsabs.harvard.edu/abs/1991IEEEP..79.1442R.

[183] B. Rahman and J. Davies. Finite-element solution of integrated optical waveguides. *Journal of Lightwave Technology*, 2(5):682–688, October 1984. ISSN 0733-8724. doi: 10.1109/JLT.1984.1073669. URL http://ieeexplore.ieee.org/articleDetails.jsp?arnumber=1073669.

[184] F. Brechet, J. Marcou, D. Pagnoux, and P. Roy. Complete Analysis of the Characteristics of Propagation into Photonic Crystal Fibers, by the Finite Element Method. *Optical Fiber Technology*, 6(2):181–191, 2000. URL http://www.sciencedirect.com/science/article/pii/S1068520099903206.

[185] Jian-Ming Jin and Jiamming Jin. *The finite element method in electromagnetics*. Wiley New York, 2002.

[186] Hendrik Rogier and Daniël De Zutter. Berenger and Leaky Modes in Optical Fibers Terminated With a Perfectly Matched Layer. *J. Lightwave Technol.*, 20(7):1141–, 2002. URL http://jlt.osa.org/abstract.cfm?URI=jlt-20-7-1141.

[187] K. Saitoh and M. Koshiba. Full-vectorial imaginary-distance beam propagation method based on a finite element scheme: application to photonic crystal fibers. *IEEE Journal of Quantum Electronics*, 38(7):927–933, July 2002. ISSN 0018-9197. doi: 10.1109/JQE.2002.1017609. URL http://ieeexplore.ieee.org/articleDetails.jsp?arnumber=1017609.

[188] J. C. Knight, T. A. Birks, P. St. J. Russell, and D. M. Atkin. All-silica single-mode optical fiber with photonic crystal cladding. *Optics Letters*, 21(19):1547, October 1996. ISSN 0146-9592. doi: 10.1364/OL.21.001547. URL http://ol.osa.org/abstract.cfm?URI=ol-21-19-1547.

[189] T. A. Birks, J. C. Knight, and P. St.J. Russell. Endlessly single-mode photonic crystal fiber. *Optics Letters*, 22(13):961, July 1997. ISSN 0146-9592. doi: 10.1364/OL.22.000961. URL http://ol.osa.org/abstract.cfm?URI=ol-22-13-961.

[190] J.C. Knight, T.A. Birks, R.F. Cregan, P.St.J. Russell, and J.-P. de Sandro. Large mode area photonic crystal fibre. *Electronics Letters*, 34(13):1347, June 1998. ISSN 00135194. doi: 10.1049/el:19980965. URL http://ieeexplore.ieee.org/articleDetails.jsp?arnumber=707260.

[191] Charlene M Smith, Natesan Venkataraman, Michael T Gallagher, Dirk Müller, James A West, Nicholas F Borrelli, Douglas C Allan, and Karl W Koch. Low-loss hollow-core silica/air photonic bandgap fibre. *Nature*, 424(6949):657–9, August 2003. ISSN 1476-4687. doi: 10.1038/nature01849. URL http://dx.doi.org/10.1038/nature01849.

[192] W.Q. Zhang, V.S. Afshar, H. Ebendorff-Heidepriem, and T.M. Monro. Record nonlinearity in optical fibre. *Electronics Letters*, 44(25):1453, 2008. ISSN 00135194. doi: 10.1049/el:20083094. URL http://digital.library.adelaide.edu.au/dspace/handle/2440/51263.

[193] Laurent Brilland, Fréderic Smektala, Gilles Renversez, Thierry Chartier, Johan Troles, Thanh Nguyen, Nicholas Traynor, and Achille Monteville. Fabrication of complex structures of Holey Fibers in Chalcogenide glass. *Optics Express*, 14(3):1280, 2006. ISSN 1094-4087. doi: 10.1364/OE.14.001280. URL http://www.opticsexpress.org/abstract.cfm?URI=oe-14-3-1280.

[194] Benjamin Eggleton, Charles Kerbage, Paul Westbrook, Robert Windeler, and Arturo Hale. Microstructured optical fiber devices. *Optics Express*, 9(13):698, December 2001. ISSN

1094-4087. doi: 10.1364/OE.9.000698. URL http://www.opticsexpress.org/abstract.cfm?URI=oe-9-13-698.

[195] Meisong Liao, Chitrarekha Chaudhari, Guanshi Qin, Xin Yan, Chihiro Kito, Takenobu Suzuki, Yasutake Ohishi, Morio Matsumoto, and Takashi Misumi. Fabrication and characterization of a chalcogenide-tellurite composite microstructure fiber with high nonlinearity. *Optics express*, 17(24):21608–14, November 2009. ISSN 1094-4087. doi: 10.1364/OE.17.021608. URL http://www.opticsexpress.org/abstract.cfm?URI=oe-17-24-21608.

[196] Xian Feng, Francesco Poletti, Angela Camerlingo, Francesca Parmigiani, Peter Horak, Periklis Petropoulos, Wei H. Loh, and David J. Richardson. Dispersion-shifted all-solid high index-contrast microstructured optical fiber for nonlinear applications at 155μm. *Optics Express*, 17(22):20249, October 2009. ISSN 1094-4087. doi: 10.1364/OE.17.020249. URL http://www.opticsexpress.org/abstract.cfm?URI=oe-17-22-20249.

[197] Wen Qi Zhang, Shahraam Afshar V., and Tanya M. Monro. A genetic algorithm based approach to fiber design for high coherence and large bandwidth supercontinuum generation. *Optics Express*, 17(21):19311, October 2009. ISSN 1094-4087. doi: 10.1364/OE.17.019311. URL http://www.opticsinfobase.org/viewmedia.cfm?uri=oe-17-21-19311&seq=0&html=true.

[198] Manya V Afonso, José M Bioucas-Dias, and Mário A T Figueiredo. An augmented Lagrangian approach to the constrained optimization formulation of imaging inverse problems. *IEEE transactions on image processing : a publication of the IEEE Signal Processing Society*, 20(3):681–95, March 2011. ISSN 1941-0042. doi: 10.1109/TIP.2010.2076294. URL http://ieeexplore.ieee.org/articleDetails.jsp?arnumber=5570998.

[199] Eldad Haber, Uri M Ascher, and Doug Oldenburg. On optimization techniques for solving nonlinear inverse problems. *Inverse Problems*, 16(5):1263–1280, October 2000. ISSN 0266-5611. doi: 10.1088/0266-5611/16/5/309. URL http://iopscience.iop.org/0266-5611/16/5/309.

[200] P Rocca, M Benedetti, M Donelli, D Franceschini, and A Massa. Evolutionary optimization as applied to inverse scattering problems. *Inverse Problems*, 25(12):123003, December 2009. ISSN 0266-5611. doi: 10.1088/0266-5611/25/12/123003. URL http://iopscience.iop.org/0266-5611/25/12/123003.

[201] John A Nelder and Roger Mead. A simplex method for function minimization. *Computer journal*, 7(4):308–313, 1965.

[202] Jeffrey Horn and David E Goldberg. Genetic algorithm difficulty and the modality of fitness landscapes. In *Foundations of genetic algorithms 3*. Citeseer, 1994.

[203] J. Michael Fitzpatrick and John J. Grefenstette. Genetic algorithms in noisy environments. *Machine Learning*, 3(2-3):101–120, October 1988. ISSN 0885-6125. doi: 10.1007/BF00113893. URL http://link.springer.com/10.1007/BF00113893.

[204] F. Poletti, V. Finazzi, T. M. Monro, N. G. R. Broderick, V. Tse, and D. J. Richardson. Inverse design and fabrication tolerances of ultra-flattened dispersion holey fibers. *Optics Express*, 13(10):3728, May 2005. ISSN 1094-4087. doi: 10.1364/OPEX.13.003728. URL http://www.opticsexpress.org/abstract.cfm?URI=oe-13-10-3728.

[205] Lawrence Davis. *Handbook of genetic algorithms*. Van Nostrand Reinhold, 1991. URL http://books.google.com.au/books/about/Handbook_of_genetic_algorithms.html?id=Kl7vAAAAMAAJ&redir_esc=y.

[206] A. Cucinotta, S. Selleri, L. Vincetti, and M. Zoboli. Holey fiber analysis through the finite-element method. *IEEE Photonics Technology Letters*, 14(11):1530–1532, November 2002. ISSN 1041-1135. doi: 10.1109/LPT.2002.803375. URL http://ieeexplore.ieee.org/articleDetails.jsp?arnumber=1041992.

[207] Wen Qi Zhang. *Soft-glass microstructured optical fibres for nonlinear applications*. Doctor of philosophy, University of Adelaide, 2012.

[208] Wen Qi Zhang. Nonlinear Pulse Propagation Solver, 2014. URL http://sourceforge.net/projects/npps/.

[209] David Milam. Review and assessment of measured values of the nonlinear refractive-index coefficient of fused silica. *Applied optics*, 37(3):546–550, 1998.

[210] T R Taha and M I Ablowitz. Analytical and numerical aspects of certain nonlinear evolution equations. II. Numerical, nonlinear Schr{ö}dinger equation. *Journal of Computational Physics*, 55(2):203–230, 1984.

[211] O V Sinkin, R Holzlöhner, J Zweck, and C R Menyuk. Optimization of the split-step Fourier method in modeling optical-fiber communications systems. *Journal of lightwave technology*, 21(1):61, 2003.

[212] R. H. Stolen, J. P. Gordon, W. J. Tomlinson, and H. A. Haus. Raman response function of silica-core fibers. *Journal of the Optical Society of America B*, 6(6):1159, June 1989. ISSN 0740-3224. doi: 10.1364/JOSAB.6.001159. URL http://josab.osa.org/abstract.cfm?URI=josab-6-6-1159.

[213] James W. Cooley, Peter A. W. Lewis, and Peter D. Welch. The Fast Fourier Transform and Its Applications. *IEEE Transactions on Education*, 12(1):27–34, March 1969. ISSN 0018-9359. doi: 10.1109/TE.1969.4320436. URL http://ieeexplore.ieee.org/articleDetails.jsp?arnumber=4320436.

[214] G. H. Weiss and A. A. Maradudin. The Baker-Hausdorff Formula and a Problem in Crystal Physics. *Journal of Mathematical Physics*, 3(4):771, December 1962. ISSN 00222488. doi: 10.1063/1.1724280. URL http://scitation.aip.org/content/aip/journal/jmp/3/4/10.1063/1.1724280.

[215] Thiab R Taha and Mark I Ablowitz. Analytical and numerical aspects of certain nonlinear evolution equations. II. Numerical, nonlinear Schrödinger equation. *Journal of Computational Physics*, 55(2):203–230, August 1984. ISSN 00219991. doi: 10.1016/0021-9991(84)90003-2. URL http://www.sciencedirect.com/science/article/pii/0021999184900032.

[216] Wen Qi Zhang, Heike Ebendorff-Heidepriem, Tanya M. Monro, and Shahraam Afshar V. Fabrication and supercontinuum generation in dispersion flattened bismuth microstructured optical fiber. *Optics Express*, 19(22):21135–21144, October 2011. ISSN 1094-4087. doi: 10.1364/OE.19.021135. URL http://www.opticsexpress.org/abstract.cfm?URI=oe-19-22-21135.

[217] K Inoue. Optical level equalisation based on gain saturation in fibre optical parametric amplifier. *Electronics Letters*, 36(12):1016–1017, 2000.

[218] M Shtaif and G Eisenstein. Noise properties of nonlinear semiconductor optical amplifiers. *Optics letters*, 21(22):1851–1853, 1996.

[219] M Shtaif and G Eisenstein. Experimental study of the statistical properties of nonlinearly amplified signals in semiconductor optical amplifiers. *Photonics Technology Letters, IEEE*, 9(7):904–906, 1997.

[220] K Inoue and T Mukai. Experimental study on noise characteristics of a gain-saturated fiber optical parametric amplifier. *Journal of lightwave technology*, 20(6):969, 2002.

[221] M Matsumoto and K Sanuki. Performance improvement of DPSK signal transmission by a phase-preserving amplitude limiter. *Optics Express*, 15(13):8094–8103, 2007.

[222] J Hansryd, P A Andrekson, M Westlund, J Li, and P O Hedekvist. Fiber-based optical parametric amplifiers and their applications. *Selected Topics in Quantum Electronics, IEEE Journal of*, 8(3):506–520, 2002.

[223] Ju Han Lee, Tatsuo Nagashima, Tomoharu Hasegawa, Seiki Ohara, Naoki Sugimoto, and Kazuro Kikuchi. Bismuth-Oxide-Based Nonlinear Fiber With a High SBS Threshold and Its Application to Four-Wave-Mixing Wavelength Conversion Using a Pure Continuous-Wave Pump. *J. Lightwave Technol.*, 24(1):22–, 2006. URL http://jlt.osa.org/abstract.cfm?URI=jlt-24-1-22.

[224] Quentin Coulombier, Laurent Brilland, Patrick Houizot, Thierry Chartier, Thanh Nam N'guyen, Frédéric Smektala, Gilles Renversez, Achille Monteville, David Méchin, Thierry Pain, Hervé Orain, Jean-Christophe Sangleboeuf, and Johann Trolès. Casting method for producing low-loss chalcogenide microstructured optical fibers. *Optics express*, 18(9): 9107–12, April 2010. ISSN 1094-4087. doi: 10.1364/OE.18.009107. URL http://www.opticsinfobase.org/viewmedia.cfm?uri=oe-18-9-9107&seq=0&html=true.

[225] D.C. Tran, C.F. Fisher, and G.H. Sigel. Fluoride glass preforms prepared by a rotational casting process. *Electronics Letters*, 18(15):657, July 1982. ISSN 00135194. doi: 10.1049/el:19820448. URL http://ieeexplore.ieee.org/articleDetails.jsp?arnumber=4246587.

[226] J. Massera, A. Haldeman, D. Milanese, H. Gebavi, M. Ferraris, P. Foy, W. Hawkins, J. Ballato, R. Stolen, L. Petit, and K. Richardson. Processing and characterization of coreclad tellurite glass preforms and fibers fabricated by rotational casting. *Optical Materials*, 32(5):582–588, March 2010. ISSN 09253467. doi: 10.1016/j.optmat.2009.12.003. URL http://linkinghub.elsevier.com/retrieve/pii/S0925346709003632.

[227] Christopher J. Voyce, Alistair D. Fitt, John R. Hayes, and TanyaM. Monro. Mathematical Modeling of the Self-Pressurizing Mechanism for Microstructured Fiber Drawing. *J. Lightwave Technol.*, 27(7):871–878, 2009. URL http://jlt.osa.org/abstract.cfm?URI=jlt-27-7-871.

[228] VITRON-Spezialwerkstoffe. Infrared Chalcogenide Glass IG5, 2014. URL http://www.infrared-materials.com/en/files/chalkonidglaeser/english/1219schott_ig5.pdf.

[229] W Egel-Hess and E Roeder. Extrusion of glass melts: influence of wall friction effects on the die swell phenomenon. *Glastechnische Berichte*, 62(8):279–284, 1989. ISSN 0017-1085. URL http://cat.inist.fr/?aModele=afficheN&cpsidt=6576929.

[230] Mohamed Trabelssi, Heike Ebendorff-Heidepriem, Kathleen C. Richardson, Tanya M. Monro, and Paul F. Joseph. Computational Modeling of Die Swell of Extruded Glass Preforms at High Viscosity. *Journal of the American Ceramic Society*, 97(5):1572–1581, May 2014. ISSN 00027820. doi: 10.1111/jace.12913. URL http://doi.wiley.com/10.1111/jace.12913.

[231] Amorphous Materials. AMTIR amorphous material transmitting IR radiation. URL http://www.amorphousmaterials.com/app/download/6552854504/AMTIR-1+Information.pdf.

[232] E. Roeder. Flow behaviour of glass during extrusion. *Journal of Non-Crystalline Solids*, 7(2):203–220, March 1972. ISSN 00223093. doi: 10.1016/0022-3093(72)90290-6. URL http://www.sciencedirect.com/science/article/pii/0022309372902906.

[233] Sean Manning. *A study of tellurite glasses for electro-optic optical fibre devices.* PhD thesis, University of Adelaide, 2011. URL http://digital.library.adelaide.edu.au/dspace/handle/2440/71483.

[234] Keiron Boyd, Heike Ebendorff-Heidepriem, Tanya M. Monro, and Jesper Munch. Surface tension and viscosity measurement of optical glasses using a scanning CO_2 laser. *Optical Materials Express*, 2(8):1101, July 2012. ISSN 2159-3930. doi: 10.1364/OME.2.001101. URL http://www.opticsinfobase.org/ome/abstract.cfm?URI=ome-2-8-1101.

[235] Heike Ebendorff-Heidepriem, Tze-Cheung Foo, Roger C. Moore, Wenqi Zhang, Yahua Li, Tanya M. Monro, Alexander Hemming, and David G. Lancaster. Fluoride glass microstructured optical fiber with large mode area and mid-infrared transmission. *Optics Letters*, 33(23):2861, November 2008. ISSN 0146-9592. doi: 10.1364/OL.33.002861. URL http://ol.osa.org/abstract.cfm?URI=ol-33-23-2861.

[236] H. Ebendorff-Heidepriem, P. Petropoulos, R. Moore, K. Frampton, D.J. Richardson, and T.M. Monro. Fabrication and optical properties of lead silicate glass holey fibers. *Journal of Non-Crystalline Solids*, 345-346:293–296, October 2004. ISSN 00223093. doi: 10.1016/j.jnoncrysol.2004.08.098. URL http://www.sciencedirect.com/science/article/pii/S0022309304005666.

[237] H. Ebendorff-Heidepriem, Y. Li, and T.M. Monro. Reduced loss in extruded soft glass microstructured fibre. *Electronics Letters*, 43(24):1343, November 2007. ISSN 00135194. doi: 10.1049/el:20072562. URL http://ieeexplore.ieee.org/articleDetails.jsp?arnumber=4390982.

[238] Véronique Pagé and Lawrence R. Chen. Measuring chromatic dispersion of optical fiber using time-of-flight and a tunable multi-wavelength semiconductor fiber laser. *Optics Communications*, 265(1):161–170, 2006. URL http://www.sciencedirect.com/science/article/pii/S0030401806002355.

[239] Y. Horiuchi, Y. Namihira, and H. Wakabayashi. Chromatic dispersion measurement in 1.55 mu m narrow-band region using a tunable external-cavity laser. *IEEE Photonics Technology Letters*, 1(12):458–460, December 1989. ISSN 1041-1135. doi: 10.1109/68.46049. URL http://ieeexplore.ieee.org/articleDetails.jsp?arnumber=46049.

[240] Hen-Tai Shang. Chromatic dispersion measurement by white-light interferometry on metre-length single-mode optical fibres. *Electronics Letters*, 17(17):603, August 1981.

ISSN 00135194. doi: 10.1049/el:19810424. URL http://ieeexplore.ieee.org/articleDetails.jsp?arnumber=4245900.

[241] Ji Yong Lee and Dug Young Kim. Versatile chromatic dispersion measurement of a single mode fiber using spectral white light interferometry. *Optics Express*, 14(24):11608, 2006. ISSN 1094-4087. doi: 10.1364/OE.14.011608. URL http://www.opticsexpress.org/abstract.cfm?URI=oe-14-24-11608.

[242] L. Cohen. Comparison of single-mode fiber dispersion measurement techniques. *Journal of Lightwave Technology*, 3(5):958–966, October 1985. ISSN 0733-8724. doi: 10.1109/JLT.1985.1074327. URL http://ieeexplore.ieee.org/articleDetails.jsp?arnumber=1074327.

[243] G S Han and S W Kim. Numerical correction of reference phases in phase-shifting interferometry by iterative least-squares fitting. *Applied optics*, 33(31):7321–5, November 1994. ISSN 0003-6935. doi: 10.1364/AO.33.007321. URL http://ao.osa.org/abstract.cfm?URI=ao-33-31-7321.

[244] Ocean Optics. NIRQuest Series of Near Infrared Spectrometers. URL http://oceanoptics.com/product-category/nirquest-series/.

[245] L. Amato, A. Fellegara, P. Sacchetto, P. Boffi, A. Melloni, and M. Martinelli. Polarization-independent Kerr coefficient measurement in optical fibers. *Optics Letters*, 21(8):612, April 1996. ISSN 0146-9592. doi: 10.1364/OL.21.000612. URL http://ol.osa.org/abstract.cfm?URI=ol-21-8-612.

[246] A. Fellegara, L. Amato, P. Sacchetto, P. Boffi, A. Melloni, and M. Martinelli. Polarization insensitive measurement of the fiber-optic nonlinear refractive index. In *Optical Fiber Communications, OFC.*, pages 288–289. Opt. Soc. America, 1996. doi: 10.1109/OFC.1996.908301. URL http://ieeexplore.ieee.org/lpdocs/epic03/wrapper.htm?arnumber=908301.

[247] M. Artiglia, R. Caponi, F. Cisternino, C. Naddeo, and D. Roccato. A New Method for the Measurement of the Nonlinear Refractive Index of Optical Fiber. *Optical Fiber Technology*, 2(1):75–79, January 1996. ISSN 10685200. doi: 10.1006/ofte.1996.0007. URL http://www.sciencedirect.com/science/article/pii/S1068520096900073.

[248] C. Vinegoni, M. Wegmuller, and N. Gisin. Measurements of the nonlinear coefficient of standard, SMF, DSF, and DCF fibers using a self-aligned interferometer and a Faraday mirror. *IEEE Photonics Technology Letters*, 13(12):1337–1339, December 2001. ISSN 1041-1135. doi: 10.1109/68.969900. URL http://ieeexplore.ieee.org/articleDetails.jsp?arnumber=969900.

[249] R. Stolen and Chinlon Lin. Self-phase-modulation in silica optical fibers. *Physical Review A*, 17(4):1448–1453, April 1978. ISSN 0556-2791. doi: 10.1103/PhysRevA.17.1448. URL http://link.aps.org/doi/10.1103/PhysRevA.17.1448.

[250] M. Monerie and Y. Durteste. Direct interferometric measurement of nonlinear refractive index of optical fibres by crossphase modulation. *Electronics Letters*, 23(18):961, August 1987. ISSN 00135194. doi: 10.1049/el:19870676. URL http://ieeexplore.ieee.org/articleDetails.jsp?arnumber=4258744.

[251] Ilaria Cristiani, Riccardo Tediosi, Luca Tartara, and Vittorio Degiorgio. Dispersive wave generation by solitons in microstructured optical fibers. *Optics Express*, 12(1):124, January 2004. ISSN 1094-4087. doi: 10.1364/OPEX.12.000124. URL http://www.opticsexpress.org/abstract.cfm?URI=oe-12-1-124.

[252] Dane R. Austin, C. Martijn de Sterke, Benjamin J. Eggleton, and Thomas G. Brown. Dispersive wave blue-shift in supercontinuum generation. *Optics Express*, 14(25):11997, December 2006. ISSN 1094-4087. doi: 10.1364/OE.14.011997. URL http://www.opticsexpress.org/abstract.cfm?URI=oe-14-25-11997.

[253] A. Demircan and U. Bandelow. Analysis of the interplay between soliton fission and modulation instability in supercontinuum generation. *Applied Physics B*, 86(1):31–39, November 2006. ISSN 0946-2171. doi: 10.1007/s00340-006-2475-8. URL http://link.springer.com/10.1007/s00340-006-2475-8.

[254] J. P. Gordon. Dispersive perturbations of solitons of the nonlinear Schrödinger equation. *Journal of the Optical Society of America B*, 9(1):91, January 1992. ISSN 0740-3224. doi: 10.1364/JOSAB.9.000091. URL http://josab.osa.org/abstract.cfm?URI=josab-9-1-91.

[255] D. Kaup. Perturbation theory for solitons in optical fibers. *Physical Review A*, 42(9):5689–5694, November 1990. ISSN 1050-2947. doi: 10.1103/PhysRevA.42.5689. URL http://link.aps.org/doi/10.1103/PhysRevA.42.5689.

[256] F. M. Mitschke and L. F. Mollenauer. Experimental observation of interaction forces between solitons in optical fibers. *Optics Letters*, 12(5):355, May 1987. ISSN 0146-9592. doi: 10.1364/OL.12.000355. URL http://ol.osa.org/abstract.cfm?URI=ol-12-5-355.

[257] J C Eilbeck, J D Gibbon, P J Caudrey, and R K Bullough. Solitons in nonlinear optics. I. A more accurate description of the 2π pulse in self-induced transparency. *Journal of Physics A: Mathematical, Nuclear and General*, 6(9):1337–1347, September 1973. ISSN 0301-0015. doi: 10.1088/0305-4470/6/9/009. URL http://iopscience.iop.org/0301-0015/6/9/009.

[258] J. Scott Russell. Report of the British Association for the Advancement of Science. *Report of the British Association for the Advancement of Science.*, 14th Meeti:311–390, 1844. URL http://www.biodiversitylibrary.org/item/47344.

[259] Chaohao Gu. Soliton Theory and Its Applications. *NASA STI/Recon Technical Report A*, -1, 1995. URL http://adsabs.harvard.edu/abs/1995stia.book.....G.

[260] Alan C Newell. *Solitons in mathematics and physics*. SIAM, 1985.

[261] Akira Hasegawa, editor. *Optical Solitons in Fibers*, volume 116 of *Springer Tracts in Modern Physics*. Springer-Verlag, Berlin/Heidelberg, 1989. ISBN 3-540-50668-3. doi: 10.1007/BFb0041283. URL http://www.springerlink.com/index/10.1007/BFb0041283.

[262] Linn F. Mollenauer and James P. Gordon. *Solitons in Optical Fibers: Fundamentals and Applications(Google eBook)*. Academic Press, 2006. ISBN 0080465064. URL http://books.google.com/books?hl=en&lr=&id=rz8N4li-pdkC&pgis=1.

[263] Zhigang Chen, Mordechai Segev, and Demetrios N Christodoulides. Optical spatial solitons: historical overview and recent advances. *Reports on progress in physics. Physical Society (Great Britain)*, 75(8):086401, August 2012. ISSN 1361-6633. doi: 10.1088/0034-4885/75/8/086401. URL http://www.ncbi.nlm.nih.gov/pubmed/22836010.

[264] A. Weiner, J. Heritage, R. Hawkins, R. Thurston, E. Kirschner, D. Leaird, and W. Tomlinson. Experimental Observation of the Fundamental Dark Soliton in Optical Fibers. *Physical Review Letters*, 61(21):2445–2448, November 1988. ISSN 0031-9007. doi: 10.1103/PhysRevLett.61.2445. URL http://link.aps.org/doi/10.1103/PhysRevLett.61.2445.

[265] Akira Hasegawa. Transmission of stationary nonlinear optical pulses in dispersive dielectric fibers. II. Normal dispersion. *Applied Physics Letters*, 23(4):171, October 1973. ISSN 00036951. doi: 10.1063/1.1654847. URL http://scitation.aip.org/content/aip/journal/apl/23/4/10.1063/1.1654847.

[266] S Novikov. *Theory of solitons: the inverse scattering method*. Springer, 1984.

[267] J. Herrmann, U. Griebner, N. Zhavoronkov, A. Husakou, D. Nickel, J. C. Knight, W. J. Wadsworth, P. St. J. Russell, and G. Korn. Experimental Evidence for Supercontinuum Generation by Fission of Higher-Order Solitons in Photonic Fibers. *Phys. Rev. Lett.*, 88 (17):173901–173905, 2002. doi: 10.1103/PhysRevLett.88.173901. URL http://link.aps.org/doi/10.1103/PhysRevLett.88.173901.

[268] J. P. Gordon. Theory of the soliton self-frequency shift. *Optics Letters*, 11(10):662, October 1986. ISSN 0146-9592. doi: 10.1364/OL.11.000662. URL http://ol.osa.org/abstract.cfm?URI=ol-11-10-662.

[269] X. Liu, C. Xu, W. H. Knox, J. K. Chandalia, B. J. Eggleton, S. G. Kosinski, and R. S. Windeler. Soliton self-frequency shift in a short tapered airsilica microstructure fiber. *Optics Letters*, 26(6):358, March 2001. ISSN 0146-9592. doi: 10.1364/OL.26.000358. URL http://ol.osa.org/abstract.cfm?URI=ol-26-6-358.

[270] E A Golovchenko, E M Dianov, A M Prokhorov, and V N Serkin. Self-effect of femtosecond optical wave packets. In *Soviet Physics Doklady*, volume 31, page 494, 1986.

[271] F. Matera, A. Mecozzi, M. Romagnoli, and M. Settembre. Sideband instability induced by periodic power variation in long-distance fiber links. *Optics Letters*, 18(18):1499, September 1993. ISSN 0146-9592. doi: 10.1364/OL.18.001499. URL http://ol.osa.org/abstract.cfm?URI=ol-18-18-1499.

[272] Nail Akhmediev and Magnus Karlsson. Cherenkov radiation emitted by solitons in optical fibers. *Physical Review A*, 51(3):2602–2607, 1995.

[273] Yuri S Kivshar and Govind Agrawal. *Optical solitons: from fibers to photonic crystals*. Academic press, 2003.

[274] P. K. A. Wai, C. R. Menyuk, Y. C. Lee, and H. H. Chen. Nonlinear pulse propagation in the neighborhood of the zero-dispersion wavelength of monomode optical fibers. *Optics Letters*, 11(7):464, July 1986. ISSN 0146-9592. doi: 10.1364/OL.11.000464. URL http://ol.osa.org/abstract.cfm?URI=ol-11-7-464.

[275] Hermann A Haus and William S Wong. Solitons in optical communications. *Reviews of modern physics*, 68(2):423, 1996.

[276] J. M. Dudley and J. R. Taylor. *Supercontinuum Generation in Optical Fibers (Google eBook)*. Cambridge University Press, 2010. ISBN 1139486187. URL http://books.google.com/books?hl=en&lr=&id=JunF8uN2kFIC&pgis=1.

[277] G. Genty, M. Lehtonen, and H. Ludvigsen. Effect of cross-phase modulation on supercontinuum generated in microstructured fibers with sub-30 fs pulses. *Optics Express*, 12(19):4614, 2004. ISSN 1094-4087. doi: 10.1364/OPEX.12.004614. URL http://www.opticsexpress.org/abstract.cfm?URI=oe-12-19-4614.

[278] D. J. Dougherty, F. X. Kärtner, H. A. Haus, and E. P. Ippen. Measurement of the Raman gain spectrum of optical fibers. *Optics Letters*, 20(1):31, January 1995. ISSN 0146-9592. doi: 10.1364/OL.20.000031. URL http://ol.osa.org/abstract.cfm?URI=ol-20-1-31.

[279] Dawn Hollenbeck and Cyrus D. Cantrell. Multiple-vibrational-mode model for fiber-optic Raman gain spectrum and response function. *Journal of the Optical Society of America B*, 19(12):2886, December 2002. ISSN 0740-3224. doi: 10.1364/JOSAB.19.002886. URL http://josab.osa.org/abstract.cfm?URI=josab-19-12-2886.

[280] Govind P. Agrawal. Effect of intrapulse stimulated Raman scattering on soliton-effect pulse compression in optical fibers. *Optics Letters*, 15(4):224, February 1990. ISSN 0146-9592. doi: 10.1364/OL.15.000224. URL http://ol.osa.org/abstract.cfm?URI=ol-15-4-224.

[281] Govind P. Agrawal. Effect of gain dispersion and stimulated Raman scattering on soliton amplification in fiber amplifiers. *Optics Letters*, 16(4):226, February 1991. ISSN 0146-9592. doi: 10.1364/OL.16.000226. URL http://ol.osa.org/abstract.cfm?URI=ol-16-4-226.

[282] Jennifer H Lee, James van Howe, Xiang Liu, and Chris Xu. Soliton Self-Frequency Shift: Experimental Demonstrations and Applications. *IEEE journal of selected topics in quantum electronics : a publication of the IEEE Lasers and Electro-optics Society*, 14 (3):713–723, January 2008. ISSN 1077-260X. doi: 10.1109/JSTQE.2008.915526. URL http://ieeexplore.ieee.org/articleDetails.jsp?arnumber=4538044.

[283] F. M. Mitschke and L. F. Mollenauer. Discovery of the soliton self-frequency shift. *Optics Letters*, 11(10):659, October 1986. ISSN 0146-9592. doi: 10.1364/OL.11.000659. URL http://ol.osa.org/abstract.cfm?URI=ol-11-10-659.

[284] Esben Ravn Andresen, Victoria Birkedal, Jan Thø gersen, and Søren Rud Keiding. Tunable light source for coherent anti-Stokes Raman scattering microspectroscopy based on the soliton self-frequency shift. *Optics Letters*, 31(9):1328, May 2006. ISSN 0146-9592. doi: 10.1364/OL.31.001328. URL http://www.osapublishing.org/viewmedia.cfm?uri=ol-31-9-1328&seq=0&html=true.

[285] W. Hartig and W. Schmidt. A broadly tunable IR waveguide Raman laser pumped by a dye laser. *Applied Physics*, 18(3):235–241, March 1979. ISSN 0340-3793. doi: 10.1007/BF00885508. URL http://adsabs.harvard.edu/abs/1979ApPhy..18..235H.

[286] Samuli Kivisto, Tommi Hakulinen, Mircea Guina, and Oleg G. Okhotnikov. Tunable Raman Soliton Source Using Mode-Locked TmHo Fiber Laser. *IEEE Photonics Technology Letters*, 19(12):934–936, June 2007. ISSN 1041-1135. doi: 10.1109/LPT.2007.898877. URL http://ieeexplore.ieee.org/articleDetails.jsp?arnumber=4214869.

[287] B.R. Washburn, S.E. Ralph, P.A. Lacourt, J.M. Dudley, W.T. Rhodes, R.S. Windeler, and S. Coen. Tunable near-infrared femtosecond soliton generation in photonic crystal fibres. *Electronics Letters*, 37(25):1510, December 2001. ISSN 00135194. doi: 10.1049/el:20011047. URL http://ieeexplore.ieee.org/articleDetails.jsp?arnumber=972182.

[288] J.Y.Y. Leong, P. Petropoulos, J.H.V. Price, H. Ebendorff-Heidepriem, S. Asimakis, R.C. Moore, K.E. Frampton, V. Finazzi, X. Feng, T.M. Monro, and D.J. Richardson.

High-nonlinearity dispersion-shifted lead-silicate holey fibers for efficient 1um pumped supercontinuum generation. *Journal of Lightwave Technology*, 24(1):183–190, January 2006. ISSN 0733-8724. doi: 10.1109/JLT.2005.861114. URL http://ieeexplore.ieee.org/articleDetails.jsp?arnumber=1589049.